



**HAL**  
open science

# Modeling of the negative ion source and accelerator of the ITER Neutral Beam Injector

G. Fubiani

► **To cite this version:**

G. Fubiani. Modeling of the negative ion source and accelerator of the ITER Neutral Beam Injector. Plasma Physics [physics.plasm-ph]. Université Toulouse III Paul Sabatier, 2016. tel-01414273

**HAL Id: tel-01414273**

**<https://theses.hal.science/tel-01414273>**

Submitted on 22 Dec 2016

**HAL** is a multi-disciplinary open access archive for the deposit and dissemination of scientific research documents, whether they are published or not. The documents may come from teaching and research institutions in France or abroad, or from public or private research centers.

L'archive ouverte pluridisciplinaire **HAL**, est destinée au dépôt et à la diffusion de documents scientifiques de niveau recherche, publiés ou non, émanant des établissements d'enseignement et de recherche français ou étrangers, des laboratoires publics ou privés.



# Modeling of the negative ion source and accelerator of the ITER Neutral Beam Injector.

Gwenaël Fubiani

GREPHE, CNRS/LAPLACE Laboratory  
University of Toulouse (Paul Sabatier)



Université  
de Toulouse

Accreditation to supervise research

**Date of defence:** 09/12/2016

**Location:** University of Toulouse (Paul Sabatier)

**Members of the jury:**

Anne Bourdon (LPP, CNRS)

Khaled Hassouni (LSPM, U. of Paris XIII)

Minh Quang Tran (EPFL, Switzerland)

Jean-Pierre Boeuf (LAPLACE, CNRS)

Richard Fournier (LAPLACE, U. of Toulouse)

Vanni Antoni (RFX, Italy)

REFEREE

REFEREE

REFEREE

PRESIDENT



*To my two boys, my dear wife, my family and friends.*



# Who am I?

- Well, first of all, I am a proud father of two young boys! I guess this gives me a “dad index”  $d = 2$ .
- I also have a h-index  $h = 13$  corresponding to 850 citations (excluding self-citations) on September 23<sup>rd</sup> 2016.
- I am first author of 9 articles in peer-reviewed journals and of 3 conference proceedings.
- I co-authored 13 articles in peer-reviewed journals and 9 in conference proceedings.
- 28 oral presentations at international conferences and workshops (1 invited talk in a workshop, Yokohama, 2013). 15 posters.
- 2 invited seminars:
  - Chamber of Commerce, Reggio Calabria, Italy, December 2011.
  - AFRD, Lawrence Berkeley National Laboratory, Berkeley, CA, USA, June 2014.
- 1 technical report (LBNL 57514, <http://escholarship.org/uc/item/1wf8w5fs>).
- Co-author in 1 review paper (Reffet de la Physique, 2014)
- Member of the international committee of the NIBS conference (“Negative ions, Beams and Sources”) since 2012

- We have a grant from EUROfusion (for the moment until 2018). I am in charge of the project.
- I designed the EAMCC model which simulates secondary particle production in the accelerator of the ITER Neutral Beam Injector (NBI). It is used nowadays by 4 laboratories in the fusion community (RFX - Italy, CEA - France, JAEA - Japan and CCFE - UK).
- I co-directed the thesis of 2 PhD students:
  - N. Kohen (defended in 2015). Nicolas worked on the modeling of the neutral depletion inside fusion-type ion sources (chapter 5). He participated with a former student to the coupling of the Direct-Simulation-Monte-Carlo algorithm (DSMC) with a 2D implicit fluid model (developed by G. Hagelaar) and analyzed neutral depletion versus the external parameters of the negative ion source (power, background gas pressure and the incidence of the magnetic filter field). Nicolas was co-author in one peer-reviewed article.
  - J. Claustre (defended in 2013). Jonathan developed a 2D and 3D PIC-MCC model parallelized on a graphic card (Graphics Processing Unit, GPU). He applied his model to the simulation of the ITER prototype BATMAN ion source. Jonathan wrote 2 papers as first author (1 peer reviewed journal and 1 conference proceeding) and was co-author in 1 peer-reviewed article. He is currently a post-doctoral researcher in Canada.
- Lastly, I had 3 students for an internship:
  - One student from an engineer school (Polytech Orleans) for a duration of 3 month (2014). She learned how to model differential equations numerically using the finite difference technique. At the end of her internship, she studied a 2D multigrid solver applied to the Poisson equation.
  - I had two students in Bachelor (University of Toulouse III, Paul Sabatier) for a duration of 2 month (2016). I taught them the basic plasma physics of a negative ion source.

- I will be in charge of a PhD student next fall. He will work on the CYBELE project in collaboration with IRFM (CEA, France), EPFL (Switzerland) and LPSC (Grenoble, France).
- I was hired by CNRS in 2007 (but started work in January 2008). I am currently in the GREPHE group at the LAPLACE laboratory (University of Toulouse, Paul Sabatier, Toulouse, France).
- I was a post-doctoral researcher at IRFM, CEA, Cadarache for 2 years (2006-2007).
- I did my PhD thesis at the LOASIS group, Lawrence Berkeley National Laboratory, Berkeley, CA, USA (2000-2005). I worked on laser-plasma interactions (modeling)
- I studied theoretical physics at the University of Paris XI, Orsay (Bachelor and Master).
  - My Bachelor internship was at the Stanford Linear Accelerator Center (SLAC), Stanford University, CA, USA (4 month, 1998). I developed a model to analyze the background noise in the PEP-II accelerator. I was co-author in 1 conference proceedings.
  - During my Master, I had a 4 month internship at Thales Electron Device (TED), Velizy, France (1999). I worked on the design of a Gyrotron.



# Table of Contents

<b>1</b>	<b>Introduction</b>	<b>1</b>
<b>2</b>	<b>Numerical model</b>	<b>13</b>
2.1	Particle-in-Cell model of a negative ion source . . . . .	14
2.1.1	Parallelization . . . . .	14
2.1.2	Scaling . . . . .	17
2.1.3	2.5D PIC-MCC approximation . . . . .	18
2.1.4	External RF power absorption and Maxwellian heating in the discharge . . . . .	21
2.2	Implementation of collisions in a particle model - MC and DSMC methods	22
2.3	Elastic and inelastic collision processes . . . . .	25
2.3.1	Physical chemistry of charged particles . . . . .	26
2.3.2	Physical chemistry of neutrals . . . . .	29
2.4	Negative ions . . . . .	30
2.5	Simulation domain . . . . .	31
<b>3</b>	<b>The Hall effect in plasmas</b>	<b>35</b>
3.1	General features . . . . .	36
3.2	Simplified geometry . . . . .	37
<b>4</b>	<b>Comparisons between 2D and 3D PIC simulations</b>	<b>43</b>
4.1	Introduction . . . . .	44
4.2	Simulation characteristics . . . . .	44
4.2.1	Plasma dynamics in the plane perpendicular to the magnetic field lines . . . . .	45
4.2.2	Plasma dynamics in the plane parallel to the filter field lines .	47

4.3	2D and 2.5D models . . . . .	48
4.4	Error induced by increasing the vacuum permittivity constant . . . . .	54
4.5	Conclusion . . . . .	55
<b>5</b>	<b>Neutral depletion</b>	<b>57</b>
5.1	Introduction . . . . .	58
5.2	Modeling of neutral depletion in the ITER BATMAN prototype . . . . .	59
<b>6</b>	<b>Role of positive ions on the production of negative ions on the cesiated plasma grid</b>	<b>67</b>
6.1	Introduction . . . . .	68
6.2	General plasma properties from a simplified model without negative ions	69
6.2.1	Characteristics of the plasma potential . . . . .	71
6.2.2	Charged particle flux onto the PG . . . . .	72
6.3	Results with negative ions . . . . .	74
6.3.1	Charged particle currents versus bias on the PG . . . . .	75
6.3.2	Positive ion energy and mean-free-path in the expansion chamber	77
6.4	Conclusion . . . . .	78
<b>7</b>	<b>Effect of biasing the plasma electrode on the plasma asymmetry</b>	<b>81</b>
7.1	Introduction . . . . .	82
7.2	3D PIC model of the one-driver prototype source at BATMAN . . . . .	83
7.2.1	Plasma characteristics in the drift plane versus the PG bias voltage . . . . .	84
7.2.2	Plasma parameters in the vicinity of the PG . . . . .	86
7.2.3	Comparison with experiments . . . . .	91
7.3	2.5D PIC-MCC model of the half-size ITER prototype ion source ELISE	93
7.3.1	Hall effect in ELISE as predicted by 2.5D PIC simulations . . . . .	94
7.3.2	Plasma parameters in the vicinity of the PG . . . . .	97
7.3.3	Comparison with experimental observations . . . . .	98
7.4	Conclusion . . . . .	99
<b>8</b>	<b>Negative ions</b>	<b>101</b>
8.1	Introduction . . . . .	102
8.2	Negative ion dynamics inside the ion source volume . . . . .	103

8.3	Electron and negative ion extraction versus the PG bias voltage . . .	105
8.4	Extracted electron and negative ion beamlet profiles on the extraction grid . . . . .	108
<b>9</b>	<b>Extraction of negative ions</b>	<b>111</b>
9.1	Introduction . . . . .	112
9.2	Numerical issues . . . . .	112
9.3	Model . . . . .	113
9.4	Convergence . . . . .	114
9.5	Plasma meniscus . . . . .	115
9.6	Virtual cathode profile . . . . .	118
9.7	Scaling laws . . . . .	120
9.8	Extracted beam properties . . . . .	121
9.9	Application to a 3D PIC-MCC model of negative ion extraction . . .	122
9.9.1	Low density calculation . . . . .	123
9.9.2	Scaled parameters . . . . .	124
<b>10</b>	<b>Secondary emission processes in the negative ion based electrostatic accelerator of the ITER NB injector</b>	<b>127</b>
10.1	Introduction . . . . .	128
10.2	Detailed description of the numerical approach . . . . .	130
10.2.1	Electron impact on accelerator grids . . . . .	130
10.2.2	Negative ion stripping inside the accelerator downstream of the extraction grid . . . . .	135
10.2.3	Heavy particle impact with accelerator grids . . . . .	139
10.3	Applications . . . . .	142
10.3.1	Negative ion induced secondary emission . . . . .	143
10.3.2	Power deposition induced by beamlet halos . . . . .	147
10.3.3	Co-extracted plasma electrons . . . . .	150
10.4	Conclusion . . . . .	152
<b>11</b>	<b>Modeling of the two ITER NBI accelerator concepts</b>	<b>155</b>
11.1	Introduction . . . . .	156
11.2	Numerical method . . . . .	157
11.3	The SINGAP accelerator . . . . .	158

11.3.1	Secondary particle power deposition . . . . .	160
11.3.2	Experimental measurements . . . . .	162
11.4	ITER accelerator power supply characteristics . . . . .	166
11.5	Conclusion . . . . .	168
<b>12</b>	<b>Conclusions and perspectives</b>	<b>171</b>
<b>A</b>	<b>Implicit PIC modeling</b>	<b>179</b>
A.1	Introduction . . . . .	180
A.2	Comparison between explicit and implicit PIC calculations . . . . .	180
A.3	The direct implicit particle in cell method . . . . .	185
A.3.1	Leap-frog Poisson system . . . . .	185
A.3.2	Boundary conditions . . . . .	188
	<b>References</b>	<b>190</b>

# Chapter 1

## Introduction

Negative ion sources are used in a variety of research fields and applications [1] such as in tandem type electrostatic accelerators, cyclotrons, storage rings in synchrotrons, nuclear and particle physics (for instance to produce neutrons in the Spallation Neutron Source [2]) and in magnetic fusion devices (generation of high power neutral beams [3]). High brightness negative ion sources (i.e., which produces large negative ion currents) use cesium vapor to significantly enhance the production of negative ions on the source cathode surface. Cesium lowers the work function of the metal and hence facilitate the transfer of an electron from the metal surface to a neutral hydrogen atom by a tunnelling process. Main types of devices which use cesium are magnetrons, penning and multi-cusps ion sources. The former have applications in accelerators for instance. The latter are often large volume ion sources and are the type currently developed for fusion applications. The plasma in large volume devices is generated typically by hot cathodes (heated filaments) or Radio-Frequency (RF) antennas (Inductively-Coupled-Plasma discharges) standing either inside or outside the discharge [1]. Fusion type ion sources are tandem type devices with a so-called expansion chamber juxtaposed next to the discharge region. The expansion chamber is often magnetized with magnetic field lines perpendicular to the electron flux exiting the discharge. The magnetic field strength is typically of the order of  $\sim 100\text{G}$  and is generated either by permanent magnets placed along the lateral walls of the ion source or via a large current flowing through the plasma electrode (which is also called “plasma grid”). The latter separates the ion source plasma from the accelerator region, where the extracted negative ions are accelerated to high energies (typically on a MeV scale). The axial electron mobility is strongly reduced by the magnetic field inside the expansion chamber and the electron temperature is hence significantly lowered as electrons loose energy through collisions. In fusion-type ion sources, the background gas pressure (either hydrogen or deuterium type) is  $\sim 0.3\text{ Pa}$  and the electron temperature is of the order of  $10\text{ eV}$  inside the discharge region. The magnetic filter reduces the electron temperature down to the electron-Volts level in the extraction region, close to the plasma grid (PG). The role of the magnetic filter field in the expansion chamber is threefold: (i) a large versus low electron temperature between the discharge and the extraction region allows the production of negative ions through the dissociative impact between an electron and a hydrogen (or deuterium) molecule  $\text{H}_2(\nu \geq 4)$ , where  $\nu$  is the vibrational level. The vibrational excitation of the

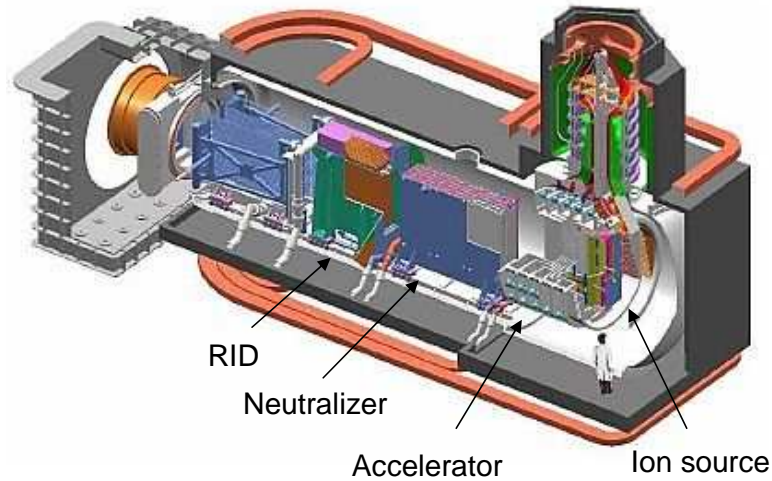


Figure 1.1: The ITER Neutral Beam Injector (NBI). The high power, low pressure, large volume negative ion source produces about 55A of ions split over 1280 beamlets. The latter are accelerated to 1 MeV inside the electrostatic accelerator. 40A of negative ions are accelerated, the rest is lost inside the accelerator through collisions with the residual background gas. The ions exiting the accelerator are neutralized inside the gas neutralizer (Deuterium). The Residual Ion Dump (RID) collects the remaining ions.

hydrogen molecule is maximised at high electron temperatures (typically  $T_e \sim 10$  eV) while the cross-section for the dissociative attachment of  $H_2$  and hence the production of a negative ion is the largest for  $T_e \sim 1$  eV. (ii) A low electron temperature in the vicinity of the PG significantly increases the survival rate of the negative ions and (iii) the magnetic filter lowers the electron flux onto the PG and hence the co-extracted electron current from the negative ion source. Co-extracted electrons have a damaging effect inside the electrostatic accelerator [4]. The electron beam is unfocused and induces a large parasitic power deposition on the accelerator parts. Note that in fusion-type, high power, large volume and low pressure ion sources, negatives ions produced via dissociative attachment of the background gas molecules (so called “volume processes”) range between 10–20% of the total amount of extracted negative ion current [5, 6], the remaining part corresponds to ions generated on the cesiated PG surface through neutral atom and positive ion impacts. In magnetic fusion applications, negative ion sources are a subset of a Neutral Beam Injector (NBI) producing a high power neutral beam which is injected into the Tokamak plasma (Fig. 1.1). Neu-

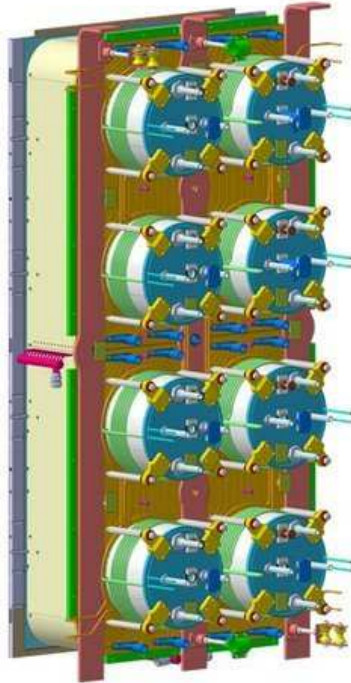


Figure 1.2: ITER high power, low pressure, tandem type negative ion source.

trals are insensitive to magnetic fields and can hence penetrate into the hot plasma core. The neutral beam provides power to the plasma, current (which is necessary to sustain the poloidal magnetic field) and are helpful to minimize the buildup of some type of instabilities. In the future International Thermonuclear Experimental Reactor (ITER), NBIs are designed to inject 33 MW of power (split over two beam lines) with an energy of 1 MeV into the Tokamak plasma [7]. The ITER project is the first fusion device which will mainly be heated by alpha particles ( $\text{H}_e^{2+}$ ). The plasma will consist of Deuterium and Tritium ions providing 500 MW of fusion power. 50 MW of additional external power will be necessary in order to heat and control the plasma during the operating phase while the alpha particles will re-inject 100 MW of power to the fusion plasma (the total heating power is 150 MW). The remaining 400 MW is carried by the neutrons toward the wall of the Tokamak [8]. The external heating system for ITER also includes 20 MW of electron cyclotron heating at 170 GHz and 20 MW of ion cyclotron heating in the 35 – 65 MHz frequency range [9]. Total power is consequently 73 MW (including neutral beams), slightly above the required 50 MW

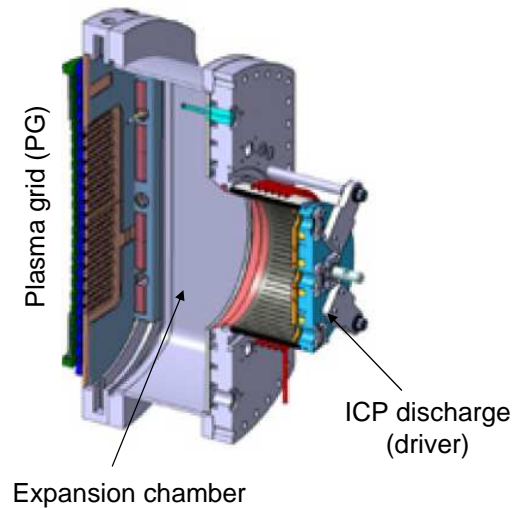


Figure 1.3: The 1/8th ITER prototype negative ion source at BATMAN (BAvarian Test MACHine for Negative ions).

for ITER.

The ITER negative ion source [10], which is shown in Fig. 1.2, is a tandem-type device composed of eight Inductively Coupled Plasma (ICP) discharges (so-called drivers) each with a radius of 13.7 cm and length 14.8 cm. The large Radio-Frequency (RF) power (typically  $\sim 100$  kW per driver) is coupled to the plasma by cylindrical coils. The drivers are attached to a large magnetized expansion chamber whose dimensions are 1.8 m x 0.9 m of cross sectional area and 0.23 m in length [11, 12]. The magnetic field profile is generated by a high current ( $\sim 5$  kA) flowing through the plasma grid (PG). The latter is in contact with the ion source plasma and has 1280 apertures through which the negative ion beamlets are extracted toward an electrostatic accelerator. The field strength is of the order of 10 to 60G inside the plasma region [13, 14].

In this work we analyse in details the plasma and neutral particle transport properties of high RF power fusion-type magnetized negative ion sources, including negative ion extraction. As an example, we model the ITER prototype negative ion source at BATMAN [5, 12, 15, 16] (BAvarian Test MACHine for Negative ions, Max-Planck-Institut für Plasmaphysik, Garching, Germany). The source is a tandem type device similar to the ITER configuration but with one ICP discharge (driver) and a smaller

expansion chamber volume, accordingly. BATMAN is hence better suited to numerical modeling due to its smaller volume (about 1/8th of the ITER negative ion source). The driver dimensions are a cylinder of diameter 24.5 cm and length 16 cm [15, 17]. An external cylindrical antenna confers to the background gas (either molecular hydrogen or deuterium) about 100 kW of RF power, which generates a high density plasma of the order of  $4 \times 10^{17} \text{ m}^{-3}$  (averaged over the whole ion source volume). The expansion chamber, which is connected to the driver, has a larger volume and is magnetized; its size is approximately 57.9 cm in height, width of 30.9 cm and 24.4 cm in depth. The magnetic filter field in BATMAN is generated by permanent magnets in a dipole configuration positioned against the lateral walls of the ion source near the PG (the field strength is maximum on axis close to the PG with  $B_{\text{max}} = 75\text{G}$ ). The direction of the magnetic field is parallel to the PG. Electrons are strongly magnetized inside the expansion chamber contrary to the positive ions which flow down the ambipolar potential toward the ion source walls. Note that with a PG biased positively with respect to the other ion source surfaces, some subset of positive ions may be slightly magnetized (typically ions which experienced a binary collision inside the expansion chamber or which were created by an ionization process). The flow of electrons  $\Gamma_e$  diffusing away from the discharge region is re-directed toward the lateral walls of the ion source by the Lorentz force inside the expansion chamber. The plasma quasi-neutrality (restoring force) self-generates an electric field which opposes to the electron flux (the losses on the ion source walls are hence minimized). This is a phenomenon analogous to the Hall effect in semi-conductors. The Hall electric field counteracts the Lorentz force and is hence directed along  $\mathbf{J}_e \times \mathbf{B}$  (where  $\mathbf{J}_e = -e\Gamma_e$  and  $e$  is the elementary charge), i.e., parallel to the PG [18–22]. The Hall effect generates a transverse asymmetry in the plasma which is further enhanced by the PG bias voltage [16, 23]; the plasma asymmetry peaks around the location of maximum potential. This is a critical issue for ITER as the acceptance for the electrostatic accelerator is confined to deviations of  $\pm 10\%$  of the extracted negative ion current density.

Furthermore, a background gas pressure of  $\sim 0.3 \text{ Pa}$  and a 100 kW scale RF power induce a large depletion of neutrals. We demonstrate using a Direct-Simulation-Monte-Carlo (DSMC) method [24, 25] that the distribution functions of the neutral species are non-Maxwellian. In addition, we show that the depletion of molecular

hydrogen is  $\sim 65\%$  for an absorbed RF power of 60 kW in the model ( $T_{H_2} \simeq 700$  K). The neutral atom density saturates around  $n_H \simeq 8 \times 10^{18} \text{ m}^{-3}$  beyond a power of 40 kW while the temperature increases steadily ( $T_H = 0.85$  eV for  $P_{\text{abs}} = 60$  kW). These values are consistent with experimental measurements [26].

The numerical method employed in this work is essentially based on the Particle-In-Cell algorithm with Monte-Carlo collisions (PIC-MCC). The ITER prototype source at BATMAN is large volume (i.e., a driver of  $\sim 7500 \text{ cm}^3$  and an expansion chamber of  $\sim 44000 \text{ cm}^3$ ) with a plasma density of the order of  $\sim 1.5 \times 10^{18} \text{ m}^{-3}$  in the driver [15]. This implies cumbersome constraints on the PIC-MCC modeling which must solve for the Debye length on the numerical grid and use time steps smaller than the transit time for a thermal electron to cross a grid cell (so-called Courant-Friedrichs-Lewy, CFL, condition), otherwise a numerical instability will be generated. The lowest value for the electron Debye length in BATMAN is  $\lambda_{De} \sim 10 \text{ }\mu\text{m}$  and the time step is typically limited to  $\Delta t \simeq 2 \times 10^{-12} \text{ s}$  (i.e.,  $\omega_{pe} \sim 6 \times 10^{10} \text{ s}^{-1}$ , where  $\omega_{pe}$  is the electron plasma frequency). The numerical resolution must hence be  $\sim 10^{14}$  grid points in 3-dimensions (3D). The time for the model to converge is based approximately on the residence time of the ions, which is of the order of  $30 \text{ }\mu\text{s}$  (i.e.,  $2 \times 10^7$  time steps). We developed a parallel PIC-MCC algorithm with a hybrid OpenMP [27] and Message-Passing-Interface (MPI) parallelization scheme. The performance of the particle pusher is  $\sim 150 \text{ ns} \cdot \text{core} \cdot \text{particle}^{-1}$ . Using such a small time step and grid size is hence not practical even with today's computers. We show in this work that modeling lower plasma densities is a solid alternative to provide a detailed description of the plasma transport properties in a fusion-type high power, large volume, negative ion source [18, 19, 23].

A similar numerical issue applies to the modeling of negative ion extraction from the PG apertures. Slit apertures may be modeled in 2D geometry for the typical plasma densities found in the extraction region of fusion-type negative ion sources. In the one-driver prototype source at BATMAN, a positive ion density of  $n_p \simeq 1.5 \times 10^{17} \text{ m}^{-3}$  for 60 kW of RF power in the discharge and a hydrogen background gas pressure of 0.3 Pa [15, 16] is measured 2.2 cm from the cesiated PG surface (there is 140 chamfered cylindrical apertures on the electrode [5]). The simulation domain is restricted to a zoom around a single aperture, with transverse dimensions related to the spacing between aperture rows and columns and axially a length of the order of the

distance from the PG where the plasma properties are measured experimentally [28–31]. For BATMAN, the size of the simulation box is typically a length  $\Delta x \simeq 3.2$  cm (including the first accelerator grid downstream the PG) and a transverse cross-section of  $1.2 \times 1.2$  cm<sup>2</sup> with an aperture radius of  $r = 4$  mm (not chamfered). Simulating negative ion extraction produced on the PG surface in the case of cylindrical apertures requires the implementation of a 3D PIC-MCC model and consequently the restriction on the numerical grid size to be of the order of the Debye length is still a hefty constrain, with about  $10^9$  grid points necessary and  $5 \times 10^6$  time steps (corresponding again to an integrated time of  $\sim 30$   $\mu$ s).

In this work, as frequently as possible, we will compare the numerical model to experimental measurements. In order to facilitate the reading, figures, equations, chapters, sections and references are hyperlinked (a simple click will bring you directly to their location within the text). This manuscript is organized in a logical order, where we first start with the numerical model, followed by the properties of a typical fusion-type negative ion source, negative ion extraction and lastly electron and ion transport inside the NBI electrostatic accelerator (including secondary particle production):

- In the next chapter, we describe in details the hybrid OpenMP and MPI 3-dimensional (3D) Particle-In-Cell model with Monte-Carlo Collisions (PIC-MCC), which I developed. The whole algorithm, including the Poisson solver and the parallelization has been designed by myself. I consider that in this way, the chances to misinterpret the numerical results due to either a simple bug in the model or the inherent physical simplifications which can be found in any type of codes even commercial are minimized. The 3D PIC-MCC model includes collisions between charged particles and neutral. The complex physical chemistry for Hydrogen together with the mean to compute the collisions numerically are provided. This model was designed specifically to study the particle transport inside the magnetized expansion chamber and the extraction of negative ions. The ICP discharge is described in a simple manner. Due to the fact that the background gas pressure is low ( $\sim 0.3$  Pa) and the influence of the DC magnetic field from the expansion chamber is negligible, we assume that the mean-free-path of the electrons is of the order of the dimension of the discharge

---

and we hence consider that the RF power absorption profile is constant. The non-linear ponderomotive force resulting from the photon pressure generated by the high RF power as well as any anomalous power absorption (non-local effects) which are found with MHz-scale antenna frequencies are consequently neglected. This is left for future work. The numerical model of the discharge may be simply viewed as a particle source term for the flow toward the expansion chamber which we aim to assess precisely.

- Chapter 3 analyses the Hall effect in magnetized plasma sources. We model a simple square geometry in 2D without any ionization processes in order to draw an electron current, exclusively generated inside the discharge, across the magnetic filter. This configuration reduces the complexity which is found in the real negative ion source. The incidence of the Hall effect in BATMAN and the resulting plasma asymmetry will be discussed in the subsequent chapters. Lastly, in this chapter we will demonstrate the invariance of the plasma characteristics when either scaling down the plasma density or similarly artificially increasing the vacuum permittivity. This observation is critical to simulate high density plasma sources with PIC-MCC models.
- Chapter 4 compares 3D versus 2D PIC-MCC estimates for the BATMAN 1/8 th ITER prototype. Numerical calculations with a high resolution may be performed in 2D. The lack of one dimension is accounted for with the implementation of a simple particle loss model on the ion source walls. The plane perpendicular to the magnetic field lines is simulated for the description of the Hall effect without any loss of generality compared to a 3D calculation.
- The depletion of the neutrals (molecular and atomic hydrogen) is modeled in chapter 5. For this specific case, a Direct-Simulation-Monte-Carlo (DSMC) method is coupled to an implicit fluid model for the charged particles (developed by my colleague G. Hagelaar). The DSMC algorithm was written by our PhD students P. Sarrailh and N. Kohen. We will estimate the negative ion current produced on the cesiated plasma grid from the calculated flux of neutral atoms.
- The role of the positive ions on the production of negative ions on the (cesiated) PG surface is analysed in chapter 6. This was a matter debated a couple of

years ago in the ITER community. This is one of the questions which could be easily studied with a numerical model.

- In chapter 7, we model the incidence of the PG bias voltage on the plasma asymmetry both for the BATMAN and the half-size ELISE prototype negative ion sources. The latter has 4 ICP discharges (drivers) instead of 8. The PG bias modulates the electron current drawn from the drivers and hence the incidence of the Hall effect.
- The negative ion dynamics inside the ion source volume is modeled in chapter 8. We assess the ions mean-free-paths as well as the extracted currents (electron and negative ions) versus the PG bias voltage. We simulate the whole ion source geometry with a 2.5D PIC-MCC model (particle losses along the direction parallel to the magnetic field lines are approximated), including 7 slit apertures. A discussion on the asymmetry of the extracted negative ion beamlets is provided.
- A PIC-MCC model restricted to a small area around a single PG aperture is described in chapter 9. This allows us to increase the numerical resolution. In 2D, we can actually simulate the real ITER plasma density. In 3D however, we still need to use scaling factors. We hence derive scaling laws from a 2D model for slit apertures (where we correlate the plasma characteristics for plasma densities varying by up to 2 order of magnitudes) which we later apply to model cylindrical apertures in 3D.
- A critical issue for the ITER NBI accelerator concerns the production of secondary particles by both the electrons and the negative ions extracted from the negative ion source. Secondary particles may damage the accelerator parts. The 3D particle tracking model with Monte-Carlo collisions which I developed to model the secondary particle dynamics (EAMCC) is described in chapter 10. The accelerator designed for ITER (so called “MAMuG”) is modeled in this chapter.
- EAMCC is used as of today by 4 laboratories in the fusion community worldwide. This numerical model together with experimental measurements provided physical arguments to exclude the SINGAP accelerator as a concept for

the ITER NBI. In addition, the MAMuG power supplies characteristics were calculated by EAMCC. This is summarized in chapter 11.

- Lastly, conclusions are provided in chapter 12. We will summarize the work presented in this manuscript. A discussion on how well the model compares to experimental measurements together with the remaining open questions which should be studied in the future is included in this chapter.
- I also developed an implicit PIC-MCC model which is described in Appendix A.



# Chapter 2

## Numerical model

### Contents

---

2.1	Particle-in-Cell model of a negative ion source . . . . .	14
2.2	Implementation of collisions in a particle model - MC and DSMC methods . . . . .	22
2.3	Elastic and inelastic collision processes . . . . .	25
2.4	Negative ions . . . . .	30
2.5	Simulation domain . . . . .	31

---

## 2.1 Particle-in-Cell model of a negative ion source

We calculate plasma transport in a fusion-type negative ion source using a 3D parallel Cartesian electrostatic explicit PIC-MCC model [32, 33]. This model was entirely developed by myself, including the Poisson solver. In an explicit algorithm, the particle trajectories are calculated based on the fields evaluated at the previous time step. The (self) electric field is derived self-consistently from the densities estimated on the grid nodes of the simulation domain. The magnetic fields, filter and suppression fields (the latter is generated by permanent magnets embedded in the first grid of the accelerator), are prescribed in this work. The time step must be a fraction of the electron plasma period and the grid size close to the electron Debye length, accordingly (both are set by the lightest of the simulated particles).

### 2.1.1 Parallelization

The parallelization is performed in a hybrid manner using OpenMP [27] and MPI libraries. We use a particle-decomposition scheme for the particle pusher where each core (thread) have access to the whole simulation domain (as opposed to a domain-decomposition approach). The number of particles per core is nearly identical. We further implemented a sorting algorithm [34] in order to limit the access to the computer memory (RAM) and boost the execution time,  $\Delta t_{\text{push}}$ , of the pusher subroutine. The subroutine includes electron heating (inside the ICP discharge), field interpolations, update of the velocities and positions together with the charge deposition on the grid nodes. Particles are sorted per grid cell. The field and density arrays are hence accessed sequentially.  $\Delta t_{\text{push}}$  is shown in Fig 2.1 normalized to the number of particles in the simulation. The best performance is obtained by attaching a MPI thread per socket and a number of OpenMP threads identical to the number of cores per socket. For the simulations of Fig. 2.1, we set the number of OpenMP threads to 10. We sort particles every 10 time steps without any loss of performance. The calculation is performed with a 3D PIC-MCC model and the numerical resolution is either  $96 \times 64 \times 128$  grid nodes or eight times larger with 80 particles-per-cell (ppc). The time gained in the pusher with the particle sorting is a factor  $\sim 4$ . The sorting algorithm remains efficient as long as there is on average at least one particle per cell

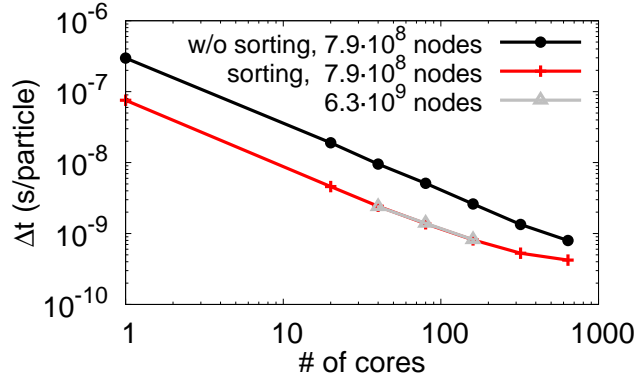


Figure 2.1: (Color) Execution time of the particle pusher (per time step) normalized to the number of macroparticles in the simulation versus the number of cores. The time is shown either with (red and grey lines) or without implementing a sorting algorithm (black-line). We use 80 particles-per-cell (ppc), a numerical resolution of  $96 \times 64 \times 128$  grid nodes (black and red lines) and  $192 \times 128 \times 256$  (grey line). The calculation is performed with a 3D PIC-MCC model on a 10 cores Intel Xeon processor E5-2680 v2 (25M cache, 2.80 GHz). There is 2 sockets per CPU, 20 cores in total.

per thread. Beyond this limit  $\Delta t_{\text{push}}$  converges toward the value without sorting as shown in Fig. 2.1. We define the efficiency of the pusher without sorting as,

$$\beta = \frac{\Delta t_{\text{push}}^{(1)}}{\Delta t_{\text{push}} N_{\text{core}}} , \quad (2.1)$$

where  $N_{\text{core}}$  is the number of cores (threads) and  $\Delta t_{\text{push}}^{(1)}$  the execution time of the pusher for  $N_{\text{core}} = 1$ . We find  $\beta \simeq 78\%$  for 20 cores, 70% for 320 cores and lastly, dropping to  $\sim 60\%$  for 640 cores (i.e., about 23% loss in efficiency with respect to 20 cores).

Poisson's equation is solved iteratively on the grid nodes with a 3D multi-grid solver [35]. The latter is parallelized via a domain-decomposition approach. In multi-grid algorithms, a hierarchy of discretizations (i.e., grids) is implemented. A relaxation method (so-called Successive-Over-Relaxation, SOR, in our case) is applied successively on the different grid levels (from fine to coarse grid levels and vice-versa). Multigrid algorithms hence accelerate the convergence of a basic iterative method because of the fast reduction of short-wavelength errors by cycling through the different

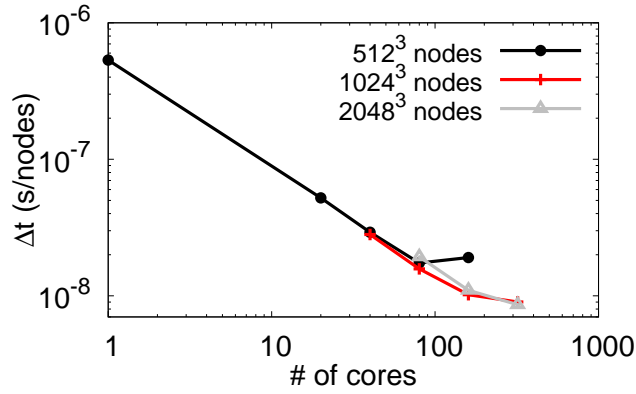


Figure 2.2: (Color) Execution time of the geometric multigrid Poisson solver (per time step) normalized to the number of grid nodes in the simulation versus the number of cores. the numerical resolution is  $512^3$  (black line),  $1024^3$  (red) and  $2048^3$  (grey) grid nodes, respectively. The calculation is performed on a 10 cores Intel Xeon processor E5-2680 v2 (25M cache, 2.80 GHz). We set the number of OpenMP threads to 10.

sub-grid levels. Each sub-domain (i.e., a slice of the simulated geometry) is attached to a MPI thread while the do-loops are parallelized with OpenMP (SOR, restriction and prolongation subroutines [35]). Once there is less than one node per MPI thread in the direction where the physical domain is decomposed then the numerical grid is merged between all the MPI threads. The parallelization for the coarsest grids is consequently only achieved by the OpenMP threads. This is clearly a limiting factor and more work is needed to further improve the algorithm. As an example, using a mesh of  $512^3$  nodes, the speedup is about  $\sim 30$  for 80 cores ( $\beta \simeq 40\%$ ). The execution time of the Poisson solver (normalized to the number of grid nodes) versus the number of cores in the simulation is shown in Fig. 2.2

Lastly, for the numerical resolution which we typically implement to characterize the plasma properties of the ITER-prototype ion source at BATMAN, that is,  $192 \times 128 \times 256$  grid nodes with 20 ppc, the fraction of the execution time per subroutine averaged over one time step is,  $\sim 55\%$  for the particle pusher,  $\sim 8\%$  for the Poisson solver,  $\sim 16\%$  for Monte-Carlo collisions,  $\sim 4\%$  for the sorting. The remaining time concerns both the evaluation of the electric field and the calculation of the total charge density on the grid nodes (which involve some communication between MPI threads).

### 2.1.2 Scaling

In order to provide a qualitative understanding for the plasma behaviour in the ion source, we derive an analytical plasma model which describes approximately conditions where the plasma is non-magnetized and the diffusion is ambipolar [18, 36] (the flux of electrons and ions impacting the ion source walls are equal locally). Steady-state conditions are posited. From the continuity equation we deduce the equilibrium temperature in the plasma (here we only consider one ion specie and electrons, without any loss of generality),

$$\frac{hu_B S}{V} = \nu_i, \quad (2.2)$$

where  $u_B = \sqrt{eT_e/m_i}$  is the Bohm velocity,  $S$  is the surface area of the device,  $V$  the corresponding volume,  $\nu_i = n_g \langle \sigma_i v \rangle$  the total ionization frequency,  $n_g$  the background gas density,  $\sigma_i$  the ionization cross-section and  $h = n_s / \langle n \rangle$  is the ratio of density at the sheath edge to the averaged plasma density, respectively.  $h$  is independent of the absorbed power and is a function of the discharge geometry, background gas pressure and electron temperature (at high pressure) [37]. In principle  $S/V$  corresponds to the volume over surface ratio of the quasi-neutral volume but for high density plasmas which have sheaths of negligible lengths one may use the actual device size instead. In a similar way, the volume integration of the energy balance equation

$$P_{\text{abs}} = n_s u_B \varepsilon_T S, \quad (2.3)$$

gives a relationship for the averaged plasma density versus the absorbed power, i.e.,

$$\langle n \rangle = \frac{P_{\text{abs}}}{\nu_i \varepsilon_{\text{tot}} V}, \quad (2.4)$$

with  $P_{\text{abs}}$  the external power absorbed by the electrons,  $\varepsilon_{\text{tot}} = \varepsilon_c + \varepsilon_{\text{ew}} + \varepsilon_{\text{iw}}$  the total energy lost per ion lost in the system which includes the collisional energy losses  $\varepsilon_c$ , the kinetic energy carried to the walls by both electrons and ions ( $\varepsilon_{\text{ew}} = 2T_e$  and  $\varepsilon_{\text{iw}}$ ). For Maxwellian electrons the mean energy lost per electron lost is  $2T_e$ . Ion kinetics is dominated by the directed motion and,

$$\varepsilon_{\text{iw}} \simeq T_e \left( \frac{1}{2} + \ln \sqrt{\frac{m_i}{2\pi m_e}} \right), \quad (2.5)$$

where the first term on the right-hand-side (RHS) of Eq. (2.5) corresponds to the Bohm energy reached on average by the ions at the end of the pre-sheath region and the last term is the energy gain inside a collision-less sheath. The latter is obtained assuming that the total positive and negative particle fluxes are equal and that the electrons are Maxwellian [37]. Equation (2.4) shows that the average plasma density is proportional to the absorbed power and depends on the gas pressure, electron temperature and source geometry. Note that adding a magnetic field changes the distribution of the particles losses on the walls and the “effective” volume-to-surface ratio but the overall properties deduced from Eqs. (2.2)-(2.4) are preserved.

These equations provide also a justification for the use of scaling factors in PIC-MCC models based on the observation that for a given background gas density, the plasma characteristics (density, temperature, potential, current profiles, etc.) are practically insensitive to either artificial variations of the vacuum permittivity constant  $\epsilon_0$  or similarly to the amplitude of the plasma density provided that the sheath volume stays small with respect to the chamber volume (the sheath length, which is of the order of a couple electron Debye lengths, increases with increasing permittivity or a lower plasma density). Both type of scaling will be used alternatively in this work. Scaling (down) the plasma density instead of the vacuum permittivity requires to multiply the cross-sections associated with collisions between charged particles by the same factor  $\alpha = n_{\text{sim}}/n_p$ , where  $n_p$  is the plasma density and  $n_{\text{sim}}$  the simulated density.

### 2.1.3 2.5D PIC-MCC approximation

3D PIC-MCC calculations are restricted to low plasma densities, typically  $\sim 10^{13} \text{ m}^{-3}$  on 40 cores with  $192 \times 128 \times 256$  grid nodes (20 ppc) for the prototype source at BATMAN. The density is about  $10^5$  times lower than the real density. A solution to increase the numerical resolution is to approximate the particle losses in one direction (which we call a 2.5D PIC-MCC model) [23, 38]. For magnetized plasmas, the particle transport is simulated in the plane perpendicular to  $\mathbf{B}$  (i.e. where the magnetized drift motion takes place). We assume that the plasma is uniform along the un-simulated direction, perpendicular to the 2D simulation plane (i.e., parallel to the magnetic field lines), and we use the following considerations to estimates the charged particle

losses:

- The ions dynamics in the direction perpendicular to the 2D simulation plane is not calculated but we estimate the ion losses from the Bohm fluxes to the walls. The loss frequency at a given location in the simulation plane is obtained from [37]  $\nu_L = 2hu_B/L_y$  [Eq. (2.2)], where  $u_B = \sqrt{eT_e(x,z)/m_i}$  is the local Bohm velocity,  $L_y$  is the length of the ion source in the third dimension,  $h = n_s/\langle n \rangle$ ,  $n_s$  is the local plasma density at the sheath edge,  $\langle n \rangle$  the average density,  $T_e$  ( $m_i$ ), the local electron temperature (ion mass), respectively.
- The electron and negative ion trajectories are followed in the third dimension assuming that the plasma potential is flat (i.e., no electric field). When a negatively charged particle reaches a wall, it is removed if its kinetic energy along the un-simulated dimension is greater than the difference between the plasma potential and the wall, i.e.,  $1/2 m_p v_z^2 \geq \phi(x, z)$  for a grounded wall.  $m_p$  is the particle mass.

Macroparticles are created anywhere between  $0 \leq y \leq L_y$  in the third dimension (via ionization processes). The 2.5D model estimates plasma characteristics which are averaged over  $L_y$ . This approach is restricted to simplified magnetic field maps, where the field lines are straight in the un-simulated direction.

The  $h$  factor may be calculated analytically with a 1D fluid model for a non-magnetized discharge with ambipolar diffusion to the walls and without negative ions\*. In the case of the 2.5D PIC-MCC model of the BATMAN ITER-prototype ion source, this derivation is approximately valid along the magnetic field lines because the electrons may still be considered in Boltzmann equilibrium. The flux equation for the ions, neglecting pressure terms, is written as follows,

$$\frac{\partial n_i u_i}{\partial t} + \frac{\partial n_i u_i^2}{\partial x} = \frac{e n_i}{m_i} E - n_i \sum_j \nu_{m,j} (u_i - u_j), \quad (2.6)$$

where  $\nu_m$  is the momentum transfer frequency,  $E$  the ambipolar electric field,  $u_i$  the mean velocity,  $m_i$  ( $n_i$ ) the ion mass (density), respectively. Positive ions generated by ionization processes are assumed at rest. The ionization frequency hence does not

---

\*This was originally derived by my colleague G. Hagelaar.

appear in Eq. (2.6). Adding the continuity equation and Boltzmann electrons,

$$\frac{\partial n_i}{\partial t} + \frac{\partial n_i u_i}{\partial x} = n_i \nu_i, \quad (2.7)$$

$$-eE = T_e \frac{\partial \ln(n_e/n_0)}{\partial x}, \quad (2.8)$$

we have a closed set of equations.  $\nu_i$  is the ionization frequency. Assuming quasi-neutrality ( $n_i = n_e = n$ ), ion-neutral collisions exclusively (we further neglect neutral velocities) and lastly steady state conditions, we find,

$$u_i \frac{dn}{dx} + n \frac{du_i}{dx} = \nu_i n, \quad (2.9)$$

$$u_i \frac{du_i}{dx} + (\nu_i + \nu_m) u_i = -\frac{1}{u_B^2} \frac{d \ln n}{dx}. \quad (2.10)$$

Normalizing the latter with  $\tilde{u}_i = u_i/u_B$ ,  $\tilde{x} = \nu_i x/u_B$ ,  $\tilde{n} = n/n_0$  and  $\tilde{z} = \ln \tilde{n}$  (note that ionization appears in the momentum equation as a loss term), we have

$$\tilde{u} \frac{d\tilde{z}}{d\tilde{x}} + \frac{d\tilde{u}}{d\tilde{x}} = 1, \quad (2.11)$$

$$\tilde{u} \frac{d\tilde{u}}{d\tilde{x}} + (1+k)\tilde{u} = -\frac{d\tilde{z}}{d\tilde{x}}, \quad (2.12)$$

where  $k = \nu_m/\nu_i$ . Combining the two equations, we get

$$\frac{d\tilde{u}}{d\tilde{x}} = \frac{1 + (1+k)\tilde{u}^2}{1 - \tilde{u}^2}. \quad (2.13)$$

$\tilde{u}$  varies from 0 to 1. The equation is diverging for  $\tilde{u} \rightarrow 1$  (i.e.,  $u \rightarrow u_B$ ). Solving for  $\tilde{x}$  instead,

$$d\tilde{x} = \frac{(1 - \tilde{u}^2)d\tilde{u}}{1 + (1+k)\tilde{u}^2}, \quad (2.14)$$

and integrating, we find,

$$\tilde{x} = \frac{2+k}{(1+k)^{3/2}} \arctan\left(\tilde{u}\sqrt{1+k}\right) - \frac{\tilde{u}}{1+k}. \quad (2.15)$$

For  $\tilde{u} = 1$ , we may deduce an expression for  $h$  [Eq. (2.2)] versus  $k = \nu_m/\nu_i$ ,

$$h = \frac{L\nu_i}{2u_B} = \frac{2+k}{(1+k)^{3/2}} \arctan\left(\sqrt{1+k}\right) - \frac{1}{1+k}, \quad (2.16)$$

where the sheath length was neglected and  $L \simeq 2x_s$  was assumed (the electron Debye length is of micrometre size in fusion-type ion sources). For  $k = 0$  (i.e., without any ion-neutral collisions) we find  $h \simeq 0.57$ . Note that from Eqs. (2.11) and (2.13), we may deduce the density as a function of ion velocity, that is,

$$\tilde{z} = \ln \tilde{n} = - \int_0^{\tilde{u}} \frac{(2+k)\tilde{u}d\tilde{u}}{1+(1+k)\tilde{u}^2}, \quad (2.17)$$

$$= -\frac{(2+k)}{2(1+k)} \ln [1+(1+k)\tilde{u}^2]. \quad (2.18)$$

For  $\tilde{u} = 1$  (i.e.,  $u = u_B$ ) and  $k = 0$ , we find  $n_s = n_0/2$ , where  $n_s$  is the plasma density at the sheath edge. The ambipolar potential  $\phi_s$  at this location is hence,

$$\phi_s = \phi_0 - T_e \ln 2, \quad (2.19)$$

with  $\phi_0$  the potential at the center of the discharge.

#### 2.1.4 External RF power absorption and Maxwellian heating in the discharge

The ITER-type tandem reactors have an ICP discharge which couples a high RF power (typically 100 kW at 1 MHz frequency) to a hydrogen or deuterium plasma. We do not simulate directly the interaction of the RF field with the plasma but assume instead, as an initial condition, that some power is absorbed. Every time step, macroparticles which are found inside the region of RF power deposition are heated according to some artificial heating collision frequency. Electrons, being the lightest particles, are assumed to absorb all of the external power. Redistribution of energy to the heavier ions and neutrals is done through collisions (both elastic and inelastic) and the ambipolar potential. Electrons undergoing a heating collision have their velocities replaced by a new set sampled from a Maxwellian distribution with

a temperature calculated from the average specie energy inside the power deposition region added to the absorbed energy per colliding particles, i.e.,

$$\frac{3}{2}T_h = \langle E_k \rangle_h + \frac{P_{\text{abs}}}{eN_{eh}\nu_h}, \quad (2.20)$$

where  $T_h$  (eV) is the heating temperature in electron-Volts (eV),  $\langle E_k \rangle_h$  is the average electron energy,  $P_{\text{abs}}$  (W) is the absorbed power,  $\nu_h$  the heating frequency and  $N_{eh}$  the number of electrons, respectively. For a given time step,  $N_{em}\nu_h\Delta t$  colliding macro-electrons are chosen randomly where  $N_{em}$  is the total number of macroparticles inside the heating region.

## 2.2 Implementation of collisions in a particle model - MC and DSMC methods

In a PIC-MCC algorithm, the Boltzmann equation,

$$\frac{\partial f_i}{\partial t} + v \frac{\partial f_i}{\partial x} + \frac{F}{m_i} \frac{\partial f_i}{\partial v} = \left( \frac{\partial f_i}{\partial t} \right)_c, \quad (2.21)$$

is solved numerically in two steps [24, 39].

$$\left( \frac{\partial f_i}{\partial t} \right)_c = \sum_t \iint (f'_i f'_t - f_i f_t) v_r \sigma_t^T d\Omega dv_t, \quad (2.22)$$

is the collision operator,  $f_i$  ( $f_t$ ) is the distribution function for the incident (target) specie, respectively,  $m_i$  the mass,  $F$  the force field,  $v_r = |v_i - v_t|$  the relative velocity,  $\sigma_t^T(v_r)$  the total differential cross-section (summed over all the collision processes between the incident and the target particles) and, lastly,  $\Omega$  the solid angle. Primes denote the distribution function after the collision. For small time steps, Eq. (2.21) may be rewritten as,

$$f_i(x, v, t + \Delta t) = (1 + \Delta t J) (1 + \Delta t D) f_i(x, v, t), \quad (2.23)$$

where  $f_i(x, v, t)$  is known explicitly from the previous time step. This finite-difference analogue of Eq. (2.21) is second order correct in  $\Delta t$ . The operators  $D$  and  $J$  are,

$$D(f_i) = -v \frac{\partial f_i}{\partial x} - \frac{F}{m_i} \frac{\partial f_i}{\partial v}, \quad (2.24)$$

and  $J(f_i) = (\partial f_i / \partial t)_c$ . Applying the operator  $(1 - \Delta t D)$  on the distribution function  $f_i$  is equivalent to solving the Vlasov equation,

$$\frac{\partial f_i}{\partial t} + v \frac{\partial f_i}{\partial x} + \frac{F}{m_i} \frac{\partial f_i}{\partial v} = 0. \quad (2.25)$$

The Particle-In-Cell (PIC) procedure [32, 33] is a characteristic solution of Eq. (2.25). Once the particle trajectories have been updated, then the second operator  $(1 - \Delta t J)$  may be applied on the (updated) distribution function. A macroparticle is equivalent to a Dirac delta function in position-velocity space (Eulerian representation of a point particle) and hence a probability may be derived from Eq. (2.23) for each collision processes [24, 39]. The probability for an incident particle to undergo an elastic or inelastic collision with a target particle during a time step  $\Delta t$  is

$$(P_i)_{\max} = \Delta t \sum_{c=1}^{N_c} (n_c \sigma_c v_r)_{\max}, \quad (2.26)$$

with  $N_c$  corresponding to the total number of reactions for the incident specie,  $n_c$  the density of the target specie associated with a given collision index and  $v_r = |v_i - v_c|$ .  $(\sigma_c v_r)_{\max}$  is artificially set to its maximum value and hence  $(P_i)_{\max}$  is greater than the real probability and is constant over the entire simulation domain. There is consequently a probability,

$$(P_i)_{\text{null}} = 1 - \sum_{c=1}^{N_c} \frac{P_c}{(P_i)_{\max}}, \quad (2.27)$$

that a particle undergoes a fake collision (dubbed “null” collision), which will be discarded.  $P_c = n_c \sigma_c (v_r) v_r \Delta t$ . The total number of incident particles which will

hence collide during a time step  $\Delta t$  (including a “null” collision) is,

$$N_{\max} = N_i(P_i)_{\max}, \quad (2.28)$$

where  $N_i$  is the number of incident macroparticles in the simulation.  $N_i$  must be replaced by  $(N_i - 1)/2$  for collisions with another particle of the same specie [24].  $(P_i)_{\max}$  is equiprobable for any pairs of incident-target particles and consequently the latter may be chosen randomly inside the simulation domain. In the model, one checks first if the incident macroparticle experienced a real collision,

$$r \leq 1 - (P_i)_{\text{null}}, \quad (2.29)$$

where  $r$  is a random number between 0 and 1. The probabilities  $P_c$  for each reactions (whose total number is  $N_c$  for a given incident specie) are ordered from the smallest to the largest and a reaction  $k$  occurred if,

$$r \leq \sum_{c=1}^k \frac{P_c}{(P_i)_{\max}}. \quad (2.30)$$

Once a collision type is selected then the macroparticles (both incident and target) are scattered away in the center-of-mass (CM) frame (see next section). In the model, neutrals are either considered as a non-moving background specie with a given density profile or are actually implemented as macroparticles and their trajectories integrated. In the case of the former, collisions between charged particles and neutrals are performed by the so-called Monte-Carlo (MC) method while for the latter, actual particle-particle collisions are evaluated using a Direct-Simulation-Monte-Carlo (DSMC) algorithm [25]. Both are similar except that in the MC method, one artificially extract a neutral particle velocity from a Maxwellian distribution function. Collisions between charged particles are always performed by a DSMC algorithm in the model.

## 2.3 Elastic and inelastic collision processes

Collisions in the PIC-MCC algorithm (both elastic and inelastic), are implemented assuming that particles (incident, target or newly created) are scattered isotropically in the center of mass (CM). Energy and momentum is conserved in the model and we posit for simplicity that each byproduct partner after the collision have identical momentum in the CM frame<sup>†</sup>. This implies that the lightest particles will equally share most of the available energy [18]. Cross-sections for light versus heavy or similarly heavy-heavy particle collisions are often solely function of the relative velocity (especially when originating from experimental measurements), i.e., information about the differential cross-section is lacking. It is the case for nearly all of the cross-sections associated with molecular hydrogen (or deuterium) gas chemistry. Consequently, we implemented a simple MC collision model derived from the isotropic character of a collision. This has the advantage of being versatile (easily adaptable to different types of collision processes both elastic and inelastic) and to conserve exactly energy and momentum. In the center of mass (CM) of the two interacting particles, one assume that each byproduct of the collision have identical momentum, that is,

$$|\mathbf{p}'_1| = |\mathbf{p}'_2| = \dots |\mathbf{p}'_n|, \quad (2.31)$$

where  $|\mathbf{p}'_n| = m_n v'_n$ , with  $m_n$  the mass of the nth byproduct particle and  $v'_n$  its velocity, respectively. Note that the use of Eq. (2.31) impose a strict energy equipartition between particles of equal mass. We find after the collision,

$$E'_{kr} = \mu v_r^2 / 2 - E_{th}, \quad (2.32)$$

with  $E'_{kr}$  the relative kinetic energy in the CM frame,  $v_r = |\mathbf{v}_1 - \mathbf{v}_2|$  the relative velocity in the laboratory frame,  $\mu = m_i m_t / (m_i + m_t)$  the reduced mass of the system,  $m_i$  ( $m_t$ ) the incident (target) particle mass and  $E_{th}$  the threshold energy of the reaction. The relative kinetic energy is shared between all byproduct particles, i.e.,

$$E'_{kr} = m_1 v_1'^2 / 2 + m_2 v_2'^2 / 2 + \dots + m_n v_n'^2 / 2, \quad (2.33)$$

---

<sup>†</sup>This assumption and the following collision model was derived by G. Hagelaar.

and using the equality defined in Eq. (2.31), one deduces the kinetic energy of each particle,

$$\frac{m_k v_k'^2}{2} = \frac{E'_{kr}/m_k}{1/m_1 + 1/m_2 + \dots + 1/m_n}, \quad (2.34)$$

where  $k$  is the index of the  $k$ th particle. For instance in a system with three particles after the collision, say two electrons and one ion, the electrons share the same and almost all the available energy, that is,

$$E'_{ke} \simeq \frac{E'_{kr}}{2} \left( 1 - \frac{m_e}{2m_i} \right), \quad (2.35)$$

while the ion takes the remaining part,

$$\frac{E'_{ki}}{E'_{kr}} \simeq \frac{m_e}{2m_i} \ll 1. \quad (2.36)$$

Lastly, momentum conservation is preserved by assuming equal angle spread between momentum vectors in the CM frame, i.e.,  $\theta_k = \theta_1 + 2\pi(k-1)/n$ . The angle  $\theta_1 = \arccos(1-2r_1)$  is calculated using a random number  $r_1$  between 0 and 1. The particle velocity in the laboratory frame is derived from,

$$\mathbf{v}_k = \mathbf{v}_{\text{CM}} + v_k' \mathbf{e}_k, \quad (2.37)$$

and,

$$\begin{aligned} e_{kx} &= \cos \theta_k, \\ e_{ky} &= \sin \theta_k \sin \phi, \\ e_{kz} &= \sin \theta_k \cos \phi, \end{aligned} \quad (2.38)$$

where  $\mathbf{v}_{\text{CM}} = (m_i \mathbf{v}_i + m_t \mathbf{v}_t)/(m_i + m_t)$  is the CM velocity,  $\phi = 2\pi r_2$  and  $r_2$  is another random number.  $\phi$  is assumed identical for all byproduct particles.

### 2.3.1 Physical chemistry of charged particles

In this work, the plasma consists of electrons, molecular hydrogen (background) gas  $\text{H}_2$ , hydrogen atoms  $\text{H}$ , molecular ions  $\text{H}_2^+$  and  $\text{H}_3^+$ , protons and lastly negative ions  $\text{H}^-$ . Collisions between electrons, ions and neutrals are considered; the set of reactions is presented in tables 2.1 and 2.2 (66 collision processes in total) and is very

similar to the one used by previous authors [36, 54]. Table 2.1 corresponds to the collision processes associated with electrons. Reactions #2, 6, 7, 8 and 14 combine multiple inelastic processes included in the model in order to correctly account for the electron energy loss. Reaction #2 regroups the excitation of the hydrogen atom from the ground state to the electronic level  $n = 2 - 5$  [45]. Reaction #7 combines the ground state excitation of the hydrogen molecule  $\text{H}_2(\text{X}^1\Sigma_g^+; \nu = 0)$  to the vibrational levels  $\nu' = 1 - 3$  [45, 51], electronic levels (for all  $\nu'$ )  $\text{B}^1\Sigma_u$ ,  $\text{B}'^1\Sigma_u$ ,  $\text{B}''^1\Sigma_u$ ,  $\text{C}^1\Pi_u$ ,  $\text{D}^1\Pi_u$ ,  $\text{D}'^1\Pi_u$ ,  $\text{a}^3\Sigma_g^+$ ,  $\text{c}^3\Pi_u$ ,  $\text{d}^3\Pi_u$  [45], Rydberg states [52] and lastly rotational levels  $J = 2$  [47, 48] and 3 [49, 50]. Reaction #17 models in a simple manner the generation of negative ions in the ion source volume, which are a byproduct of the dissociative impact between an electron and molecular hydrogen  $\text{H}_2(\nu \geq 4)$  [45]. The concentration of excited species is not calculated self-consistently in the model. To estimate

Table 2.1: Electron collisions.

#	Reaction	Cross section ref.
1	$e + \text{H} \rightarrow e + \text{H}$ (elastic)	[40–44]
2	$e + \text{H} \rightarrow e + \text{H}$ (inelastic, 4 proc.)	[45]
3	$e + \text{H} \rightarrow 2e + \text{H}^+$	[45]
4	$e + \text{H}_2 \rightarrow e + \text{H}_2$ (elastic)	[46]
5	$e + \text{H}_2 \rightarrow 2e + \text{H}_2^+$	[45]
6	$e + \text{H}_2 \rightarrow 2e + \text{H}^+ + \text{H}$ (2 proc.)	[45]
7	$e + \text{H}_2 \rightarrow e + \text{H}_2$ (inelastic, 16 proc.)	[45, 47–52]
8	$e + \text{H}_2 \rightarrow e + 2\text{H}$ (3 proc.)	[45, 53]
9	$e + \text{H}_3^+ \rightarrow 3\text{H}$	[45]
10	$e + \text{H}_3^+ \rightarrow \text{H} + \text{H}_2$	[45]
11	$e + \text{H}_3^+ \rightarrow e + \text{H}^+ + 2\text{H}$	[45]
12	$e + \text{H}_3^+ \rightarrow e + \text{H}^+ + \text{H}_2$	[45]
13	$e + \text{H}_2^+ \rightarrow 2\text{H}$	[45]
14	$e + \text{H}_2^+ \rightarrow e + \text{H}^+ + \text{H}$ (2 proc.)	[45, 53]
15	$e + \text{H}_2^+ \rightarrow 2e + 2\text{H}^+$	[53]
16	$e + \text{H}^- \rightarrow 2e + \text{H}$	[45]
17	$e + \text{H}_2^* \rightarrow \text{H}^- + \text{H}$ (1% of $\text{H}_2$ )	[53]
18	$e + \text{H}_2^+ \rightarrow e + \text{H}_2^+$	(Coulomb) [19]
19	$e + \text{H}^+ \rightarrow e + \text{H}^+$	(Coulomb) [19]
20	$e + \text{H}_3^+ \rightarrow e + \text{H}_3^+$	(Coulomb) [19]

Table 2.2: Heavy particle processes.

#	Reaction	Cross section ref.
1	$\text{H}_3^+ + \text{H}_2 \rightarrow \text{H}_3^+ + \text{H}_2$ (elastic)	[60]
2	$\text{H}_3^+ + \text{H} \rightarrow \text{H}_3^+ + \text{H}$ (elastic)	
3	$\text{H}_2^+ + \text{H}_2 \rightarrow \text{H}_3^+ + \text{H}$	[59, 60]
4	$\text{H}_2^+ + \text{H}_2 \rightarrow \text{H}_2 + \text{H}_2^+$	[60]
5	$\text{H}_2^+ + \text{H} \rightarrow \text{H}_2^+ + \text{H}$ (elastic)	[61]
6	$\text{H}^+ + \text{H} \rightarrow \text{H} + \text{H}^+$	[62]
7	$\text{H}^+ + \text{H} \rightarrow \text{H}^+ + \text{H}$ (elastic)	[62]
8	$\text{H}^+ + \text{H}_2 \rightarrow \text{H}^+ + \text{H}_2$ (elastic)	[60]
9	$\text{H}^+ + \text{H}_2 \rightarrow \text{H}^+ + \text{H}_2$ (inelastic, 4 proc.)	[57–60]
10	$\text{H}^- + \text{H} \rightarrow \text{e} + 2\text{H}$	[45]
11	$\text{H}^- + \text{H} \rightarrow \text{e} + \text{H}_2$	[45]
12	$\text{H}^- + \text{H}_2 \rightarrow \text{H}^- + \text{H}_2$ (elastic)	[59]
13	$\text{H}^- + \text{H} \rightarrow \text{H}^- + \text{H}$ (elastic)	[59]
14	$\text{H}^+ + \text{H}^- \rightarrow 2\text{H}$ (2 proc.)	[45]
15	$\text{H}^+ + \text{H}^- \rightarrow \text{H}_2^+ + \text{e}$	[45]
16	$\text{H}^- + \text{H}_2 \rightarrow \text{H}_2 + \text{H} + \text{e}$	[45]
17	$\text{H}^- + \text{H} \rightarrow \text{H} + \text{H}^-$	[63]
18	$\text{H} + \text{H} \rightarrow \text{H} + \text{H}$	[62]
19	$\text{H} + \text{H}_2 \rightarrow \text{H} + \text{H}_2$	[62]
20	$\text{H}_2 + \text{H}_2 \rightarrow \text{H}_2 + \text{H}_2$	[64]

the volume production of negative ions, we assume that 1% of  $\text{H}_2$  molecules are excited in vibrational levels with  $\nu \geq 4$ . This is in accordance with the  $\text{H}_2$  vibrational distribution function calculated either with a 0D model [55] or a 3D particle tracking code [56]. Table 2.2 summarizes the collision processes of heavy ions with neutrals. Reaction #9 corresponds to the excitation of the hydrogen molecule from the ground state to vibrationally excited levels  $\nu' = 1 - 2$  [57, 58] and to the rotational levels  $J = 2 - 3$  [59]. To our knowledge there is no reliable data available for the elastic collision between  $\text{H}_3^+$  and neutral atoms (reaction #2), we consequently use the same cross-section as in reaction #1.

Coulomb collisions between electrons and ions are implemented (reaction #18 of table 2.1) using the standard expression for the cross section [65, 66],

$$\sigma_{ei} \simeq \frac{e^4}{4\pi\epsilon_0^2 m_e^2} \frac{\log \lambda}{v_r^4}, \quad (2.39)$$

where  $v_r$  is the relative velocity in the CM frame,  $e$  is the elementary charge,  $m_e$  the electron mass and  $\log \lambda$  the Coulomb logarithm with,

$$\lambda = \left[ 12\pi n_e \left( \frac{\epsilon_0 k_B T_e}{n_e e^2} \right)^{3/2} \right]. \quad (2.40)$$

$n_e$  is the electron density,  $k_B$  the Boltzmann constant and  $T_e$  the electron temperature. The Coulomb logarithm does not vary much over the range of plasma parameters typically found in an ITER-type source. We consequently keep  $\lambda$  constant in the model with  $\log \lambda = 12.5$  obtained assuming  $\langle T_e \rangle \simeq 6$  eV and  $\langle n_e \rangle \simeq 8 \times 10^{17} \text{ m}^{-3}$ .

### 2.3.2 Physical chemistry of neutrals

Cross-sections for collisions between neutrals inside the ion source volume, which are summarized in table 2.2 (reactions #18-20), as well as backscattering, dissociation or recombination probabilities against the ion source walls are required for the modeling of the neutral particle dynamics (and the associated neutral depletion). Table 2.3 shows the surface processes and corresponding coefficients. In a low-pressure plasma device such as the one used for ITER, the plasma-wall processes have a strong impact on the source characteristics. Low-temperature backscattered molecular hydrogen is assumed to be in thermal equilibrium with the wall. An average backscattered energy is considered for fast atoms and ions, i.e., a thermal accommodation coefficient  $\gamma$  ( $\gamma = 1$  corresponds to the temperature of the wall). These estimates are based on Monte Carlo calculations from the code TRIM [67]. Average reflection probability is also taken from the same database. Furthermore, we assume that atoms which are not backscattered will recombine. The interaction of  $\text{H}_3^+$  and  $\text{H}_2^+$  ions with the walls and the corresponding coefficients are not well known. The coefficients used in the simulations are reported in table 2.3. For  $\text{H}_2^+$  we use coefficients that are consistent with the measurements of [68]. For  $\text{H}_3^+$  we assume guessed values (the  $\text{H}_3^+$  flux to the walls is relatively small with respect to the  $\text{H}_2^+$  and  $\text{H}^+$ , and the results are not very sensitive to these coefficients).

Table 2.3: Surface processes.

#	Reaction	Probability	Accommodation coef. $\gamma$	Ref.
1	$\text{H}^+ \rightarrow \text{H}_2$	0.4	1	[67]
2	$\text{H}^+ \rightarrow \text{H}$	0.6	0.5	[67]
3	$\text{H}_2^+ \rightarrow \text{H}_2$	0.2	1	[68]
4	$\text{H}_2^+ \rightarrow \text{H}$	0.8	0.5	[68, 69]
5	$\text{H}_3^+ \rightarrow \text{H}_2$	1/3	1	none
6	$\text{H}_3^+ \rightarrow \text{H}$	2/3	0.5	none
7	$\text{H} \rightarrow \text{H}_2$	0.4	1	[67]
8	$\text{H} \rightarrow \text{H}$	0.6	0.5	[67]
9	$\text{H}_2 \rightarrow \text{H}_2$	1	1	none
10	$\text{H}^- \rightarrow \text{H}$	1	1	none

## 2.4 Negative ions

Negative ions are produced on the cesiated PG surface as a byproduct of the impact of hydrogen atoms and positive ions. The former are not simulated and we consider, as an input parameter, a given negative ion current generated by the neutrals; its magnitude is either deduced from plasma parameters measured experimentally or from DSMC calculations. The flux of atoms on the PG considering the distribution function to be Maxwellian is,

$$\Gamma_H = \frac{1}{4} n_H \sqrt{\frac{8eT_H}{\pi m_H}}, \quad (2.41)$$

where  $n_H$  is the atomic hydrogen density,  $m_H$  the mass and  $e$  the electronic charge. The negative ion current is deduced from,

$$j_n = eY(T_H)\Gamma_H, \quad (2.42)$$

with  $Y(T_H)$  the yield [70], which was not obtained in a plasma (the experiment produced hydrogen from thermal dissociation in a tungsten oven) and consequently remains approximate for the ITER-type ion sources. For typical BATMAN working conditions, we find  $n_H \simeq 10^{19} \text{ m}^{-3}$ ,  $T_H \sim 1 \text{ eV}$  which gives  $j_n \sim 600 \text{ A/m}^2$  [26, 71, 72]. Negative ions are generated on the PG assuming a Maxwellian flux dis-

tribution function with a temperature  $T_n = 1$  eV in the model. Furthermore, the surface production of negative ions resulting from positive ion impacts is calculated self consistently. For each ion impinging the PG, the yield is evaluated assuming a molecular ion may be considered as an ensemble of protons sharing the incident ion kinetic energy (a  $H_3^+$  ion for instance would be equivalent to three protons each with an energy  $E_k(H^+) = E_k(H_3^+)/3$ ). Each of these “protons” may produce a negative ion. The condition  $r \leq Y$  must be fulfilled for the negative ion to be generated with  $r$  a random number between 0 and 1. The yield is taken from Seidl *et al.* [70] for Mo/Cs surface with dynamic cesiation. The negative ions are scattered isotropically toward the ion source volume with a kinetic energy assumed to be  $E_k(H^-) = E_k(H^+)/2$ . There is experimental evidence that negative ions may capture a large amount of the incident positive ion energy [69]. In addition, for clean metallic surfaces (tungsten) the reflected atomic hydrogen particle energy is numerically evaluated to be around 65% of the impact energy at normal incidence and for  $E_k = 1$  eV [73]. Lastly, it has been reported in the experiments that the extracted negative ion current improve only slightly with cesium when the PG is water-cooled [74] while a PG heated to a temperature of  $\sim 100^\circ$ - $250^\circ$ C induce a significant increase of the negative ion current, by a factor  $\sim 4 - 5$  in the experimental conditions of ref. [5, 74] (the other walls of the ion-source were water-cooled). In the model, we consequently assume that negative ions may only be produced on the cesiated PG surface.

## 2.5 Simulation domain

The simulation domain for the 3D PIC-MCC modeling of the BATMAN device is shown in Fig. 2.3(a) and (b). The magnetic field barrier is generated in the model by permanent magnet bars which are located on the lateral side of the ion source walls close to the PG. The field is calculated by a third-party code [75]. Due to the fact that the magnetic field strength is quite high, especially near the source walls where the magnets are located ( $|\mathbf{B}| \gg 100\text{G}$ ), the normalized time step  $\Omega_e \Delta t$  (where  $\Omega_e = qB/m_e$  is the electron Larmor frequency) may exceed unity locally in the simulation domain. We have verified numerically that this feature has no strong incidence on the calculated plasma characteristics; we compared a case where

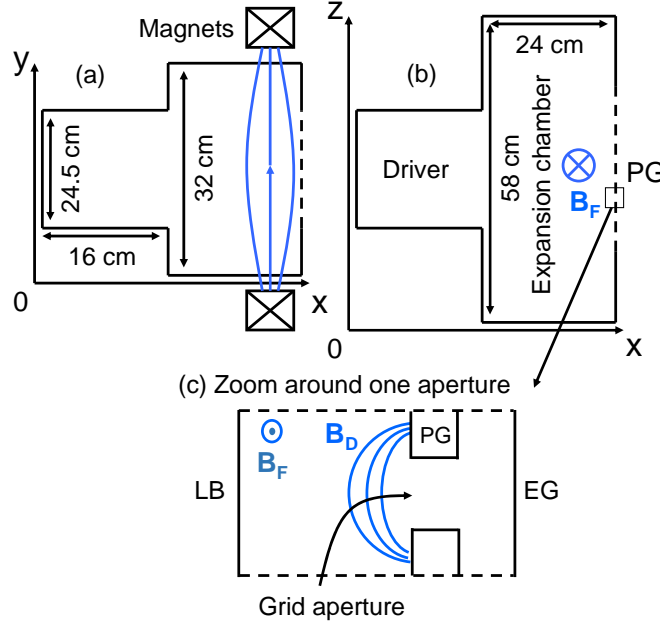


Figure 2.3: (Color) Schematic view of the BATMAN geometry. On the left side, the driver where the power from RF coils (unsimulated) is coupled to the plasma. The box on the RHS is the expansion chamber which is magnetized. The magnetic filter field  $\mathbf{B}_F$  is generated by a set of permanent magnets located on the lateral walls of the chamber near the plasma grid (PG). Field lines are outlined in blue. The dashed line on the RHS of (a) and (b) correspond to the PG. The simulation domain for the modeling of negative ion extraction from the PG surface with a higher numerical resolution is displayed in (c).  $\mathbf{B}_D$  is the magnetic field from permanent magnet bars embedded inside the extraction grid (EG).

$\Omega_e \Delta t \simeq 5$  near the walls with  $\Omega_e \Delta t \simeq 1$ . In the model, the electron motion is calculated using the Boris method; the correct drift motion is retained for large  $\Omega_e \Delta t$  and the scheme is numerically stable [76]. For  $\Omega_e \Delta t \gg 1$ , the numerical value of the Larmor radius  $r_L^*$  is larger than the real one with

$$r_L^* \simeq \frac{1}{2} v_{e\perp} \Delta t, \quad (2.43)$$

where  $v_{e\perp}$  is the electron velocity in a frame perpendicular to the magnetic field lines. Since  $r_L^* \sim O(v_{e\perp} \Delta t)$ , the Larmor radius remains  $\lesssim 1$  mm even for  $\Omega_e \Delta t \gg 1$  (which is smaller than the size of a grid cell). For  $\Omega_e \Delta t \simeq 1$ , the numerical error on the Larmor radius is  $\sim 10\%$  and  $7\%$  for the gyro-phase. Note that PIC calculations using

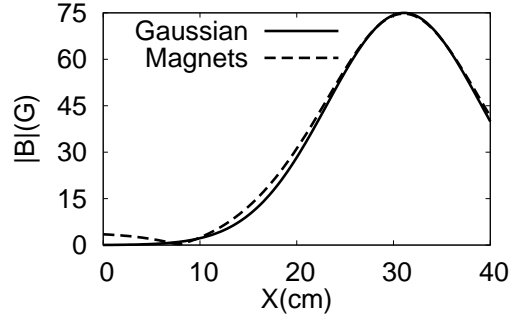


Figure 2.4: Magnetic filter field profile on the ion source axis ( $Y = Z = 0$ ) for both the Gaussian case (solid line), Eq. (2.44) and the field generated by permanent magnets standing against the lateral side of the ion source walls (dashed lines).  $B_0 = 75\text{G}$ ,  $L_m = 8\text{ cm}$  and  $x_0 = 31\text{ cm}$  in this example (i.e., 9 cm from the PG).

large  $\Omega_e \Delta t$  (and  $\omega_p \Delta t < 1$ ) have been reported elsewhere in the literature [76].

In 2.5D, solely the XZ plane is considered [Fig. 2.3(b)] but with a higher numerical resolution (or similarly plasma density) than in 3D. We implemented a Gaussian profile for the magnetic filter (i.e., mirror effects are neglected [23]),

$$B_y(x, z) = B_0 \exp \left[ \frac{-(x - x_0)^2}{2L_m^2} \right], \quad (2.44)$$

with an amplitude  $B_0$ , width  $L_m$  and a maximum located at  $x_0$ . The magnetic field generated by the permanent magnets has a shape very similar to a Gaussian profile on the ion source axis [23], as shown in Fig. 2.4.

Lastly, Fig. 2.3(c) shows the simulation domain for higher numerical resolution 2D and 3D PIC-MCC modeling of negative ion extraction from the PG surface.  $\mathbf{B}_D$  corresponds to the deflection magnetic field from permanent magnets embedded into the extraction grid (EG). A domain restricted to the vicinity of the PG allows the implementation of plasma densities closer to the real one. This will be discussed in chapter 9.



# Chapter 3

## The Hall effect in plasmas

### Contents

---

3.1	General features . . . . .	36
3.2	Simplified geometry . . . . .	37

---

### 3.1 General features

In this chapter, we demonstrate that the magnetized electron drift dynamics inside the magnetic filter induce a transverse plasma asymmetry in the expansion chamber [18–21]. The effect of the magnetic field on electron transport can be analyzed from the fluid representation of the momentum equation (considering steady-state conditions),

$$\mathbf{\Gamma}_e = -\mu_e (\nabla P_e + n_e \mathbf{E} + \mathbf{\Gamma}_e \times \mathbf{B}) , \quad (3.1)$$

where  $\mu_e = |e|/m_e \nu_e$  is the electron mobility without magnetic field,  $e$  is the elementary charge,  $P_e = n_e T_e$  is the electron pressure,  $n_e$  the electron density,  $T_e$  the temperature (in electron-Volts),  $\mathbf{\Gamma}_e = n_e \mathbf{u}_e$  the electron flux and lastly,  $\mathbf{B}$  the magnetic filter field. Equation (3.1) assumes that the electron distribution function is approximately a Maxwellian and neglects viscosity and inertia effects (these effects are of course taken into account in a PIC simulation). Positive ions are not magnetized. The electron flux in Eq. (3.1) may be expressed as follows [18],

$$\mathbf{\Gamma}_e = \frac{1}{1+h^2} [\mathbf{G} + \mathbf{h} \times \mathbf{G} + (\mathbf{h} \cdot \mathbf{G}) \mathbf{h}] , \quad (3.2)$$

with,

$$\mathbf{G} = -\mu_e (n_e \mathbf{E} + \nabla P_e) , \quad (3.3)$$

where  $h_B = \Omega_e/\nu_e = \mu_e B$  is the Hall parameter. Note that  $\mathbf{\Gamma}_e = \mathbf{G}$  when  $\mathbf{B} = \mathbf{0}$ . In fusion-type negative ion sources  $h \gg 1$  and in the plane perpendicular to the magnetic field lines ( $\mathbf{h} \cdot \mathbf{G} = 0$ ), we have,

$$\mathbf{\Gamma}_e \simeq -\frac{\mathbf{G} \times \mathbf{B}}{\mu_e B^2} . \quad (3.4)$$

The electron motion is consequently dominated by the magnetic drift which is composed of a diamagnetic (collective effects) and  $\mathbf{E} \times \mathbf{B}$  terms [20, 77]. The electric field is a combination of the Hall and the ambipolar fields. The electron flux diffusing from the driver toward the extraction region experiences a drift perpendicular to the direction of the flux and the magnetic field. The drift is directed toward the bottom surface of the ion source for the filter configuration schematically shown in

Fig 2.3(b). The presence of walls induces a charge separation (polarization) and the creation of an average electric field that opposes the effect of the Lorentz force, as in the Hall effect. This Hall electric field (which is consequently downward-directed),  $\mathbf{E}_H$ , generates in turn an  $\mathbf{E}_H \times \mathbf{B}$  drift along the X-axis which significantly increases electron transport across the magnetic filter with respect to an ideal 1D filter without transverse walls [20, 78]. We therefore expect that the Hall effect will create a plasma asymmetry with an electric potential and a plasma density higher in the top of the chamber (large Z) than in the bottom (small Z).

The Hall effect in low temperature plasmas and its impact on plasma asymmetry have been studied analytically in the simple conditions of a positive column [22, 79]. The situation is more complicated in the magnetic filter of the negative ion source because of the non-uniform magnetic field and of the presence of axial plasma density and temperature gradients. Furthermore, the general features of the Hall effect (i.e., production of a voltage difference across an electrical conductor, perpendicular to both the direction of the electric current in the conductor and the applied magnetic field) have been clearly observed in other magnetized plasma sources with particle transport properties comparable to those of the ITER prototype ion sources. Experimental measurements have been recently performed in a low power inductively coupled plasma with a magnetic filter and have shown the presence of a strong asymmetry in the collected current density [80]. Note finally that the Hall effect is not present in devices such as Hall thrusters where the electron drift perpendicular to the discharge current is closed and is not impeded by the presence of walls.

## 3.2 Simplified geometry

In order to illustrate the Hall effect in magnetized plasmas in a simplified manner, we implemented a 2D simulation domain which is a square box of dimensions  $20 \times 20 \text{ cm}^2$ . The model is a 2D PIC-MCC and there is no particle losses in the plane perpendicular to the simulation domain. This is the only difference between a 2D and a 2.5D PIC algorithm. We model the XZ plane and the magnetic filter field is along (OY) as in Fig 3.2(b). The magnetic field profile is given by Eq. (2.44) with  $B_0 = 20\text{G}$ ,  $L_m = 2 \text{ cm}$  and  $x_0 = 10 \text{ cm}$ . We consider only electrons and  $\text{H}_2^+$  ions as particle

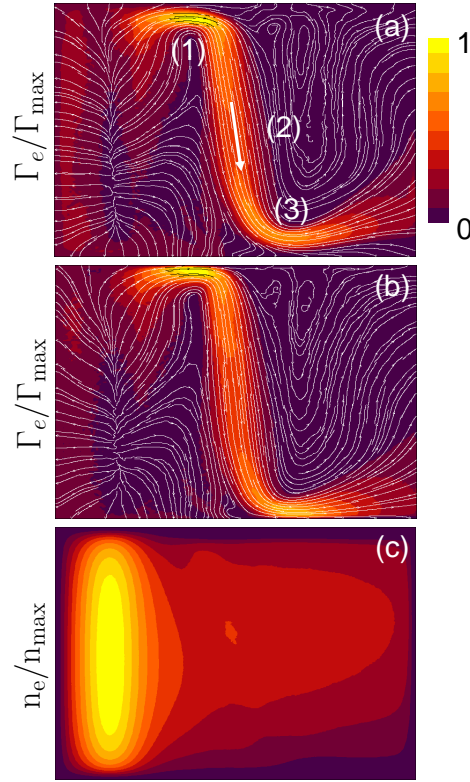


Figure 3.1: (Color) Electron flux profile in the XZ plane for an average plasma density of  $\langle n_p \rangle = 10^{14} \text{ m}^{-3}$  (with  $\Gamma_{\text{max}} = 2.5 \times 10^{19} \text{ m}^{-2} \cdot \text{s}^{-1}$ ) in (a), and  $\langle n_p \rangle = 6.4 \times 10^{15} \text{ m}^{-3}$  ( $\Gamma_{\text{max}} = 1.45 \times 10^{21} \text{ m}^{-2} \cdot \text{s}^{-1}$ ) in (b). The electron density is shown in (c).  $n_{\text{max}} = 2.75 \times 10^{14} \text{ m}^{-3}$ . The magnetic filter field is directed along (OY) with a Gaussian profile axially ( $B_0 = 20\text{G}$ ,  $L_m = 2 \text{ cm}$  and  $x_0 = 10 \text{ cm}$ ). The boundaries of the simulation domain are of Dirichlet type and grounded except the RHS surface which is biased,  $V_{\text{bias}} = 20\text{V}$ . The numerical resolution is  $256^2$  grid nodes in (a) and  $2048^2$  nodes in (b) with 40 ppc. The model is a 2D PIC-MCC.

species composing the plasma and therefore we use a subset of the physical-chemistry described in tables 2.1 and 2.2. Instead of assuming that an external power is absorbed by the plasma, as described in Sec. 2.1.4, we keep the plasma density constant by re-injecting an electron-ion pair each time a positive ion is lost on the external boundaries of the simulation domain. The latter are absorbing surfaces. The particle re-injection is set inside a magnetic field free region between  $x = 1.5 \text{ cm}$  and  $4.5 \text{ cm}$ . Furthermore, the electron temperature is maintained constant in that area with  $T_e = 10 \text{ eV}$ . The scope is to draw an electron current (flux from left to right) through the magnetic

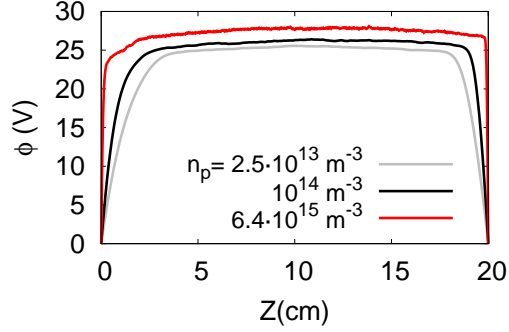


Figure 3.2: (Color) Transverse plasma potential profile (at  $X \simeq 13.4$  cm) versus the average plasma density inside the simulation domain. The numerical resolution is  $128^2$  grid nodes for  $\langle n_p \rangle = 2.5 \times 10^{13} \text{ m}^{-3}$  up to  $2048^2$  nodes for  $\langle n_p \rangle = 6.4 \times 10^{15} \text{ m}^{-3}$  with 40 ppc.

filter and evaluate the Hall effect. For that purpose we assume that there is no ionization processes and hence reaction #5 in Table 2.1 is artificially replaced by an inelastic collision (excitation). The density profile of molecular hydrogen is constant with  $n_{H_2} = 5 \times 10^{19} \text{ m}^{-3}$  and we bias the RHS electrode positively with respect to the other surfaces,  $V_{\text{bias}} = 20\text{V}$ . Figure 3.1 shows the electron flux profile in the XZ plane for two plasma densities, that is,  $\langle n_p \rangle = 10^{14} \text{ m}^{-3}$  in (a) and  $\langle n_p \rangle = 6.4 \times 10^{15} \text{ m}^{-3}$  in (b). The profiles are very similar except that the electron flux channels closer to the walls in the higher density case. This is due to the transverse shape of the plasma potential. The size of the Debye sheath is smaller and hence the pre-sheath extends closer to the boundaries. This also indicates that the electron motion across the magnetic filter field occurs mainly in the pre-sheath. This is confirmed by quasi-neutral fluid calculations. The maximum value of the Hall parameter is  $h_{\text{max}} \simeq 40$  in the model and the electron flux is hence well described by Eq. (3.4). The electron flux is a combination of a diamagnetic drift, which is a consequence of the particle random motion (i.e., the velocity spread) expressed mathematically in the pressure term and an  $\mathbf{E} \times \mathbf{B}$  drift. The two terms are often of opposite sign, i.e., cancelling each others. The electric field is itself a combination of the Hall (which is downward directed) and ambipolar fields. In the regions (1) and (2) highlighted in Fig. 3.1(a), we find  $|\nabla P_e| > |\mathbf{E}|$  and the electron transport is driven by the diamagnetic drift while in (3),  $|E_y| > |\partial P_e / \partial y|$ , i.e., the drift is of  $\mathbf{E} \times \mathbf{B}$  type, respectively. The electron current density profile depends on the shape and magnitude of the magnetic

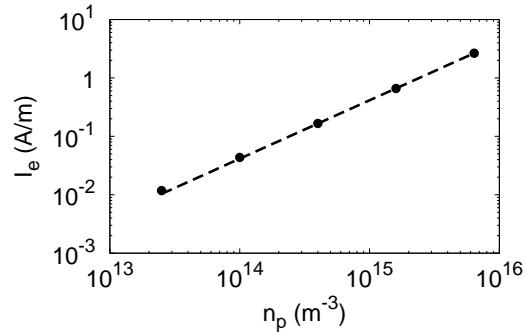


Figure 3.3: Electron current (black dots) collected on the biased electrode (RHS of the simulation domain) versus the plasma density. The dashed line corresponds to a straight line between the origin ( $n_p = 0$ ) and the last data point.

filter field but the general features described in this section are reproduced in any type of magnetized plasma sources where a current is drawn across the magnetic field (biasing the RHS electrode hence enhance the Hall effect). The plasma density, which is asymmetric, is plotted in Fig. 3.1(c).

Lastly, Fig. 3.1 demonstrate that the plasma density has a negligible influence on the plasma properties. Charged particle transport in the plasma occurs mainly inside the quasi-neutral region. A smaller plasma density implies a larger Debye sheath. A necessary requirement is hence that the physics of the Debye sheath must be preserved, that is, in our case remains a collision-less sheath. Note that magnetic fields might induce some plasma instabilities which are seeded by charge separation. In this case, as long as the particle transport generated by the instability is small compared to the collective motion then the plasma properties will stay approximately independent of the plasma density. Scaling down the plasma density or similarly artificially increasing the vacuum permittivity constant  $\epsilon_0$  is hence a strong alternative for modeling the charged particle kinetics with PIC-MCC algorithms as one acts solely on the Debye sheath. This is illustrated in Fig. 3.2 which shows the transverse plasma potential profile versus the average plasma density. The latter is increased from  $\langle n_p \rangle = 2.5 \times 10^{13} \text{ m}^{-3}$  up to  $\langle n_p \rangle = 6.4 \times 10^{15} \text{ m}^{-3}$ . The ratio of the densities between the two extreme cases is  $\alpha = 256$ . The variations between the potential profiles in Fig. 3.2 lie essentially on the size of the Debye sheath. The amplitude of the potential in the quasi-neutral region is similar within  $\sim 10\%$ . The Hall electric

---

field  $E_H$  is about 15 V/m (measured between the top and bottom plasma sheath edges). Figure 3.3 shows the electron current collected on the biased electrode (RHS of the simulation domain) versus the plasma density. The current increases linearly with the plasma density as expected. Note that scaling the plasma density requires to multiply also the cross-section for non-linear collision processes (i.e., elastic and inelastic collisions between charged particles). This is not necessary when scaling instead the vacuum permittivity constant  $\epsilon_0$ .



# Chapter 4

## Comparisons between 2D and 3D PIC simulations

### Contents

---

4.1	Introduction . . . . .	44
4.2	Simulation characteristics . . . . .	44
4.3	2D and 2.5D models . . . . .	48
4.4	Error induced by increasing the vacuum permittivity constant . . . . .	54
4.5	Conclusion . . . . .	55

---

## 4.1 Introduction

The purpose of this chapter is the comparison between 3D and 2D models. Scaling [18] (chapter 3) is employed to simulate the large plasma densities of negative ion sources for fusion. We use a simplified plasma chemistry where only electron and molecular hydrogen ion  $H_2^+$  dynamics are considered (subset of the reactions described in tables 2.1 and 2.2). The influence of the neutral hydrogen molecules on the plasma characteristics are included assuming a constant density and temperature profile inside the ion source volume. There are different ways to compare 2D (rectangular geometry) and 3D results. One possibility is to use the same dimensions in the plane modeled in 2D as in the 3D simulations. Doing so, the wall surface to volume ratio, which is an important scaling parameter of plasma sources, is however not conserved [36]. This parameter determines the charged particle balance (volume ionization vs wall losses) and therefore controls the electron temperature, ambipolar field, etc. Consequently, one approach is to use 2D reactor dimensions different from those of the real configuration, but which preserve the same surface-to-volume ratio as the 3D device (this approach will be referred to as “2D” model hereafter). Another solution is to use the exact dimensions in the plane of the 2D simulation, but with an approximate way of taking into account the charged particle losses in the direction perpendicular to the simulation domain (which we call a “2.5D” PIC-MCC model). This is particularly relevant under conditions where the third direction, perpendicular to the 2D simulation plane is either non-magnetized or parallel to the magnetic field lines.

## 4.2 Simulation characteristics

We calculate in 3D the plasma characteristics of the BATMAN ion source for working conditions typically encountered in the experiments [81] except for the magnetic field strength. The magnetic filter is generated by permanent magnets positioned against the lateral walls of the device, 9 cm from the PG. We chose a configuration with a 30G maximum magnetic field amplitude on the ion source axis. A sketch of the field lines and the ion source geometry is displayed in Fig 2.3. The magnetic field line density increases as one gets closer to the permanent magnets (where typically

$\mathbf{B} \gg 100\text{G}$ ) inducing mirror-like motion on the electrons which are reflected from the denser magnetic field regions. With  $B_{\text{max}} = 30\text{G}$  on axis (instead of  $\sim 75\text{G}$  in BATMAN), the Hall parameter is still large ( $h \gg 1$ ) and consequently the plasma behavior properties are preserved by the lower magnetic field while the numerical resolution is better (the scaling factor  $\alpha = \varepsilon/\varepsilon_0$  is smaller, where  $\varepsilon$  is the vacuum permittivity constant employed in the model).

The numerical grid has  $128 \times 96 \times 192$  nodes and the vacuum permittivity is artificially increased by a factor  $\alpha = 25000$  in the simulations discussed hereafter. The neutral particle transport is not modeled and the molecular hydrogen density profile is assumed constant with  $n_{\text{H}_2} = 4 \times 10^{19} \text{ m}^{-3}$ . The density is derived from experimental measurements [26] performed at a filling gas pressure of  $0.3 \text{ Pa}$  (measured without a plasma discharge). Furthermore, we assume a  $60 \text{ kW}$  absorbed power by the electrons (which is then redistributed to the neutral gas via elastic, ionization or inelastic collisions and to the ions through the ambipolar field), a  $30\text{V}$  PG bias voltage and a neutral gas temperature  $T_{\text{H}_2} = 0$  (in order to keep the model simple). The  $30\text{V}$  PG bias corresponds in the model to a situation where the current collected on the plasma electrode (PG) is dominated by electrons, i.e.,  $|I_e| > |I_i|$ , where  $I_e$  is the electron current and  $I_i$  the molecular hydrogen ion current. It was demonstrated experimentally that a PG bias sufficiently high and adjusted such that the total PG current is close to zero provides the optimum negative ion extraction conditions (where co-extracted electron current is significantly lowered) [82].

### 4.2.1 Plasma dynamics in the plane perpendicular to the magnetic field lines

Figure 4.1 shows the electron density, temperature and current density in the  $Y = 0$  plane, perpendicular to the magnetic filter field lines. The electron motion is dominated by the magnetic drift (diamagnetic and  $\mathbf{E} \times \mathbf{B}$  terms). The Hall electric field is downward directed. The plasma density is asymmetric with a maximum near the driver exit located in the upper half of the expansion chamber and moving gradually down as one gets closer to the PG. Near the PG, the density peaks in the lower half of the ion source. An asymmetry in the same direction is also observed experimentally [81]. The electron temperature drops sharply inside the magnetic filter field

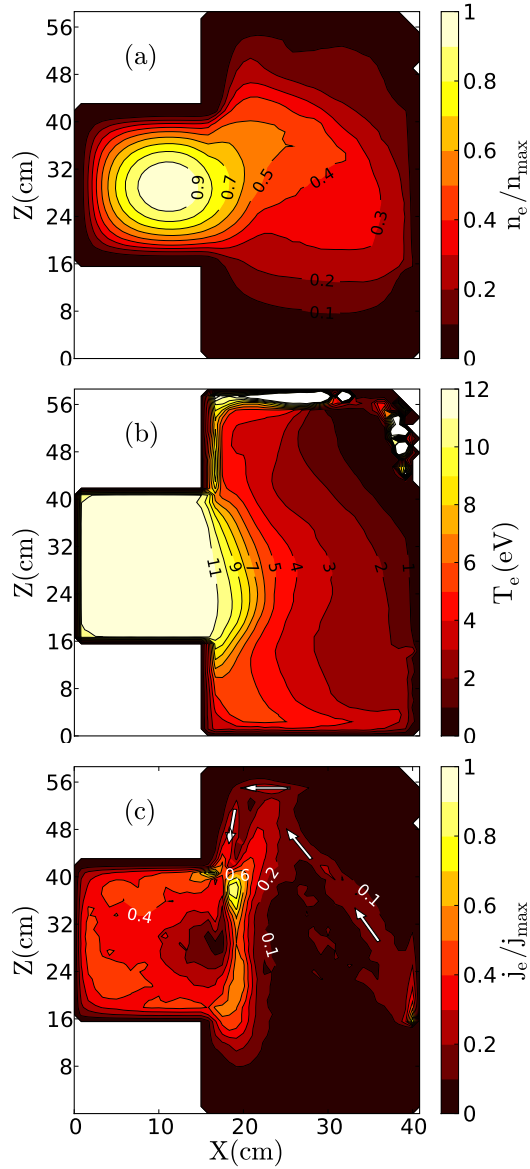


Figure 4.1: 3D plasma properties of the BATMAN negative ion source for a hydrogen density  $n_{\text{H}_2} = 4 \times 10^{19} \text{ m}^{-3}$  (i.e, a filling pressure of 0.3 Pa without plasma discharge), a magnetic filter field generated by permanent magnets (located 9 cm from the PG), with  $B_{\max} = 30\text{G}$  on axis, a PG bias voltage  $V_{\text{PG}} = 30\text{V}$  and an absorbed power  $P_{\text{abs}} = 60 \text{ kW}$ . The dimensions of the PG are  $20.5 \times 27.8 \text{ cm}^2$ . In (a), normalized plasma density in the  $Y = 0$  plane, perpendicular to the magnetic field lines.  $n_{\max} = 2.3 \times 10^{18} \text{ m}^{-3}$ . The 2D electron temperature profile in displayed in (b) and, in (c), the normalized electron current density, with  $j_{\max} = 1.6 \times 10^4 \text{ A/m}^2$ .

due to the larger electron residence time which increases the elastic and inelastic collision rates (resulting in a significant energy loss). The temperature in the model is typically  $\simeq 12$  eV inside the driver and  $< 1$  eV near the PG, in the vicinity of the top wall. Note that for  $\sim 75$ G on axis and permanent magnets close to the PG (which corresponds to the “standard configuration” in BATMAN), the calculated electron temperature is  $\simeq 14$  eV in the discharge and  $\sim 1$  eV in the extraction region [19]. Similar values are observed experimentally [15]. The temperature profile is also asymmetric (oblique isothermals) due to the magnetized electron drift dynamics which evolve into an oblique electron flux across the magnetic filter. The electron current density is shown in Fig. 4.1(c); the preferred path followed by the electrons in the  $Y = 0$  plane is highlighted by the white arrows (which show the direction of the electron current).

Positive ions are non-magnetized (or only slightly) and flow down the ambipolar potential toward the ion source walls. In the expansion chamber, the electron and ion current density distribution is strongly non-ambipolar; i.e.,  $\mathbf{j}_e \neq \mathbf{j}_i$  locally and only the total electron and ion currents collected on the ion source walls are equal. The transverse asymmetry of the ambipolar potential due to the Hall effect impacts on the plasma density which has a maximum off (the OX) axis inside the expansion chamber. The asymmetry is a strong function of the PG bias [15].

### 4.2.2 Plasma dynamics in the plane parallel to the filter field lines

The magnetic filter field is generated in the model by permanent magnet bars which are located on the lateral side of the ion source, close to the walls. The field is calculated by a third-party code [75]. The magnets have the same length along the top/bottom direction as the BATMAN device, i.e.,  $\simeq 58$  cm. Consequently the magnetic field lines are approximately parallel to any of the planes perpendicular to the (OZ) axis, i.e.,  $|B_z| \ll \sqrt{B_x^2 + B_y^2}$  (except in the near vicinity of the top and bottom walls). In these planes, electrons oscillate back and forth between the lateral walls following the field lines; hence the plasma characteristics are expected to be symmetric. This can be clearly seen for instance on the electron temperature profile in the  $Z = 0$  plane displayed in Fig. 4.2. The contours of constant electron

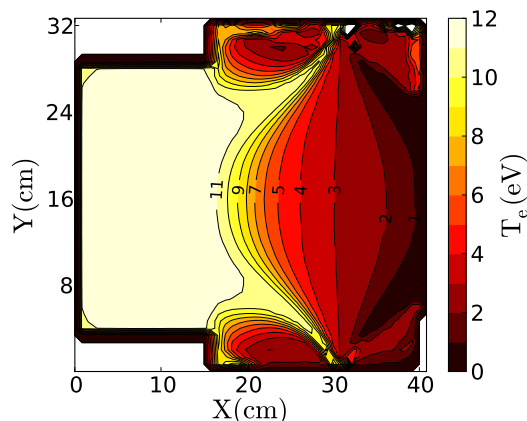


Figure 4.2: Electron temperature profile in the  $Z = 0$  plane, which is parallel to the magnetic field lines. The plasma parameters are identical to those of Fig. 4.1; the magnetic field barrier is generated by permanent magnets.

temperature follow approximately the magnetic field lines. The electrons exiting the driver penetrate inside the expansion chamber up to the position of the permanent magnets near the side walls.

### 4.3 2D and 2.5D models

Since the 2D PIC-MCC models are much less computationally intensive than 3D models it is useful to characterize the accuracy of their predictions. To reproduce approximately the 3D plasma characteristics with 2D simulations, it is necessary to preserve the charged particle balance properties in 2D as occurring in the 3D model. This observation is based on a global model (0D) derived from volume averaging the particle equations of motion using the fluid framework [Eqs. (2.2)-(2.4) of chapter 2]. One finds that the production of particles in volume is counterbalanced by the losses on the device walls; a similar observation for the power is deduced from the energy balance equation. These equations demonstrate that an average electron temperature may be estimated from the background gas density and the ion source geometry (via the volume over surface ratio). The plasma density is proportional to the absorbed power (for a given background gas density). In the 2D model, the geometry is consequently re-sized with a volume-over-surface ratio identical to the 3D ion source geometry. The length of the driver and the expansion chamber is kept the

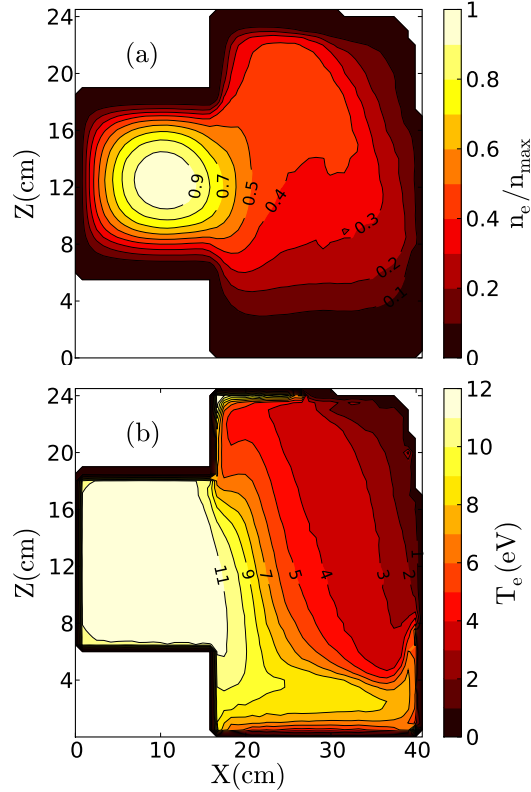


Figure 4.3: (a) Normalized electron density profile and (b) electron temperature calculated by the 2D model. The dimensions of the rescaled ion source are a driver of  $16 \times 12 \text{ cm}^2$  (length $\times$ width), an expansion chamber of  $24 \times 24 \text{ cm}^2$  and a PG of 8.9 cm (surface area of  $890 \text{ cm}^2$ ). The absorbed power is  $160 \text{ kW/m}$ , vacuum permittivity scaling factor  $\alpha = 4200$  and  $n_{\max} \simeq 2 \times 10^{18} \text{ m}^{-3}$ .

same and the transverse dimensions of the source are reduced. This gives a driver of length 16 cm, transverse size 12 cm and an expansion chamber box of  $24 \times 24 \text{ cm}^2$  (length $\times$ width). The surface area of the PG is  $890 \text{ cm}^2$  which is larger than the actual size of the grid in BATMAN ( $S_{\text{PG}} = 570 \text{ cm}^2$ ). It remains small in both cases compared to the total ion source wall surface,  $S_{\text{PG}}/S < 10\%$ . The rescaled geometry conserves both the  $V/S$  ratio of the driver and the expansion chamber. For the conditions of the BATMAN device, that is a low gas flow leading to a pressure of 0.3 Pa (without discharge) and an RF power of  $\sim 60 \text{ kW}$ , the background gas density is depleted [26] and the neutral density which is implemented in the 2D model is the one derived from experimental measurements ( $n_{\text{H}_2} \simeq 4 \times 10^{19} \text{ m}^{-3}$ , as in the 3D model).

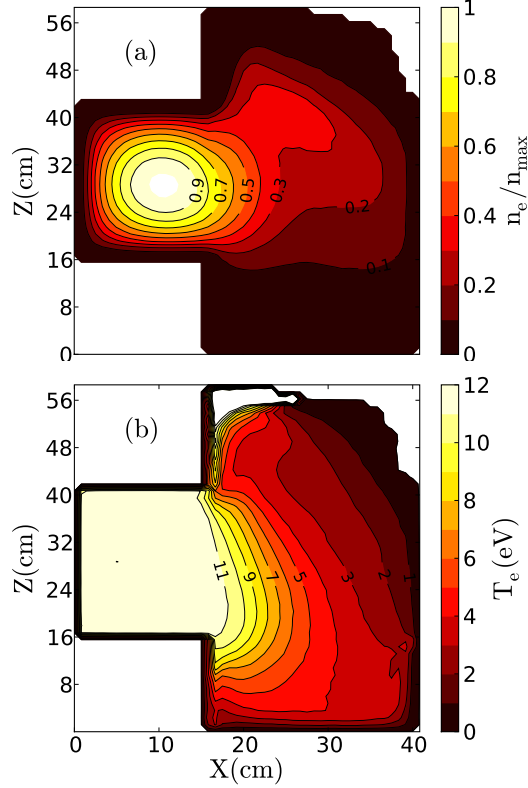


Figure 4.4: (a) Normalized electron density and (b) electron temperature profiles in the  $Y = 0$  plane calculated by the 3D model. The magnetic filter field is Gaussian with the parameters of Eq. (2.44). The simulation parameters are a 60 kW absorbed power, a PG bias voltage of 30V, a numerical grid resolution of  $128 \times 96 \times 192$  nodes and a scaling factor  $\alpha = 25000$ . The dimensions of the PG are  $32 \times 27.8 \text{ cm}^2$  ( $890 \text{ cm}^2$ ) and  $n_{\max} \simeq 2.6 \times 10^{18} \text{ m}^{-3}$ . Note that the plasma characteristics are nearly identical for a PG surface area of  $570 \text{ cm}^2$ .

In order to be able to compare 2D and 3D algorithms, we changed the shape of the magnetic filter into a configuration where the magnetic field depends only on the X coordinate and has a Gaussian profile along this direction, (i.e., no mirror effect), as in Eq. (2.44) with an amplitude  $B_0 = 30 \text{ G}$ , width  $L_m = 8 \text{ cm}$  and a maximum located at  $x_0 = 31 \text{ cm}$  (i.e., 9 cm from the PG). The magnetic field profiles for both the Gaussian filter and the case of permanent magnets are very similar on the ion source axis, as shown in Fig. 2.4.

Figure 4.3 plots the electron density and temperature profiles simulated by the 2D model. The absorbed power is set to 160 kW/m in order to keep the ratio  $P_{\text{abs}}/S_D$

identical to the 3D case. In the simulations, most of the power losses occur on the driver walls and consequently we considered the driver surface area  $S_D$  instead of the whole ion source surface  $S$  in Eq. (2.3). The 2D model reproduces qualitatively the 3D plasma characteristics including the plasma behaviour associated with the variation of external parameters such as the PG bias voltage, the amplitude or position of the magnetic filter field, etc (see for instance ref. [20] for an extensive discussion on the subject). Figure 4.4 plots the 3D electron density in the  $Y = 0$  plane (perpendicular to the magnetic field lines) for the same Gaussian magnetic filter field profile. The dimensions of the PG are  $32 \times 27.8 \text{ cm}^2$  ( $890 \text{ cm}^2$ ). The maximum density  $n_{\text{max}}$  is about 30% lower in 2D. This is because (i) the volume of the driver is  $\simeq 2.5$  times larger and (ii) the magnitude of the Hall electric field in the expansion chamber is greater due to the smaller transverse dimensions. Lastly, the plasma density distribution along the Z direction in the expansion chamber is narrower in the 3D case [Fig. 4.4(a)] than in the 2D case [Fig. 4.3(a)].

A significantly better agreement with 3D calculations can be achieved using a 2.5D PIC-MCC model. The 2.5D model is also two-dimensional in the (X,Z) plane, but rather than resizing the simulation domain to keep the same volume-to-surface ratio, we keep the (X,Z) dimensions of the simulation domain the same as in the 3D case, but we account for the charged particle losses in the third (Y) direction with some simple approximations described in Sec. 2.1.3 of chapter 2. We assume that the plasma is uniform and parallel to the magnetic field lines along the un-simulated direction Y (perpendicular to the 2D simulation plane). The magnetic filter field profile is Gaussian with the parameters of Eq. (2.44).  $L_y = 24.5 \text{ cm}$  in the driver and  $32 \text{ cm}$  in the expansion chamber. The plasma parameters are averaged over  $L_y$  in a 2.5D model. Poisson's equation is solved with a 2D multi-grid solver [35]. Figure 4.5 shows the electron density, temperature and current density profiles calculated in 2.5D. The simulation parameters are a 60 kW absorbed power, a PG bias voltage of 30V, a numerical grid resolution of  $128 \times 192$  nodes and a vacuum permittivity scaling factor  $\alpha = 15000$ . The plasma properties are very similar to those of the 3D simulations with a Gaussian filter (see Fig. 4.4). The density ratio is  $n_e / \langle n_e \rangle \simeq 1.6$  where  $n_e(x, z)$  is the density calculated by the 3D model in the  $Y = 0$  plane (Fig. 4.4) and  $\langle n_e \rangle$  the density in 2.5D (Fig. 4.5). The computation time of the 2.5D model is  $\sim 300$  times shorter than its 3D counterpart (for the grid resolutions used in this

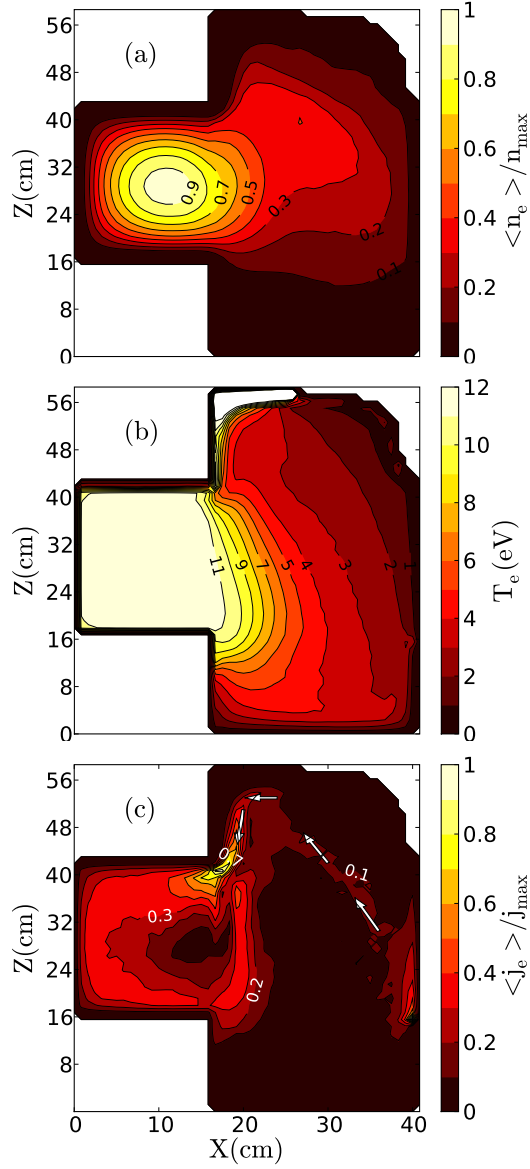


Figure 4.5: (a) Normalized electron density, (b) electron temperature and (c) electron current density profiles calculated by the 2.5D model. The plasma parameters are identical to the 3D case displayed in Fig. 4.4. The filter field profile is Gaussian.  $L_y = 24.5$  cm in the driver and 32 cm in the expansion chamber. The dimensions of the PG are  $32 \times 27.8$  cm<sup>2</sup> ( $S_{\text{PG}} = 890$  cm<sup>2</sup>),  $n_{\max} = 1.6 \times 10^{18}$  m<sup>-3</sup> and  $j_{\max} = 1.5 \times 10^4$  A/m<sup>2</sup>.

work) and consequently it may be considered as an effective alternative to obtain a qualitative assessment of the plasma kinetics.

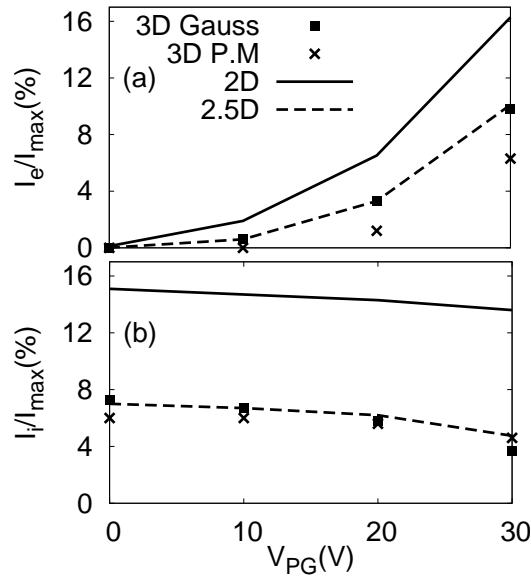


Figure 4.6: (a) Normalized electron and (b) positive ion currents impacting the PG surface vs the PG bias voltage.  $I_{max}$  is the total electron (ion) current collected on the ion source walls, respectively. Results from the 3D model with a Gaussian filter field profile (squared symbols), a magnetic filter generated by permanent magnets (cross symbols), the 2D case (solid line) and lastly, from the 2.5D model (dashed line) are shown.

The 2D and 2.5D simulations cannot describe in a simple way the curvature of the magnetic field lines in the (OY) direction. This is the reason why the 2D/2.5D and 3D comparisons above have been performed assuming a uniform magnetic field in the (OY) direction (and with a Gaussian profile along the X coordinate). The curvature of the magnetic field lines affects the plasma properties as can be seen by comparing the 3D simulation results with a magnetic field generated by permanent magnets (Fig. 4.1) and with a Gaussian profile uniform in the (OY) direction (Fig. 4.4). The mirror effect in the permanent magnet configuration reduces the charged particle losses in the (OY) direction but the general trends concerning the plasma asymmetry and the drop of the electron temperature are the same in both magnetic field configurations. Figure 4.6 shows the electron and positive ion currents collected on the PG vs the PG bias voltage calculated by the 3D model (for both the magnetic field produced by permanent magnets and the Gaussian filter profile), the 2D and the 2.5D algorithms. Considering the 3D calculation with permanent magnets as the reference case: (i) the

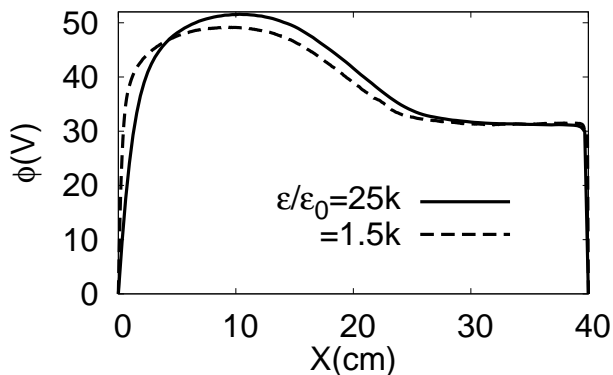


Figure 4.7: Plasma potential profiles on the ion source axis ( $Y = Z = 0$ ) calculated by the 2.5D model PIC-MCC model for (i) a numerical resolution of  $128 \times 192$  grid nodes (same as in Fig 4.5), scaling factor  $\alpha = 25 \times 10^3$  (solid line) and (ii)  $512 \times 768$  nodes, i.e.,  $\alpha = 1.5 \times 10^3$  (dashed lines).

2D model significantly overestimates the currents impacting the PG and (ii) there is a  $\sim 50\%$  increase in the electron current which crossed the magnetic field barrier in 3D with the Gaussian filter. Lastly, the currents calculated by the 3D PIC-MCC model with the Gaussian magnetic filter and its 2.5D counterpart are very similar.

#### 4.4 Error induced by increasing the vacuum permittivity constant

Artificially increasing the value of the vacuum permittivity constant results in larger plasma sheath which could potentially deteriorate the evaluation of the ion source plasma parameters in the 2D and 3D PIC-MCC models. Equation (3.4) shows that the electron magnetized drift motion depends on the pressure gradient, electric and magnetic fields. The 2.5D model with a Gaussian filter field profile hence includes all the relevant physics and is sufficient to assess the role of the larger sheaths on the plasma transport properties. Figure 4.7 displays the plasma potential on axis calculated by the 2.5D model for the same numerical resolution than Fig 4.5, i.e.,  $128 \times 192$  grid nodes ( $\alpha = \varepsilon/\varepsilon_0 = 25 \times 10^3$ , where  $\varepsilon$  is the vacuum permittivity used in the PIC calculation) and for a grid size four times smaller ( $512 \times 768$  nodes and  $\alpha = 1500$ ). The two potential profiles are very similar; the difference between

the maximum amplitudes is below 10%. The error induced by scaling ( $\alpha$  factor) is consequently small. The numerical error resulting from the large magnetic field gradients near the ion source walls for the configuration with permanent magnets has not been estimated. Doubling the numerical resolution multiplies by 16 the computation time. Nevertheless, results from the 2D, 2.5D and 3D models all show qualitatively that the magnetic filter induce a plasma asymmetry.

## 4.5 Conclusion

The purpose of this chapter is to compare plasma characteristics simulated by a 3D PIC-MCC model with solutions provided by 2D-class PIC-MCC algorithms (so called “2D” without any charged particle losses in the direction perpendicular to the simulation domain and “2.5D” when the losses in the third dimension are implemented with a simple loss model). The principal numerical assumptions are the artificial use of a larger vacuum permittivity constant (or similarly a smaller plasma density, without any loss of generality), which was shown to have little influence on the calculated plasma parameters and of a simplified RF-plasma coupling model in the ICP discharge (Maxwellian electrons absorbing at each time step a given power, which is an external parameter to the model).

As an example, the plasma properties of the one driver IPP prototype ion source operated at BATMAN (Max-Planck-Institut für Plasmaphysik, Garching, Germany) was calculated. The 2D model tends to overestimate the electron current through the filter for a given bias voltage. The 2.5D model provides plasma properties (plasma potential, density, temperatures, current density profiles) and electron current through the filter that are in good quantitative agreement with the 3D model when the magnetic field lines are posited to be parallel (constant magnetic field amplitude along the field lines). In a more complex magnetic field distribution generated by permanent magnets (and including mirror effects) the 3D model still predicts a similar asymmetry in the plasma properties but the quantitative agreement with the 2.5D model is degraded. The 2.5D and 3D PIC-MCC methods will be used alongside in the next chapters to characterise distinct features of fusion-type ion sources.



# Chapter 5

## Neutral depletion

### Contents

---

5.1	Introduction . . . . .	58
5.2	Modeling of neutral depletion in the ITER BATMAN prototype . . . . .	59

---

## 5.1 Introduction

In this chapter we couple a fluid plasma model with a kinetic description of neutral transport based on a DSMC (Direct Simulation Monte Carlo) method. The latter was described in chapter 2, section 2.2. The objective is to estimate the consequences of the fact that the gas flow is rarefied (Knudsen number not small with respect to 1) on the model results and on the velocity distribution of hydrogen atoms and molecules.

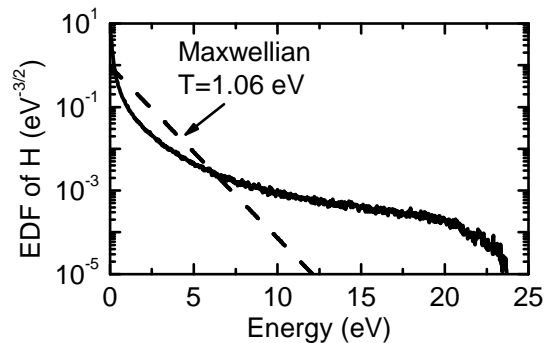


Figure 5.1: Energy distribution function for atomic hydrogen in the center of the negative ion source. We implemented a 60 kW absorbed power, 0.3 Pa background gas pressure and no magnetic filter field.

Table 5.1: Particle and power source (loss) terms for the production (destruction) of hydrogen atoms inside the ion source (60 kW absorbed power, 0.3 Pa, no magnetic filter field).

#	Reaction	Particles	Power
Source terms			
1	$H_x^+ \rightarrow H$ (surface)	45.6%	77.2%
2	$e + H_2 \rightarrow e + 2H$	47.6%	19.6%
3	Other processes	6.8%	3.2%
Loss terms			
4	$e + H \rightarrow 2e + H^+$	14.2%	2.4%
5	$H + H_2 \rightarrow H + H_2$	-	3.6%
6	$H \rightarrow H$ (surface)	-	40.4%
7	$H \rightarrow H_2$ (surface)	85.8%	53.6%

## 5.2 Modeling of neutral depletion in the ITER BATMAN prototype

In the ITER prototype source at BATMAN, the typical working conditions correspond to a low background gas pressure (molecular Hydrogen or Deuterium) of  $\sim 0.3$  Pa, together with a high RF power (coupled to the plasma by an external antenna),  $\sim 100$  kW. Such conditions depletes the neutrals in the experiments [26]. Note that neutral kinetics was described first by modeling [36] and then confirmed by experiments [26]. We model neutral depletion by coupling a DSMC algorithm for the neutrals (both molecular and atomic hydrogen in our case) with a 2D implicit fluid model. The latter is described in details in Ref. [21]. It is required to have a charged particle balance (volume ionization vs wall losses) analogous to the one occurring in the real device in order to recover similar plasma properties with a 2D model. The 2D geometry is hence re-scaled preserving the surface over volume ratio of BATMAN [23]. The dimensions of the ion source in the model is a driver of length 9 cm, height 8 cm and an expansion chamber of  $16 \times 16$  cm<sup>2</sup>. The flow rate for the molecular hydrogen gas injected into the ion source volume is adjusted,  $Q_{\text{H}_2} \simeq 0.17$  Pa  $\cdot$  m<sup>3</sup>  $\cdot$  s<sup>-1</sup> (i.e.,  $4.2 \times 10^{19}$  H<sub>2</sub>  $\cdot$  s<sup>-1</sup>), in order to conserve a residence time for the molecules similar to the experiments ( $\tau \simeq 57$  ms in BATMAN). Neutrals are pumped-out of the ion source through the PG. The physical-chemistry of neutrals is given in tables 2.1, 2.2 and 2.3 (chapter 2).

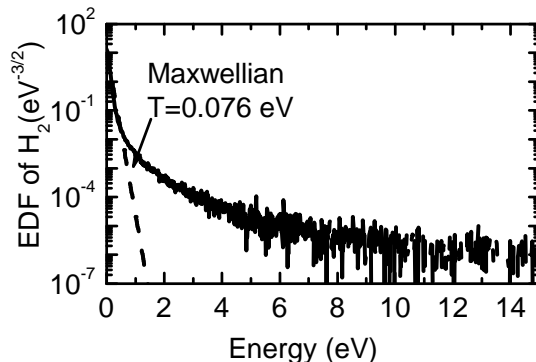


Figure 5.2: Energy distribution function for molecular hydrogen in the center of the negative ion source (60 kW absorbed power, 0.3 Pa, no magnetic filter field).

Table 5.2: Particle and power source (loss) terms for the production (destruction) of  $H_2$  (60 kW absorbed power, 0.3 Pa, no magnetic filter field).

#	Reaction	Particles	Power
Source terms			
1	$H + H_2 \rightarrow H + H_2$	-	66%
2	$e + H_2 \rightarrow e + H_2$	-	13.7%
3	$H_x^+ \rightarrow H_2$ (surface)	17.3%	1.4%
4	$H \rightarrow H_2$ (surface)	82.7%	6.7%
5	Other processes	< 0.1%	12.2%
Loss terms			
6	$e + H_2 \rightarrow e + 2H$	45.9%	6.4%
7	$e + H_2 \rightarrow 2e + H_2^+$	46.5%	6.5%
8	$H_2 \rightarrow H_2$ (surface)	-	85.9%
9	Other processes	7.2%	1.2%

Figure 5.1 shows the atomic hydrogen energy distribution function in the center of the negative ion source for a 60 kW absorbed power and 0.3 Pa background gas pressure. The distribution function is highly non-Maxwellian and its properties are mostly controlled by the production and collisions of H atoms against the walls of the ion source (the total mean-free-path is of the order of 1 m, i.e., significantly larger than the dimensions of the device). Reactions which either generate (so-called source term) or remove (loss term) hydrogen atoms from the ion source volume are summarized in table 5.1. Particle and power (gain or loss) are shown as a percentage of the total. H atoms are mostly created and heated by the wall recombination of protons and molecular ions on the ion source walls (reaction #1 with  $\simeq 45\%$  of the particle production and  $\simeq 77\%$  of the energy gain) and by the volume dissociation of  $H_2$  (reaction #2).  $H_x^+$  ions (where  $x=1-3$ ) are mainly generated inside the discharge and are accelerated by the plasma potential toward the walls of the ion source. The amplitude of the potential in the driver is about  $\sim 50V$  for 60 kW of RF power at 0.3 Pa in the experiments [15] and hence  $H_x^+$  ions impact the walls with a high energy. This explains the origin of the large energy tail in the distribution function of atomic hydrogen as shown in Fig. 5.1. Lastly, H atoms loose most of their energy through collisions with the ion source walls ( $\sim 95\%$ , reactions #6 and 7). The H and  $H_2$

temperatures are strongly dependent on the assumptions that are made on the wall reactions (accommodation coefficients provided in table 2.3).

The energy distribution function for molecular hydrogen is shown in Fig. 5.2.  $\text{H}_2$  molecules are created uniquely through the recombination of  $\text{H}_x^+$  ions and H atoms on the walls. Molecular hydrogen is emitted from the surfaces as a Maxwellian flux at  $T_w = 300$  K (where  $T_w$  is the temperature of the surface). The energy distribution function is well fitted by a Maxwellian (up to about  $6T_{\text{H}_2}$ ). The mean-free-path is  $\sim 10$  cm, i.e., smaller than the dimension of the ion source. The energy tail is induced by the collisions with the warm H atoms ( $T_{\text{H}} \sim 1$  eV while  $T_{\text{H}_2} \simeq 0.08$  eV for 60 kW and 0.3 Pa in the center of the discharge). Molecular hydrogen is mainly heated through elastic collisions with atoms ( $\sim 65\%$  of power gain, reaction #1) and by electrons (reaction #2) as shown in table 5.2.

The calculations have been performed either with or without a magnetic filter field in the expansion chamber. The magnetized case corresponds to a maximum field amplitude of  $B_{\text{max}} = 15\text{G}$  close to the PG, which is lower than the field in the actual experiment ( $\sim 75\text{G}$  on axis) but nevertheless  $h_B = \mu_e B \gg 1$  and the electrons

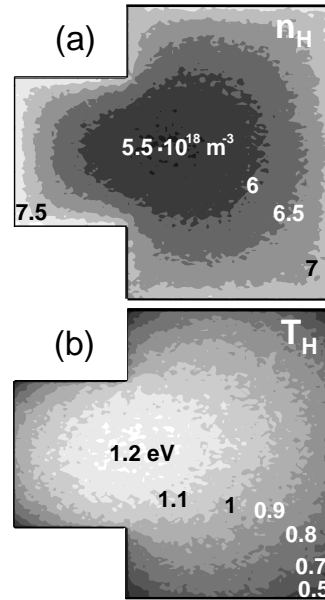


Figure 5.3: Atomic hydrogen density (a) and temperature (b) profiles. 2D DSMC calculation with  $P_{\text{abs}} = 60$  kW, a background gas pressure of 0.3 Pa,  $B_{\text{max}} = 15$  G and a PG bias voltage of 10 V.

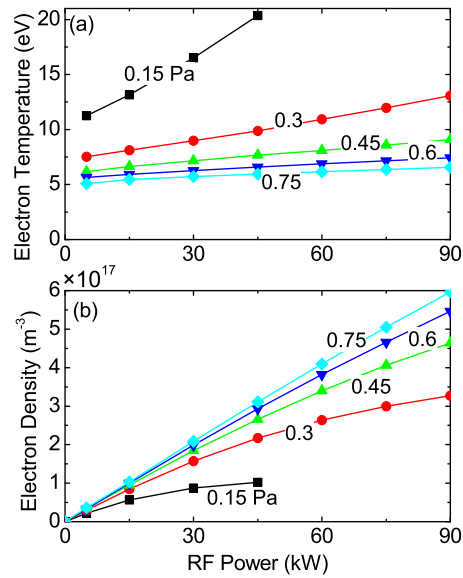


Figure 5.4: Electron density and temperature averaged over the ion source volume. 2D DSMC model, no magnetic filter field.

are fully magnetized. The indirect effect of the magnetic field on the neutral dynamics is that the depletion of  $\text{H}_2$  occurs in the area where the electron density is highest (i.e. in the driver when the expansion chamber is magnetized) because molecular hydrogen is dissociated or ionized mainly by electrons (table 5.2). The density profile of hydrogen atoms is on the contrary quite insensitive to the magnetic field due to the fact that the volume losses (ionization) are significantly smaller than for  $\text{H}_2$  (i.e.,  $\sim 14\%$  of the total losses, see table 5.1) and that the mean free path,  $\sim 1$  m, greatly exceeds the ion source dimensions. The 2D density and temperature profiles for the H atoms are shown in Fig. 5.3.

Figure 5.4 plots the electron density and temperature averaged over the negative ion source volume versus the absorbed RF power in the discharge and the background gas pressure. For a pressure of 0.75 Pa, the electron temperature is almost independent of the external power while the electron density increases quasi-linearly with power. This behavior may be explained again by a global model. Positing steady-state conditions, the total amount of particles created through ionization in the ion source volume at a given time are equal to the number of particles lost on the device

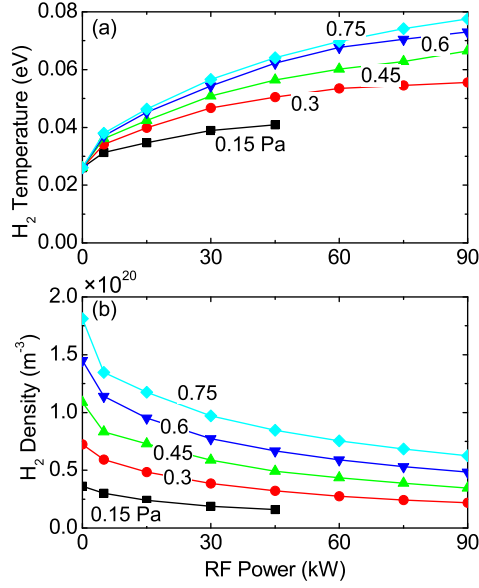


Figure 5.5: Molecular hydrogen density and temperature averaged over the ion source volume. 2D DSMC model, no magnetic filter field.

walls (see Sec. 2.1.2 of chapter 2 for more details),

$$n_s u_B S = n_g k_i \langle n \rangle V, \quad (5.1)$$

where  $n_s$  is the plasma density at the sheath edge,  $\langle n \rangle$  is the average plasma density ( $n_e = n_i$  is assumed),  $u_B = \sqrt{eT_e/m_i}$  is the Bohm velocity,  $m_i$  is the mass of  $\text{H}_2^+$ ,  $k_i(T_e)$  is the ionization rate (which is a function of the electron temperature),  $n_g$  is the background gas density and  $S$  ( $V$ ) is the ion source wall surface area (volume), respectively. Equation (5.1) is derived from the volume integration of the electron continuity equation. The term on the left-hand-side (LHS) corresponds to the electron flux impacting the ion source walls and the RHS term is the volume integrated ionization rate. If the neutral gas density  $n_g$  is fixed then Eq. (5.1) provides an estimate for the average electron temperature. The average plasma density may be deduced from the power balance equation, that is, the power absorbed ( $P_{\text{abs}}$ ) in the ion source volume is equal to the power lost on the walls,

$$P_{\text{abs}} = n_s u_B \varepsilon_T S, \quad (5.2)$$

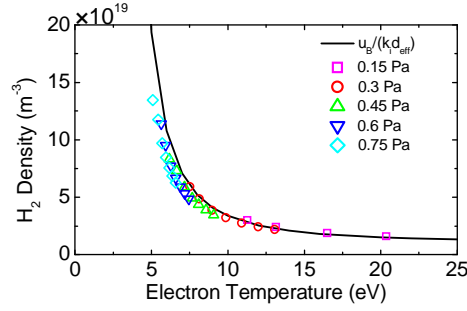


Figure 5.6: Average gas density versus the electron temperature (symbols).  $u_B/(k_i d_{\text{eff}})$  is plotted (black solid line), Eq. (5.1), where  $d_{\text{eff}} = V/(hS)$  and  $h = n_s/\langle n \rangle$ . 2D DSMC model, no magnetic filter field.

where  $\varepsilon_T(T_e)$  is the average energy lost per electron-ion pair lost on the walls [18, 36, 37]. For a given value of the background gas density  $n_g$ , the electron density hence increases linearly with the absorbed power. The gas density does vary with power as shown in Fig. 5.5. The latter is depleted by a ratio of  $\sim 65\%$  compared to the density without a discharge ( $P_{\text{RF}} = 0$ ) at 0.75 Pa and a RF power of 90 kW for instance. The electron temperature is only slightly modified beside the significant drop of the gas density because  $u_B/k_i$  in Eq. (5.1) is almost independent of  $T_e$  for high gas densities. This is illustrated in Fig 5.6. Data points from Fig. 5.4 are also plotted for convenience. For lower gas pressures,  $n_g \lesssim 5 \times 10^{19} \text{ m}^{-3}$ , the electron temperature increases sharply. Since both  $\varepsilon_T$  and  $u_B$  in Eq. (5.2) increase with electron temperature, the plasma density growth with power is less than linear (Fig. 5.4). At 0.15 Pa, the density saturates for  $P_{\text{abs}} \gtrsim 30 \text{ kW}$  and beyond 45 kW, the discharge cannot be maintained ( $n_g < 1.3 \times 10^{19} \text{ m}^{-3}$ ), i.e.,  $T_e \rightarrow +\infty$  in Eq. (5.1).

The gas density variations with power are displayed in Fig 5.5(b) and Fig 5.7(b) for different pressures (the plotted densities are averaged over the whole ion source volume). The atomic hydrogen density increases with power because the dissociation rate increases with increasing plasma density and electron temperature while the  $\text{H}_2$  density decreases with power because of gas heating (the pumping rate through the PG is constant) and dissociation. However, the average H density reaches a limit when the power increases, because of the increase in the hydrogen atom temperature. The variations with power and pressure of the volume averaged molecular and atomic hydrogen temperatures are shown in Fig 5.5(a) and Fig 5.7(a). The H temperature

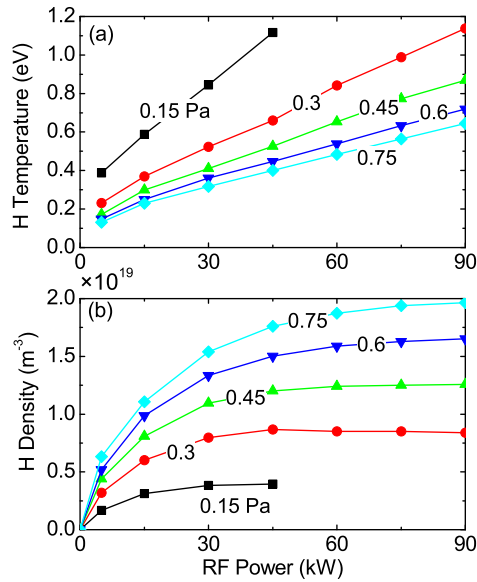


Figure 5.7: Atomic hydrogen density and temperature averaged over the ion source volume. 2D DSMC model, no magnetic filter field.

(in the 0.1 to 1.2 eV range) is much larger than the  $H_2$  temperature (on the order of 0.02 up to 0.08 eV). Both temperatures increase continuously with power. It is interesting to note that, for a given input power, the H temperature increases with decreasing pressure while the opposite is true for  $H_2$ . This is due to the larger energy exchange rate (between H and  $H_2$ ) at higher pressure. The large H temperature is due (1) to the fact that H atoms are generated with a large energy during electron impact dissociation of  $H_2$  and (2) to the generation of fast atoms at the walls resulting from the recombination of positive ions.

The wall accommodation coefficients are unknown experimentally. Assuming that the neutral hydrogen particles are backscattered off the walls with the same temperature as the surface (accommodation of 1) for the reactions # 2,4,6 and 8 of Table 2.3 instead of  $\gamma = 0.5$ , we find that (1) the amplitudes of the molecular hydrogen temperature and density are only slightly modified while (2) the H atom temperature is on average divided by 5 and the density as a consequence is larger by a factor of 2. The relationship between the accommodation coefficient and the neutral atom temperature is almost linear. The calculation was performed for a background gas pressure of 0.3 Pa and an absorbed power of 60 kW.



# Chapter 6

## Role of positive ions on the production of negative ions on the cesiated plasma grid

### Contents

---

6.1	Introduction . . . . .	68
6.2	General plasma properties from a simplified model without negative ions . . . . .	69
6.3	Results with negative ions . . . . .	74
6.4	Conclusion . . . . .	78

---

## 6.1 Introduction

The scope of this chapter is to estimate the negative ion current produced on the PG by the positive ion impacts. The BATMAN ion source typically produces a hydrogen atom density  $\sim 10^{19} \text{ m}^{-3}$  with a temperature near 1 eV [15, 26] which can potentially generate a negative ion current on the PG surface of  $\sim 60 \text{ mA/cm}^2$ . This estimate considers the yield derived for an optimal cesium coverage on the PG (i.e., lowering the work function to its minimum) [70]; these characteristics might not be attained during standard working conditions of the ion source. The typical energy cost associated with the generation and losses to the walls of one electron-ion pair is on the order of 100 eV in the model which is equivalent to a total ion current of 500 A for a 50 kW absorbed power in the driver. Furthermore, due to the relatively low electron temperature in the expansion chamber, one might consider that most of the ion current is generated in the driver. Its surface (including the driver exit) is approximately  $S_d = 2\pi R_d(R_d + L_d) \simeq 2175 \text{ cm}^2$ , with  $R_d = 12.25 \text{ cm}$  the cylinder radius and  $L_d = 16 \text{ cm}$  its length. The total ion current exiting the driver toward the expansion chamber is consequently  $\langle J_d \rangle \simeq 230 \text{ mA/cm}^2$ .

Taking as a crude estimate an ion density ratio of 40%/40%/20% for  $\text{H}^+/\text{H}_2^+/\text{H}_3^+$  as was measured experimentally in a fusion-type positive ion source [15] and further assuming that the ion kinetic energies are the same at the driver exit, one obtain an ion flux ratio of 50%/35.5%/14.5%. The latter provides an estimation for  $\langle J_d \rangle$  as a “proton” equivalent current,  $\langle J_p \rangle \simeq 380 \text{ mA/cm}^2$ , which is a more relevant quantity to evaluate negative ion production on the PG surface. The plasma potential is typically  $\sim 50 \text{ V}$  in the driver and down to about  $\sim 20 \text{ V}$  in the extraction region [15] which means that ions might impact the PG with a large kinetic energy. In addition, negative ion conversion yield (for the lowest work function) is  $\sim 0.3$  for ions kinetic energies exceeding 15 eV [70]. One important unknown remains, which is the trajectory followed by the ions once in the expansion chamber. Considering, as an upper limit, a directed flux with all the ions reaching the PG (the driver exit is facing the PG with  $S_d < S_{PG}$ , where  $S_d = \pi R_d^2 = 470 \text{ cm}^2$  and  $S_{PG} = 570 \text{ cm}^2$  [5]); this will induce a negative ion surface production on PG of  $\sim 115 \text{ mA/cm}^2$  (taking the maximum conversion yield, 30%, for all incident ions). This is about twice the current generated by neutral atoms. A lower limit can be obtained by assuming

that the ions are uniformly redirected toward the expansion chamber walls by the plasma potential. The PG surface area is  $\sim 8.5\%$  of the expansion chamber one ( $S_c = 6550 \text{ cm}^2$ ) which would result in a total positive ion current impacting the PG of order 10 A and a surface produced negative ion current density of  $10 \text{ mA/cm}^2$  (i.e., six times smaller than the current generated by neutral atoms). Clearly from the simple calculations reported above, it appears that the positive ions could potentially enhance significantly the negative ion production rate on the PG. However it is difficult to draw clear conclusions from these estimates since the gap between the upper and lower limit is rather large and additional parameters like the PG bias can certainly have a strong impact on the positive ion kinetics. We therefore conclude that an accurate estimation of the role of positive ions can only be obtained through a detailed self-consistent model. Such a model is described and used in the present paper to quantify more precisely the role of positive ions in the generation of negative ions on the PG.

The positive ion transport in an ITER-type ion source has been studied by other authors. The models were either analytical estimates [83] or tracking particle simulations [84]. Both used experimental data as input to their calculations. This work provides for the first time a fully self-consistent approach. It is a necessary step as many microscopic effects which are not directly measured experimentally turn out to be key elements to the ion kinetics (for instance the electron drift dynamics which results in an asymmetric plasma potential).

## **6.2 General plasma properties from a simplified model without negative ions**

In this section, we analyse the positive ion transport properties in a plasma which is artificially simplified in order to single out the processes which control the ion kinetics. The plasma consists uniquely of electrons and positively charged ions. The external power coupled to the plasma in the driver (absorbed) is assumed to be  $P_{\text{abs}} = 60 \text{ kW}$  and a numerical heating frequency  $\nu_H = 10^8 \text{ s}^{-1}$  is set. The 3D grid resolution is  $128 \times 96 \times 192$  nodes, 4 particles per cell on average, a time step  $\Delta t \simeq 1 \text{ ns}$  ( $\omega_p \Delta t \simeq 0.1$ ) and a vacuum permittivity  $\epsilon_0$  increased by a factor  $9 \times 10^4$  (i.e., a Debye length 300

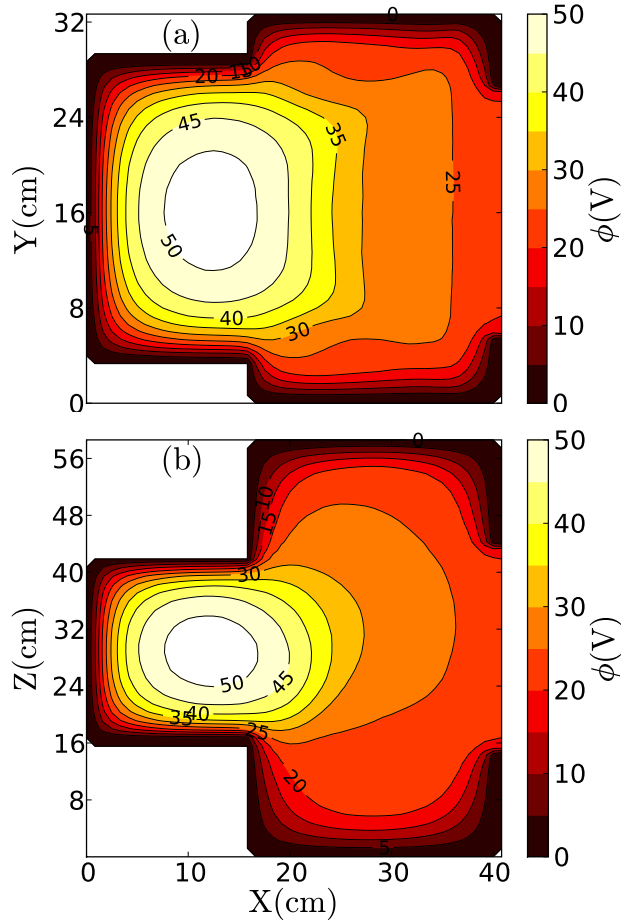


Figure 6.1: 2D profiles of the plasma potential are shown in the XY ( $Z=0$ ) and XZ ( $Y=0$ ) planes. Iso-potential lines are also displayed. The PG is biased at 20 V. The plasma asymmetry in the electron magnetic drift plane ( $Y=0$ ) is clearly visible.

times larger). The model takes a couple of hours to reach convergence on 40 nodes. The grid resolution is quite low in this example but nevertheless the extension of the plasma sheath compared to the quasi-neutral volume remains within acceptable limits. One may qualitatively estimate the volume occupied by the plasma sheath by comparing the average scaled Debye length  $\bar{\lambda}_D$  with respect to a characteristic length defined as  $L_s = \sqrt[3]{V_s} \simeq 37$  cm, where  $V_s$  is the ion source volume. For the simulation conditions considered in this work, we typically find  $\bar{\lambda}_D \simeq 1$  cm and a sheath width of  $L_{sh} \sim 3.5\bar{\lambda}_D$ , giving a ratio of  $2L_{sh}/L_s \sim 20\%$ . Using a 2D PIC-MCC model and for a similar numerical resolution, there is for instance a  $\sim 15\%$  difference for the peak

plasma potential ( $\sim 20\%$  for the electron temperature in the driver) compared to a case where the sheath length is significantly smaller.

The magnetic field profile considered in this example is generated by two permanent magnets located on the lateral side of the ion source (as shown schematically on Fig. 2.3), similar to the one found in the BATMAN device. The field is calculated by a third-party code [75]. On the source symmetry axis, the field is well fitted by a Gaussian, Eq. (2.44), with  $B_0 \simeq 75$  G,  $L \simeq 8.5$  cm and  $x_0 \simeq 40$  cm (which is on the PG).

Lastly, the ITER negative ion source operates at a gas pressure around 0.3 Pa. The background gas density in the simulations is set to  $n_{H_2} = 3.2 \times 10^{19} \text{ m}^{-3}$  and the atomic density to  $n_H = 0.8 \times 10^{19} \text{ m}^{-3}$ . Temperatures are  $T_{H_2} = 0.1$  eV and  $T_H = 1$  eV. The neutral profiles are assumed constant over the whole simulation domain. The densities are chosen according to typical values found in the BATMAN device during a plasma discharge [26].

### 6.2.1 Characteristics of the plasma potential

The plasma potential is the most relevant parameter for the positive ion kinetics. The latter are not strongly magnetized and their motion is controlled by the ambipolar electric field. Figure 6.1 shows the 2D profiles in the  $Y = 0$  and  $Z = 0$  planes for a 20 V bias on the PG. The potential is typically larger in the driver area (about 50 V) and decreases toward the PG grid (at least for a PG bias below the value of the potential inside the driver). The electron temperature is high in the driver ( $\simeq 14$  eV calculated by the model) and sharply drops in the expansion region due to the magnetic field barrier. It is below 1 eV in the vicinity of the PG. As a consequence, most of the positive ions are generated inside the driver near its exit (through ionization processes). Elsewhere inside the expansion chamber, ions experience mostly elastic or inelastic collision processes with the background gas. The plasma potential in the  $Z = 0$  plane is symmetric; the magnetic filter field vector lies mostly in that plane (see sketch on Fig 2.1) and electrons simply oscillate back and forth between the lateral walls of the ion source following the field lines (hence the symmetric profile). In the  $Y = 0$  plane, electron experience a magnetic drift. The plasma is asymmetric due to the Hall effect (chapter 3). The combined  $\mathbf{E} \times \mathbf{B}$  and diamagnetic drifts, which are

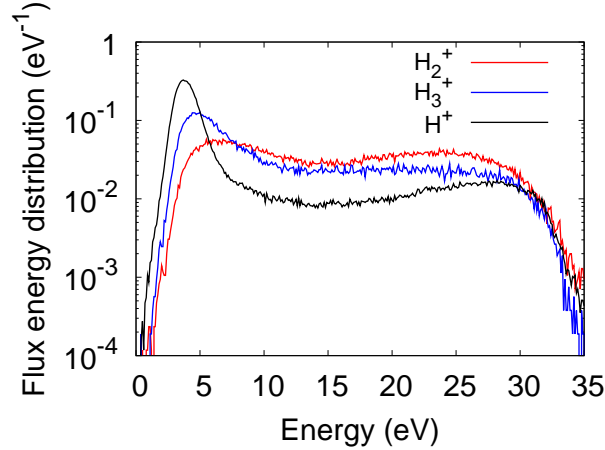


Figure 6.2: Positive ion flux energy distribution functions (edf) on the PG for the three ion species,  $H_2^+$ ,  $H_3^+$  and  $H^+$ .

usually in opposite directions, result in a skewed transport of the electron current across the magnetic filter toward the PG grid (this effect is enhanced by the PG bias). Note that positive ions are insensitive to the magnetic field but their motion is affected by the asymmetric potential.

### 6.2.2 Charged particle flux onto the PG

For 60 kW of absorbed power and a 20 V PG bias, the total electron current lost on the source walls is about 540 A (and is equal to the total ion current impacting the walls). For these specific ion source working conditions, most of the electrons impact the driver inner surfaces and the back of the expansion chamber ( $\simeq 99\%$ ). The remaining percent is shared between the lateral walls of the chamber and the PG, with an electron current of about 0.5 A on the PG. The magnetic field does consequently significantly lower the electron current which flows toward the RHS of the ion source and to the PG. The positive ion current collected on the PG is also a small fraction of the wall losses, it amounts to 6.3 A for  $H_2^+$ , 3.9 A for  $H_3^+$  and 8.3 A for  $H^+$ . Furthermore, the average kinetic energy of these ions is largely below the potential difference between the driver and the PG bias voltage,  $\Delta\phi = 32.5$  V. We find  $\langle E_k \rangle \simeq 16.3$  eV impacting the PG for  $H_2^+$ , 12.7 eV for  $H_3^+$  and lastly, 9 eV for  $H^+$ .

Figure 6.2 shows the positive ion flux energy distribution functions on the PG. A large fraction of ions have a high kinetic energy on impact. The low energy peaks especially apparent for the  $\text{H}_3^+$  ions and protons are a result of the production of ions in the expansion chamber and collisions. Seidl et *al.* calculated the negative ion conversion yield for a Mo/Cs surface [70], which is,

$$Y(E_{ki}) = \frac{R_N \eta_0}{E_{ki}} \left( E_{ki} - \frac{E_{th}}{R_E} \right), \quad (6.1)$$

where  $E_{ki}$  is the positive ion impact energy per atomic mass unit (amu) on PG. For Mo/Cs surfaces (dynamical cesiation),  $R_N \eta_0 = 0.3$  and the threshold is  $E_{th}/R_E = 2$  eV. For  $E_{ki}$  exceeding 15 eV, the probability to produce a negative ion may be as high as 30% (18% at 5 eV). Note that these data were not obtained in a plasma but through a beam-surface interaction experiment. For the distribution functions displayed in Fig. 6.2, we find 53% of  $\text{H}_2^+$  with an energy above 15 eV, 35% of  $\text{H}_3^+$  and 22% of protons. A significant fraction of the ions which impact the PG may consequently produce negative ions. Nevertheless, due to the relatively low positive ion current density flowing onto the PG,  $\langle j_+ \rangle \simeq 32$  mA/cm<sup>2</sup>, this is insufficient to out-compete the large negative ion current density generated by neutral atom impacts ( $j_n^0 \simeq 60$  mA/cm<sup>2</sup>). Lastly note that a small amount of positive ions have an impact energy  $E_{ki} > \Delta\phi$  (see Fig. 6.2); this is due to the particle collisions processes.

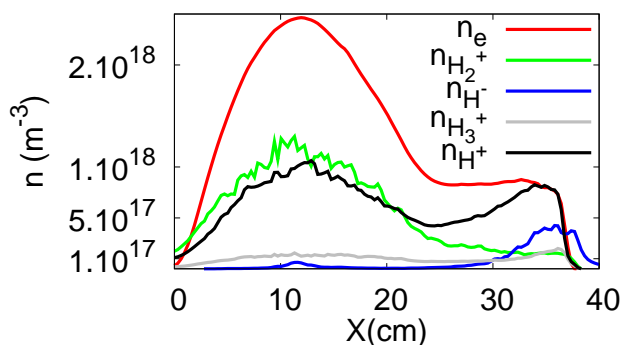


Figure 6.3: Charged particle density profiles on the ion source axis ( $Y = Z = 0$ ).

### 6.3 Results with negative ions

In this section, we include negative ions produced on the PG surface by neutral and positive ion impact, as well as negative ions produced in the discharge volume by attachment. The negative ions generated by neutral atoms impacting the surface are supposed to be emitted with a Maxwellian flux distribution at a temperature  $T_n = 1$  eV. The negative ion current density due to neutral atom impact is taken as a free parameter and supposed to be  $j_n^0 = 40$  mA/cm<sup>2</sup>. This is lower than the value of 73 mA/cm<sup>2</sup> given by analytical estimations using Eqs. (2.41)-(2.42) for  $n_H = 0.8 \times 10^{19}$  m<sup>-3</sup>, but this value is probably overestimated because the yield provided in ref. [70] used in this estimation was not obtained under plasma conditions, and the cesium coverage is likely not optimum in the ITER-type BATMAN device.

Negative ions originating from positive ion impacts are self-consistently included in the model; the numerical method is described in Sec. 2.4. Negative ions are scattered isotropically with respect to the PG surface normal, toward the ion source volume. Negative ions produced via volume processes are taken into account in a simple, non-self-consistent way by assuming that 1% of the hydrogen molecules (H<sub>2</sub>) are in the required excited states ( $\nu \geq 4$ , where  $\nu$  is the vibrational quantum number) for a dissociative capture to occur (reaction #17 in table 2.1). The other parameters of the simulated device are the ones of Sec. 6.2.

Figure 6.3 shows the electron and ion density profiles on the ion source axis ( $Y = Z = 0$ ). The electron density is about  $2.2 \times 10^{18}$  m<sup>-3</sup> inside the driver and drops to  $7 \times 10^{17}$  m<sup>-3</sup> near the PG for an *absorbed* power of 60 kW. In the driver area, the ion population is mainly H<sub>2</sub><sup>+</sup> ions and protons and inside the expansion chamber protons become the dominant species. In the vicinity of the PG, H<sub>2</sub><sup>+</sup> and H<sub>3</sub><sup>+</sup> have about the same density while the negative ion density peaks due to the surface production. The peak also observed in the proton density is induced by the chemistry and the plasma quasi-neutrality.

The total electron losses on the device walls amount, like in the previous example, to 540 A. Concerning the positive ions, we find 246 A for H<sub>2</sub><sup>+</sup>, 46 A for H<sub>3</sub><sup>+</sup> and 246 A for H<sup>+</sup>. For a 20 V PG bias, the particle currents impacting the PG surface are about 1.7 A for the electrons and in total  $I_+ \simeq 16.3$  A for the positive ions. The distribution of the ion current on the different parts of the chamber walls is as follows: 77% of

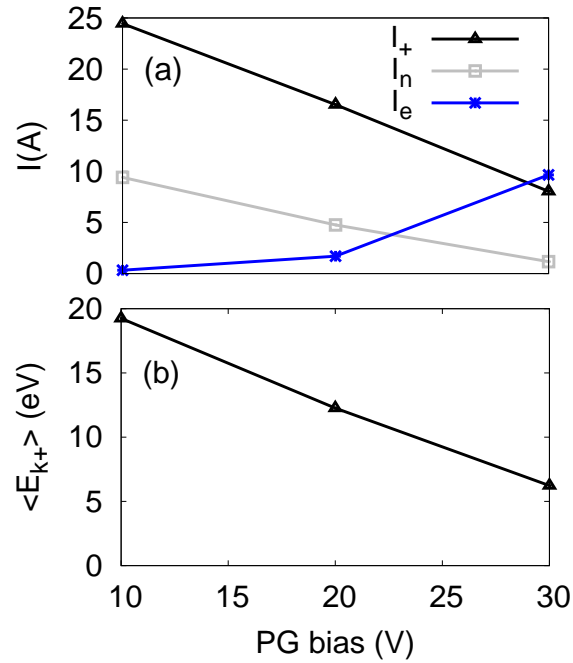


Figure 6.4: (a) Electron ( $I_e$ ) and total positive ion ( $I_+$ ) currents on PG versus bias. The negative ion current  $I_n$  corresponds only to negative ions produced by positive ion impact on the PG. (b) Average kinetic energy of the incident positive ions on PG.

$\text{H}_2^+$ , 51% of  $\text{H}_3^+$ , 69% of protons impact the driver walls and the back of the expansion chamber, 18%/32%/24% the lateral surfaces of the chamber and lastly, approximately 5%/17%/7% the RHS wall of the ion source (the PG and bias plate).

### 6.3.1 Charged particle currents versus bias on the PG

Figure 6.4(a) shows the electron and ion currents impacting the PG. The fraction of negative ion current generated solely by positive ion impacts is also plotted (production by impact of hydrogen atom and negative ions returning to the PG are not included). Note that the model does not describe negative ion extraction through the grid holes. A large part of the negative ions returns to the PG (space charge saturation). The average positive ion kinetic energy on impact is displayed in Fig. 6.4(b). These quantities are plotted as a function of the PG bias. The positive ion current on PG is a small fraction of the total amount produced in the ion source volume. The positive ion flux to the PG significantly decreases with an increasing bias and so

does the production of negative ions by positive ion impact on the grid. It is clear from Fig. 6.4 that the production of negative ions by positive ion impact is a strong function of the bias voltage and tends to be larger at lower bias voltages. For example, for a bias of 10 V, the negative ion current produced by positive ions impacting the PG is 10 A. This is to be compared with the negative ion current produced by atom impact on the PG, which is on the order of 30 A. This estimation is obtained from Ref. [71, 72] where the authors assumed a H atom density and temperature of  $10^{19} \text{ m}^{-3}$  and 0.8 eV, and a yield of 0.12 negative ion per atom impacting the grid (note that the extracted negative ion current in the BATMAN ion source is typically about 2 A [5], i.e. much less than the current actually produced on the grid). We can conclude that for a 10 V bias (or lower) the negative ion current produced by positive ion impact is not negligible with respect to the negative ion current produced by atom impact, while it is much smaller for a bias voltage of e.g., 30 V. In practice, in the experiments (see, e.g., Ref. [82, 84]), the applied bias voltage is chosen so that the net current to the PG is positive (i.e. the electron flux to the PG is larger than the positive ion flux plus the flux of negative ions either extracted or lost in volume). In our numerical example [see Fig. 6.4(a)], this would correspond to a bias voltage larger than 30 V, i.e. to a very low production of negative ions by positive ion impact on the PG.

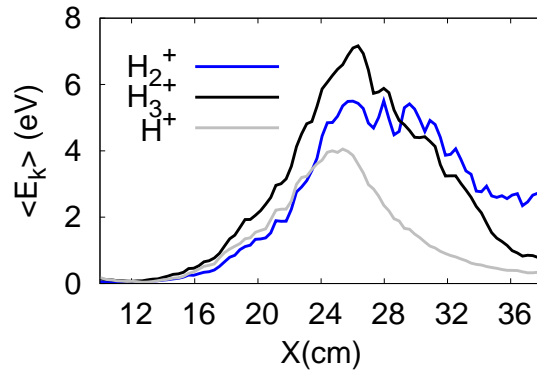


Figure 6.5: Average positive ion kinetic energy on the ion source axis,  $\langle E_k \rangle = \frac{1}{2} m_i \langle v_i \rangle^2$ . Profiles are shown from the middle of the driver up to 2 cm from the PG. The potential gap in this region is  $\Delta\phi \simeq 25$  eV and the PG bias is 20 V.

### 6.3.2 Positive ion energy and mean-free-path in the expansion chamber

It is interesting to look in details at the transport of positive ions in the expansion chamber and to quantify the role of collisions on the ion kinetic energy in that region. Figure 6.5 shows the average positive ion kinetic energy on axis  $\langle E_k \rangle = 1/2 m_i \langle v_i \rangle^2$ , calculated for the BATMAN ITER-type source between the middle of the driver up to 2 cm from the PG, for a bias voltage of 20 V.  $m_i$  and  $v_i$  are the mass and velocity of any of the three positive ion species. We see on this figure that the mean ion energy is much smaller than the potential difference between the driver and the expansion chamber (on the order of 25 V in these conditions, see Fig. 6.1), meaning that collisions and ion generation by ionization play an important role. The average energy peaks around 10 cm after the driver exit and then starts decreasing. Ions gain energy on average before the peak because of the large potential drop, while energy losses due to collisions are dominant after  $X \simeq 25$  cm. Ionization in the expansion chamber can lower the ion mean energy since ions resulting from ionization are generated at low energy and do not see the total voltage drop. The simulations show that 30% of  $H_3^+$ , 12.5% of protons and 10% of  $H_2^+$  ions are generated through ionization processes inside the expansion chamber (for  $X \gtrsim 20$  cm). Consequently, except for the  $H_3^+$  ions, ionization is actually not responsible for the relatively low ion energy in the expansion chamber; elastic and charge exchange collisions play the most important role. Figure 6.6 shows the positive ion mean-free-path (mfp) as a function of position inside the chamber. The mean free path  $\lambda_{\text{col}}$  includes elastic, charge exchange and inelastic collisions between ions and neutrals.  $\lambda_{\text{des}}$  is the mean free path for the destruction of a particular type of positive ion (i.e. reactions #14 and 15 of table 2.2 for  $H^+$ , reaction #3 for  $H_2^+$ , reactions #9, 10, 11 and 12 of table 2.1 for  $H_3^+$ ). The mean free paths are calculated as  $\lambda^{-1} = \nu/v_i$  where  $\nu$  is the sum of the average collision frequencies for the different collision processes, and  $v_i$  is the mean velocity deduced from the mean kinetic energy of the ions. We see on Fig. 6.6 that the ion mean free paths  $\lambda_{\text{col}}$  are significantly smaller than the chamber dimensions, i.e. between 5 and 10 cm for  $H^+$  and  $H_3^+$ , and slightly larger than 10 cm for  $H_2^+$ . The mean free paths,  $\lambda_{\text{des}}$  for the destruction of the different ions are much larger than the mean free paths for collisions,  $\lambda_{\text{col}}$ , except for  $H_2^+$  at the driver exit

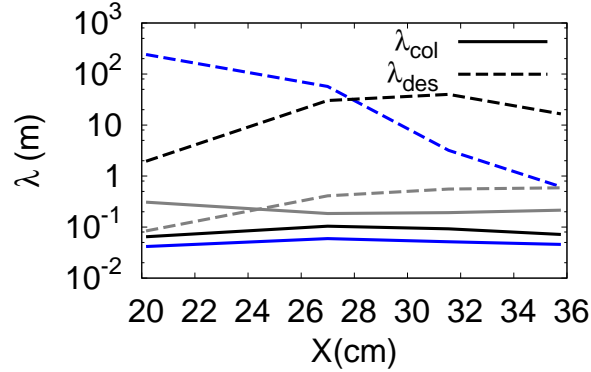


Figure 6.6: Positive ion mean free paths (mfp). Total elastic, charge exchange and inelastic collision mfp  $\lambda_{\text{col}}$  (solid lines) and destruction mfp  $\lambda_{\text{des}}$  (dashed-lines) are shown. The blue color corresponds to protons, black for  $\text{H}_3^+$  and grey  $\text{H}_2^+$  ions. The PG bias is set to 20 V.

( $\text{H}_2^+$  ions are converted into  $\text{H}_3^+$  and protons). We can conclude that positive ion transport in the expansion chamber is quite collisional, which explains the relatively low mean ion kinetic energy, compared with the potential drop in that area. Lastly, the positive ion temperature in the vicinity of the PG is  $T_i \simeq 3.2$  eV for  $\text{H}_2^+$ , 1.6 eV for  $\text{H}_3^+$  and 1 eV for protons in the model.

## 6.4 Conclusion

A 3D Particle-In-Cell model with Monte-Carlo collisions has been used to analyse positive ion transport in an ITER-type negative ion source and the role of positive ions in the production of negative ions on the cesiated plasma grid surface (compared with the production of negative ions by impact of neutral atoms). We found that the electron and positive ion currents collected on the PG amount only to a small fraction of what is actually impacting the other device walls. For typical ion source working conditions, that is, for a PG bias voltage such that the total current on the PG is above floating potential  $I_{\text{PG}} \simeq 0$  (in our model, this corresponds approximately to a 30V PG bias which is consistent with experimental values [84]), the total positive ion current on the PG is  $I_i \simeq 8$  A (1.5%) while the electron current is  $I_e \simeq 10$  A (1.8%). The resulting negative ion current which is generated by the positively charged particles is  $j_n^+ \simeq 2.5$  mA/cm<sup>2</sup> (1.4 A) which is significantly below the fraction produced by

neutrals ( $j_n^0 \simeq 60 \text{ mA/cm}^2$ ,  $\sim 34 \text{ A}$ ). The positive ion flux and average kinetic energy on PG strongly depends on the value of the bias. When the bias voltage is increased, both the positive ion flux and energy decrease (and consequently  $j_n^+$  gets also smaller). For lower bias voltages the negative ion current due to positive ion impact becomes more significant. For instance, for a 10 V bias, the model predicts  $j_n^+ \simeq 20 \text{ mA/cm}^2$  (i.e.,  $j_n^+/j_n^0 \simeq 0.3$ ). However, for PG biases below the floating potential, the plasma potential may be significantly above the PG voltage, which does not seem to be favourable conditions for efficient negative ion extraction.

Inside the expansion chamber, positive ions typically have a kinetic energy significantly smaller than the difference between the plasma potential in the driver and the PG bias. This is essentially due to the elastic and inelastic collision processes with the neutral particles. The mean-free-path is  $\lambda_{\text{col}} \simeq 13 \text{ cm}$  for  $\text{H}_2^+$  ions,  $\lambda_{\text{col}} < 10 \text{ cm}$  for protons and  $\text{H}_3^+$ . The length of the expansion chamber in the model is 24 cm. The ion distribution function is typically non-Maxwellian; the temperature in the vicinity of the PG is higher for the  $\text{H}_2^+$  ions,  $T_i \simeq 3.2 \text{ eV}$ ; we calculate 1.6 eV for  $\text{H}_3^+$  and lastly for the protons, which are the most collisional, 1 eV.



# Chapter 7

## Effect of biasing the plasma electrode on the plasma asymmetry

### Contents

---

7.1	Introduction . . . . .	82
7.2	3D PIC model of the one-driver prototype source at BATMAN . . . . .	83
7.3	2.5D PIC-MCC model of the half-size ITER prototype ion source ELISE . . . . .	93
7.4	Conclusion . . . . .	99

---

## 7.1 Introduction

In this chapter, we analyse to what extent the PG bias voltage enhances the plasma asymmetry. We simulate both the single driver (i.e., ICP discharge) prototype ion source at BATMAN and the 4-drivers ELISE device:

- The simulation parameters for the single driver prototype ion source at BATMAN are identical to the one used in the previous chapter (Sec. 6.2) except that the magnetic field is lower (30G on the ion source axis instead of 75G). The simulation domain for BATMAN is shown in Fig. 2.3.  $\varepsilon_0$  is rescaled by a factor  $\alpha = 36 \times 10^3$ . This corresponds to a ratio of  $2L_{sh}/L_s \simeq 12\%$  where  $L_s = \sqrt[3]{V_s} \simeq 37$  cm,  $V_s$  is the ion source volume,  $L_{sh} \sim 4\bar{\lambda}_{De}$  is the sheath length and  $\bar{\lambda}_{De} \simeq 5.7$  mm (average Debye length in the calculation).
- The large size 4-drivers ELISE source is characterized using the 2.5D PIC-MCC model [23] (Sec. 2.1.3 of chapter 2 ). The plasma is simulated in the plane perpendicular to B (i.e. where the magnetized drift motion takes place). This model is restricted to simplified magnetic field maps, where the field lines are straight in the un-simulated direction. This is particularly relevant for the ELISE ion source prototype because the magnetic field is generated by a large current circulating through the PG ( $\sim 4$  kA). The magnetic field profile in ELISE is reported in Fröschle *et al.* [13] (configuration “a”); the field lines are approximately straight except inside the driver. Figure 7.1 shows the

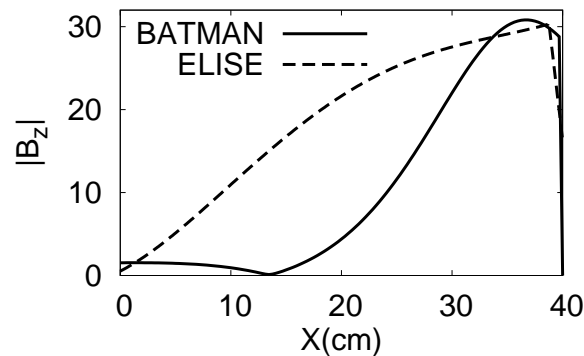


Figure 7.1: Magnetic field profiles on axis for the BATMAN and ELISE ITER negative ion source prototypes.

field profile on axis. Plasma transport properties inside the expansion chamber should consequently be reproduced quite accurately. The driver is magnetized ( $|B| \lesssim 15$  G) and the simulation of the external RF power absorption by the electrons, which is modeled by an artificial Maxwellian heating algorithm, is probably not adequate. Nevertheless, we may still consider the plasma generated inside the driver as a source term for the particles flowing toward the expansion chamber with the correct characteristics on average (density, temperature, etc.). Note that Maxwellian heating generates a constant temperature profile inside the driver (we choose a heating frequency  $\nu_H \ll \Omega_e$ , where  $\Omega_e$  is the electron cyclotron frequency).

Figure 7.2 shows the 2D simulation domain (XZ plane) for the ELISE ion source modeled with the 2.5D PIC-MCC algorithm. The magnetic field lines are perpendicular to the simulated plane. The ELISE device is half the size of the foreseen ITER negative ion source (it has four drivers). In the 2.5D model, we simulate two drivers in the XZ plane and assume that along the third direction (OY), the length of the drivers is equal to the width of the ion source  $L_y$ . The absorbed power per driver in 2.5D is consequently equivalent to the total power of a pair of two lateral drivers along (OY) in ELISE.

## 7.2 3D PIC model of the one-driver prototype source at BATMAN

We assume a 60 kW absorbed power by the electrons inside the driver, a maximum magnetic field amplitude along the X-axis of  $B_{\max} = 30$  G, a numerical heating frequency  $\nu_H = 10^8$  s<sup>-1</sup> and a grid resolution of  $128 \times 96 \times 192$  nodes.  $\varepsilon_0$  is rescaled by a factor  $\alpha = 36 \times 10^3$ . Other numerical parameters in the simulation are a time step  $\Delta t \simeq 1$  ns ( $\omega_{pe}\Delta t \simeq 0.15$ ), 6 particles per cell on average (summed over the positively charged ions), a molecular hydrogen density  $n_{\text{H}_2} = 3 \times 10^{19}$  m<sup>-3</sup>, temperature  $T_{\text{H}_2} = 0.1$  eV, neutral atom density  $n_{\text{H}} = 10^{19}$  m<sup>-3</sup>, temperature  $T_{\text{H}} = 1$  eV and a negative ion current density generated on the PG from neutral atom impacts [19, 71, 72]  $j_n = 60$  mA/cm<sup>2</sup> (we assume a Maxwellian flux distribution with  $T_n = 1$  eV).

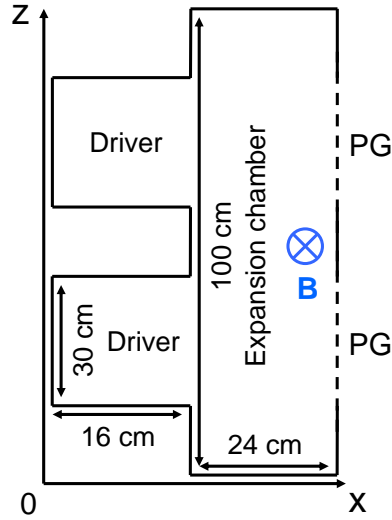


Figure 7.2: Schematic view of the 2D geometry implemented in the 2.5D PIC-MCC model to calculate the plasma characteristics of the half-size ITER ion source prototype at the ELISE testbed in IPP Garching, Germany. The magnetic field is generated by  $\sim 4$  kA currents flowing through the plasma grid (PG). The (OZ) axis corresponds to the vertical axis. The length of the ion source along (OY) is  $L_y = 86$  cm.

### 7.2.1 Plasma characteristics in the drift plane versus the PG bias voltage

Simulations have been performed in the BATMAN source for increasing values of the PG bias. In this section we show the 2D space distributions of the electric potential (Fig. 7.3) and electron density and temperature (Fig. 7.4) in a plane perpendicular to the magnetic field (XZ plane displayed in Fig. 2.3) for two values of the PG bias voltage, 25V and 35V. As can be seen in Fig. 7.5(c), 25V and 35V bias voltages are respectively below and above the voltage (about 30V) for which the total current collected by the PG passes through zero. Roughly speaking (for more details see the discussion on Fig. 7.5(c) below), this means that above a PG bias of 30V (the floating potential) the plasma grid collects more electrons than positive ions, while the opposite is true below 30V. This has some visible consequences on the distributions of electric potential and plasma density. In Fig. 7.3(a), the potential in the vicinity of the PG is below the value of the bias applied on the grid (35V) while in Fig. 7.3(b) the potential next to the PG is slightly above the bias voltage. The fact that, for a

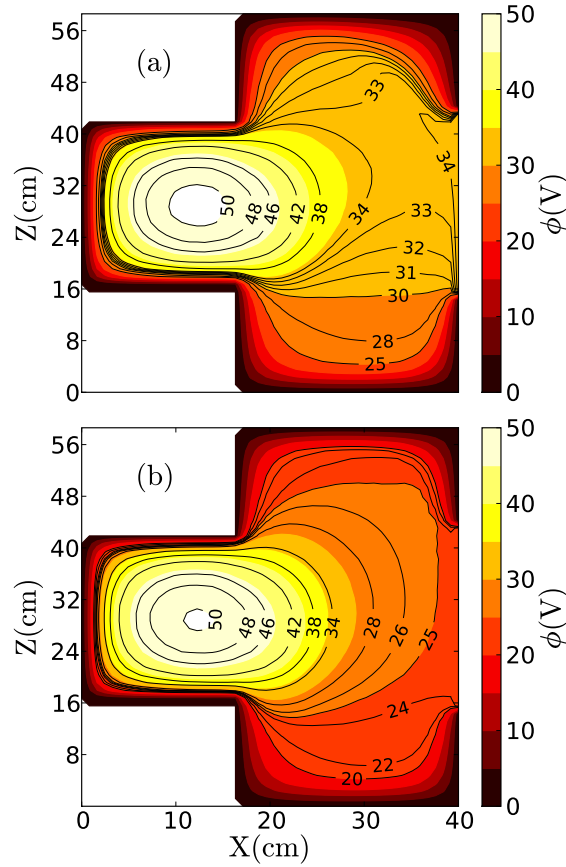


Figure 7.3: 3D plasma characteristics of the BATMAN ion source for a filling gas pressure of 0.3 Pa and an absorbed power of 60 kW. The plasma potential profiles in the  $Y = 0$  plane, i.e, perpendicular to the magnetic field lines, for (a) a 35V and (b) a 25V PG bias voltage are shown. The magnetic filter is generated by permanent magnets. The field is maximum on the PG with  $B_{\max} = 30\text{G}$  along the X-axis. The numerical resolution is  $128 \times 96 \times 192$  grid nodes and the scaling factor  $\alpha = 36 \times 10^3$ . The dimensions of the PG are  $20.5 \times 27.8 \text{ cm}^2$ .

PG bias of 35V, the potential is not monotonically decreasing from the driver to the PG but presents a flatter part in the filter and increases closer to the PG is correlated with an increase of the plasma density in the vicinity of the PG. This can be seen in Figure 7.4(a) which exhibits a local relative maximum of the plasma density a few cm before the plasma grid. This is because some low energy positive ions (resulting mainly from ionization) cannot reach the PG and spend a long time in this region while slowly going down the potential in a direction parallel to the PG. This effect

tends to enhance the asymmetry of the plasma density (compare the plasma density of Fig. 7.4(b) calculated for a PG bias of 25V, below the floating potential with that of Figure 7.4(a) corresponding to a 35V PG bias, i.e. above the floating potential).

The electron temperature distribution is shown in Fig. 7.4(c) for a 25V bias voltage. It is about 12 eV inside the driver and down to  $\simeq 1.5$  eV in the extraction region. The temperature profile is also asymmetric (oblique isothermals) due to the magnetized electron drift dynamics. The electron residence time inside the expansion chamber is greatly increased by the magnetic filter field. Electrons loose energy via elastic and inelastic collision processes, hence the sharp temperature drop from the driver region to the PG.

### 7.2.2 Plasma parameters in the vicinity of the PG

In this section we assess the effect of the PG bias potential on the plasma characteristics in front of the electrode (extraction region). This corresponds to an area of the ion source where many experimental measurement campaigns were performed [15, 81, 85]; a clear knowledge of the plasma in front of the PG is necessary to fully characterize negative ion extraction dynamics. In addition, we correlate the plasma parameters with the total current collected on the PG in order to evaluate the breaking point above which the plasma asymmetry is significantly increased.

Figure 7.5 shows in (a) the plasma potential, (b) the electron density and (c) the total particle current onto the PG ( $I_{PG}$ ) vs the PG bias voltage. We did not simulate apertures in the grid. The bias current is given by  $I_{PG} = I_e + I_n + I_p - I_{sn}$  where

$$I_\beta = q_\beta \iint_{S_{PG}} \Gamma_\beta \cdot dS, \quad (7.1)$$

$q_\beta$  ( $\Gamma_\beta$ ) is the particle charge (flux), respectively.  $I_e$  ( $< 0$ ) corresponds to the electron current impinging the PG ( $S_{PG}$  is the PG surface area),  $I_p$  ( $> 0$ ) the total positive ion current,  $I_n$  ( $< 0$ ) the negative ion current and  $I_{sn}$  ( $< 0$ ) is the negative ion current produced on the PG by neutral atom and positive ion impacts.  $I_{sn}$  is subtracted because negative ions produced on the PG “remove” electrons from the electrode; this is equivalent to a “positive” current circulating through the PG. The total current collected on the PG is electronegative when  $I_{PG} < 0$ .

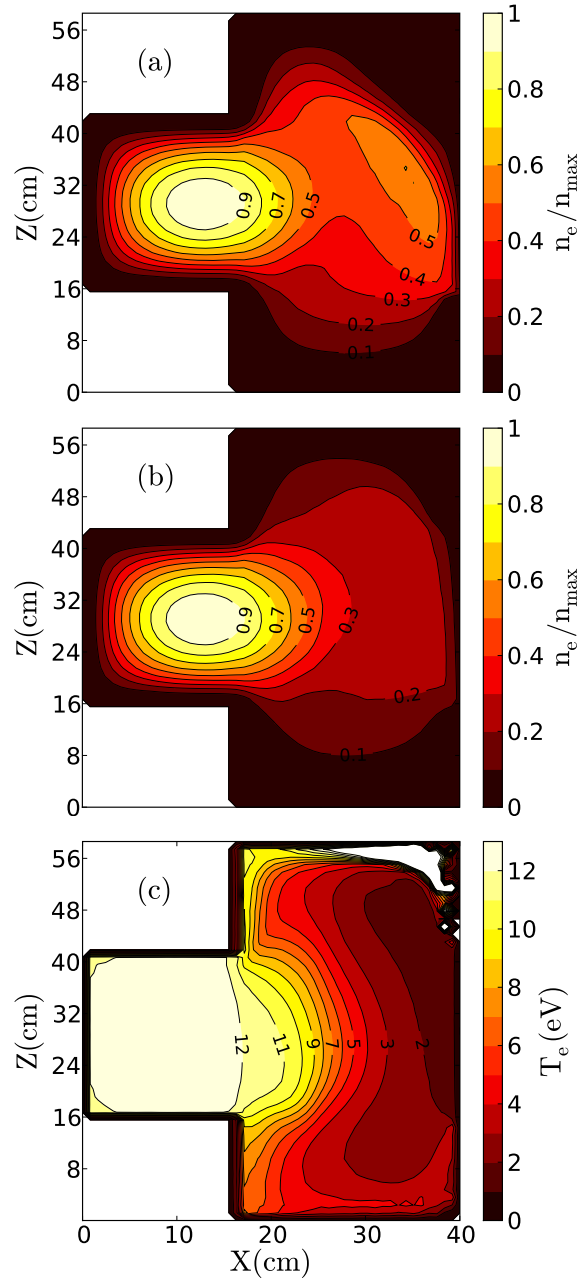


Figure 7.4: The normalized electron density profiles for the one-driver BATMAN ion source in the  $Y = 0$  plane is shown for (a) a 35V and (b) a 25V PG bias voltage. The electron temperature profile in (c) corresponds to a bias of 25V.  $n_{\max} = 2 \times 10^{18} \text{ m}^{-3}$  in both (a) and (b). The plasma parameters are calculated by a 3D PIC-MCC model.

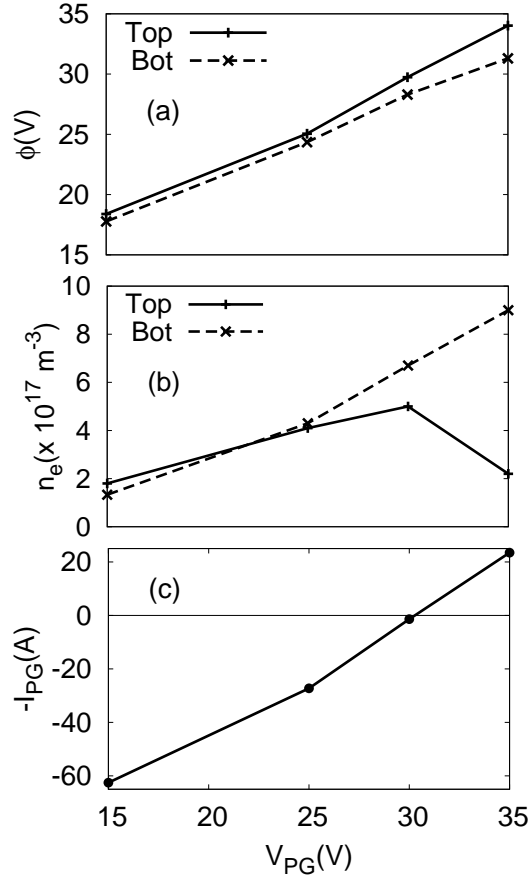


Figure 7.5: The plasma potential, electron density and total particle current collected on the PG ( $I_{PG}$ ) in the one-driver ITER prototype source are shown vs the PG bias voltage for the “top” ( $Y = 0$  and  $Z \simeq 39$  cm) and “bottom” ( $Y = 0$  and  $Z \simeq 19$  cm) coordinates and for a distance  $\simeq 2.5$  cm from the PG (i.e.,  $X = 37.5$  cm). These locations are similar to Langmuir probe and laser photo-detachment measurements performed in experiments [15, 81, 85]. Note that  $-I_{PG}$  is plotted in accordance with the sign convention used in the experiments.

Note that a negative ion current sufficiently large is produced on the PG (typically  $j_n \simeq 60 \text{ mA/cm}^2$ , i.e.,  $\simeq 30\text{A}$  in BATMAN) to generate a virtual cathode in front of the grid [71, 72] (a sharp and localized drop of the plasma potential profile) because the plasma cannot cancel out the space charge resulting from the negative ion charge density. A large fraction of the negative ions are hence reflected back on the PG grid surface. About 3A ( $\sim 10\%$ ) of negative ions are extracted toward the accelerator in BATMAN for  $I_{PG} \lesssim 0$  and a small fraction is flowing toward the plasma volume, i.e.,

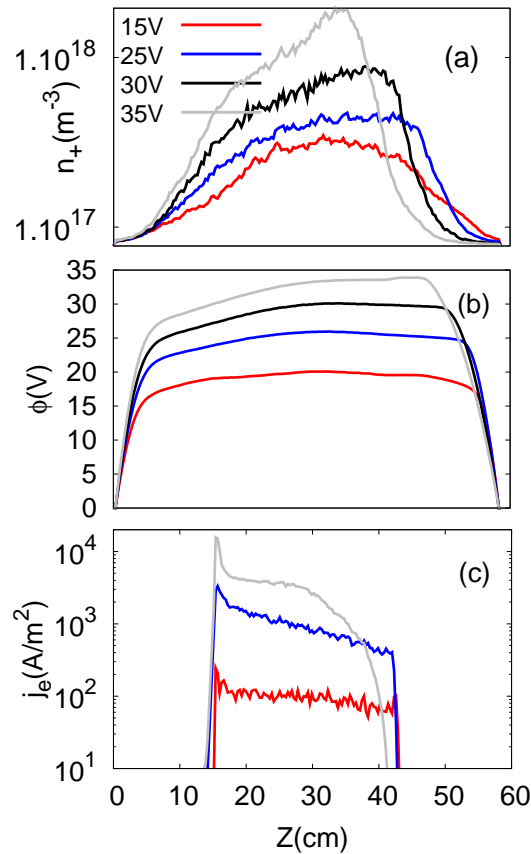


Figure 7.6: Distributions along the  $Z$  direction (in the  $Y = 0$  plane and about 5.5 cm from the plasma grid) of (a) the electron density and (b), the electric potential, for 4 values of the bias voltage; (c) shows the distribution along the  $Z$  direction and at  $Y = 0$  of the electron current density collected by the plasma grid, for 3 values of the bias voltage.

approximately  $< 10\%$  as calculated by the 3D PIC-MCC model. As a consequence, in this regime  $I_{sn} \sim I_n$  (the contribution to  $I_n$  from negative ions produced in volume via dissociative attachment between an electron and a vibrationally excited  $H_2$  is small).

The potential and electron density of Fig. 7.5(a) and (b) are calculated at a distance of approximately 2.5 cm from the PG and for both the “top” (located at  $Y = 0$  and  $Z \simeq 39$  cm in the model) and “bottom” coordinates ( $Y = 0$ ,  $Z \simeq 19$  cm).  $-I_{PG}$  is plotted in accordance with the sign convention employed in the experiments. For a low bias voltage, that is,  $V_{PG} < 25V$  in our case ( $-I_{PG} < 0$ ), the plasma

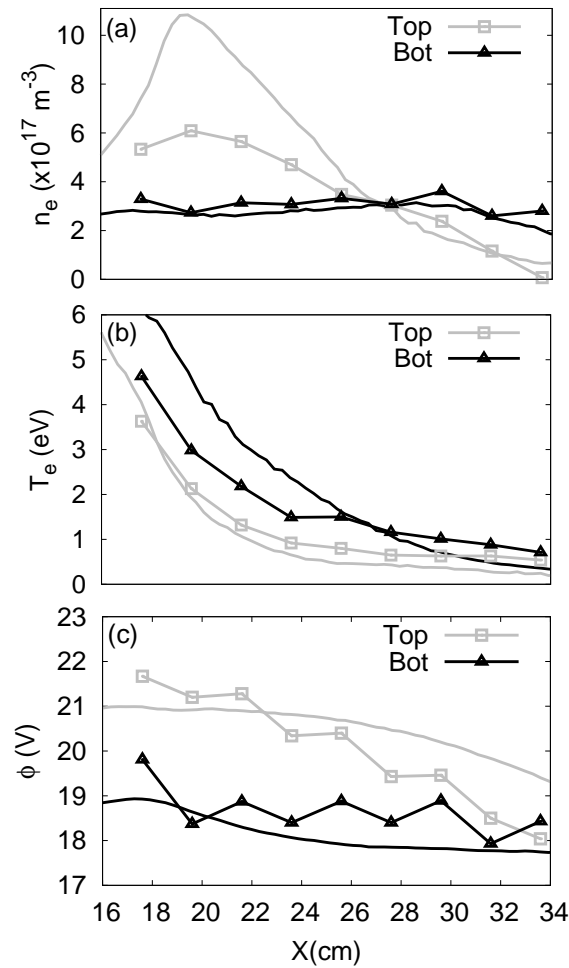


Figure 7.7: Axial electron density, temperature and plasma potential profiles for two Langmuir probe positions along (OZ), that is,  $Z = -10$  cm (bottom) and  $Z = 10$  cm (top). Both probes are positioned at  $Y = -5$  cm. Experimental data [81, 86] are also plotted (square and triangles). The experimental conditions correspond to a background hydrogen gas pressure of 0.6 Pa, a RF power of 40 kW and a magnetic filter field generated by permanent magnets on the side walls of the ion source, 9 cm from the PG.

asymmetry in front of the PG is small. The plasma potential amplitude remains above the bias voltage. As the bias voltage is further increased, the gap between the “top” and “bottom” value of the potential and electron density amplifies in a non-linear manner. This is corroborated by experimental measurements [15, 16]. For  $V_{PG} = 35\text{V}$  ( $-I_{PG} > 0$ ), the plasma potential amplitude is inferior to the bias voltage

by up to  $\simeq 4$  eV and the electron density is significantly larger at the “bottom” location. The ratio between the “top” and “bottom” value of the density is  $\simeq 4.5$ . The effect of the bias voltage and current on the asymmetry of the plasma properties in the simulations can also be seen on Fig. 7.6. This figure shows the distribution of plasma density (a) and electric potential (b) as a function of position along the Z direction at  $Y = 0$  and  $\simeq 5.5$  cm from the PG. The transverse electron current density profile on the PG is plotted in Fig. 7.6(c). For low bias voltages (25V or below), the asymmetry along Z is relatively small. The plasma asymmetry is increasingly more pronounced with larger PG biases and is enhanced when the bias voltage is above the floating potential.

### 7.2.3 Comparison with experiments

In this section, we compare the model to experimental measurements. We simulate the conditions reported in Schieko et al. [81]. The model is a 3D PIC-MCC algorithm with a numerical resolution of  $128 \times 96 \times 192$  grid nodes, a scaling factor  $\alpha = 5 \times 10^4$  and 20 ppc. The magnetic filter field is generated by permanent magnets, positioned against the lateral wall of the BATMAN prototype source and 9 cm for the PG. The simulation domain is displayed in Fig. 2.3(a) and (b). Note that the discharge is approximated as a rectangular box in the model instead of a cylinder. The filter field map is calculated by a third party software [75]. The background hydrogen gas pressure in the experiment was 0.6 Pa and the RF power  $P_{\text{RF}} = 40$  kW. The properties of the neutrals are unknown experimentally and we implemented the values derived from the DSMC model (Fig. 5.5 and 5.7), i.e., a molecular hydrogen density of  $n_{\text{H}_2} = 9 \times 10^{19} \text{ m}^{-3}$ , temperature  $T_{\text{H}_2} = 0.07$  eV, atomic hydrogen density  $n_{\text{H}} = 10^{19} \text{ m}^{-3}$  and temperature  $T_{\text{H}} = 0.3$  eV, respectively. The PG bias voltage is set to  $V_{\text{PG}} = 18.5\text{V}$  [86] and we assumed an absorbed power of 15 kW. The conversion yield for hydrogen atoms on a cesiated PG surface is derived from Eq. (2.42). We find  $\langle Y \rangle \simeq 1.3\%$  for  $T_{\text{H}} = 0.3$  eV which translates into a negative ion current produced on the PG of  $j_n \sim 5 \text{ mA/cm}^2$  (this is about 12 times smaller than for a pressure of 0.3 Pa). The latter corresponds to an optimal cesiation of the PG. Lastly, we assumed that  $T_n \simeq T_{\text{H}}$ . Figure 7.7 shows the axial profile for the electron density, temperature and plasma potential for two Langmuir probe positions along (Oz), that is,  $Z = -10$  cm (bottom)

and  $Z = 10$  cm (top). Both probes are positioned at  $Y = -5$  cm. The experimental data [81, 86] are plotted in Fig. 7.7 for comparison. Both the experiment and the 3D PIC-MCC model exhibit similar features. The magnetic filter field generates an asymmetry in the plasma parameters (the gap in the plasma potential is the hallmark of the Hall effect). The main discrepancy between the experiments and the model comes from the external power (we assumed 15 kW of *absorbed* power versus 40 kW of RF power in the experiments). The peak for the electron density near the exit of the driver is also more pronounced in the model. This may be due to the oversimplifying assumption of implementing a rectangular geometry for the discharge. The scaled electron Debye length is  $\bar{\lambda}_{De} \simeq 6.5$  mm on average in the calculation. The fraction of the volume occupied by the plasma sheath is  $2L_{sh}/L_s \sim 15\%$ , where

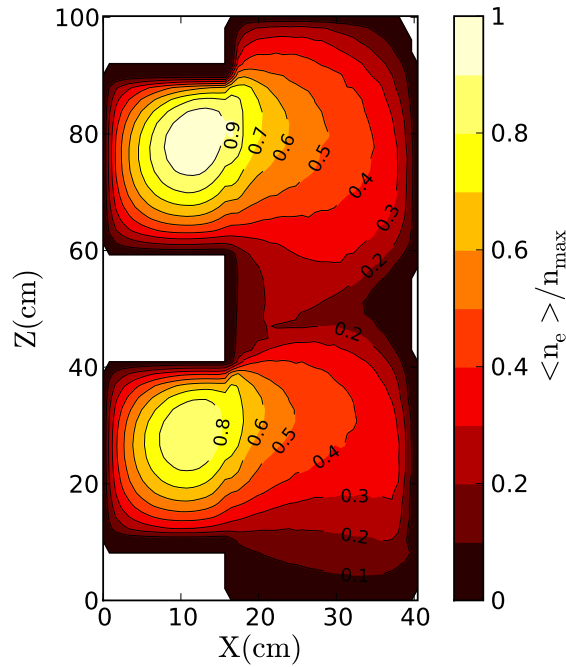


Figure 7.8: 3D plasma characteristics of the half-size ITER prototype ion source ELISE for a filling gas pressure of 0.3 Pa and an absorbed power of 240 kW. The electron density profile in the plane perpendicular to the magnetic filter field lines is shown (i.e., where electrons experience a magnetic drift).  $n_{max} = 1.5 \times 10^{18} \text{ m}^{-3}$ . A 2.5D PIC-MCC model was used to characterize the plasma properties. We use a numerical resolution of  $512 \times 1024$  grid nodes, a scaling factor  $\alpha = 2500$ , a PG bias voltage of 25V and a length along the un-simulated direction  $L_y = 86$  cm.

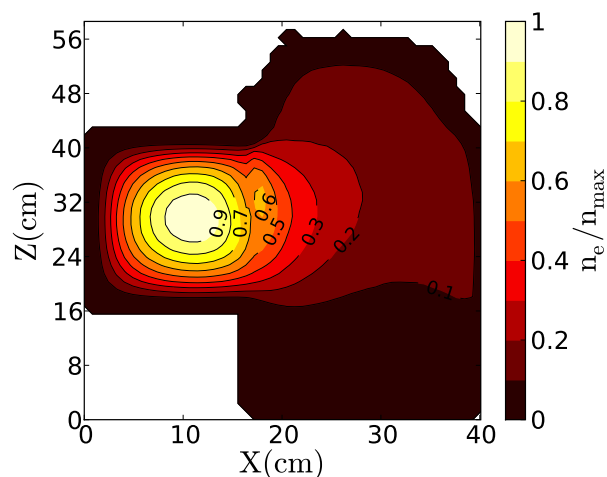


Figure 7.9: 3D plasma characteristics of the BATMAN ion source for the same magnetic filter field profile as in the ITER prototype ELISE (see Fig 7.1). The normalized electron density profile in the  $Y = 0$  plane for a 35V PG bias is shown.  $n_{\max} = 2.4 \times 10^{18} \text{ m}^{-3}$ . The simulation characteristics are identical to those of Fig 7.4, that is a resolution of  $128 \times 96 \times 192$  grid nodes, 60 kW of absorbed power, a scaling factor  $\alpha = 36 \times 10^3$  and a negative ion current  $j_n = 60 \text{ mA/cm}^2$  produced on the cesiated PG surface from neutral hydrogen atom impacts. The value of the Maxwellian heating frequency is  $\nu_H = 5 \times 10^7 \text{ s}^{-1}$ .

$L_s = \sqrt[3]{V_s} = 37 \text{ cm}$  with  $V_s$  the ion source volume and  $L_{sh} \sim 4\bar{\lambda}_{De}$  the size of the sheath. The numerical resolution is similar to the example shown in Sec. 3.2 for an average plasma density of  $\langle n_p \rangle = 2.5 \times 10^{13} \text{ m}^{-3}$  (Fig. 3.2).

### 7.3 2.5D PIC-MCC model of the half-size ITER prototype ion source ELISE

We now look at the plasma properties in the 4-drivers ITER prototype negative ion source at ELISE using a 2.5D PIC-MCC model. The 2D grid resolution is  $512 \times 1024$  nodes and the scaling factor  $\alpha = 2500$ . The Maxwellian heating frequency is  $\nu_H = 5 \times 10^7 \text{ s}^{-1}$  (it acts as an artificial collision on the electron trajectory; the electrons are consequently magnetized for a magnetic filter field strength inside the driver  $\gtrsim 3\text{G}$ ). The absorbed power per driver (two in the 2.5D model) is 120 kW. Other numerical parameters in the simulation are a time step  $\Delta t \simeq 0.25 \text{ ns}$  ( $\omega_{pe}\Delta t \simeq 0.15$ ),

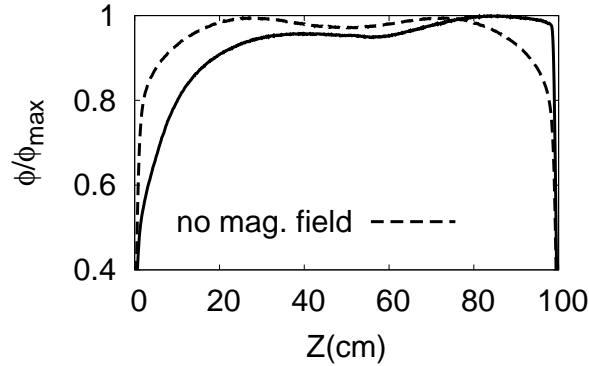


Figure 7.10: Normalized plasma potential profile along the Z-axis calculated 5 cm from the PG in the ITER prototype ion source ELISE. The Z-axis corresponds to the vertical direction. The magnetic filter field lines are parallel to the Y-axis. The potential profile is shown for a configuration without magnetic field (dashed-lines,  $\phi_{\max} \simeq 40\text{V}$ ) and for the filter field of ELISE with a 25V PG bias voltage (solid line,  $\phi_{\max} \simeq 27\text{V}$ ), respectively.

25 particles per cell on average (summed over the positively charged ions) and an ion source length along the un-simulated dimension (parallel to the magnetic filter field lines)  $L_y = 86$  cm. We assume a 0.3 Pa background gas filling pressure and due to the lack of experimental data at the present time for the neutral density and temperature, we posit the latter are similar to the one-driver BATMAN device. We consequently assume a molecular hydrogen density  $n_{\text{H}_2} = 4 \times 10^{19} \text{ m}^{-3}$ , temperature  $T_{\text{H}_2} = 0.1$  eV, neutral atom density  $n_{\text{H}} = 10^{19} \text{ m}^{-3}$  and temperature  $T_{\text{H}} = 1$  eV. Lastly, negative ions are produced only in volume via dissociative attachment between an electron and a hydrogen molecule (we model working conditions without cesium [14]).

### 7.3.1 Hall effect in ELISE as predicted by 2.5D PIC simulations

In this section we describe the effect of the magnetic filter field and the PG bias voltage on the electron dynamics in large volume plasma sources. Figure 7.8 shows the plasma density profile in the plane perpendicular to the magnetic field lines, i.e., where the electron magnetized drift dynamics occurs. The PG bias voltage is set to 25V and there is a gap between the two PG segments (in 2.5D) which is at ground potential (together with the remaining surfaces of the ion source). The electron density profile

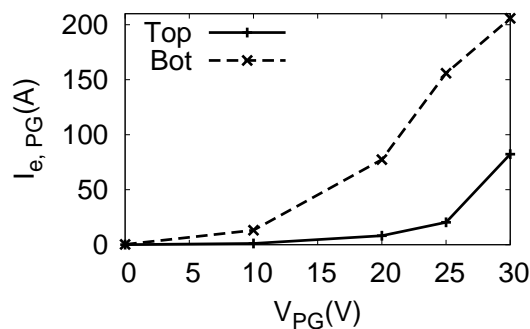


Figure 7.11: Electron current collected on the top and bottom PG segments of the half-size ITER prototype ion source ELISE vs. the PG bias potential.

is indeed asymmetric between the top and bottom drivers although the effect of the magnetic filter field on the plasma characteristics is not as pronounced as in the one-driver BATMAN example (see Fig. 7.4). The total electron current collected on the PG is  $I_e/I_{tot} \simeq 10\%$  where  $I_{tot} = 1.7$  kA is the total current (positive or negative) produced in the ion source. This current is comparable to the working conditions of the BATMAN ion source with a 35V PG bias ( $I_e/I_{tot} \simeq 6\%$ ). The reason why the asymmetry is less significant lies in the shape of the magnetic filter field profile. This is clearly visible on Fig. 7.9 which shows the normalized electron density profile ( $Y = 0$  plane) in the one-driver BATMAN ion source for the same magnetic field configuration used in the ELISE prototype (see Fig 7.1). The plasma properties are calculated with the 3D PIC-MCC model and the numerical parameters are identical to those of Fig 7.4. The PG bias voltage is set to 35V. The asymmetry is hence reduced compared to the case shown in Fig. 7.4(a) which corresponds to a magnetic field generated by permanent magnets located close to the PG. The second maxima in the extraction region disappeared and the density is monotonically decreasing from the driver down to the PG. The plasma potential in the expansion chamber is similar to the profile of Fig 7.3(a).

Note that we observe plasma density profiles in BATMAN comparable to those of Fig. 7.4 when fitting the magnetic field along the X-axis with a Gaussian distribution [23] and assuming that the field amplitude is constant along the (OY) and (OZ) directions. This indicates that the mirror effect due to the increased magnetic field lines density as one gets closer to the magnets (i.e., to the lateral walls of the BATMAN device; see Fig. 2.1) is not responsible for the formation of the second maxima

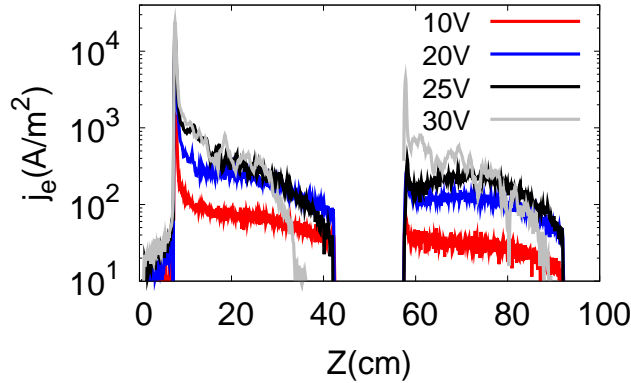


Figure 7.12: Distribution along  $Z$  (at  $Y = 0$ ) of the electron current density collected by the ELISE PG segments for 4 values of the PG bias voltage.

in the density when  $I_{PG} > 0$ . It is caused instead by the fact that when the magnetic field is sufficiently large at the exit of the driver, such that  $h \gg 1$  ( $h$  is the Hall parameter), the electron temperature drops significantly faster inside the expansion chamber and consequently ionization processes are drastically reduced. Creation of slow positive ions (via ionization) is one of the main parameters for the appearance of a second peak in density inside the expansion region. The production rate of positive ions (for  $X \gtrsim 20$  cm) is lowered by a factor  $\sim 7$  (i.e.,  $\simeq 3.3\%$  of the total ion current generated inside the ion source volume) for the ELISE-type filter field (Fig. 7.9) compared to a configuration with permanent magnets positioned near the PG (Fig. 7.4). A clear imprint of the Hall effect in the half-size ITER prototype ELISE can be seen on the plasma potential profile. Figure 7.10 displays the potential along the  $Z$ -axis (between the top and bottom surfaces of the ion source) at a distance of 5 cm from the PG ( $X = 35$  cm). The magnetic field lines are parallel to the  $Y$ -axis and consequently the Lorentz force (at the exit of the drivers) and the Hall electric field  $E_H$  are directed along  $(OZ)$ . In Fig. 7.10, we show the plasma potential for conditions without magnetic field and for the ELISE filter with a 25V PG bias (same simulation parameters as in Fig. 7.8, the model is a 2.5D PIC-MCC). For  $|B| = 0$ , the plasma potential profile is symmetric and exhibits two maxima at the center location of the two drivers. With a magnetic filter field, the potential is asymmetric and the two maxima are shifted toward the top surface of the ion source. The potential difference between the maxima is about  $\Delta\phi \simeq 1.1V$ . This asymmetry reflects on the electron dynamics.

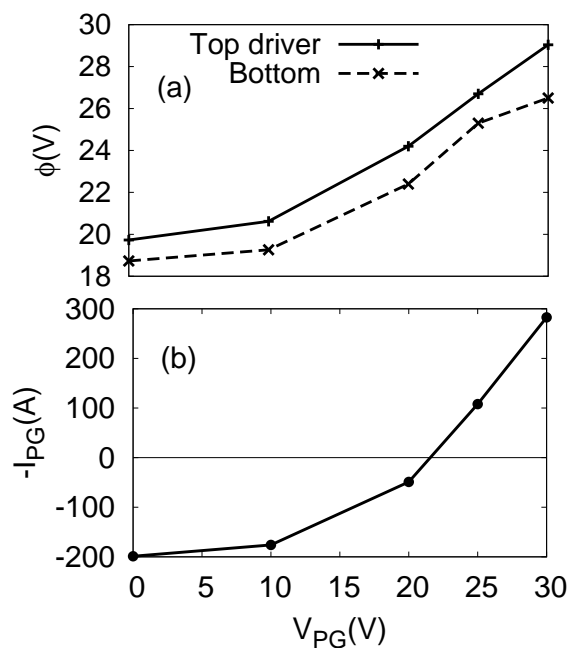


Figure 7.13: The plasma potential, plasma asymmetry coefficient and total particle current collected on the PG ( $I_{PG}$ ) in the half-size ITER prototype source ELISE are shown vs the PG bias voltage for the pair of top and bottom drivers (measured  $\simeq 4$  cm from the PG surface).  $-I_{PG}$  is plotted in accordance with the sign convention used in the experiments.

Figure 7.11 shows the electron current impacting the top and bottom segments of the PG versus the bias potential applied to the latter. The current is significantly larger on the top segment. The ratio  $I_{bot}/I_{top}$  is monotonically decreasing as the bias is increased ( $\sim 9$  for  $V_{PG} = 20$  V and  $\sim 2.5$  for  $V_{PG} = 30$  V). This is due to the flattening of the plasma potential profile in the regime where  $I_{PG} < 0$ . It is also interesting to look at the distribution of the collected electron current along the PG segments. This is shown in Fig. 7.12 for 4 different values of the PG bias. The current density is non-uniform along each segment and is significantly larger on the bottom grid in accordance with Fig. 7.11 (note the log scale in Fig. 7.12).

### 7.3.2 Plasma parameters in the vicinity of the PG

In this section we analyse the plasma characteristics in the extraction region of the large volume ITER prototype negative ion source ELISE. Figure 7.13 shows the

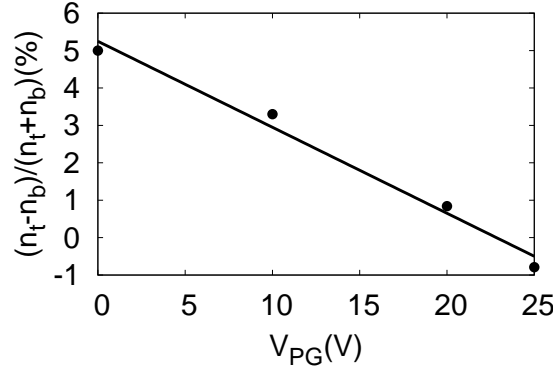


Figure 7.14: Asymmetry in the electron density between the top and bottom pairs of ICP discharges (drivers). The density at the top ( $n_t$ ) and bottom ( $n_b$ ) locations are measured at the center of each drivers and at a distance of 2.5 cm from the PG, respectively. The calculation was performed with a 2.5D PIC-MCC model and for a grid resolution of  $512 \times 1024$  nodes (scaling factor  $\alpha = 2500$ ).

plasma potential and the total particle current impacting the PG as a function of the PG bias potential. The potential is calculated for each of the two drivers (top and bottom) at a distance of  $\simeq 4$  cm from the PG ( $X = 36$  cm). In Fig. 7.13(a), the potential is measured transversely at the center location of the drivers, i.e.,  $Z = 75$  cm (top) and  $Z = 25$  cm (bottom). Similarly to the case of BATMAN, Fig. 7.5(a), the plasma potential increases with the bias voltage. It is greater than the bias potential for  $-I_{PG} \lesssim 0$  (we use the same sign convention as in the experiments). For PG bias voltages sufficiently high such that the current collected on the PG is electronegative (i.e.,  $-I_{PG} > 0$  and  $I_e > I_p$ ) then the plasma potential in the extraction region is lower than the bias applied on the PG.

### 7.3.3 Comparison with experimental observations

Franzen *et al.* in Ref. [14] analysed experimental data for the ELISE device corresponding to working conditions without cesium. Negative ions were consequently only produced inside the ion source volume via collisions between electrons and vibrationally excited hydrogen molecules. Measurements of the plasma density at the center location of each of the two drivers (top and bottom) and at a distance of 3.4 cm from the PG shows similar amplitudes for the density. They derived a coefficient for

the asymmetry,

$$A = \frac{n_t - n_b}{n_t + n_b}, \quad (7.2)$$

where  $n_t$  ( $n_b$ ) is the plasma density for the top (bottom) driver, respectively. It is found that  $A$  varies only slightly as the PG bias voltage is increased (remaining always below 10% in absolute value, see Fig. 8 in Ref. [14]). The background gas filling pressure was set to 0.6 Pa in the experiment (which is twice larger than the pressure foreseen for the ITER ion source) and the bias potential varied from 10V to 30V. The asymmetry in the density induced by the Hall effect is consequently small, which is in accordance with the conclusions derived from the 2.5D PIC-MCC calculations. Figure 7.14 shows the variations of the asymmetry coefficient  $A$  versus the PG bias potential deduced from the PIC model. The simulation characteristics are identical to those of Fig. 7.8. The calculation was performed for a background gas pressure of 0.3 Pa (without a plasma discharge). The magnetic field direction is flipped in the model and consequently  $A > 0$  contrary to the experiments. In Fig. 7.14, the asymmetry is small ( $< 10\%$ ) and its magnitude is indeed insensitive to the variations of the PG bias voltage as in the experiment. Note that a similar behavior is observed for a gas pressure of 0.6 Pa in the model.

## 7.4 Conclusion

We modeled the effect of biasing the plasma electrode (PG) on two of the ITER prototype magnetized tandem-type ion sources, that is BATMAN (one-driver) and ELISE (4-drivers); both devices are operated at the Max-Planck-Institut für Plasmaphysik (IPP) in Garching, Germany. The models are parallelized 2.5D (used for ELISE) and 3D (used for BATMAN) explicit Particle-In-Cell algorithms with Monte-Carlo collisions. In 2.5D, the simulation domain is 2D and particle losses in the un-simulated dimension are approximated.

In tandem-type plasma sources the plasma is mostly generated inside the discharge region, diffuses into the second chamber and must flow through a magnetic filter placed before the extraction region. In this configuration a plasma asymmetry occurs because of the presence of walls perpendicular to the  $\mathbf{J}_e \times \mathbf{B}$  electron drift motion, which leads to the formation of a potential drop along the direction of the drift

(i.e., perpendicular to the electron flow from the driver to the plasma grid), as in the Hall effect. We find that the asymmetry in the potential and plasma density generated by the Hall effect in the BATMAN source increases with increasing bias voltage applied to the PG and is even more important for PG bias voltages above the floating potential (i.e. when the plasma grid collects more negative charges than positive ions). This was observed recently in the experiments [15, 16]. The extent of the asymmetry depends on the shape of the magnetic filter field. In ELISE, electrons are magnetized already at the exit of the drivers (contrary to the case of BATMAN) and consequently the electron temperature drops faster inside the expansion chamber. This significantly reduces the generation of slow positive ions in that area, that tend to enhance the asymmetry in the plasma density. The plasma asymmetry remains relatively small for the filter field configuration of ELISE (and for the maximum magnetic field considered in the simulations, i.e. 30G) even in the regime where the current measured on the PG is electronegative. Nevertheless, the Hall effect does have an impact on the electron dynamics and the electron current density profile on the PG is itself highly nonuniform. This has implications for the co-extraction of electrons toward the electrostatic accelerator. In the model, the difference in amplitude between the electron current collected on the top and bottom segments of the PG is reduced by increasing the bias potential (from a ratio of about 9 for  $V_{PG} = 20V$  down to  $\sim 2.5$  with  $V_{PG} = 30V$ ).

# Chapter 8

## Negative ions

### Contents

---

8.1	Introduction . . . . .	102
8.2	Negative ion dynamics inside the ion source volume . .	103
8.3	Electron and negative ion extraction versus the PG bias voltage . . . . .	105
8.4	Extracted electron and negative ion beamlet profiles on the extraction grid . . . . .	108

---

## 8.1 Introduction

In this chapter we analyse the negative ion properties inside a fusion-type ion source. We model the drift plane of the one-driver prototype ion source at BATMAN with a 2.5D PIC-MCC model. The simulation domain is shown in Fig. 2.3(b). The magnetic

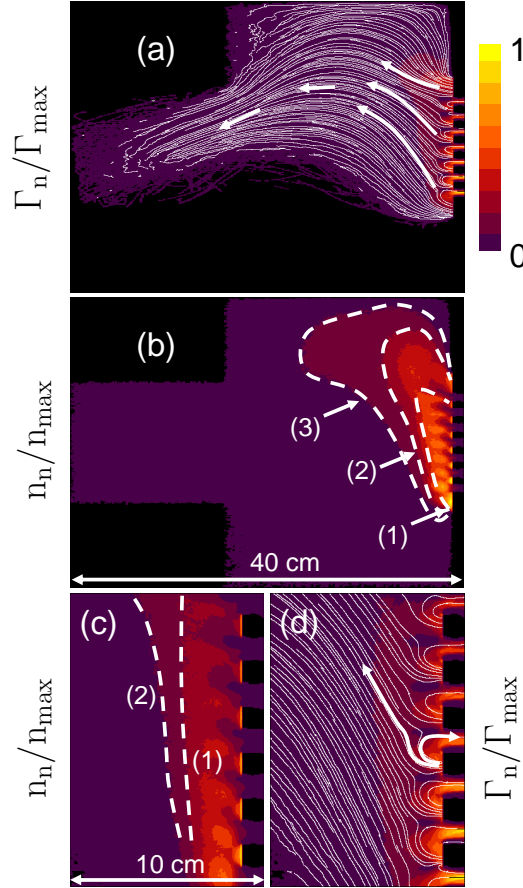


Figure 8.1: (Color) Normalized negative ion flux (a) and density (b) profiles in the XZ plane of the ITER prototype ion source at BATMAN. A zoom in the vicinity of the PG is shown in (c) for the density and (d) for the flux. 2.5D PIC-MCC model, 60 kW absorbed power, 0.3 Pa, a numerical grid resolution of  $1024 \times 1536$  nodes,  $\sim 35$  ppc and a scaling factor  $\alpha = 400$ . The PG bias voltage is 20V,  $n_{\max} = 2.8 \times 10^{17}/\alpha \text{ m}^{-3}$  and  $\Gamma_{\max} = 4 \times 10^{21}/\alpha \text{ m}^{-2} \cdot \text{s}^{-1}$ . Negative ions are generated only on the PG in this example and by neutral atom impacts. The arrows (white color) show the direction of the flux. The dashed lines are isocontours corresponding to  $\alpha n_n = 10^{17} \text{ m}^{-3}$  in (1),  $5 \times 10^{16} \text{ m}^{-3}$  (2) and  $3 \times 10^{16} \text{ m}^{-3}$  (3).

filter field profile is Gaussian following Eq. (2.44) with  $B_0 = 75\text{G}$ ,  $L_m = 8\text{ cm}$  and  $x_0 = 39\text{ cm}$ . The magnetic field is directed along (OY). The length of the third, un-simulated dimension, is  $L_y = 32\text{ cm}$  (also for the discharge). The numerical resolution is  $1024 \times 1536$  grid nodes with  $\sim 35$  ppc and we model a lower plasma density, that is,  $\langle n_p \rangle = 7.5 \times 10^{14}\text{ m}^{-3}$ . The density (or similarly the vacuum permittivity constant) was hence rescaled by a factor  $\alpha = 400$ . The Debye sheath is larger by  $\sqrt{\alpha}$  and has a negligible influence on the plasma properties (chapter 3). We simulate 7 slit apertures in the PG, each with a diameter of 1.5 cm and length  $L_y = 32\text{ cm}$ . The deflection magnetic field  $\mathbf{B}_D$  is calculated with a third-party algorithm [75] (permanent magnet bars between each EG apertures). Lastly, we consider an absorbed power of 60 kW and a background gas pressure of 0.3 Pa. The external RF power is coupled to the plasma in the model by artificially heating macroparticles in the driver region following the method described in Sec. 2.1.4 ( $\nu_H = 10^8\text{ s}^{-1}$ ). Plasma particle species are electrons, negative ions  $\text{H}^-$  and positive ions (protons,  $\text{H}_2^+$  and  $\text{H}_3^+$  ions). The physical-chemistry is summarized in tables 2.1 and 2.2. The neutrals are not modeled and a constant density and temperature profile is implemented instead with  $n_{\text{H}_2} \simeq 4 \times 10^{19}\text{ m}^{-3}$ ,  $T_{\text{H}_2} \simeq 0.1\text{ eV}$  (Fig. 5.5),  $n_{\text{H}} \simeq 10^{19}\text{ m}^{-3}$  and  $T_{\text{H}} \simeq 1\text{ eV}$  (Fig. 5.7), respectively. The latter are consistent with experimental observations [26]. Negative ions are produced inside the ion source volume (reaction #17 of table 2.1) and on the cesiated PG surface either as a byproduct of positive ion impacts or atomic hydrogen. We assume a negative ion current density of  $\alpha j_G = 600\text{ A/m}^2$  generated by H atoms and an ion temperature of  $T_n = 1\text{ eV}$ .

## 8.2 Negative ion dynamics inside the ion source volume

Figure 8.1 shows the negative ion flux (a) and density (b) profiles in the XZ plane of BATMAN. The PG bias voltage is 20V. Negative ions are produced solely on the PG and by neutral atom impacts in this example. Streamlines are displayed in Fig. 8.1(a) to indicate the direction of the negative ion flux. Except close to the PG, the flux is directed toward the ion source volume. Negative ions which are extracted originate consequently from the PG surface surrounding the apertures.

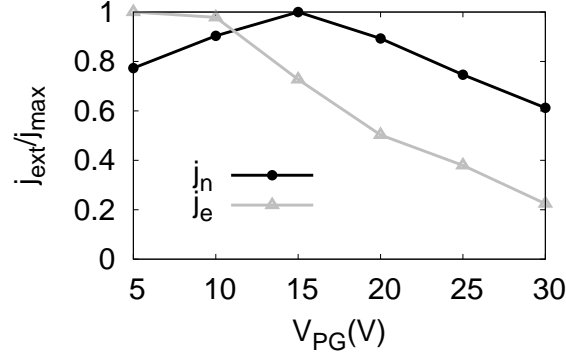


Figure 8.2: Normalized extracted electron and negative ion current versus the PG bias voltage. The extraction grid voltage is  $V'_{EG} = 210V$  and  $\alpha = 400$ . The PG is floating for  $V_{PG} \simeq 20V$ .

Negative ions are somewhat magnetized, which significantly enhance the skewness of the density profile displayed in Fig. 8.1(b). The negative ions drift toward the top wall. The average kinetic energy about 2 cm from the PG is  $\langle E_k \rangle \simeq 1.3$  eV translating into a Larmor radius of  $r_L \simeq 2.2$  cm with  $|\mathbf{B}| \simeq 75G$ . The shortest mean-free-path for the negative ions corresponds to the charge exchange collisions with atomic hydrogen (reaction #17, table 2.2). We find  $\lambda_{CEX} \simeq 6$  cm near the PG ( $\sim 2$  cm). The ions are hence magnetized,  $r_L/\lambda_{CEX} < 1$ . Other mean-free-paths are  $\lambda_{DES} \simeq 40$  cm for the destruction (sum of the reactions #16 of table 2.1, #10, #11, #14, #15 and #16 of table 2.2, respectively) and  $\lambda_{EL} \simeq 20$  cm for the elastic collisions with neutrals (reactions #12 and #13 of table 2.2). The negative ion density averaged over a line-of-sight (LOS) parallel to the PG (from the top to the bottom wall) and 2 cm from the latter is  $\alpha \langle n_n \rangle \simeq 6.5 \times 10^{16} \text{ m}^{-3}$  which is of the order of experimental measurements [16]. At the same distance from the PG, the negative ion density averaged over the width of the grid is  $\alpha n_n \simeq 1.3 \times 10^{17} \text{ m}^{-3}$  while  $\alpha n_e \simeq 1.7 \times 10^{17} \text{ m}^{-3}$ . Lastly, a negative ion current of  $\alpha j_G = 600 \text{ A/m}^2$  produced on the PG is space charge saturated and a virtual cathode forms in the plasma sheath in front of the electrode surface (the plasma potential presents a minimum which limits the extracted negative ion current). The depth of the virtual cathode is  $\phi_c \simeq -1V$  in the model and hence the saturation current (corresponding to the ion current which escapes the PG surface) is  $j_{sat} = j_G \exp(-|\phi_c|/T_n) \simeq 220/\alpha \text{ A/m}^2$  for a Maxwellian flux distribution function [72]. Note that the probability for a negative ion produced

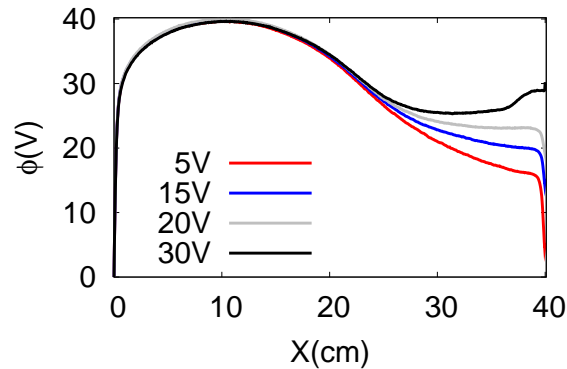


Figure 8.3: Axial plasma potential profile versus the PG bias voltage.  $V'_{EG} = 210\text{V}$  and  $\alpha = 400$ .

on the PG to be extracted from the ion source is on the order of 50% for a PG bias voltage of 20V.

### 8.3 Electron and negative ion extraction versus the PG bias voltage

Figure 8.2 shows the electron and negative ion current extracted from the 7 slit apertures of diameter 1.5 cm versus the PG voltage. The extraction grid (EG) potential is set to  $V'_{EG} = 210\text{V}$ . We posited that the extracted currents scale with the Child-Langmuir law  $\alpha j_n = \mu V_{EG}^{3/2}$  in order to estimate the EG voltage for a plasma density  $\alpha = 400$  times smaller than the value encountered in the actual ITER prototype ion source at BATMAN. This approximation will be further discussed in chapter 9.  $\mu$  is the perveance and  $V_{EG}$  is the potential for  $\alpha = 1$ . We find  $V'_{EG} = V_{EG}/\alpha^{2/3}$  assuming  $V_{EG} = 11.4\text{ kV}$  on the EG, which is located 9 mm from the back of the PG in the model (this corresponds to a potential  $V_{EG} \simeq 7.5\text{ kV}$  for the 6 mm gap of the ITER accelerator). The other parameters of the simulation are identical to the ones of the preceding section.

The positive ion flux on the PG decreases with a larger bias voltage [19] (chapter 6) which has two consequences: (1) the negative ion current produced on the PG by positive ion impacts decreases as well and (2) a smaller positive ion density in the Debye sheath results in a larger virtual cathode depth  $\phi_c$ . The latter reduces the

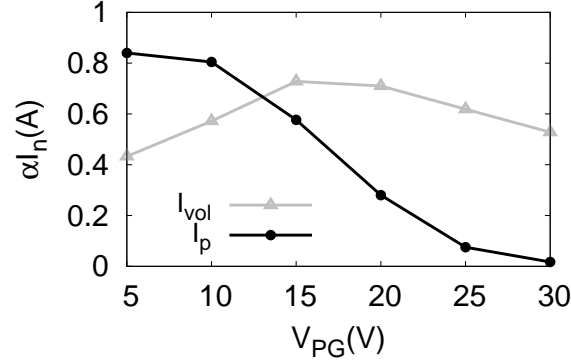


Figure 8.4: Extracted negative ion current versus the PG bias voltage. The fraction of ion current resulting from positive ion impacts on the cesiated PG is shown ( $I_p$ ) as well as ions produced in volume via a dissociative collision between an electron and molecular hydrogen  $H_2(\nu \geq 4)$  ( $I_{vol}$ ). Lastly,  $\alpha = 400$  and  $\alpha \langle n_p \rangle = 3 \times 10^{17} \text{ m}^{-3}$ , where  $\langle n_p \rangle$  is the plasma density averaged over the whole simulation domain.

magnitude of the negative ion current density escaping the PG ( $j_{sat}$ ). The PG bias voltage changes also the shape of the plasma potential in the vicinity of the apertures as shown in Fig. 8.3. The potential profile flattens with an increasing bias voltage until the PG is floating (i.e., an equal amount of positive and negative charges are impacting the grid). The PG is floating for  $V_{PG} = 20\text{V}$  in the model ( $\sim 5\%$  of the extracted negative ions are produced by positive ions). The flattening of the plasma potential greatly enhance the residence time of the negative ions in the extraction region and beside a lower saturation current  $j_{sat}$ , the extracted negative ion current increases with the PG bias up to a floating PG (Fig. 8.2). For  $V_{PG} > 20\text{V}$ , the amplitude of the plasma potential is gradually getting lower than the applied bias voltage everywhere parallel to the PG. Negative ions are hence increasingly trapped near the PG surface and the extracted current is dropping as shown in Fig. 8.2. The potential in the pre-sheath 1 cm from the PG is 1.2V below the electrode voltage for  $V_{PG} = 30\text{V}$  in Fig. 8.3. This behaviour is confirmed by experimental measurements [16]. The flattening of the plasma potential with the bias has been observed experimentally with filamented negative ion sources [87].

Lastly, the gap between the plasma potential at the edge of the Debye sheath in front of the PG and the bias voltage ( $V_{PG}$ ) decreases with a larger value of the bias (Fig. 8.3). The Electron temperature in the extraction region is  $T_e \simeq 1.5 \text{ eV}$  in the

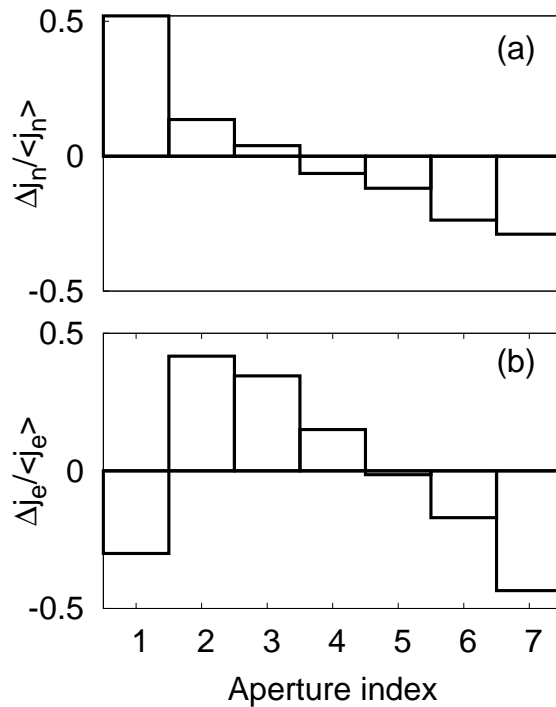


Figure 8.5: Extracted negative ion and electron beamlet profiles on the extraction grid (EG). The deviation from the average extracted current density is shown for the negative ions,  $\Delta j_n / \langle j_n \rangle$ , in (a) and electrons,  $\Delta j_e / \langle j_e \rangle$ , in (b), where  $\Delta j_n = j_n - \langle j_n \rangle$  ( $\Delta j_e = j_e - \langle j_e \rangle$ ), respectively.

model and consequently more electrons may cross the sheath barrier (and be collected on the PG surface). This explains the continuous drop of the co-extracted electron current versus the PG bias voltage shown in Fig. 8.2.

Figure. 8.4 shows both the (scaled) fraction of the extracted negative ion current originating from positive ion impacts on the cesiated PG ( $\alpha I_p$ ) and the ions produced in volume as a byproduct of a dissociative collision between an electron and molecular hydrogen  $\text{H}_2(\nu \geq 4)$  [45] ( $\alpha I_{\text{vol}}$ ).  $\alpha = 400$  and  $\alpha \langle n_p \rangle = 3 \times 10^{17} \text{ m}^{-3}$ . The total extracted negative ion current, including ions produced by neutrals on the PG, amounts to  $\alpha I_n \simeq 5\text{A}$  for a 20V bias voltage in the model while  $\alpha I_p \simeq 0.3\text{A}$  (i.e., 5.5% of the total) and  $\alpha I_{\text{vol}} \simeq 0.7\text{A}$  ( $\sim 14\%$  of the total). For a 10V PG bias, extracted ions produced by positive ion impacts represents  $\sim 20\%$  of the total. The extracted current associated with volume processes is maximum slightly before floating potential conditions ( $V_{\text{PG}} = 20\text{V}$  in our case) and then decreases for a larger bias. This confirms

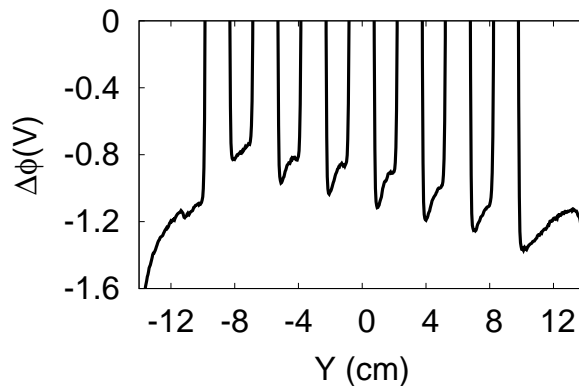


Figure 8.6: Virtual cathode profile in front of the PG surface.  $\Delta\phi = \phi - V_{\text{PG}}$  where  $V_{\text{PG}} = 20\text{V}$  is the PG bias potential. The extraction voltage is set to  $V'_{\text{EG}} = 210\text{V}$ . Negative ions are only produced on the cesiated PG by neutral atom impacts in this example. The numerical resolution is  $1024 \times 1536$  grid nodes with  $\alpha = 400$  and  $\sim 32$  ppc.  $\alpha \langle n_p \rangle = 3 \times 10^{17} \text{ m}^{-3}$ .

experimental measurements performed with a filamented negative ion sources [87].

## 8.4 Extracted electron and negative ion beamlet profiles on the extraction grid

Figure 8.5 shows in (a) the extracted negative ion and, in (b), the electron beamlet profiles on the EG (i.e., the first grid of the accelerator).  $\Delta j = j - \langle j \rangle$  is the deviation from the average extracted current density. Both the extracted electron and ion beam profiles are asymmetric. This is a direct consequence of the magnetic filter field and the Hall effect which induce an asymmetry in the plasma as well (chapter 3 and 7). The latter influence in turn the virtual cathode profile in front of the PG which is plotted on Fig. 8.6. The virtual cathode depth  $\phi_c$  is increasing toward the top wall of the negative ion source in our conditions. This is related to the plasma density (Fig. 7.4), which is lower in the vicinity of the PG in that area. A lower plasma density, which counteracts the space charge limited negative ion density near the PG surface, results logically in a larger cathode potential  $\phi_c$  (and hence a smaller saturation current  $j_{\text{sat}}$ ). This has important consequences on the negative ion beamlet profile as shown in Fig. 8.5(a). The beamlet current may deviate by as much as 50% from the

average in the model. The ITER accelerator has a  $\pm 10\%$  acceptance and this will translate into some beam interception on the accelerator grids. The asymmetry on the co-extracted electron beamlet profile is related to the electron magnetized drift motion inside the expansion chamber (Fig. 4.1). The electron current is drawn mostly from the driver. A similar profile should be hence expected also for the larger volume ITER prototype ion sources. In ELISE for instance, the electron current on the PG is asymmetric, as shown in Fig. 7.11. This should reflect on the electron beamlet profile as well.



# Chapter 9

## Extraction of negative ions

### Contents

---

9.1	Introduction . . . . .	112
9.2	Numerical issues . . . . .	112
9.3	Model . . . . .	113
9.4	Convergence . . . . .	114
9.5	Plasma meniscus . . . . .	115
9.6	Virtual cathode profile . . . . .	118
9.7	Scaling laws . . . . .	120
9.8	Extracted beam properties . . . . .	121
9.9	Application to a 3D PIC-MCC model of negative ion extraction . . . . .	122

---

## 9.1 Introduction

In this chapter, we simulate the extraction of negative ions from a fusion-type ion source using a model which is restricted to a single aperture [31]. The simulation domain is shown in Fig 2.3(c).

The numerical method employed in this work is based on the Particle-In-Cell algorithm with Monte-Carlo collisions (PIC-MCC) [32, 33]. PIC-MCC algorithms must solve for the Debye length on the numerical grid and use time steps smaller than the transit time for a thermal electron to cross a grid cell (so-called Courant-Friedrichs-Lewy, CFL, condition), otherwise a numerical instability will be generated. The restriction on the numerical grid spacing to be of the order of the Debye length implies that about  $10^9$  grid points are necessary and  $\sim 5 \times 10^6$  time steps (corresponding to an integrated time of  $\sim 30 \mu\text{s}$ ) for the simulation domain shown in Fig 2.3(c). A steady state solution is reached after a large number of time steps because of the slow buildup of the negative ion density around the grid aperture. The performance of the particle pusher for our hybrid OpenMP/MPI parallel (2D and 3D) PIC-MCC model lies between  $10^{-7}$  and  $2 \times 10^{-7} \text{ s} \cdot \text{core} \cdot \text{particle}^{-1}$  depending on the number of particles per cell (we implemented a particle-decomposition scheme for the pusher). Using such a large number of mesh points and time steps is hence not practical even with today's computers.

One possible workaround is to derive scaling laws from a 2D model of negative ion extraction (slit instead of cylindrical apertures), i.e., we compare the real plasma density to lower densities and analyse the correlations (virtual cathode depth, magnitude of the extracted negative ion current, shape of the plasma meniscus, etc.). The numerical models are strictly identical except for the geometry of the apertures and we may hence posit that the scaling laws are preserved.

## 9.2 Numerical issues

Recently published results from PIC-MCC models [29, 88, 89] have led to a counter-intuitive and unexpected description of negative ion extraction. Using chamfered apertures in the simulations, the models [88, 89] show that only those negative ions emitted from the tip of the chamfered aperture can be extracted, which is rather

surprising and does not seem to correspond to a proper operation of the extraction system. A very small negative ion current is emitted from the rest of the grid surface due to space charge saturation associated with very large values of the potential drop in front of the emitting surface (i.e., a virtual cathode). The numerical grid spacing used in the simulations was much larger than the Debye length (typically by a factor between 5 and 10). Experiments, on the other hand, have shown that extraction of a negative ion beam from a plasma electrode with a flat surface around the aperture is actually possible [5, 90, 91].

We show in Sec. 9.4 that a grid spacing smaller than the Debye length is required for a proper description of the plasma in the vicinity of the PG (including the shape of the virtual cathode). In Sec. 9.5, we discuss the shape of the plasma meniscus versus both the plasma density and the extraction potential. Section 9.6 analyses the impact of the extraction potential on the shape of the virtual cathode. Scaling laws are derived for slit apertures (2D PIC-MCC model) in Sec. 9.7. Section 9.8 calculates the plasma properties for cylindrical apertures (3D PIC-MCC model).

## 9.3 Model

The simulation domain is described in Fig 2.3(c). The model is a zoom around a single aperture of dimensions  $3.2 \times 16 \text{ cm}^2$  in 2D. The aperture (slit) is not chamfered and with a diameter of 8 mm as in the prototype ion source at BATMAN described in ref. [5]. The top and bottom boundaries are periodic while all the others are of Dirichlet type. The PG is set at a given reference potential (0V in our case) and the Left-Hand-Side (LHS) boundary voltage  $V_{LB}$  is adjusted in order to simulate the effect of a bias potential. The plasma is numerically sustained by re-injecting an electron-positive ion pair for each positive ions lost on the walls of the simulation domain. Particles are re-injected on the LHS of the domain between  $x = 2$  and 4 cm and the electron temperature is maintained by replacing the macroparticle velocity by a new one sampled from a Maxwellian distribution at a preset temperature  $T_e = 2 \text{ eV}$ . Negative ions are uniquely produced on the PG surface (we specifically want to assess the dynamics of negative ions which are produced on the electrode). The physical chemistry is simplified. We only consider negative hydrogen ions,  $\text{H}_2^+$  and electrons

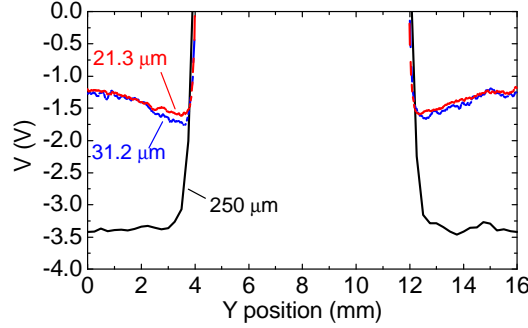


Figure 9.1: (Color) Transverse virtual cathode potential profile (parallel to the PG) versus the numerical grid spacing ( $\Delta x = \Delta y$ ) in the model.  $\Delta x / \langle \lambda_{De} \rangle \simeq 6$  for  $\Delta x = 250 \mu\text{m}$  where  $\langle \lambda_{De} \rangle$  is the electron Debye length averaged over the entire simulation domain.

(reactions #14 and #15 of table 2.2 have a negligible contribution). We implemented a background gas density  $n_{H_2} = 4 \times 10^{19} \text{ m}^{-3}$ , temperature  $T_{H_2} = 0.1 \text{ eV}$  and an atomic hydrogen density of  $n_H = 10^{19} \text{ m}^{-3}$  with  $T_H = 1 \text{ eV}$ , respectively. The positive ion temperature is  $T_p = 2 \text{ eV}$ . The magnetic filter field profile is assumed constant with  $B_z = 75\text{G}$  and the cusp field from the suppression magnets  $B_D$  is derived from an analytical formulation,

$$B_x = B_0 \sin\left(\frac{\pi y}{d}\right) \exp\left[\frac{-\pi(x_R - x)}{d}\right], \quad (9.1)$$

$$B_y = B_0 \cos\left(\frac{\pi y}{d}\right) \exp\left[\frac{-\pi(x_R - x)}{d}\right], \quad (9.2)$$

where  $x_R = 3.2 \text{ cm}$  is the position of the extraction grid (EG),  $d = 1.6 \text{ cm}$  is the distance between magnet bars and lastly  $B_0 = 600\text{G}$  for the BATMAN configuration.

## 9.4 Convergence

Figure 9.1 shows the transverse virtual cathode potential profile (at its minimum), parallel to the PG, versus the numerical grid spacing ( $\Delta x = \Delta y$ ) in the model. The latter is varied between  $\Delta x = 250 \mu\text{m}$  ( $\Delta x / \langle \lambda_{De} \rangle \simeq 6$ ) down to  $\Delta x = 21.3 \mu\text{m}$  ( $\Delta x / \langle \lambda_{De} \rangle \simeq 0.5$ ), where  $\langle \lambda_{De} \rangle$  is the electron Debye length averaged over the whole simulation domain. The average plasma density in the calculation was  $\langle n_p \rangle =$

$6 \times 10^{16} \text{ m}^{-3}$  and  $V_{\text{LB}} = -5\text{V}$ . The virtual cathode profile converge for a grid spacing of the order of the Debye length (or below) [32, 33]. For  $\Delta x / \langle \lambda_{De} \rangle \gtrsim 1$ , numerical heating increases the electron temperature which in turn modifies the plasma parameters. The virtual cathode depth drops in the model and the negative ion saturation current escaping the PG is hence also significantly reduced.

## 9.5 Plasma meniscus

In this section, we show that the plasma meniscus profile is either modified by the value of the plasma density or the extraction voltage in cesiated negative ion sources. We demonstrate that aberrations appears for a meniscus with a curvature radius of the order of the radius of the extraction aperture. Figure 9.2 shows the extracted negative ion current density profile for  $\alpha = 16$  in (a),  $\alpha = 64$  in (b) and  $\alpha = 256$  in (c). The meniscus profile is highlighted in white. It is defined as the boundary between the plasma and the vacuum of the electrostatic accelerator, i.e., where the plasma quasi-neutrality breaks,  $(n_n + n_e)/n_p > 1$  with  $n_p$  the positive ion density and  $n_e$  ( $n_n$ ) the electron (negative ion) density, respectively. The average plasma density in Fig. 9.2 is  $\langle n_p \rangle = 3 \times 10^{17}/\alpha \text{ m}^{-3}$  and the extraction potential is set to  $V_{\text{EG}} = 250\text{V}$ . The curvature radius of the meniscus is modified by the plasma density. The capability of the plasma to screen off the external potential is related to the electron Debye length. An increasing value of the Debye length (associated with a lower plasma density) leads to a meniscus with a larger curvature radius. The meniscus is approximately flat for the conditions of Fig. 9.2(a). The meniscus shape is posited to be circular with a (curvature) radius  $r_c$  centered on the aperture symmetry axis [Fig. 2.3(c)]. The curvature radius may be deduced numerically from the penetration depth  $s$  of the plasma boundary into the plasma volume, i.e.,  $s = r_c(1 - \cos \theta)$  with  $\sin \theta = a/r_c$ . We find  $s \simeq 0.25 \text{ mm}$  in Fig. 9.2(a) which gives  $r_c \simeq 32 \text{ mm}$  associated with an aperture radius  $a = 4 \text{ mm}$ .

The space charge limited current may be calculated from the Child-Langmuir law for a negative hydrogen ion source with slit apertures [92],

$$I_n = \mu \frac{2a}{d^2} \left( 1 - 0.8 \frac{d}{r_c} \right) V_{\text{EG}}^{3/2} \quad (9.3)$$

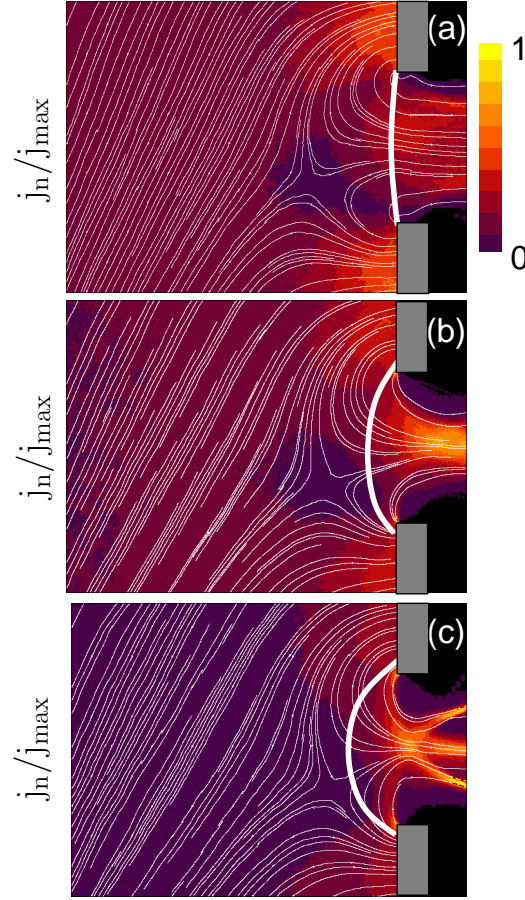


Figure 9.2: (Color) Normalized negative ion current density profile versus the plasma density. The model is a 2D PIC-MCC algorithm with slit apertures. The average plasma density in the simulation domain is  $\alpha \langle n_p \rangle = 3 \times 10^{17} \text{ m}^{-3}$  with  $\alpha = 16$  in (a), 64 in (b) and 256 in (c), respectively. The meniscus profile is highlighted in white.

with

$$\mu = \frac{4}{9} \varepsilon_0 \sqrt{\frac{2e}{m_n}} \quad (9.4)$$

where  $d = s + d'$  is the distance between the extraction electrode and the plasma boundary,  $d'$  is the inter-electrode length,  $m_n$  the mass of a negative hydrogen ion. Equation (9.3) assumes that  $d/r_c \ll 1$  and was derived for two concentric cylinders of curvature radius  $r_1 > r_2$  with  $d = r_1 - r_2$  ( $r_c \equiv r_1$ ). Cylindrical symmetry was assumed for the beam and consequently there is no transverse space charge effect. Applying Eq. (9.3) to the extraction of negative ions from a plasma source is indeed

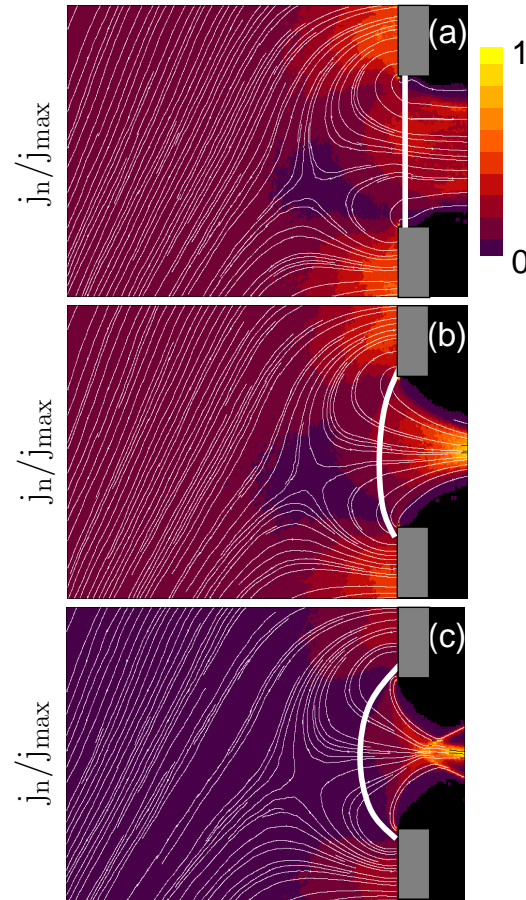


Figure 9.3: (Color) Normalized negative ion current density profile versus the EG potential  $V_{EG}$ . The average plasma density in the simulation domain is  $\alpha \langle n_p \rangle = 3 \times 10^{17} \text{ m}^{-3}$  with  $\alpha = 4$ .  $V_{EG} = 450\text{V}$  in (a),  $900\text{V}$  in (b) and  $1800\text{V}$  in (c), respectively. The meniscus profile is highlighted in white.

already an approximation. An aperture is posited to be an arc of angle  $2\theta$  of a cylinder with a radius  $r_c$ .

For  $V_{EG} = 250\text{V}$ ,  $d' = 5.5 \text{ mm}$ ,  $s = 0.25 \text{ mm}$ ,  $a = 4 \text{ mm}$  and  $r_c = 32 \text{ mm}$ , we find  $I_n \simeq 44.5 \text{ mA/m}$  which is close to the current calculated numerically  $I_n \simeq 47 \text{ mA/m}$ . For  $\alpha = 64$  [Fig. 9.2(b)], the extracted current is  $I_n = 13.5 \text{ mA/m}$  which is nearly scaling like the plasma density (a factor of 4); the difference is  $\sim 15\%$ . The curvature radius of the meniscus is smaller as expected,  $r_c \simeq 5 \text{ mm}$  ( $r_c/a \simeq 1.25$ ). Lastly, for a plasma density  $\langle n_p \rangle \simeq 10^{15} \text{ m}^{-3}$  ( $\alpha = 256$ ), we have  $r_c \simeq 4 \text{ mm}$  (i.e.,  $r_c/a \simeq 1$ ) and aberrations in the beam profile are well developed, as shown in Fig. 9.2(c).

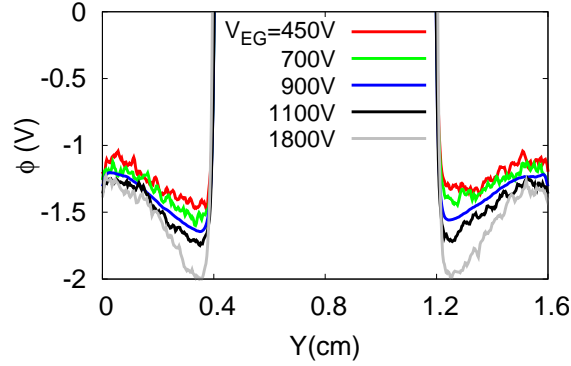


Figure 9.4: Transverse virtual cathode potential profile (along its minimum) versus the EG voltage. The plasma density averaged over the entire simulation domain is  $\alpha \langle n_p \rangle = 3 \times 10^{17} \text{ m}^{-3}$  with  $\alpha = 4$ .

The plasma boundary is further displaced toward the left-hand-side (LHS) of the simulation domain. The extracted current does not scale with the plasma density anymore. The threshold for the appearance of aberrations in the extracted negative ion beam profile occurs consequently around  $1 \lesssim r_c/a \lesssim 1.2$ .

Similar properties for the meniscus may be obtained by varying the extraction potential instead of the plasma density. Figure 9.3 shows the normalized negative ion current density profile versus the extraction grid (EG) potential for  $V_{EG} = 450\text{V}$  in (a),  $900\text{V}$  in (b) and  $1800\text{V}$  in (c), respectively. The numerical resolution is  $1024 \times 512$  grid nodes with 100 ppc and  $\alpha = 4$ . The curvature radius of the meniscus is decreasing with a larger extraction potential.

## 9.6 Virtual cathode profile

In this section we show that the virtual cathode is modified by the extraction voltage. Figure 9.4 plots the plasma potential profile along the minimum of the virtual cathode versus the extraction voltage  $V_{EG}$ . The plasma density  $\langle n_p \rangle = n_{\text{max}}/\alpha$  is kept constant with  $n_{\text{max}} = 3 \times 10^{17} \text{ m}^{-3}$  and  $\alpha = 4$ . The extraction potential modifies the amplitude of the plasma potential in the extraction region (it acts similarly to a bias voltage applied on the PG). The virtual cathode depth increases with the extraction potential in the model. The plasma meniscus recedes toward the plasma volume (Fig. 9.3) and hence the transverse electric field grows larger in the vicinity of the PG, which

tends to deflects positive ions toward the center of the grid spacing between two apertures. Less positive charges near the aperture corners generates a larger virtual cathode depth in that area. As a consequence, the virtual cathode profile is also more pronounced. Furthermore, a larger virtual cathode translates into a lower saturation current density  $j_{\text{sat}}$  which escapes the PG surface. Negative ions which have a kinetic energy  $E_0 \geq \sqrt{2e|\phi_c|/m_n}$  can escape the PG surface ( $e$  is the elementary charge). The ion (saturation) current density is consequently,

$$j_{\text{sat}} = -e \int_{E_0}^{+\infty} v_x f(v_x) dv_x. \quad (9.5)$$

Assuming that the ion distribution function along (Ox) is Maxwellian,

$$f(v_x) = n_G \left( \frac{m_n}{2\pi T_n} \right)^{1/2} \exp\left(-\frac{m_n v_x^2}{2T_n}\right), \quad (9.6)$$

and that no collisions occur between the PG and the minimum of the virtual cathode ( $\phi_c$ ), we have [72],

$$j_{\text{sat}} = j_G \exp\left(-\frac{e|\phi_c|}{T_n}\right), \quad (9.7)$$

with  $j_G = -en_G\bar{v}/4$ , the negative ion current produced on the cesiated PG from neutral atom impacts,  $n_G$  is the negative ion density on the PG and  $\bar{v} = \sqrt{8T_n/\pi m_n}$  is the average speed. Alternatively, the negative ion density at the location of the virtual cathode depth is,

$$n_0 = n_G \exp\left(-\frac{e|\phi_c|}{T_n}\right). \quad (9.8)$$

Lastly, defining the probability to extract a negative ion as  $P_{\text{ext}} = I_n/I_{\text{sat}}$ , with  $I_n$  the extracted negative ion current and  $I_{\text{sat}}$  the saturation current on the PG, we find that  $P_{\text{ext}}$  is not very sensitive to the value of the extraction voltage  $V_{\text{EG}}$  because the residence time of a negative ion in the vicinity of the aperture is only slightly altered.  $P_{\text{ext}} \sim 50\%$  for the parameters of Fig. 9.4. As a consequence, increasing  $V_{\text{EG}}$  induces a decrease in the extracted negative ion current  $I_n$  in the model by  $\sim 20\%$  between  $V_{\text{EG}} = 450\text{V}$  and  $1100\text{V}$  solely because of the reduction in the amplitude of the saturation current (the plasma potentials differ by  $\sim 10\%$ ).

## 9.7 Scaling laws

In order to derive scaling laws, i.e., to correlate the plasma properties between high ( $\alpha = 1$ ) versus low ( $\alpha \gg 1$ ) plasma densities, we must preserve the curvature radius of the meniscus. The extraction voltage must be adjusted accordingly. One approximate solution is to calculate the extraction potential with the Child-Langmuir law,

$$V_{\alpha,EG} = V_{EG} \left( \frac{I_{\alpha,n}}{I_n} \right)^{2/3}, \quad (9.9)$$

where the extracted negative ion currents have been retained due to the influence of both the extraction voltage and the plasma density on the virtual cathode. Note that the currents are only known a posteriori in the model.  $V_{\alpha,EG} (I_{\alpha,n})$  is the extraction voltage (current) for a density scaled by a factor  $\alpha$  ( $V_{EG}$  and  $I_n$  correspond to the case  $\alpha = 1$ ). Figure 9.5 shows the extracted negative ion current versus the plasma density. The negative ion current is normalized to the scaling factor  $\alpha$ . A current scaling with the plasma density would be constant in Fig. 9.5. We find  $\langle \phi_c \rangle \simeq -1V$  ( $-1.6V$ ) for  $\alpha = 64$  ( $\alpha = 1$ ), respectively and

$$\frac{I_n}{I_{\alpha,n}} \sim \exp\left(\frac{\phi_c - \phi_{\alpha,c}}{T_n}\right) \quad (9.10)$$

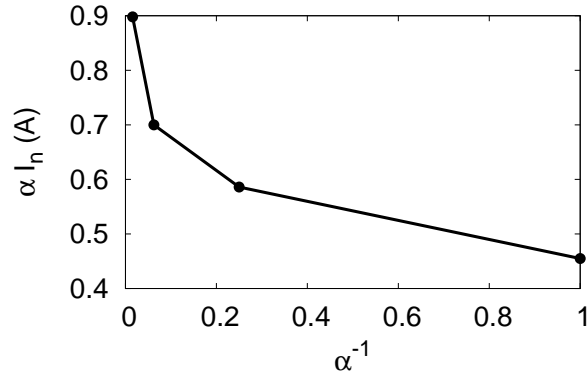


Figure 9.5: Extracted negative ion current versus the average plasma density in the simulation domain  $\alpha = \langle n_p \rangle / n_{\max}$  with  $n_{\max} = 3 \times 10^{17} \text{ m}^{-3}$ . 2D PIC-MCC model of a slit aperture geometry.

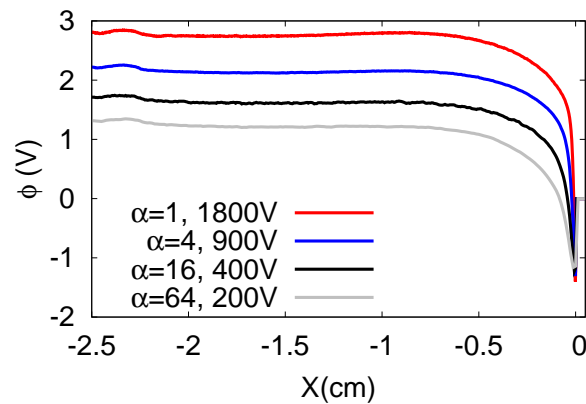


Figure 9.6: (Color) Axial plasma potential profile along a line of sight  $y = 0$  versus the plasma density. The curvature radius of the plasma meniscus  $r_c$  is kept constant.

(the negative ion extraction probability remains approximately constant beside the wide range covered by the parameter  $\alpha$  with  $P_{\text{ext}}$  on the order of 50%). The plasma potential profile is shown in Fig. 9.6.

## 9.8 Extracted beam properties

In this section, we show that the extracted negative ion beam properties are well reproduced at low plasma densities ( $\alpha \gg 1$ ). Figure 9.7 plots the negative ion beam profile on the extraction grid (EG), i.e., at  $X = 3.2$  cm. Figure 9.7(a) and (b) show the beam profile versus the extraction voltage for  $\alpha = 64$  and  $\alpha = 4$ , respectively, where  $\langle n_p \rangle = n_{\text{max}}/\alpha$  (the average plasma density in the simulation domain) with  $n_{\text{max}} = 3 \times 10^{17} \text{ m}^{-3}$ . The meniscus curvature radius is large,  $r_c/a \gg 1$  for  $V_{\text{EG}} = 200\text{V}$  (900V) while  $r_c/a \simeq 1.1$  for  $V_{\text{EG}} = 400\text{V}$  (1800V), respectively, in Fig. 9.7(a),(b) and consequently above a certain value of the extraction potential, there is an onset of aberrations in the beam. This leads to an increase in the beam divergence. The threshold is independent of the plasma density and occurs for  $r_c \sim a$  with  $r_c > a$ . Lastly, Fig. 9.7(c) plots the normalized beam profiles versus the plasma density for similar curvature radius  $r_c$ . The width of the beam on the EG are nearly identical except for the lowest density case,  $\alpha = 64$ , which is wider. This is due to the increasingly larger transverse space charge force (correlated with the negative ion current, see Fig. 9.5).

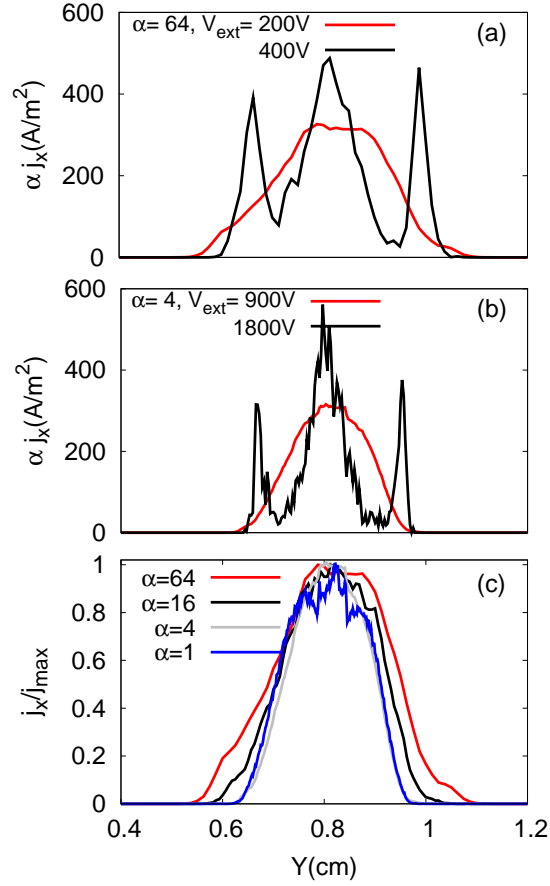


Figure 9.7: (Color) Transverse negative ion current density profile on the EG grid versus the extraction voltage and the plasma density. The average plasma density in the calculation is  $\alpha \langle n_p \rangle = 3 \times 10^{17} \text{ m}^{-3}$  with  $\alpha$  ranging from  $\alpha = 1$  to 64.  $V_{\text{EG}} = 200\text{V}$  in (a) and 900V in (b) correspond to plasma meniscus with similar curvature radius.  $r_c/a \gg 1$ .

## 9.9 Application to a 3D PIC-MCC model of negative ion extraction

In this section, we first analyze both the plasma and negative ion beam properties for the extraction of negative ions from a cylindrical aperture. The calculation is performed at low plasma density  $\langle n_p \rangle = n_{\max}/\alpha$  with  $n_{\max} = 3 \times 10^{17} \text{ m}^{-3}$  and  $\alpha = 64$ . Next, we apply the scaling laws derived in Sec. 9.7 and 9.8 for the extraction of negative ions from slit apertures to the case of cylindrical apertures. The numerical

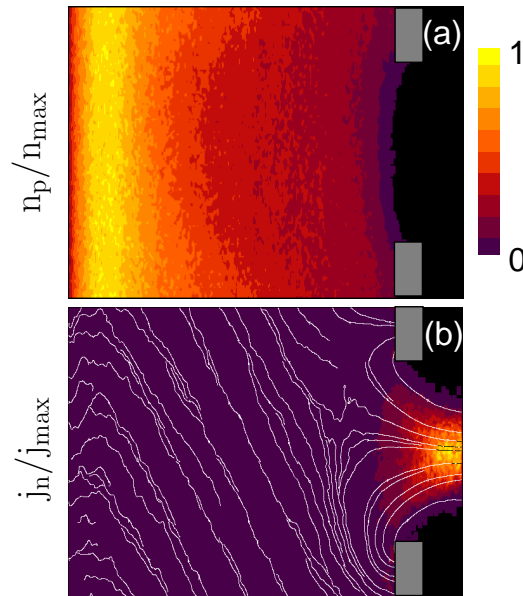


Figure 9.8: (Color) 3D PIC-MCC model of a cylindrical aperture of width 2 mm and radius  $a = 4$  mm. The plasma density profile is shown in (a) and the negative ion current density in (b). Both profiles correspond to the plane  $Y = 0$ . The numerical resolution is  $256 \times 96^2$  nodes with 20 ppc.  $V_{LB} = 0V$ ,  $V_{EG} = 400V$ ,  $\alpha n_{\max} = 6 \times 10^{17} \text{ m}^{-3}$  with  $\alpha = 64$  and lastly, the average current density on the EG is  $\alpha \langle j_n \rangle \simeq 200 \text{ A/m}^2$ .

models are identical except for the geometry of the apertures. Consequently, we posit that the scaling laws are preserved.

### 9.9.1 Low density calculation

Figure 9.8 shows the plasma density profile and the negative ion beam current density in the  $XY$  plane. The simulation was performed using a 3D PIC-MCC model. The width of the aperture is identical to the 2D case, that is 2 mm and the radius  $a = 4$  mm.  $V_{PG} = V_{LB} = 0V$  and  $V_{EG} = 400V$ . The numerical resolution is  $256 \times 96 \times 96$  grid nodes, the electron (positive ion) temperature is  $T_e = 2 \text{ eV}$  ( $T_i = 2 \text{ eV}$ ), respectively, the negative ion current emitted on the PG is  $\alpha j_G = 600 \text{ A/m}^2$  and the negative ion temperature  $T_n = 1 \text{ eV}$ . Lastly, we use 20 particles per cell. It takes about  $60 \mu\text{s}$  to converge and using 40 cores on 4 sockets (10 OpenMP[27] times 4 MPI processes), the model calculates the equivalent of  $3.5 \mu\text{s}$  per day.

We find a negative ion extraction probability of  $P_{\text{ext}} \simeq 50\%$  which is similar to the values found with slit apertures because the plasma potentials are of the same order of magnitude (about 27% of the ions flow outward of the simulation domain through the LHS boundary and 23% are lost in volume by collisions). For the simulation parameters of Fig. 9.8, we have  $\phi_p \simeq 1\text{V}$  (with  $V_{\text{PG}} = 0\text{V}$ ). The extracted negative ion current density is  $\alpha j_n = 200 \text{ A/m}^2$ , the average virtual cathode depth is  $\phi_c \simeq -1\text{V}$ , the negative ion density inside the plasma volume is  $\alpha \langle n_n \rangle = 1.3 \times 10^{17} \text{ m}^{-3}$  and the negative ion temperature  $\sim 2 \text{ cm}$  from the PG is  $T_n \simeq 1 \text{ eV}$  (defined as  $T_n = 2/3 \langle E_k \rangle$ , with  $\langle E_k \rangle$  the average kinetic energy). The meniscus is approximately flat  $r_c/a \gg 1$  and following the analysis of Sec. 9.8, we may conclude that the extracted negative ion beamlet profile on the EG will have similar properties at the real ITER densities ( $\alpha = 1$ ).

### 9.9.2 Scaled parameters

In this section we apply the scaling laws derived from the numerical model to estimate the extracted negative ion current for a plasma density  $\langle n_p \rangle = 3 \times 10^{17} \text{ m}^{-3}$  ( $\alpha = 1$ ). Table 9.1 compares the calculated versus scaled plasma parameters. The extracted current of table 9.1 only accounts for the negative ions which were generated by neutral hydrogen atom impact on the PG. Ions produced in volume via dissociative attachment of hydrogen molecules by electron impacts as well as ions generated on the PG by positive ion are not included in the calculation. These processes should

Table 9.1: Scaled parameters. The negative ion density  $\langle n_n \rangle$  is an average over a line of sight (LOS) taken 2 cm from the PG surface. The extracted negative ion current density  $j_n$  corresponds to ions produced on the cesiated PG by neutral atom impacts. The apertures are cylindrical (not chamfered).

	Calculated ( $\alpha = 64$ )	Scaled ( $\alpha = 1$ )
$\alpha j_n$ (A/m <sup>2</sup> )	200	100
$\phi_p$ (V)	1	2
$\phi_c$ (V)	-1	-1.6
$\alpha \langle n_n \rangle$ (m <sup>-3</sup> )	$1.2 \times 10^{17}$	$4.7 \times 10^{16}$
$V_{\text{EG}}$ (V)	400	3600

increase by  $\sim 25\%$  the value of the extracted negative ion current [5, 19]. The contribution from positive ions was found to be  $\sim 5\%$  in chapter 8 for a floating PG [19]. The scaled negative ion beam current would consequently amount to about  $125 \text{ A/m}^2$  associated with a negative ion density of  $\sim 5 - 6 \times 10^{16} \text{ m}^{-3}$  at 0.3 Pa. The extracted current density in the experiments is of the order of  $150 \text{ A/m}^2$  for cylindrical apertures (not chamfered) as reported by Speth et al. [5] (the negative ion current without the addition of cesium is  $\sim 25 \text{ mA/cm}^2$ ).

Experimental measurements performed simultaneously for both the extracted negative ion current and the negative ion density  $\sim 2 \text{ cm}$  from the PG (by Cavity Ring-Down Spectroscopy, CRDS) using chamfered apertures on BATMAN may be found in refs [16, 93]. Recent work from Kashiwagi et al. [91] comparing the extracted negative ion current density from either apertures with a flat surface (facing the plasma) or chamfered ones concluded that the current scales with the surface area surrounding the aperture. The surface ratio was 1.4 times larger with chamfered apertures and this translated into a negative ion current density about 1.3 times higher. There isn't a clear explanation for this observation as one would think that chamfered apertures should increase the probability to extract a negative ion; more work is hence necessary (including numerically). In BATMAN the chamfered apertures have a surface area  $\sim 25\%$  larger compared to the existing cylindrical ones [5]. Berger et al. [93] measured a negative ion current density of  $185 \text{ A/m}^2$  together with a negative ion density of  $\sim 5 \times 10^{16} \text{ m}^{-3}$  at 0.3 Pa. Applying the correcting factor for cylindrical apertures, the latter are close to the values calculated by the 3D PIC-MCC model.



# Chapter 10

## Secondary emission processes in the negative ion based electrostatic accelerator of the ITER NB injector

### Contents

---

10.1 Introduction . . . . .	128
10.2 Detailed description of the numerical approach . . . . .	130
10.3 Applications . . . . .	142
10.4 Conclusion . . . . .	152

---

## 10.1 Introduction

1 MeV, multi-MW, neutral beam (NB) injectors [94] are required for plasma heating and current drive in the future fusion machines such as the International Thermonuclear Experimental Reactor (ITER) [95]. In the case of ITER, the NB injector is designed to deliver 1 MeV, 17 A (equivalent) of neutral deuterium atoms (i.e., 17 MW of power) to the ITER plasma. The device is mainly composed of a negative deuterium ion source delivering a current density of the order of 28 mA/cm<sup>2</sup> to an electrostatic accelerator producing a 1 MeV, 40 A D<sup>-</sup> beam, a neutralizer which converts part of the beam into high energy neutrals [3], and a residual ion dump.

This chapter will focus on the physics related to particle-particle and particle-surface interactions inside a multi-aperture, multi-grid type negative ion accelerator [94, 96]. Such an accelerator consists of a plasma grid (PG), an extraction grid (EG) and a series of acceleration grids (AG). A schematic representation of the accelerator is shown in Fig. 10.1. The D<sup>-</sup> ion source is directly connected to the plasma grid. Negative ions arriving at an aperture in the plasma grid are extracted from the plasma inside the source by applying an electric field between the extraction grid and the plasma grid. The extracted ions pass through the apertures in the extraction grid and electric fields between each of the subsequent acceleration grids accelerate the ions to the desired energy through similar apertures in each acceleration grid. The interactions considered are mainly secondary particle production processes, principally: (i) co-extracted electrons from the negative ion source, (ii) negative ion stripping inside the accelerator vessel by collisions with the residual gas and (iii) ionization of the latter. The secondary particles produced (which include electrons and heavy particles such as neutrals and positive ions) follow a path determined by the electric and magnetic fields inside the accelerator and may, in turn, cause more secondary particle production by direct impact on the extraction and acceleration grids. Short range magnetic fields generated by permanent magnets embedded in the extraction grid deflect co-extracted plasma electrons onto the extraction grid [3], whilst having little effect on the trajectories of the heavier D<sup>-</sup> ions. With the ion source designed for ITER, long range magnetic fields are produced by passing a few kA current through the plasma grid and the field from permanent magnets on the source itself.

The overall power deposition due to energetic secondary particles hitting the grids

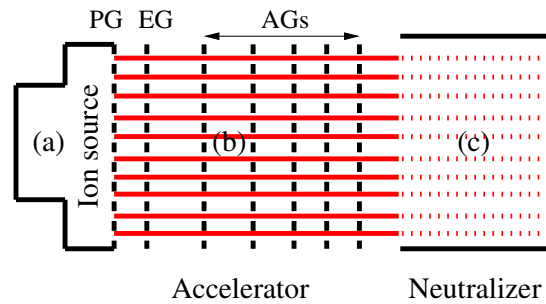


Figure 10.1: (Color) Schematic representation of a multi-aperture, multi-grid type negative ion accelerator. Neighbouring components of the neutral beam injector are also shown for clarity. In region (a), the negative ion source, region (b), a five-stage electrostatic accelerator and region (c), the neutralizer. Accelerated negative ion beamlets are shown in red. They are gradually neutralized inside the neutralizer.

may be of the order of a few MW and consequently a precise understanding of its origin and location inside the accelerator cavity is required for design improvement.

In this chapter, the work is completely theoretical. We will describe in detail the numerical code which was developed to accurately describe secondary emission issues in typical electrostatic accelerators and, as an example, we will fully simulate the Japanese Multi Aperture Multi Grid (MAMuG) accelerator [94, 96] designed for ITER. This consists of an extraction system and a five-stage electrostatic accelerator where each stage provides 200 keV of energy gain to the negative ions.

The chapter is organized as follows: Sec. 10.2 gives a detailed description of the Electrostatic Accelerator Monte Carlo Code (EAMCC\*). The code tracks test macroparticles inside the accelerator; collisions with grids and residual background gas are calculated using the conventional Monte-Carlo technique [97]. In Sec. 10.3, the simulation of the MAMuG accelerator is described, showing calculation of power deposition and current on accelerator grids induced by particle impacts, i.e., from co-extracted plasma electrons, by-products of negative ion stripping reactions, ionization of background gas and associated secondary particles generated by these processes. We also include scenarios with a highly divergent fraction of the beam within the negative ion beam, hereinafter referred to as the “halo”. In the EAMCC code the halo formation is assumed to arise from ions created on the downstream surface of the plasma grid. Caesium (Cs) is injected into the ion source to lower the work function

\*A copy of the code is available on demand

of metal surface [98], which is found to enhance the negative ion yield. Cs will migrate out of the ion source to the back of the plasma grid, inside the accelerator. Neutral atoms leaving the ion source may impinge on that surface and create negative ions. The ions can form a non-negligible halo (on the order of 5-15% of the accelerated beam current [99]). Halos in general will substantially increase power deposition due to direct impact of the negative ions on the accelerator grids.

## 10.2 Detailed description of the numerical approach

EAMCC is a 3-dimensional (3D) relativistic particle tracking code where macroparticle trajectories, in prescribed electric and magnetic fields, are calculated inside the accelerator vessel. In the code, each macroparticle represents an ensemble of rays (carrying a micro current of typically  $\simeq 50$  nA). The electric field map is obtained from the code SLAC-CAD [100] that solves Poisson's equation on a 2D cylindrically symmetric (RZ) grid. SLAC-CAD does not perform any plasma physics calculations. Consequently the plasma meniscus, which separates the source plasma from the accelerated negative ion beam, is calculated rather simply by imposing a vanishing electrostatic field inside the simulation domain dedicated to the ion source area, i.e., the region where the beam potential drops below the plasma grid potential (the negative ion beam is emitted artificially inside the plasma in the model). The magnetic field from a set of SmCo permanent magnets is calculated following a semi-analytical approach [75] while the field from the  $\simeq 4$  kA circulating through the plasma grid of the ITER accelerator is performed assuming an infinitely thin electron sheath (e.g., a surface current) [101]. Lastly, collisions are described using a Monte-Carlo method [97]. The several kinds of collisions considered in the code are: (i) electron and heavy ion/neutral collisions with accelerator grids, (ii) negative ion single and double stripping reactions and (iii) ionization of background gas.

### 10.2.1 Electron impact on accelerator grids

Particle impact with grids may have different origins. The greatest power deposition is from electrons. As mentioned earlier, electrons may originate from the ion source plasma (we assume one electron is extracted per negative ion extracted [5, 102]).

These are deflected by the magnetic fields in the accelerator, which, in the extraction gap, comes mainly from the magnets embedded in the extraction grid (EG). The second most significant source of electrons is stripping of the extracted negative ions via collisions with the background gas. Electrons produced between the accelerator grids (AG) are accelerated to high energy.

Heavy ions and neutrals also impact on the grids. The majority of such impacts are from high divergence neutrals created in the gap between the plasma grid and the first acceleration grid and consequently are from particles with a relatively low energy. Most neutrals and a large fraction of ions created after the extraction grid are either transmitted out of the accelerator, or accelerated back to the ion source (only positive ions  $H_x^+$  or  $D_x^+$  where  $x=1$  or  $2$ ).

Modelling the consequences of electron impacts with accelerator grids requires the knowledge of the energy and spatial distribution of secondary and reflected electrons. These depend mainly on the incident electron energy and angle [103–106]. Secondary electron energy emission spectra may be separated into three quasi-independent phenomena [107]: (i) true secondary electron production with a typically low energy spectra extending from 0 to 50 eV, (ii) backscattered electrons with an energy range 0 to  $E_0$ , where  $E_0$  is the energy of the incident electron, and (iii) elastically reflected electrons with  $E_{k_b} \simeq E_0$  where  $E_{k_b}$  is the reflected electron energy, i.e., electron reflection with almost no energy loss. The latter effect is negligible for energies greater than  $\simeq 500$  eV [106] and it is not included in EAMCC.

The modelling of backscattered electron processes is based on a semi-analytical approach. The backscattered integrated electron energy spectra is assumed to be [108],

$$\eta(\hat{E}) = S \exp \left[ - \left( \frac{K}{1 - \gamma \hat{E}^\alpha} \right)^p \right], \quad (10.1)$$

where  $\hat{E} = E_{k_b}/E_0$  is the normalized backscattered electron kinetic energy,

$$S = \eta_{b0} \exp(K^p), \quad (10.2)$$

$\eta_{b0} \equiv \eta(\theta_1 = 0)$  is the probability for a primary electron to be backscattered at normal

incidence,

$$\gamma = 1 - \exp[-6 |\ln B_\theta|^{-3/2}], \quad (10.3)$$

$$K = 70 |\ln B_\theta|^4, \quad (10.4)$$

and

$$B_\theta(E_0, \theta_1, \theta_2) = B_0 \prod_i^2 \exp[\tau (1 - \cos \theta_i)]. \quad (10.5)$$

In Eqs. (10.1)-(10.5), the independent variables  $p$ ,  $B_0$ ,  $\alpha$  and  $\tau$  are parameters used to fit experimental data taken for Matsukawa *et al.* [104] for incident electron energies of 10 keV and 20 keV and from Sternglass *et al.* [106] for 2 keV and 370 keV, respectively. Negligible variations are assumed for  $\eta(\hat{E})$  below 2 keV and above 370 keV [106]. For intermediate energies, a linear interpolation is performed to deduce  $p(E_0)$ ,  $B_0(E_0)$ ,  $\alpha(E_0)$  and  $\tau(E_0)$ . Table 10.1 summarizes the fitting values used in EAMCC; note that  $\alpha = 2.2$  is found for all energies.

Furthermore, it has been shown by Matsukawa *et al.* [104] that the peak value of the backscattered electron energy spectra moves toward high energy ratios  $\hat{E}$  for increasing angle of incidences  $\theta_1$  and scattering angles  $\theta_2$ . It is expected to get a maximum value at grazing incidence and scattering, i.e., for  $\theta_1 = \theta_2 = \pi/2$ . Equation (10.5) is included in EAMCC to accurately model this effect. The fitting parameter  $\tau(E_0)$  is calculated assuming

$$B_\theta(E_0, \pi/2, \pi/2) = \Omega, \quad (10.6)$$

where the value  $\Omega = 0.55$  was chosen based on measurements reported in Ref. [104].

Table 10.1: Fitting parameters deduced from experimental measurements found in Refs. [104, 106].

$E_0$ (keV)	2	10	20	370
$B_0$	0.2	0.24	0.265	0.273
$p$	0.32	0.27	0.27	0.27
$\tau$	0.51	0.412	0.365	0.35

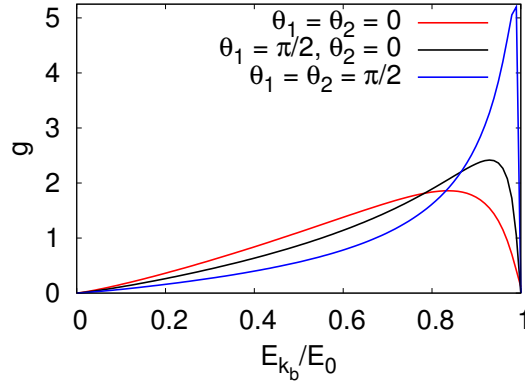


Figure 10.2: (Color) Backscattered electron energy spectra  $g(\hat{E}) = -d\eta/d\hat{E}$  as a function of  $\hat{E} = E_{k_b}/E_0$  for  $E_0 = 20$  keV and three values of incidence and scattering angles  $\theta_1$  and  $\theta_2$ . We observe the peak value of the spectra moving toward high energy ratios  $\hat{E}$  for increasing values of  $\theta_1$  and  $\theta_2$ .

Figure 10.2 shows the backscattered electron energy spectra  $g(\hat{E}) = -d\eta/d\hat{E}$  as a function of  $\hat{E} = E_{k_b}/E_0$  for  $E_0 = 20$  keV and three values of incidence and scattering angles  $\theta_1$  and  $\theta_2$ .

Lastly, in EAMCC the energy of a backscattered primary electron is obtained by normalizing and inverting Eq. (10.1) giving

$$\frac{E_{k_b}}{E_0} = \left\{ \frac{1}{\gamma} \left[ 1 - \frac{K}{\ln^{1/p}(S/P)} \right] \right\}^{1/\alpha}, \quad (10.7)$$

where  $P$  is a random number between 0 and 1.

The probability for a primary electron impacting the grid at an incidence angle  $\theta_1$  to be backscattered is modelled using the well known expression [105, 108, 109],

$$\eta_b(\theta_1) = \eta_{b0} \exp[A_{b0}(1 - \cos \theta_1)], \quad (10.8)$$

where  $\eta_{b0}$  is the backscattered probability at normal incidence and the coefficient  $A_{b0}(E_0)$  is obtained by fitting experimental data [108], giving

$$A_{b0} = \kappa(E_0) \ln(1/\eta_{b0}), \quad (10.9)$$

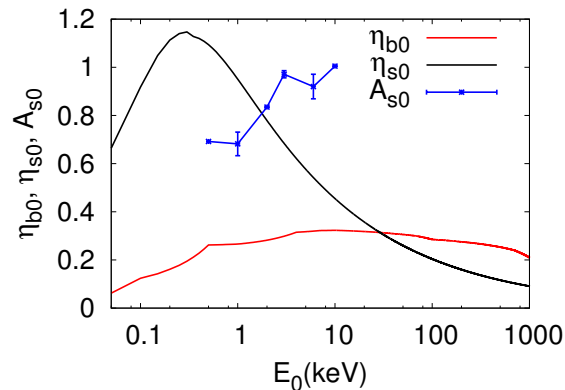


Figure 10.3: (Color) Backscattered coefficient  $\eta_{b0}$  (red), secondary emission yield  $\eta_{s0}$  (black) and coefficient  $A_{s0}$  (blue), which describes the angle dependency of true secondary emission yield, are shown for a primary electron with energy  $E_0$ (keV) impacting a copper target at normal incidence  $\theta_1 = 0$ .

with

$$\kappa = 1 - \exp\left(-1.83 E_{0[\text{keV}]}^{1/4}\right). \quad (10.10)$$

In EAMCC, a backscattered electron is re-emitted in the simulation from the location at which the primary electron impacted the grid and in an arbitrary direction  $\{\theta_2, \phi\}$  where  $\theta_2 \in [0, \pi/2]$  and  $\phi \in [0, 2\pi]$  are obtained using a random number. This assumes an isotropic scattering of the backscattered particle (i.e no preferred direction as a function of incoming angle  $\theta_1$ ) which is a good approximation in the sense that diffusion in velocity space is significant when more than a couple of collisions occur for the primary electron inside the grid material [110] (the latter argument is very likely to be true for high energy incident particles).

The backscattered probability at normal incidence  $\eta_{b0}$  on a copper target is taken from the ORNL Redbooks [111] in the energy range from 0.5 keV to 100 keV (giving a value close to  $\eta_{b0} \simeq 0.3$ ). Later measurements in the range of 0.6-6 keV from Ref. [112] confirm the Redbook data [111]. Data for 1-12 MeV are available from Ebert *et al.* [113] and Wright *et al.* [114]. Furthermore, data from Wang [115] have been used to cover energy range between 100 keV and 1 MeV. Lastly, extrapolation using Mo and Ag is used to obtain coefficients for energies of 100-500 eV [111]. Figure 10.3 shows  $\eta_{b0}$  for the energy range most relevant to NB injection devices, i.e., 100 eV to 1 MeV.

The true secondary emission yield (SEY) induced by primary electrons impacts

on grids is described in a similar manner as for the case of backscattering, that is,

$$\eta_s(\theta_1) = \eta_{s0} \exp[A_{s0}(1 - \cos \theta_1)], \quad (10.11)$$

where  $\eta_{s0}(E_0)$  is the SEY coefficient at normal incidence ( $\theta_1 = 0$ ). For copper, data found from Ref. [116, 117] are implemented in EAMCC.  $A_{s0}(E_0)$  is the coefficient associated with the angle dependency of true secondary emission yield. Values for the energy range 0.5-10 keV are obtained by fitting experimental data found in Ref. [103] for copper targets. Due to the lack of reliable information for  $E_0 < 0.5$  keV and  $E_0 > 10$  keV, constant values for  $A_{s0}(E_0 < 0.5 \text{ keV}) = A_{s0}(E_0 = 0.5 \text{ keV})$  and  $A_{s0}(E_0 > 10 \text{ keV}) = A_{s0}(E_0 = 10 \text{ keV})$  are assumed.  $\eta_{s0}$  and  $A_{s0}$  are shown in Fig. 10.3 for the energy range relevant to NB injectors.

Lastly, true secondary electron energy spectra are typically low energy (0-50 eV) and have a bell-like shape. In EAMCC, the energy of a true secondary electron produced at the grid surface is simply assumed to be constant ( $E_0 = 10$  eV) because that energy may be considered negligible compared to the particle energy gain once accelerated by the electrostatic field inside the accelerator vessel.

### 10.2.2 Negative ion stripping inside the accelerator downstream of the extraction grid

Stripping of negative ions (the loss of one or more electrons by collisions) is the main cause of high energy electron production in conventional electrostatic accelerators found on fusion machines (typically of the order of 20-30% losses). These electrons are assumed to be emitted at the location of the collision with the same direction and velocity as the parent  $D^-$ . They will be accelerated by the electric field of the accelerator and deflected by less intense magnetic fields than found in the extraction area. This implies a larger Larmor radius and consequently a longer path inside the accelerator vessel before being intercepted (i.e., a higher energy gain).

Note that most of the co-extracted plasma electrons are collected by the extraction grid ( $\simeq 98\%$ ), which corresponds to a relatively low power deposition ( $\simeq 500$  kW for the accelerator of the ITER NB injector) due to the moderate potential difference between the plasma and extraction grid ( $\simeq 9$  kV).

Negative ion stripping occurs due to collisions with the residual background gas in the accelerator which either comes from the ion source or the neutralizer.

The main reactions leading to destruction of negative hydrogen ions and production of secondary particles considered in EAMCC are summarized in Table 10.2 and are shown in Fig. 10.4. For deuterium ions, we use the same cross sections as for the case of hydrogen for identical particle velocities ( $v_H = v_D$ ). The cross section for the ionisation of  $H_2$  by  $H^-$ , i.e. reaction 3, is assumed to be equal to that of the ionisation by  $H^0$  over the energy range of interest, 10 keV to 1 MeV. This is true for  $E_0^{(H)} \leq 50$  keV [118]. The extrapolation to higher energies is justified as the plane wave Born approximation predicts that for  $E_0^{(H)} > 1.5$  MeV the cross section should be equal to that of  $H^+$ , which is slightly greater than that of  $H^0$  at lower energies [63].

In EAMCC, reactions 1-4 of Table 10.2 are calculated using a Monte-Carlo method [97]. For instance, the rate equation for destruction of negative ions may be written as follows

$$\frac{dN_-}{dz} = - \sum_{i=1}^2 \nu_i(z) N_-, \quad (10.12)$$

giving,

$$N_-(z) = N_{0-} \exp \left[ - \int_0^z \nu_{\text{tot}}(z) dz \right], \quad (10.13)$$

where  $N_-(z)$  is the number of negative ions at location  $z$  inside the accelerator,

Table 10.2: Major processes involved in the destruction of negative hydrogen ions and production of secondary particles inside the accelerator vessel [63].

Reaction #	Process	Label
1	$H^- + H_2 \rightarrow H^0 + H_2 + e^-$	Single stripping
2	$H^- + H_2 \rightarrow H^+ + H_2 + 2e^-$	Double stripping
3	$H^- + H_2 \rightarrow H^- + H_2^+ + e^-$	Ionization
4	$H^0 + H_2 \rightarrow H^0 + H_2^+ + e^-$	Ionization

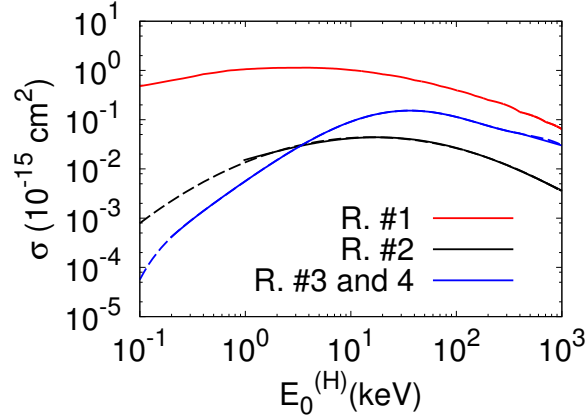


Figure 10.4: (Color) Cross sections for production of secondary particles inside the accelerator vessel due to the interaction between the accelerated negative ions and residual background gas ( $\text{H}_2$  or  $\text{D}_2$ ) are shown for the case of hydrogen (solid lines). Reactions 1 to 4 are displayed in Table 10.2. The cross sections for deuterium are found assuming  $E_0^{(D)} = 2E_0^{(H)}$ . The dashed lines correspond to the numerical fit implemented into EAMCC. Concerning the ionization of background gas ( $\text{H}_2$  or  $\text{D}_2$ ) by negative ions ( $\text{H}^-$  or  $\text{D}^-$ ) or neutrals ( $\text{H}^0$  or  $\text{D}^0$ ), we assume the same cross section for both reactions [118].

$N_{0-} = N_-(0)$  is the number at extraction (plasma grid location),

$$\nu_{\text{tot}}(z) = n_g(z) \sum_{i=1}^2 \sigma_i(z),$$

is the total frequency associated with reactions 1 and 2;  $n_g$  is the background gas density.

Consequently, one considers that a reaction occurred for a macroparticle if within a small interval  $\Delta z$  we have

$$r_1 \leq \frac{\Delta N_-(z_i)}{N_-(z_i)} = 1 - \exp[-\nu_{\text{tot}}(z_i)\Delta z], \quad (10.14)$$

where  $\Delta N_-(z_i) = N_-(z_i) - N_-(z_i + \Delta z)$  and  $r_1$  is a random number between 0 and 1. In order to determine which type of reactions occurred (1 or 2), a second random number  $r_2$  is used. If  $r_2 \leq \nu_1/\nu_{\text{tot}}$  then reaction 1 occurred, otherwise reaction 2 would have happened.

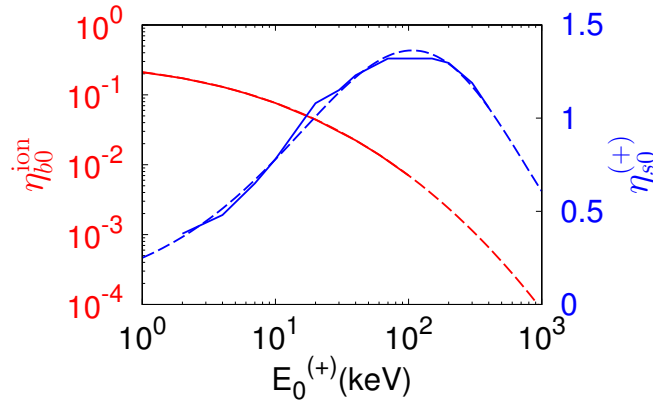


Figure 10.5: (Color) Proton backscattering coefficient  $\eta_{b0}^{\text{ion}}$  (red) and true secondary emission yield induced by proton impacts on copper targets,  $\eta_{s0}^{(+)}$  (blue), is shown as a function of incident ion kinetic energy  $E_0^{(+)}$  (keV) and at normal incidence ( $\theta_1 = 0$ ). Cross sections for heavier ions ( $\text{H}_2^+$ ,  $\text{D}^+$ , etc) are assumed to be similar at equal incident velocities. Dashed-lines correspond to the numerical fit implemented into EAMCC.

The same reasoning is applied to the ionization of the background gas ( $\text{H}_2/\text{D}_2$ ) by collisions with negative ions ( $\text{H}^-/\text{D}^-$ ) and neutrals ( $\text{H}^0/\text{D}^0$ ) [reactions 3 and 4].

Note that, in a general manner, if a particle was involved in more than two reactions, say  $k$  for instance, then reaction 1 will occur if  $r_2 \leq \nu_1/\nu_{\text{tot}}$ , reaction 2 will occur if  $r_2 \leq (\nu_1 + \nu_2)/\nu_{\text{tot}}$ , reaction  $(k - 1)$  will occur if

$$r_2 \leq \nu_{\text{tot}}^{-1} \sum_{i=1}^{k-1} \nu_i,$$

where

$$\nu_{\text{tot}} = \sum_{i=1}^k \nu_i.$$

In EAMCC, trajectories for each newly created electrons, ions or neutrals are followed together with all collision processes that may occur for those macroparticles (collisions with background gas molecules, impact with grids, etc.).

We assume that the neutral atoms and positive ions created via reactions 1 and 2 of Table 10.2, have initial velocities identical to that of their precursor negative ions, meaning  $v_0 = v_-$  and  $v_+ = v_-$ , where  $v_0$  and  $v_+$  are the atom and positive

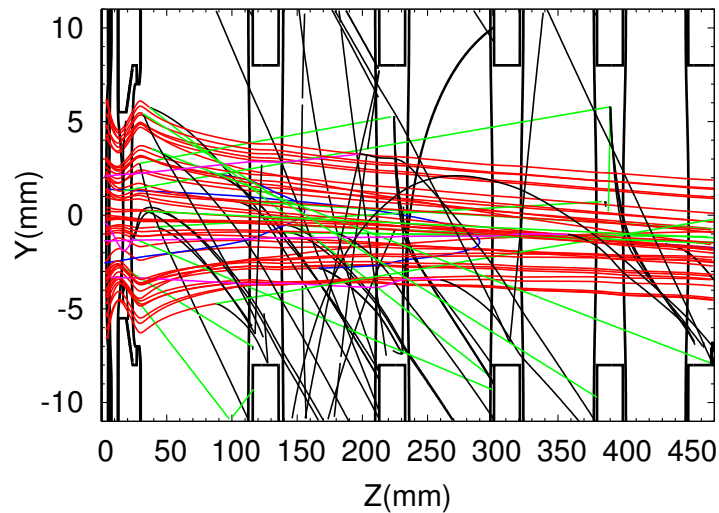


Figure 10.6: (Color) Geometry of the MAMuG negative ion based electrostatic accelerator. The plot shows a zoom over one beamlet. From left to right: plasma grid (PG), extraction grid (EG) [at an extraction voltage of 9.4 kV] and acceleration grids (AG) 1 through 5 (total acceleration voltage of 1 MV). Primary and secondary particles are shown; negative deuterium ions [red color], neutrals ( $D^0$ ) [green], positive deuterium ions ( $D^+$ ) [blue], positive deuterium molecular ions ( $D_2^+$ ) [purple] and electrons [black]. The negative ion beam aims downward with an average divergence  $\langle y' \rangle \simeq 5.5$  mrad induced by the PG magnetic filter field (generated by a 4 kA current).

ion velocities, respectively. Electrons are assumed to be emitted at rest in the centre of mass frame, i.e.,  $v_e = v_-$  and  $E_0^{(e)} = (m_e/m_-)E_0^{(i)}$  where  $m_-$  and  $m_e$  are the negative ion and electron mass, respectively (it is to be noted that when electrons are accelerated to high energy their mass is corrected for the relativistic effect).

Concerning reactions 3 and 4 of Table 10.2, the kinetic energies of the hydrogen/deuterium molecules is negligibly small  $T_i \lesssim 0.2$  eV ( $\simeq 2000$  K) compared to the energy gain of these particles once accelerated by the electric field in the accelerator vessel. Consequently electrons and positive molecular ions ( $H_2^+$  or  $D_2^+$ ) are assumed to be created at rest in the laboratory frame.

### 10.2.3 Heavy particle impact with accelerator grids

Heavy ions or neutrals induced by background gas ionization or negative ion stripping may themselves undergo collisions with the gas or impact with the accelerator grids.

Positive ions usually either go back toward the ion source or impact the back of a grid (the front of a grid is defined as facing the ion source). Heavy ion or neutral impacts with the grids may in turn result in the creation of secondary electrons together with the possibility of being backscattered. Due to their larger stopping power, the secondary emission yield (SEY) may be significantly greater than the one induced by primary electron impacts.

A complete description of ion impacts with copper surfaces needs the integration into the physical model of the energy spectrum of the backscattered particles. Simulations performed with EAMCC show that rediffused ions after impinging a grid amount for a negligible ratio of the total number of ions created in the accelerator vessel, typically  $\simeq 4.5\%$  for  $D_2^+$ ,  $\simeq 5.5\%$  for  $D^+$  and  $\simeq 8.5\%$  for  $D^0$  in the Japanese MAMuG concept [94, 96]. Furthermore, the power deposited on grids by ions and neutrals remain small compared to that from electrons, i.e.,  $\simeq 4\%$  of the total power. Consequently, a simplified description of the physics associated with ion and neutral backscattering (energy spectra, incidence angle dependency, etc.) is implemented in the algorithm. Note that backscattering may be a negligible effect but, on the contrary, true secondary electron emission induced by heavy particle impacts is not. It is essential to describe accurately the latter effect.

SEY from proton and molecular hydrogen ion ( $H_2^+$ ) impacts at normal incidence ( $\theta_1 = 0$ ) is modelled using data from Refs. [111, 119, 120]. The maximum yield for protons is found to be  $\eta_{s0}^{(+)} \simeq 1.32$  [shown in Fig. 10.5] and  $\eta_{s0}^{(2)} \simeq 2.9$  for  $H_2^+$ . In addition, the SEY ratio  $\eta_{s0}^{(2)}(v_2)/\eta_{s0}^{(+)}(v_+)$  is assumed constant for identical incident particle velocities, that is  $v_+ = v_2$  [119, 120]. The latter statement is approximately true for energies  $E_0^{(+)} \gtrsim 100$  keV, which is the relevant energy range for ions that impact the grids in a typical ITER-like electrostatic accelerator.

Similar reasoning is applied to  $D^+$  and  $D_2^+$ . For instance, there is substantial evidence that coefficients for  $H^+$  and  $D^+$  are the same at equal velocities [111, 120].

Lastly, we assume identical SEYs from neutrals:  $H^0$  or  $D^0$ , negative ions:  $H^-$  or  $D^-$ , and positive ions:  $H^+$  or  $D^+$ , which are impacting on the grids [111], that is  $\eta_{s0}^{(0)}(E_0) \sim \eta_{s0}^{(-)}(E_0) \sim \eta_{s0}^{(+)}(E_0)$ .

In addition, the corresponding angular dependency is calculated using the same

expression as in Eq. (10.11), that is

$$\eta_s^{(i)}(\theta_1) = \eta_{s0}^{(i)} \exp \left[ A_{s0}^{(i)} (1 - \cos \theta_1) \right], \quad (10.15)$$

where the parameter  $A_{s0}^{(i)}$  was found to be close to 1.45 based on data taken from Ref. [111]. The latter corresponds to measurements for protons impacting Ni targets. Due to the lack of information on copper, in EAMCC it is assumed that the same value of  $A_{s0}^{(i)} \equiv A_{s0}^{\text{ion}}$  applies to copper targets and for all heavy particle impacts (i.e., heavy ions and neutrals).

Concerning secondary electron energy spectra and following the discussion of Sec. 10.2.1, we again assume electrons are emitted at a fixed energy, that is  $E_0 = 10$  eV. The energy range is typically found to be between 0-50 eV [111].

Backscattering of heavy ions and neutrals off a grid is modelled according to data found in [111]. The particle reflection coefficient is shown in Fig. 10.5. For the angular dependence, we use a cosine law of the form,

$$\eta_b^{\text{ion}}(\theta_1) = \frac{\eta_{b0}^{\text{ion}}}{(1 - \mu) \cos \theta_1 + \mu}, \quad (10.16)$$

where  $\mu$  is a free parameter currently set to  $\mu = 1/2$  which defines a backscattering probability at grazing incidence twice as high as for the case of normal incidence. Note that the same coefficient  $\eta_{b0}^{\text{ion}}(E_0)$  is used for all types of heavy particles. Furthermore, the same reasoning is applied to describe average backscattered ion energy as a function of incident angle.

In addition, a backscattered ion may suffer a change of charge state [111]. It is typically found that for proton impacts the backscattered particles are predominantly neutrals ( $\simeq 100 - 85\%$  for backscattered energy ratios  $\hat{E} = E_{kb}/E_0$  ranging between 0 and 1), followed by positive ions ( $\simeq 0 - 13\%$ ) and lastly negative ions ( $\simeq 0 - 5.5\%$ ). Implementation of the latter effect needs the inclusion of the backscattered particle energy spectrum. In EAMCC, we use an average profile taken from [121].

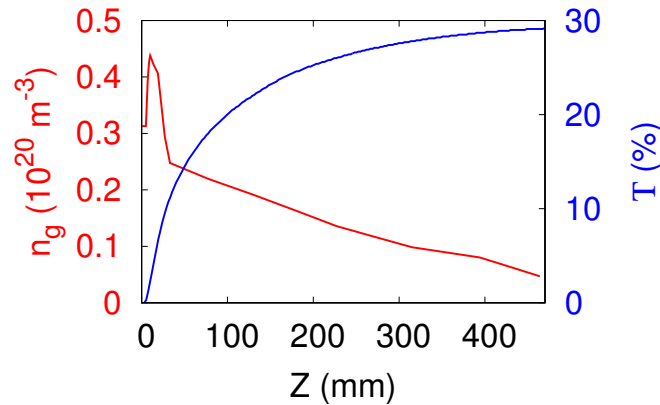


Figure 10.7: (Color) Background gas density profile  $n_g(z)$  and negative deuterium ion stripping rate  $\Gamma(z)$  as a function of propagation distance inside the accelerator vessel. The gas profile is calculated using the Monte-Carlo method described in Ref. [122]. A filling pressure of 0.3 Pa in the ion source is assumed (with no source operation and the system at room temperature) together with a residual pressure from the neutralizer  $P_N = 0.019$  Pa and a source gas temperature  $T_g = 2000$  K during discharge operation.

### 10.3 Applications

We apply the numerical method described in Sec. 10.2 to the calculation of secondary emission processes in the ITER Multi Aperture Multi Grid (MAMuG) electrostatic accelerator concept [94, 96]. As previously mentioned, MAMuG is a five stage accelerating device. The geometry of the MAMuG accelerator is shown in Fig. 10.6. Each stage corresponds to a copper grid with a total number of 1280 holes. The transverse size of a grid is of the order of  $0.8 \times 1.5$  m<sup>2</sup>, corresponding to a significantly higher cross-sectional area compared to other ion accelerators. Each of the 1280 negative ion beamlets is accelerated through one of the grid holes, gaining 200 keV between two successive acceleration grids (AG). Figure 10.6 shows one beamlet. The first grid (left side) corresponds to the plasma grid (PG), the second one is the extraction grid (EG) which is, in this configuration, at an extraction potential of 9.4 kV. Lastly, the next five grids are the AGs, each with a potential difference of 200 kV (total 1.009 MV). The total current foreseen for the ITER accelerator is 40 A of accelerated negative ions at a final kinetic energy of  $E_0 \simeq 1$  MeV (beam power of 40 MW). Consequently, such a high energy-high current accelerator may be subject to a non-negligible heat load to the grids by secondary particle impacts.

### 10.3.1 Negative ion induced secondary emission

In order to estimate power deposition and current on grids induced by secondary particles, we calculate the potential and magnetic field map inside the accelerator. In the following simulations, the potential map is calculated using SLAC-CAD [100]. The magnetic fields have different origins, namely (i) generated by a set of permanent SmCo magnets on the ion source, (ii) from a high current flowing through the PG grid (typically  $\simeq 4$  kA for the MAMuG design) and (iii) from a set of permanent magnets embedded inside the EG grid. The effect of the magnetic field from the ion source magnets and that created by the PG current is to deflect electrons generated by stripping reactions and ionization of the background gas while, as explained earlier, the aforementioned fields and the EG field are to deflect co-extracted plasma electrons and associated secondary electrons toward the EG grid. The magnetic fields are calculated numerically using the CIRIC code [75].

Furthermore, the typical design for the EG has a permanent magnet embedded between each hole in the grid with alternating polarization for one hole to the next. The alternating polarization means that the simulation domain in EAMCC has to include two adjacent beamlets to properly describe all the particle trajectories. This is done as follows: a macroparticle is allowed to cross two holes (each with the correct EG magnetic field, i.e., alternating in direction). A macroparticle leaving the calculation domain into what would be a neighbouring hole is re-injected symmetrically into the domain.

Table 10.3: Total power generated by secondary particles in MAMuG calculated by the EAMCC code.  $P_{\text{grid}}$  corresponds to the total power deposited on grids,  $P_{\text{neut}}$  power transmitted toward the neutralizer and  $P_{\text{src}}$  back into the negative ion source. The numbers shown include contribution from (i) stripping reactions, (ii) ionization of background gas and (iii) co-extracted plasma electrons.

	$P_{\text{grid}}$ (MW)	$P_{\text{neut}}$ (MW)	$P_{\text{src}}$ (MW)
$e^-$	7	0.6	None
$D^0$	0.1	2.2	None
$D^+$	Negligible	Negligible	0.14
$D_2^+$	0.13	None	0.74

Lastly, for the calculations presented here, it is assumed that a uniform negative deuterium current density is extracted from the plasma source through the 1280 holes of the PG.

In this section, we estimate the power deposition and current flowing through MAMuG grids induced by the byproducts of collisions between the extracted negative ions and the residual background gas. The latter originates mainly from the ion source. As explained above, the gas pressure in the source is assumed to be 0.3 Pa when no plasma is present in the source. The background gas density profile is calculated using a Monte-Carlo method [122], being more accurate than using a classical conductance approach [123]. Figure 10.7 shows the gas density profile for typical working conditions, that is, ion source gas temperature  $T_g = 2000$  K and residual gas pressure from the neutralizer  $P_N = 0.019$  Pa. Other relevant parameters for the MAMuG accelerator are: PG current  $I_{PG} = 4$  kA, EG voltage  $V_{EG} = 9.4$  kV and extracted negative deuterium ion current density  $J_D = 28.6$  mA/cm<sup>2</sup> (the latter ensure a 40 A accelerated current at the accelerator exit). The total extracted D<sup>-</sup> current is consequently found to be  $I_D \simeq 56.4$  A (Note that the grid apertures are:  $R_{PG} = 7$  mm for the PG,  $R_{EG} = 5.5$  mm for the EG and  $R_{AG} = 8$  mm for the AGs). For a detailed description of the permanent magnet configuration in the ITER-MAMuG design see Ref. [94, 96].

The total negative ion stripping loss is  $\simeq 29\%$  (27.8% from single stripping reactions and 1.3% for double stripping, respectively) as shown in Fig. 10.7. The background gas ionization rate is about 6.1%. Consequently, the corresponding secondary electron current generated inside MAMuG accelerator is  $I_e \simeq 20.5$  A; the latter represents the main fraction of high energy electrons. The other mechanisms for creating electrons are (i) true secondary electrons generated by electron and heavy particle impacts on grids and (ii) co-extracted plasma electrons. As explained earlier, these electrons are accelerated by the electric field, deflected by the magnetic fields and consequently will deposit power on the grids. Electrons are responsible for the majority of the grid power load (96% of total power). The total power deposition from electrons,  $P_{\text{grid}}^{(e)}$ , is calculated to be 7 MW (including contribution from co-extracted plasma electrons). The power transmitted toward the neutralizer by electrons is significantly smaller,  $P_{\text{neut}}^{(e)} \simeq 600$  kW (1.95 A). Total power deposition from electrons and heavy particles is summarized in Table 10.3.

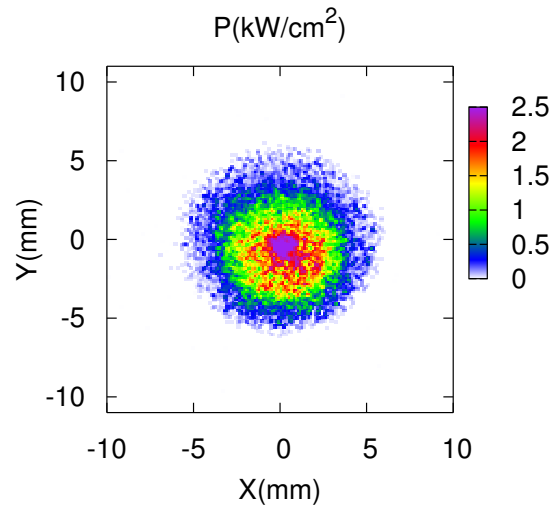


Figure 10.8: (Color) Power density profile associated with one positive ion beamlet going back toward the ion source. The plot shows the contribution from all positive ion species at the entrance of the plasma grid. The total power carried by the beamlets in the ITER-MAMuG accelerator is found to be  $P_{\text{tot}} = 880$  kW.

Stripping reactions [see Table 10.2] produce a large number of neutrals ( $\simeq 28\%$ ). These neutrals are mostly transmitted toward the neutralizer (2.2 MW) and a negligible amount of power is deposited on grids. Neutral impacts with grids are essentially from the ones created between the plasma grid (PG) and the back of the extraction grid (EG). They are consequently low energy, i.e., typically  $E_0 \lesssim 50$  keV.

Positive ions ( $D^+$  and  $D_2^+$ ) generated inside the accelerator usually go back towards the plasma source. The total power carried by these heavy particles is about 880 kW (3.2 A) at the entrance of the PG with a high maximum power density  $\mathcal{P}_{\text{max}} \simeq 2.5$  kW/cm<sup>2</sup>. The corresponding power density profile is shown in Fig. 10.8. The aperture in the PG acts on the positive ion beam as a converging lens and consequently the maximum power density increases as a function of propagation distance inside the ion source. Typically, we have  $\mathcal{P}_{\text{max}} \simeq 4$  kW/cm<sup>2</sup>, 20 cm from the PG, and  $\mathcal{P}_{\text{max}} \simeq 6$  kW/cm<sup>2</sup> at 40 cm (we did not consider the plasma in the calculation). This obviously may have negative consequences on the back side of the ion source and must be considered carefully.

Figure 10.9(a) shows the power deposited on each grid individually. We address for now the case of an ideal beam and the consequences of a beamlet “halo” will be

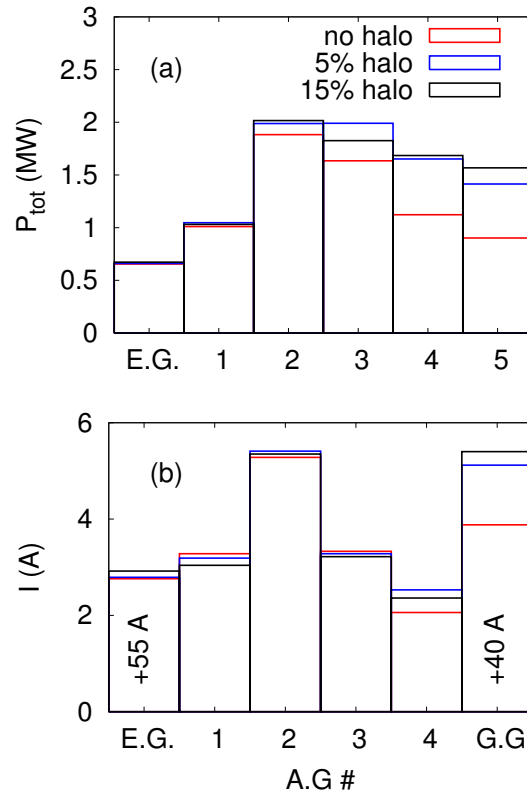


Figure 10.9: (Color) (a) Total power deposition and (b) total current flowing into accelerator grids. Three distinct cases are shown: (red color) power and current deposition produced in ideal working conditions, i.e., no beamlet halo, (blue color) power and current deposition including a halo with a current representing 5% of the total accelerated beam current transmitted toward the neutralizer (which is 40 A) and lastly, (in black) power and current deposition including a halo with a current representing a 15% halo. Label “G.G” stands for grounded grid. The total current measured at G.G is the so-called drain current, which is the total current collected at ground potential inside the neutral beam injector.

discussed in the next section. Most of the power and current to the EG comes from the co-extracted plasma electrons. The AGs, on the contrary, are heated by secondary particles which are byproducts of collisions between the accelerated negative ions and the background gas. A great fraction of the total negative ion loss occurs in the first 100 mm of the accelerator, between the PG and first AG, as demonstrated in Fig. 10.7, due to the high concentration of residual gas. Consequently the vast majority of the created secondary particles are collected by the second and third AGs [an illustration

of particle trajectories may be seen in Fig. 10.6]. It should be noted, as explained before, that due to the low mass of electrons compared to ions, most of secondary electrons are deflected onto the grids, whereas ions are mostly transmitted out of the accelerator, hence most of the power to the grids comes from electron impacts.

Note that the total power may be as high as  $\simeq 4.5\%$  of the accelerated deuterium beam power (40 MW) for A.G 2 (with no beamlet halo). In addition, the maximum power density is found to be in the range  $1.2 - 2.5 \text{ kW/cm}^2$  for all the grids. As an example, Fig. 10.10(a) shows the power density profile on the front face (i.e., that facing the ion source) of the fourth AG assuming negative ion beamlets without halos.

Figure 10.9(b) plots the total current flowing through the accelerator grids. The grounded grid (GG) measures the drain current, which is the total current collected at ground potential inside the neutral beam injector as a whole. This current includes the particles flowing into the last accelerator grid (AG 5) as well as all other transmitted particles hitting the injector walls downstream of the electrostatic accelerator, including the 40 A of the  $D^-$  beam. The electron current measured at the EG is also split into two parts for clarity purposes. The current shown in Fig. 10.9(b) corresponds to the one produced by the byproducts of stripping and ionization reactions. The additional 55 A mentioned is associated with the co-extracted plasma electrons collected by the EG.

### 10.3.2 Power deposition induced by beamlet halos

ITER requirement of producing 40 A of negative deuterium ion current implies the extraction of a higher current from the negative ion source due to the high stripping losses inside the accelerator vessel. For the ITER-MAMuG design, which has a PG grid with 1280 apertures (14 mm in diameter), we calculated an extracted current density  $J_D = 28.6 \text{ mA/cm}^2$  as reported in Sec. 10.3.1. Production of a high ion current implies the use of caesium inside the ion source in order to enhance the surface production on the PG grid, which occurs because caesium lowers the work function of the PG surface [98]; then neutrals, and to some extent positive ions from the source plasma, may trap electrons from the PG valence band during impact and be reflected back into the plasma as negative ions. This reaction can be highly efficient and allows the production of a large numbers of negative ions [124–128].

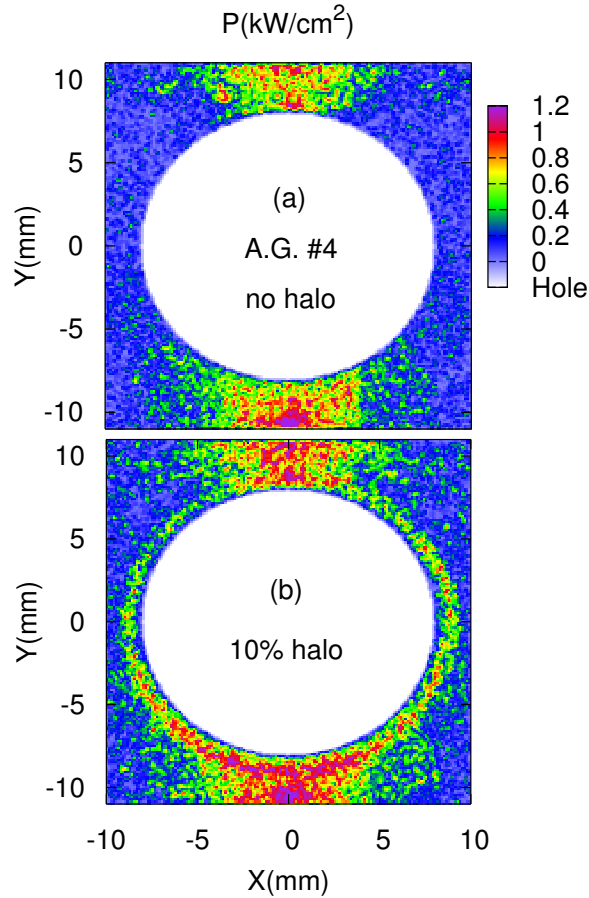


Figure 10.10: (Color) Power density profile on the front face of AG 4 induced by secondary particle impacts. (a) shows the case of beamlets without halos and (b) assuming a transmitted halo current equivalent to 10% of the total accelerated negative ion beamlet current, corresponding to  $I_D^{\text{halo}} = 4$  A for the ITER-MAMuG example. The maximum power density is found to be of the order of  $2.5 \text{ kW/cm}^2$ .

It has been found experimentally that accelerated negative ion beamlets do not have a pure Gaussian current density profile, but that they are better described by a bi-Gaussian profile [99]. The fraction of the beam with the larger divergence is referred to here as the beamlet “halo”. It is possible that the beamlet halo is formed by negative ions created on the downstream surface of the PG. Caesium will migrate from the ion source to the back of the PG and some of the  $D^0$  atoms flowing out of the source will be reflected off surfaces and hit the downstream side of the PG and be backscattered as negative ions. Here it is assumed that negative ions formed on

the rear side of the PG in an annulus around the hole are the source of the beamlet halo.

For the calculations discussed in this section, we keep the total accelerated negative ion beam current constant at 40 A, with an assumed halo fraction. The halo fraction is defined as follows: a 10% halo means that 10% of the total beam current existing the accelerator is carried by the halo, i.e., a halo current transmitted toward the neutralizer of 4 A. The remaining 36 A correspond to the accelerated low divergence beam extracted from the plasma source. It should be further noted that a halo will modify the beam optics.

Figure 10.9 shows the enhancement in power and current to the grids when a beamlet halo is present. A clear increase in total magnitude for both power and currents is calculated. The last three AGs experience the highest increase. The two distributions change when the halo is present, see Figs. 10.9(a) and (b). This arises because a large fraction of the negative ions forming the halo hits the grids, the rest is transmitted toward the neutralizer, but this does not necessarily reflect in the current to the grids as they can produce a large number of secondary electrons, which are collected further downstream. Consequently, there can be a reduction in current for a given grid but not in power deposition.

The total power deposition by beamlet halos is not negligible. We estimate an increase of the order of 1.65 MW on grids for a 15% halo and 1.55 MW for a 5% halo. The small difference between 5% and 15% halos may be explained from the fact that halo current does change significantly the beam optics inside the accelerator. The EG typically generates a strong focusing of beamlet halos, which in turns, due to its enhanced charge density induce a space charge blowout of the low divergence beamlets extracted from the plasma source. This implies an overall lower charge density for the low divergence beams and consequently a lower magnitude space charge force on the beamlet halos. The direct consequence of this effect is that the larger the extracted halo current is, the smaller is the amount of halo particles impacting the grids, i.e., there is a better transmission toward the neutralizer. We typically find a total impact ratio of  $\simeq 27\%$  of the extracted halo current for a 5% beamlet halo,  $\simeq 19\%$  impact ratio for a 10% halo and lastly  $\simeq 11\%$  impact ratio for a 15% halo.

Figure 10.10(b) shows the power density profile induced by secondary particle impacts on the front face of AG 4 with a 10% halo. The maximum power density

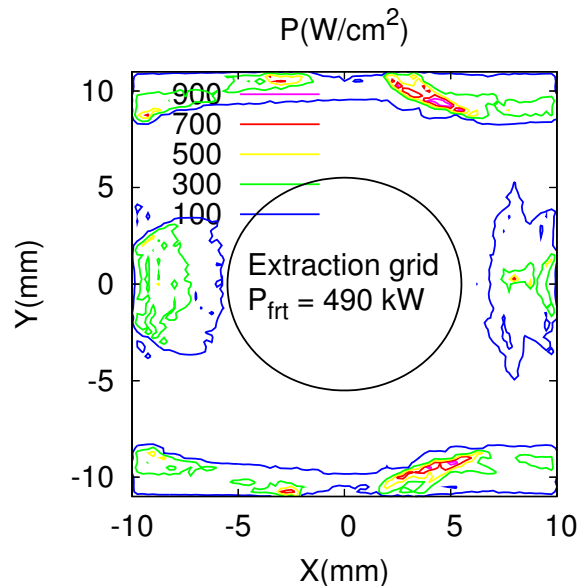


Figure 10.11: (Color) Power density profile (contour plot) on the front face of the extraction grid induced by co-extracted plasma electrons and associated secondary particles. The maximum power density is found to be  $\mathcal{P}_{\max} = 1.1 \text{ kW/cm}^2$ . Total power deposited on the grid is  $P_{\text{tot}} = 520 \text{ kW}$  (including inside the hole and the back side of the grid) and  $P_{\text{frt}} = 490 \text{ kW}$  in the front face. A 1.56% ratio of the electrons arriving at the grid are transmitted through the grid to the first acceleration gap.

does not increase significantly compared to the ideal case, see Fig. 10.10(a), and it remains in the range  $\mathcal{P}_{\max} \simeq 2.5 \text{ kW/cm}^2$ .

### 10.3.3 Co-extracted plasma electrons

As explained earlier, electrons may be extracted from the ion source together with the negative deuterium ions. In the ITER type plasma sources, we may expect as many as one electron per extracted ion [5, 102]. This translates to an electron current density on the order of  $J_e \simeq 28.6 \text{ mA/cm}^2$  for the ITER-MAMuG design. Co-extracted plasma electrons are typically collected by the EG and are responsible for the majority of the heat load on that grid.

In the simulations performed with EAMCC, we neglected space charge effects induced by the extracted electron beam when calculating the electrostatic field map inside the accelerator vessel (using the SLAC-CAD code [100]). This may be ex-

plained as follows: assuming an infinitely long cylindrically symmetric electron and ion beamlet and further neglecting relativistic effects (i.e., no self magnetic field generation), the space charge electric field, which has only a radial component, is found to be (for a detailed discussion on space charge see [129]),

$$E_{r,i}^{\text{sc}} = \begin{cases} \frac{\rho_i r}{2\epsilon_0}, & \text{for } r < R \\ \frac{\rho_i R^2}{2\epsilon_0 r}, & \text{otherwise} \end{cases} \quad (10.17)$$

where index  $i$  denotes either electrons or deuterium ions,  $\rho_i$  is the charge density, assumed constant (flattop profile),  $R$  is the beamlet radius and  $r$  the radial location. Clearly the ratio of space charge forces depends only on the ratio of charge densities, that is, expressed in terms of currents,

$$\frac{\rho_e}{\rho_D} \simeq \frac{J_e}{J_D} \sqrt{\frac{m_e}{m_D}}, \quad (10.18)$$

if we further assume similar extraction kinetic energies for both species, i.e.,  $E_0^{(e)} \simeq E_0^{(D)}$ . Consequently, for  $J_e \simeq J_D$  we have  $\rho_e \ll \rho_D$  and electron space charge may be neglected.

Figure 10.11 shows the power density profile on the front face of the EG induced by co-extracted plasma electrons and associated secondary particles for the ITER-MAMuG example. The extraction potential is currently set in the simulation to  $V_{\text{EG}} = 9.4$  kV. The total power deposited on the EG is found to be  $P_{\text{tot}} \simeq 520$  kW (including inside the hole and back side) from co-extracted electrons while the contribution from stripping and ionization reactions is significantly lower, that is,  $P_{\text{tot}} \simeq 135$  kW (including  $P_{\text{bck}} \simeq 35$  kW on the back side essentially from positive ions). Furthermore, Fig. 10.11 shows the existence of a high power density region, with a maximum  $\mathcal{P}_{\text{max}} = 1.1$  kW/cm<sup>2</sup>. It should be noted that due to the specific configuration of the static magnetic field in the extraction region with alternating magnet polarization from one hole to the next along the (Oy) direction, the high power density area jumps symmetrically from left to right.

Concerning transmission, only a small fraction of co-extracted electrons are transmitted through the EG downstream of the accelerator. We estimate around 1.6%

past the EG and down to 0.6% through AG 1, meaning 55 A of electrons are collected by the EG. Transmitted electrons, even if they represent a small fraction, still carry a non-negligible power. The total power carried by these particles amounts to  $P_{\text{tr}} \simeq 275$  kW which is almost totally collected by the grids (a negligible power is transmitted toward the neutralizer).

## 10.4 Conclusion

In this chapter, we have developed a Monte-Carlo method suitable for studying secondary emission processes in typical electrostatic accelerators designed for heavy ion acceleration. We have applied the method to the calculation of power-current deposition inside the negative deuterium ion based accelerator for a future neutral beam injector of the ITER tokamak. In the code, secondary emission processes such as negative ion stripping reactions, ionization of the background gas, electron/heavy ion/neutral backscattering of grids and true secondary electron emission are included. In addition, the code allows for a precise characterization of 3D power deposition and consequently the determination of high power density areas on accelerator grids, which makes it a useful tool for design purposes. In ITER-MAMuG accelerator the vast majority of power deposition on grids is induced by electrons (typically  $\simeq 96\%$  of total power), which amounts to an integrated power (summed over all accelerator parts) close to 15.5% of the accelerated negative ion power (40 MW, i.e., 40 A at 1 MeV).

Power transmitted outside the accelerator is mostly carried by heavy particles and is found to be also non negligible. A total power on the order of 880 kW is found for the positive ion beamlets going back toward the ion source together with a high maximum power density (approximately 6 kW/cm<sup>2</sup> at 40 cm downstream inside the ion source, neglecting any plasma effects in the calculation). This may be a critical issue regarding cooling of the ion source walls. Note that the PG hole acts as a converging lens for the positive ion beams. Power transmitted toward the neutralizer is mostly carried by neutrals (2.2 MW) and is well collimated.

Lastly, additional power may come from the existence of a beamlet halo. The latter will induce direct fast heavy ion impact with grids and injector parts further

downstream together with an increased load of true secondary electrons (heavy ion impacts may produce a high number of secondary electrons).



# Chapter 11

## Modeling of the two ITER NBI accelerator concepts

### Contents

---

11.1 Introduction . . . . .	156
11.2 Numerical method . . . . .	157
11.3 The SINGAP accelerator . . . . .	158
11.4 ITER accelerator power supply characteristics . . . . .	166
11.5 Conclusion . . . . .	168

---

## 11.1 Introduction

This chapter focus on the two accelerator concepts being developed for ITER, the Multi-Aperture-Multi-Grid (MAMuG) [94, 96] and the SINGle Gap single APerture (SINGAP) [130] accelerators. A schematic view of the two accelerators is shown in Fig. 11.1. Both accelerators consist of a plasma grid (PG) which separates the ion source from the accelerator, an extraction grid (EG) and a series of acceleration grids (AGs). The extraction grid is necessary in order to both compensate space charge defocusing of the negative ion beamlets and collect unwanted co-extracted electrons from the plasma source. The major difference between the two accelerator concepts is on the AG design. The MAMuG accelerator is a five-stage acceleration system where each grid (including the PG and EG) is divided into 16 groups of 80 apertures (1280 holes in total). The entire aperture array is rectangular,  $577 \times 1535 \text{ mm}^2$ . The potential difference between two AGs is  $\simeq 200 \text{ kV}$ . Concerning SINGAP, the main acceleration region corresponds to a single-gap, i.e., two AGs. The PG, EG and first AG are similar to the ones of the MAMuG accelerator, that is, with 1280 apertures in 16 groups of 80 apertures, while the second (and last) AG, which is at ground potential, has 16 large rectangular apertures, and the 80 beamlets from one group of apertures in the first AG pass through one of the 16 apertures. The accelerating potential across the last (main) acceleration stage is 945 kV for SINGAP. As there are more grids in the MAMuG concept, secondary particles have a higher probability of impact in that accelerator than in the SINGAP accelerator, while in the latter the secondary particles are likely to be transmitted through the large apertures in the grounded grid. These considerations have important implications for both accelerator concepts.

While the ITER-MAMuG accelerator has been simulated in the previous chapter, the SINGAP concept still needs to be theoretically investigated. The chapter is organized as follows: Sec. 11.2 gives an overview of the physics involved in secondary particle production and review the updated features of the Electrostatic-Accelerator-Monte-Carlo-simulation-Code [131] (EAMCC). EAMCC was specifically developed to model secondary emission processes inside high energy electrostatic accelerators. In Sec. 11.3, a detailed calculation of the SINGAP accelerator is performed together with a direct comparison with the features of the MAMuG concept. In Sec. 11.4, a

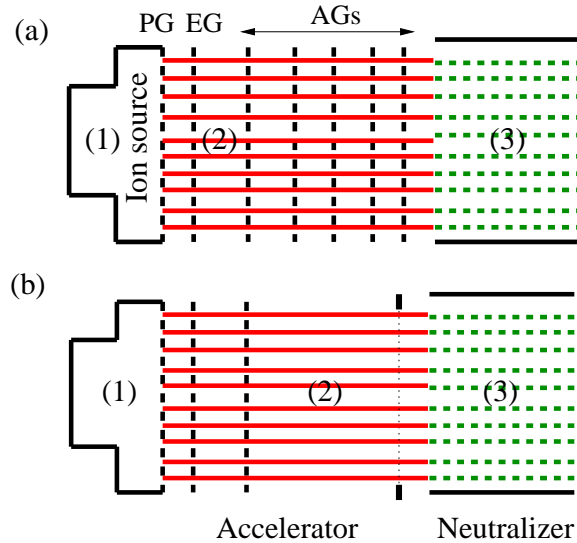


Figure 11.1: (Color) Schematic representation of a negative ion electrostatic accelerator. Neighbouring components of the neutral beam injector are also shown for clarity. In region (1), the negative ion source, region (2), the high energy electrostatic accelerator. There are currently two concepts foreseen for ITER; the Multi-Aperture-Multi-Grid accelerator (MAMuG) [upper plot, (a)], which utilizes five acceleration grids (AG) to accelerate negative ions to an energy of 1 MeV, and the SINGLE Gap single APerture (SINGAP) [lower plot, (b)] concept consisting uniquely of two AGs. The last AG for the MAMuG accelerator is similar to the other AGs, i.e. having 1280 apertures, while for SINGAP it has 16 large rectangular apertures, one per group of 80 beamlets. In region (3), the neutraliser is shown; the high energy negative ion beamlets are gradually neutralized (green dashed lines). Neutralization efficiency is around 60%.

calculation of the currents to be supplied by the power supplies is shown for the two accelerators.

## 11.2 Numerical method

The version of the EAMCC model presented in the previous chapter is fully 3-dimensional (3D) for the magnetic field and 2-dimensional (2D) cylindrical symmetric for the electric field. Negative ion transport is reduced to two beamlets, which is necessary in order to account for the asymmetry between two neighbouring apertures arising from the magnetic field from the embedded permanent magnets inside the

EG. Simulation of the full accelerator, that is including the 1280 apertures for ITER, is obtained by scaling the two-beamlets calculation. The model has been upgraded to cope with 3D electric potential maps. This modification is necessary in order to simulate accelerators with a non-cylindrical symmetric geometry, such as the SINGAP concept. The new version of the code, EAMCC-3D, can include the whole accelerator geometry in the calculation. Both algorithms allow the user to calculate 3D power deposition from secondary particles on accelerator grids (and consequently find high power density regions), compute negative ion stripping ratio, transmitted power per species (both toward the ion source and the neutraliser) and, among others, describe secondary particle production versus beam optics.

### 11.3 The SINGAP accelerator

As explained previously, the SINGAP concept [130] accelerates negative deuterium ions to high energy in several intermediate steps. The three first grids (PG, EG and the first acceleration grid, called pre-AG in the SINGAP context) are similar to the ones of MAMuG, that have aperture arrays consisting of 16 groups of 80 apertures (total 1280 holes) with a transverse cross section of  $0.89 \text{ m}^2$ . The EG voltage is set at 9.6 kV and the pre-AG at 55 kV; the final beam acceleration to 1 MeV is performed in one step. Each group of beamlets from each group of 80 apertures then passes through one of the 16 large apertures in the final (ground potential) electrode. The filling pressure in the ion source is 0.3 Pa (with no source operation and the system at room temperature).

Figure 11.2 shows the post-acceleration gap for ITER-SINGAP; for clarity the plots shows only 5 beamlets from 2 of the groups of apertures together with secondary particles. The square blocks on the left and right side of Fig. 11.2 are thick metallic structures bolted on the pre-AG and grounded grid (GG) edge [130]; these so-called “kerbs” steer the beams horizontally and help counteract the space charge repulsion between the beamlets within each group. In addition, the GG is slightly V-shaped in the vertical direction (with the tip of the “V” to the upstream side). The resulting electric field profile in the acceleration gap creates the required vertical steering of the beam groups. Due to the large openings on the GG electrode of the

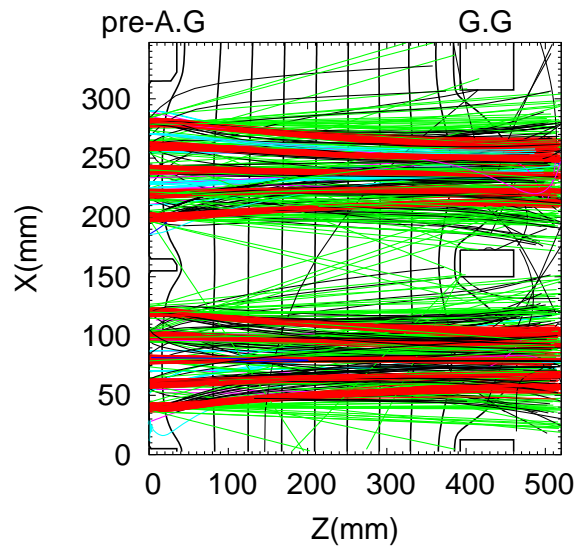


Figure 11.2: (Color) Geometry of the SINGAP negative ion based electrostatic accelerator. The plot shows five beamlets from two aperture groups over the post-acceleration gap. From left to right: pre-acceleration grid (AG) and grounded grid (GG) (total acceleration voltage of 945 kV in the post-acceleration gap). Primary and secondary particles are shown; negative deuterium ions [red color], neutrals ( $D^0$ ) [green], positive deuterium ions ( $D^+$ ) [dark blue], positive deuterium molecular ions ( $D_2^+$ ) [purple], electrons [black] and lastly electrons produced by positive ion impacts on the back side of the pre-acceleration grid [light blue].

SINGAP accelerator, most particles produced inside the post-acceleration gap are transmitted through the grounded grid towards the neutraliser (the neutraliser entrance is located at the right side of the plot; it is not shown). The total power carried toward this region of the injector is high because of the large potential difference between the pre-AG and the GG (945 kV for the ITER-SINGAP design). Furthermore, a significant amount of positive ions (which originate from either double stripping of negative ions or ionization of the background gas) will hit the back of the pre-AG grid. These backstreaming positive ions will produce secondary electrons, which are accelerated towards the grounded grid. Most reach a final energy of  $\simeq 945$  keV as interception inside the post-acceleration gap is only with residual gas molecules. They consequently pass through the large apertures in the grounded grid, towards the neutraliser.

Table 11.1: Total power generated by secondary particles for MAMuG and SINGAP accelerators calculated by the EAMCC code. The total accelerated  $D^-$  power is 40 MW.  $P_{\text{grid}}$  corresponds to the total power deposited on grids,  $P_{\text{neut}}$  power transmitted toward the neutraliser and  $P_{\text{src}}$  back into the negative ion source. The numbers shown include contribution from (i) stripping reactions, (ii) ionization of background gas, (iii) electron production from particle impacts on accelerator grids, and (iv) co-extracted plasma electrons.

	Species	$P_{\text{grid}}$ (MW)	$P_{\text{neut}}$ (MW)	$P_{\text{src}}$ (MW)
MAMuG	$e^-$	7	0.6	None
	$D^0$	0.1	2.2	None
	$D^+$	Negligible	Negligible	0.14
	$D_2^+$	0.13	None	0.74
SINGAP	$e^-$	1.7	8	None
	$D^0$	Negligible	1.7	None
	$D^+$	0.04	0.05	0.03
	$D_2^+$	0.28	None	0.36

### 11.3.1 Secondary particle power deposition

Table 11.1 shows a summary of the results of calculations using the EAMCC code for the power deposited on the accelerator grids and transmitted (toward the neutraliser and the negative ion source) by secondary particles for the two accelerators foreseen for ITER, MAMuG and SINGAP. For MAMuG, the EG voltage is set at 9.4 kV and each of the five AGs have a potential difference of 200 kV; all grids have 1280 apertures. Estimates for the ITER-MAMuG accelerator have been shown in the previous chapter [131]. Characteristics of power deposition profile from secondary particles are widely different between the two devices. In both cases, most power is carried by secondary electrons. In ITER-SINGAP, electrons absorb a total of 9.7 MW of power from the generators which is mostly transmitted toward the neutraliser (8 MW, 10.7 A), the rest is deposited on the grids. A detailed study of the origins of these electrons shows that 1.4 MW (1.5 A) is carried by particles which were produced as by-products of positive ion impacts on the back side of the pre-AG grid (facing the neutraliser), while about 1.2 MW (1.2 A) are from co-extracted electrons. It was assumed that 52 A of electrons were co-extracted with the negative

ions (one electron per extracted negative ion) corresponding to a current density of  $26.5 \text{ mA/cm}^2$ . Consequently only 1.9% of the electrons extracted from the ion source are accelerated to full energy. The remaining electron power (5.4 MW, 8 A) is produced inside the post-acceleration gap.

These estimates do not include positive ions which will be extracted from the plasma formed by beam ionisation of the background gas downstream of the grounded grid. It has been calculated that about 0.4 A may be extracted from that plasma into the post-acceleration region. Many of these ions will hit the back of the pre-AG at an energy of 945 keV and consequently produce secondary electrons. The secondary electron emission coefficient is of the order of three electrons per impact at normal incidence and significantly larger for impacts inside the pre-AG apertures (at glancing incidence) [131]. A rather conservative estimate for the electron power originating from these ions (neglecting ion impacts inside apertures) is 1.1 MW (1.2 A), and that power mostly exits the grounded grid and is transmitted towards the neutraliser.

For SINGAP, the total negative ion stripping was found to be of the order of 23% (the stripping profile is shown in Fig. 11.3); 1.7 MW of power is transmitted as neutrals towards the neutraliser, and 390 kW as positive ions (mostly molecular deuterium ions) flows back towards the ion source. The latter, though not as high as will be the case with the ITER-MAMuG accelerator (880 kW [131]), positive ion impacts will cause erosion of the back plate of the plasma source by sputtering. Footprints left by positive ion beamlet impacts have been observed experimentally inside the ion source of high energy NB injectors and are similar to those foreseen for ITER [132].

The ITER-MAMuG concept has quite a different power density deposition profile compared to ITER-SINGAP. In the case of the MAMuG, most electron power is deposited on the accelerator grids (7 MW) with a significantly lower amount transmitted toward the neutraliser ( $\simeq 820 \text{ kW}$ ). This major difference is simply due to the higher impact probability on the accelerator grids compared to SINGAP because of the low transparency of the acceleration grids in MAMuG. Furthermore, total negative ion stripping ratio is 29% (see Fig. 11.3) which is larger than for ITER-SINGAP concept due to a typically higher background gas pressure inside the accelerator [122, 131]. Consequently, this imposes a higher required negative ion current density to be extracted from the ion source in order to have 40 A of 1 MeV ions accelerated out of

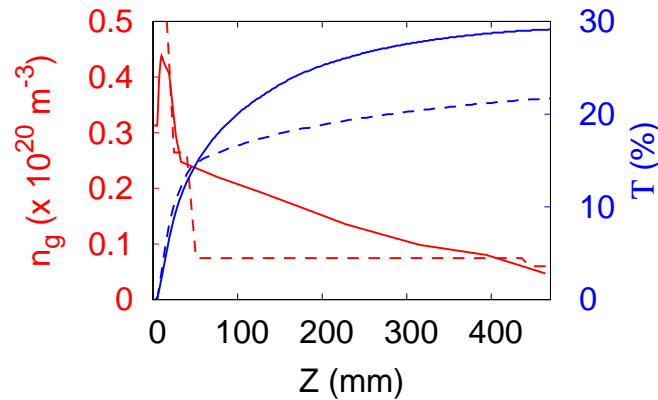


Figure 11.3: (Color) Background gas density profile  $n_g(z)$  (left axis, red color) and negative deuterium ion stripping rate  $\Gamma(z)$  (right axis, blue color) as a function of propagation distance inside the accelerator is shown for both the MAMuG accelerator (solid lines) and the SINGAP accelerator (dashed lines). The gas density for MAMuG is calculated using a Monte-Carlo (MC) method described in Ref. [122] while, for SINGAP, using a classical conductance approach [123]. A filling pressure of 0.3 Pa in the ion source is assumed (with no source operation and the system at room temperature). For SINGAP the accelerator pressure was assumed to be 0.03 Pa, for MAMuG it follows from the MC calculations in Ref. [122]. In addition, a source gas temperature  $T_g = 2000$  K during discharge operation was assumed for MAMuG and 300 K for SINGAP. This difference in assumptions matters for the extractor ( $Z < 20$  mm) but is of no consequence in the post-accelerator as the gas will have accommodated to 300 K both for SINGAP and for MAMuG.

the accelerator;  $28.5 \text{ mA/cm}^2$  for MAMuG compared to  $26.5 \text{ mA/cm}^2$  in SINGAP.

Last, the total parasitic power carried by secondary particles (obtained by summing both power deposited on accelerator grids and transmitted) is similar for the two accelerator concepts; 10.9 MW for ITER-MAMuG and 12.1 MW for ITER-SINGAP. In both cases this is a large fraction, 27% to 30%, of the total negative ion power leaving the accelerator (40 MW).

### 11.3.2 Experimental measurements

In this section, we compare EAMCC calculations with experimental data. The first experiment simulated was performed in the SINGAP-prototype at the CEA (French Atomic Energy Commission) laboratory in Cadarache, France. The Cadarache 1 MV negative ion beam facility is capable of accelerating 100 mA of negative hydrogen

Table 11.2: Processes involved in the destruction of negative ions and ionization of helium gas which are included in EAMCC [63, 133].

Reaction #	Process	Label
1	$D^- + He \rightarrow D^0 + He + e^-$	Sgl strip. neg. ion
2	$D^0 + He \rightarrow D^+ + He + e^-$	Sgl strip. neut.
3	$D^- + He \rightarrow D^+ + He + 2e^-$	Double stripping
4	$D^- + He \rightarrow D^- + He^+ + e^-$	Ionization
5	$D^0 + He \rightarrow D^0 + He^+ + e^-$	Ionization
6	$D^- + He \rightarrow D^0 + He^+ + 2e^-$	Ioniz. & strip.
7	$D^0 + He \rightarrow D^+ + He^+ + 2e^-$	Ioniz. & strip.

or deuterium ions up to 1 MeV. The negative ions are first accelerated in the pre-accelerator to energies of 10-50 keV and thereafter up to maximum energy in a single stage post-accelerator [134]. An experimental campaign was dedicated to the measurement of positive ion power deposition of the back side of the negative ion source. Most positive ions produced inside the accelerator are believed to reach the ion source. In order to verify this hypothesis, helium gas was added inside the accelerator in order to enhance positive ion production rates. The experiment was carried with one beamlet only extracted from the PG through a 14 mm hole aperture. Positive ion power deposited on a copper target located at the rear of the ion source was determined from the temperature rise of the target as measured by a thermocouple buried therein. The most relevant collision processes between deuterium ions, neutrals and helium gas were added to EAMCC [63, 133]; a summary of the reactions included is shown in Table 11.2. Figure 11.4(a) shows the ratio of positive ion beam power with respect to the negative ion power collected on the calorimeter downstream the accelerator as a function of background helium pressure for both experimental data (blue color) and EAMCC calculations (red color). A good agreement between measurements and simulations is found. For large helium pressures, typically  $P_{He} \gtrsim 0.1$  Pa, plasma effects inside the accelerator may be non-negligible. This will induce errors in EAMCC estimates.

A series of experiments have also been conducted at the megavolt test facility at the Japanese Atomic Energy Agency (JAEA) in Naka, Japan on an ITER-like

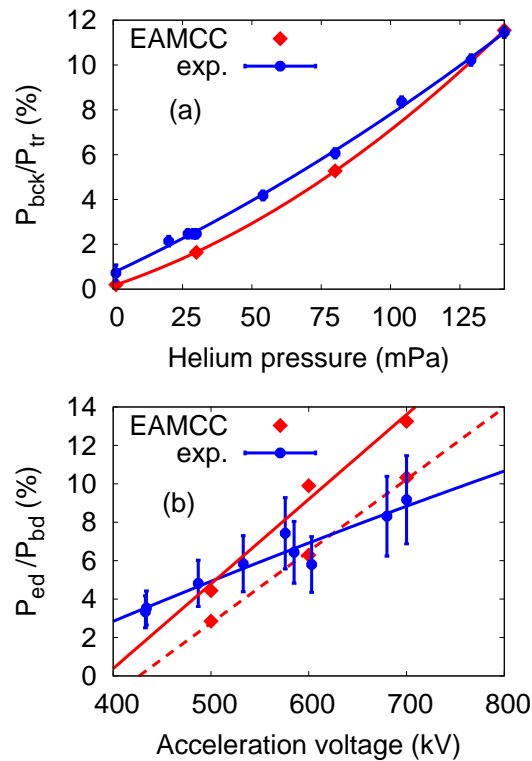


Figure 11.4: (Color) Comparison between experimental data and EAMCC. In (a), experiments conducted at the CEA laboratory in Cadarache, France on a SINGAP accelerator. Positive ion beam power measured on the back side of the ion source is shown normalised to the negative ion beam power measured downstream of the accelerator on a calorimeter versus background helium gas pressure (which was used for this series of experiments in order to enhance positive ion production). Experimental data (blue color) and simulations (red color) are reported. In (b), SINGAP experiment at JAEA in Naka, Japan. Ratio of power collected on an electron dump and the negative ion beam dump is shown versus acceleration voltage. Lines (solid and dashed) correspond to first order polynomial fits.

SINGAP accelerator [135]. For practical reasons the first stage AG of the prototype MAMuG accelerator and the first stage of the MAMuG power supply had to be used for the SINGAP pre-accelerator. Therefore the pre-AG potential was 1/5 of the total acceleration voltage. A total of 15 beamlets were accelerated. After acceleration the ions drifted towards a beam dump located  $\simeq 3$  m downstream of the grounded grid. The electrons were deflected onto two electron dumps; only one of which was equipped with a thermocouple for temperature measurement and subsequent determination of

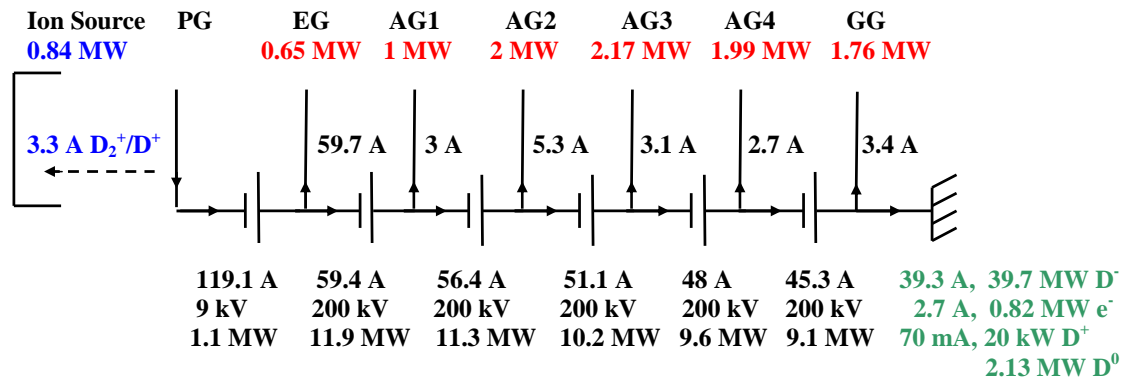


Figure 11.5: (Color) ITER-MAMuG power supply characteristics. The schematic shows the powers and corresponding currents flowing through the power supplies across each gap [bottom], generated by both negative ions and secondary particles. In dark green [bottom right], powers and currents corresponding to particles transmitted toward the neutraliser are shown. In red [top] are the impact powers from secondary particles on grids. In blue [left], power and current transmitted toward the ion source (carried by positive ions). The calculation assumed  $\simeq 40$  A of accelerated negative ions at the exit of the accelerator (total power of  $\simeq 40$  MW) including  $\simeq 14\%$  of halo current, i.e. there are 34 A of negative ions extracted from the ion source and 5.4 A produced on the back of the plasma grid. The total power to be supplied to the accelerator is 53.2 MW; 13.4 MW of which is simply parasitic power absorbed by secondary particles.

the power to the target from the measured temperature rise. The power carried by the electrons transmitted out of the accelerator was measured, and this supports the estimates from the calculations discussed in Sec. 11.3.1. Figure 11.4(b) shows the ratio of power measured on the electron dump divided by the power collected on the beam dump for both experimental data (blue color) and EAMCC calculations (red colour). The agreement between simulation and experiments is reasonable. Experimental error bars were calculated based on data fluctuations. Unfortunately there is uncertainty in the electron dump position as the latter is known to have moved during the experimental campaign. The data shown in red, solid line, represents the ratio of the power on the second electron dump for the designed electron dump locations and the dashed line is for a hypothetical location 1 cm closer to the negative ion beam path. Due to the large distance between the last AG and the beam dumps, a small variation in the electron dump position would have caused a significant change in the power collected.

Differences between simulations and experiments may originate from different sources. The main difficulty in EAMCC is to correctly estimate the plasma meniscus shape. Field maps calculated by the code SLACCAD are used. SLACCAD [100] does not perform any plasma physics calculations. Consequently, the plasma meniscus is calculated rather simply by imposing a vanishing electrostatic field inside the negative ion source. Another important source of error may be the appearance of a beamlet halo. Power density profiles of negative ion beamlets measured experimentally show that a part of the beamlet has divergence that is high compared to the bulk of the beamlet [136], which is commonly referred to as the beamlet “halo”. The optics of the main part of the beamlet and the secondary particle production in the accelerator can be affected by the presence of the divergent ions making up such a halo in the accelerator. Last, error bars on cross sections (which are sometimes quite large) for the physical-chemistry of deuterium inside the accelerator is an additional uncertainty which must be considered.

Based on the results discussed in this section, that is, the large electron production observed experimentally for SINGAP accelerators together with the calculations reported here for the reference ITER-SINGAP design (see Table 11.1) have led to the selection of the MAMuG concept for ITER.

## 11.4 ITER accelerator power supply characteristics

Required characteristics of the power-supplies for the ITER-MAMuG accelerator have been calculated using EAMCC. The parameters used are from the reference design which is a 9 kV extraction grid together with five acceleration grids, each at a potential difference of 200 kV, and a final negative ion energy of 1009 kV. We have included a beamlet halo and the following hypothetical model of the halo has been used to simulate its effect on the negative ion beam optics and secondary particle production. Caesium (Cs) is injected into the ion source to lower the work function of metal surface [98] and consequently enhance the negative ion yield from surface production. The injected Cs will cover the inner surfaces of the ion source and migrate from the ion source side of the plasma grid across the surface into the accelerator, and some

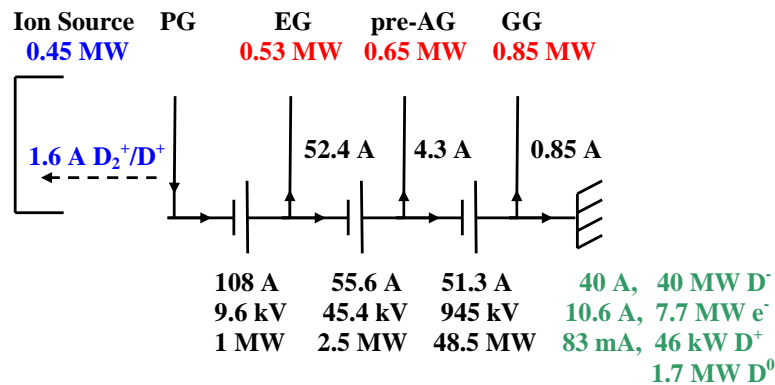


Figure 11.6: (Color) ITER-SINGAP power supply characteristics. Shown in dark green [bottom right], are the powers and currents corresponding to particles transmitted towards the neutraliser. In red [top] are the impact powers from secondary particles on grids. In blue [left], power and current transmitted toward the ion source. The calculation assumed 40 A of accelerated negative ions at the exit of the accelerator including 15% of halo current. Total power generated by the power supplies amount to 52 MW (12 MW is parasitic power absorbed by secondary particles).

Cs will enter the accelerator as vapour. Some of the Cs entering/migrating into the accelerator will cover to some degree the downstream surface of the plasma grid. Of the  $D^0$  atoms flowing out of the source, some will be reflected off surfaces and hit the downstream side of the PG. Some of the  $D^0$  impinging in an annulus around each of the 1280 apertures will be backscattered as negative ions and be accelerated through the subsequent grids, forming a divergent “halo” around each beamlet. In calculating the currents that the power supplies for the ITER-MAMuG accelerator have to deliver, the current density from the annuli on the downstream side of the plasma grid is adjusted so that a  $\simeq 14\%$  beamlet halo appears in the total accelerated current of  $\simeq 40$  A; consequently only about 34 A of negative ions emerging from the accelerator have a good divergence, as assumed for the ITER neutral beam injector design.

A summary of the required power supply capabilities for ITER-MAMuG is shown in Fig. 11.5. The plot displays the total currents flowing through each gap inside the accelerator (linked to an independent power supply) together with the associated power required to be delivered by the generators. These power estimates represent absolute minima in order to provide the necessary energy to accelerate 40 A of negative

ions to 1 MeV. Total secondary particle production is superior to the case calculated in Table 11.1 owing to the addition of a beamlet halo. Total parasitic power absorption is found to be 13.4 MW (2.5 MW in excess mostly caused by direct hitting of negative ions within the halo with the accelerator grids). Total power deposited on the accelerator grids amounts to 9.6 MW (red color in Fig. 11.5) while power transmitted toward the neutraliser is of the order of 3 MW (mostly carried by neutrals) and  $\simeq$  840 kW back inside the plasma source (exclusively from positive ions). Note that secondary electron power transmitted towards the neutraliser is significant,  $\simeq$  820 kW.

Calculation of the ITER-SINGAP power supply characteristics is shown in Fig. 11.6 using the same parameters introduced in Sec. 11.3. This simulation includes a 15% halo ratio to the total 40 A of accelerated negative ion current at the exit of the accelerator. Note that most of the negative ions within the halo are transmitted outside the accelerator. Consequently the power supply characteristics are very similar with or without halo. Total power generated by the power supplies is slightly lower than the reference design ITER-MAMuG concept, corresponding to a parasitic power absorption from secondary particles of 12 MW (which represents 30% of the negative deuterium ion beamlet power at the exit of the accelerator). Total secondary particle power transmitted toward the neutraliser amounts to 9.5 MW which is substantially higher than the MAMuG accelerator ( $\simeq$  3 MW).

## 11.5 Conclusion

In this chapter, we have compared the effects of secondary particle production inside the two electrostatic accelerator concepts being developed for the ITER high energy NB injectors. The relativistic Monte-Carlo particle tracking code EAMCC was modified in order to cope with arbitrary geometries; previous versions were suited uniquely for 2D cylindrical symmetric devices. It is found that the two accelerator concepts for ITER, MAMuG and SINGAP, have a significantly different power deposition profile induced by secondary particles inside the NB injector. In both cases, a high parasitic power absorption from the power supplies is calculated: of the order of 13.5 MW for ITER-MAMuG and 12 MW for ITER-SINGAP. In ITER-MAMuG most power

is deposited inside the accelerator (9.6 MW on grids) while a lower amount is transmitted toward the neutraliser and the negative ion source (total of 3.8 MW). For ITER-SINGAP, the power on grids is reduced,  $\simeq 2$  MW since a significant part of the power carried by the secondary particles is transmitted through the accelerator (total  $\simeq 10$  MW). This difference in the fraction of secondary particles transmitted as opposed to being intercepted inside the accelerator for the two accelerator concepts is a direct consequence of the geometry of the accelerators, MAMuG having several, sequential, small apertures through which each beamlets must pass compared to the completely open main acceleration stage and very large apertures in the grounded grid of SINGAP. The high electron fraction transmitted downstream of a SINGAP accelerator has also been observed experimentally in an ITER-like prototype. Based on the calculations presented here and those experimental results, the MAMuG concept was chosen for ITER. One of the critical issues that remain to be solved in ITER-MAMuG is the handling of the high power density deposited by positive ions on the back plate of the negative ion source. Based on calculations, it is found that the peak power density may exceed the critical value of  $2 \text{ kW/cm}^2$ .



# Chapter 12

## Conclusions and perspectives

The numerical modeling of a fusion-type negative ion source and of the particle transport inside the electrostatic accelerator brought some physical insight which when combined with experimental measurements did improve significantly the understanding of these two components of the Neutral Beam Injector (NBI). Models provided trends similar to the ones observed in the experiments but also some detailed analysis of the ion source plasma properties which would otherwise be accessible experimentally with difficulty. An exact comparison, although not really necessary in my opinion to describe correctly the physics, was not performed in this manuscript. This is quite a difficult task and many additional details would need to be implemented in the model. So how does the model compares with experiments?

- The Hall effect has not been precisely measured in the experiments but its indirect consequences have been clearly observed. The Hall electric field (polarization) resulting from the electron drift inside the magnetic filter field of the expansion chamber in fusion-types negative ion sources induce a transverse asymmetry in the plasma parameters. Two Langmuir probes, positioned transversely near the top and bottom parts of the driver and moving along the longitudinal axis of BATMAN have measured this asymmetry [16, 137] which we reproduced qualitatively in chapter 7. In addition, both the experiment and the model of the half-size ITER prototype ion source ELISE found that an expansion chamber with a larger aspect ratio seems to reduce the extent of the asymmetry. This seems directly related to the shape of the magnetic filter but more work is necessary before concluding.
- The neutral depletion was evaluated with a baratron in the experiments both inside the driver and the expansion chamber [26]. Temperatures and densities of the same order of magnitude was calculated in the model for hydrogen at 0.3 Pa (chapter 5). We confirmed that the neutral atom temperature is significantly larger than the temperature of  $H_2$  at low pressure with a ratio of densities  $n_H/n_{H_2} \sim 20\%$ .
- The flattening of the plasma potential with the PG bias voltage was reported by K. Leung et al. [87] in an ion source with a magnetic filter and driven by hot cathodes (tungsten filaments). A similar behavior was simulated in the model

(chapter 8). This explains the increase in the extracted negative ion current for a PG bias voltage such that the net particle current impacting the electrode (the so-called bias current) is negative. The positive ion flux exceeds the negatively charged particle flux in that case. For larger bias voltages, the increase in the virtual cathode depth results in a lower extracted negative ion current in the model. The ion current hence peaks near a floating PG. This is also observed in the experiments both with a cesiated ion source (BATMAN) [16] or when the negative ions were solely produced by volume processes [87]. The shape of the extracted negative ion current profile versus the PG bias is less pronounced in the experiments performed in BATMAN. The reason has not yet been clearly elucidated. Lastly, the co-extracted electron current continuously decreases with the PG bias. This is both witnessed in the experiments [16] as well as in the numerical model (chapter 8).

- In chapter 9, we modeled the negative ion extraction from a cylindrical aperture (with a flat surface facing the plasma as opposed to a chamfered geometry which is currently used nowadays in most fusion-types ion sources). The simulation domain was restricted to the vicinity of a single aperture in order to increase the numerical resolution. In 3D, modeling the real ITER density still requires a large number of grid nodes and computer cores. As an alternative, we derived scaling laws from a 2D model for slit apertures and posited that they may be applied to cylindrical apertures in 3D. We found a scaled extracted negative ion current of  $125 \text{ A/m}^2$  associated with an average negative ion density of  $5 - 6 \times 10^{16} \text{ m}^{-3}$  about 2 cm from the PG surface (we applied a correction in order to account for negative ions produced by volume processes). The average corresponds to a LOS parallel to the PG. The paper of Speth et al. [5] compiled measurements with cylindrical apertures. They found an extracted ion current of  $150 \text{ A/m}^2$  which is 20% higher than in the model. This is unfortunately not sufficient for a comparison and we need other plasma parameters. Some measurements in BATMAN using cylindrical apertures but chamfered correlated both the extracted negative ion current with the negative ion density  $\sim 2$  cm from the PG [16, 93] (CRDS). The experiment of Kashiwagi et al. [91] concluded that the extracted negative ion current is approximately proportional to the surface

area surrounding the aperture. In BATMAN the chamfered apertures have a surface area  $\sim 25\%$  larger compared to the previous cylindrical ones. Berger et al. [93] found on BATMAN a negative ion current density of  $185 \text{ A/m}^2$  together with a negative ion density of  $\sim 5 \times 10^{16} \text{ m}^{-3}$  at  $0.3 \text{ Pa}$ . Applying the correcting factor for cylindrical apertures, the latter are consistent with the values derived from the 3D PIC-MCC model. The simulation of chamfered apertures is left to future work.

- The EAMCC model (chapter 10 and 11) was designed to evaluate the secondary particle production inside the electrostatic accelerator of the ITER NBI. The scope was to map the power deposition in 3D on the accelerator grids, calculate the (parasitic) power-supply power absorbed by the secondary particles and hence provide an estimate for the characteristics of the power-supply themselves. The EAMCC algorithm was used together with experimental measurements to model the two accelerator concepts foreseen for the ITER NBI and select the MAMuG (which is the Japanese concept) as the best choice. EAMCC is currently used by 4 laboratories worldwide. The comparison with experiments discussed in chapter 11 was in fairly good agreement with the measurements performed on the SINGAP accelerator at the IRFM laboratory in France (CEA, Cadarache) but different trends were observed for the Japanese accelerator. The latter experiment had a couple of issues: (i) the detector moved accidentally during the campaign and (ii) the negative ion beamlets had likely a halo leading to some direct beam interception on the accelerator grids. This rendered the comparison quite challenging. Updated measurements by the Japanese laboratory (JAEA, Naka) found similar trends with the model and a closer agreement for the secondary particle power deposition on the accelerator parts [138].

Scaling down the plasma density in the simulations changes the ordering between the electron Larmor radius and the Debye length compared to the real device. In BATMAN, we have  $r_L > \lambda_{De}$  and hence the Debye sheath is not magnetized while in the model (in most cases)  $r_L < \lambda_{De}$ . Calculations similar to the ones discussed in chapter 3 but with a higher magnetic field ( $B_0 = 75\text{G}$ ) such that  $r_L > \lambda_{De}$  for the highest densities did not find any particular transition when the ordering was flipped. We do not know the reason at the present time and this will be the subject of a future

study.

So what's next? This manuscript was mostly devoted to the description of existing devices (BATMAN, ELISE and the two ITER NBI accelerators). We modeled the physics and compared the calculated plasma properties with available experimental data. The work on the ITER NBI accelerator was directly targeted to assist the engineers. The 3D mapping of the secondary particle power density deposition on the accelerator grids proved helpful for the design of the cooling system. The calculation for the power supply characteristics is still the best available so far. Future work will be dedicated both to the study of novel fusion-type negative ion source concepts (we have currently a grant from EUROfusion to work on the DEMO project, which is the Tokamak foreseen to replace ITER) and on basic physics problems typically found in magnetized plasma sources. We will model the CYBELE ion source concept currently developed at the IRFM laboratory in CEA, Cadarache, France. This ion source has 2 Helicon discharges which are aligned with the magnetic field lines as opposed to the current ITER prototypes which have a filter field perpendicular to the electron flux crossing the expansion chamber. The physics in CYBELE is hence different. The plasma is produced in the area directly facing the Helicons. Positive ions are not magnetized while electrons are trapped and diffuse away via drifts and collisions toward the ion source walls. This generates rotating plasma instabilities which were observed in preliminary numerical calculations where the plasma was produced by hot cathodes (filaments) [139]. Negatively charged particles will be extracted through slit apertures which may be simulated with a 2D PIC-MCC model without the need for scaling down the plasma density. The questions about the plasma behavior which need to be answered are quite profuse.

- We need to characterize the rotating instability. How is it seeded? The influence of the negative ions on the instability will be analyzed. The ions will transport negative charges toward the wall and should hence dampen the instability (assuming they are unmagnetized). This situation might produce a large negative ion to electron ratio near the ion source walls. Preliminary measurements seem to confirm this assertion [140].
- We need to study the influence of the electron distribution function on the

plasma properties, which will likely not be Maxwellian with Helicons.

- The incidence of the magnetic filter field (amplitude and shape).
- The negative ion extraction from the plasma source. The shape of the plasma potential versus the PG bias voltage. How this will impact the co-extraction of electrons? We will study the electron dynamics inside the filter. Biasing positively the PG draws an electron current and the plasma adapts such that some electrons cross the magnetic filter. What are the mechanisms? (drifts versus instabilities).
- The characteristics of the extracted negative ion beamlets will be assessed.

This list is of course not exhaustive and corresponds to the main questions which we want to solve first. This will be excellent topics for PhD students. They will have access both to a deep understanding of the physical mechanisms through modeling together with experiments. The latter will be performed at IRFM (CEA, Cadarache, France) in collaboration with EPFL (Lausanne, Switzerland) and LPSC (Grenoble, France) laboratories. Work on the DEMO project also involve the laboratories of the fusion community (RFX in Italy, JAEA in Japan, IPP in Germany, etc.).

Another field of study will be dedicated to fundamental problems encountered in magnetized plasma sources:

- The difference between cylindrical and chamfered apertures for the extraction of negative ions.
- Co-electron extraction from slit versus cylindrical apertures (relationship between the plasma meniscus and electron drifts in the magnetic field).
- Magnetized versus non-magnetized plasma sheaths (where  $r_L > \lambda_{De}$ ).
- Electron dynamics inside a cusp magnetic field.
- The Hall effect, ponderomotive force and anomalous transport in MHz-scale RF antennas with and without an additional DC magnetic field. The first model will assume prescribed RF fields (electric and magnetic) in order to assess precisely the electron dynamics and the effect of each field sub-components.

- Particle dynamics in discharges with a closed  $\mathbf{G} \times \mathbf{B}$  drift [Eq. (3.4)] as in Magnetrons for instance.
- The development of a massively parallel hybrid MPI/OpenMP PIC-MCC model (with domain decomposition for the particles) in collaboration with the P.Las.M.I research group (CNR-Nanotec, Bari, Italy).

This project provides research directions for the next 5 to 10 years approximately. This should involve several PhD students and post-doctoral researchers. Thank you for your patience while reading this manuscript ☺.

G. Fubiani, September 2016.



# Appendix A

## Implicit PIC modeling

### Contents

---

A.1	Introduction . . . . .	180
A.2	Comparison between explicit and implicit PIC calculations	180
A.3	The direct implicit particle in cell method . . . . .	185

---

## A.1 Introduction

Implicit PIC algorithms [32, 141–144] offer an interesting alternative for the modeling of high density plasmas. A detailed schematics of the method employed in this work is summarized in Sec. A.3. The attractive feature of such method is its ability to overcome the need to resolve the Debye length and plasma frequency like in conventional explicit PIC models. This results from the damping properties of the implicit leap-frog-Poisson system which curbs the numerical heating associated with frequencies not resolved by the time step, in our case the plasma frequency (the Debye length is the associated length scale). Consequently, it is possible to use large time steps and grid sizes; the prerequisite being to resolve the scale-variations (gradients) of the (averaged) plasma quantities. In this appendix, we show that the implicit PIC method is relevant to simulating electrostatic conditions regardless of the value of the plasma density but some limitations arise when a magnetic field is added. Numerical heating appears to be more difficult to control in that case due to the variation of the electron Debye length across the simulation domain, the indirect effect of the Larmor radius and the number of particles per cell. Verification of energy conservation locally during the calculation is hence necessary. Magnetized implicit PIC-MCC models should have a grid spacing no more than a few Debye lengths.

## A.2 Comparison between explicit and implicit PIC calculations

Figure A.1 displays the normalized density profiles and electron current density impacting the RHS wall (PG grid) of the source for both the implicit and explicit PIC models. Two resolutions were used for the explicit calculations, that is,  $192 \times 256$  and  $96 \times 128$  grid nodes. The source geometry is identical to the one displayed in Fig. A.2 with  $V_{PG} = 40$  V and no magnetic filter field. The absorbed RF power in the discharge area was set to  $P = 40$  kW/m, leading to a maximum plasma density of  $n_{\max} = 4.5 \times 10^{17}$  m<sup>-3</sup> which is well above what can be achieved by an explicit PIC method. For that reason, the vacuum permittivity  $\epsilon_0$  was increased up to the standard explicit limit for the grid size and time step, which is  $\Delta x_i \lesssim 2\lambda_{De}$  and

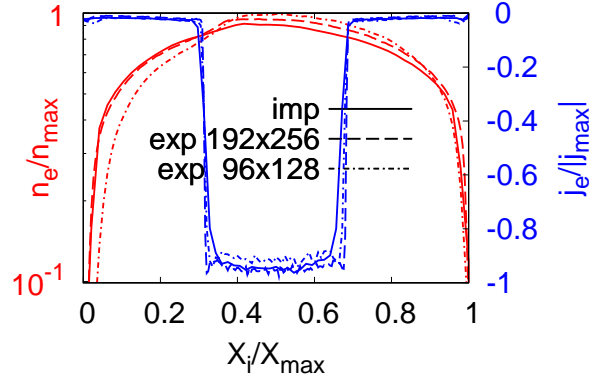


Figure A.1: (Color) Axial normalized density profile (left axis, red color) and normalized electron current density impacting the PG grid surface (right axis, blue color). The maximum current density is  $|j_{\max}| = 3500 \text{ A/m}^2$  and plasma density  $n_{\max} = 4.5 \times 10^{17} \text{ m}^{-3}$ , associated with an absorbed power  $P = 40 \text{ kW/m}$  in the discharge region. Profiles calculated by the implicit PIC model are shown (solid lines) together with solutions from the explicit PIC method: (i)  $192 \times 256$  grid nodes (dashed lines) where in order to match the absorbed power, vacuum permittivity  $\epsilon_0$  was augmented by a factor 250 and (ii)  $96 \times 128$  grid nodes (dotted-dashed lines) with  $\epsilon_0$  increased by 1500. The resolution of the implicit calculation is  $48 \times 64$  nodes. The abscissa is normalized to the length of the source for the density  $X_{\max} = 25 \text{ cm}$  and transverse size for the current density, i.e.,  $X_{\max} = 32 \text{ cm}$ .

$\bar{\omega}_p \Delta t \simeq 0.4$  ( $v_{th} \Delta t / \Delta x_i = 0.3$ ) where  $\bar{\omega}_p$  is the average plasma density in the device. Lastly, 40 ppc was used for all the simulations. The resolution of the implicit calculation is  $48 \times 64$  grid nodes, which is sufficient because the sheath does not exceed one grid cell. The sheath is consequently non-physically large but nevertheless possess the correct ambipolar potential drop, leading to an accurate evaluation of particles wall losses. The maximum grid size is  $\Delta x_i \simeq 135 \lambda_{De}$  and time step  $\bar{\omega}_p \Delta t \simeq 52$  (corresponding to  $v_{th} \Delta t / \Delta x_i = 0.65$ ). The highest explicit PIC resolution provides plasma characteristics in close agreement with the implicit calculation, as shown in Fig. A.1. In the second explicit case (grid cell size twice larger), the width of the sheath with respect to the quasi-neutral volume is large enough to alter plasma parameters. In addition, the computational cost to reach the steady-state conditions using an explicit model instead of implicit may be significant, it can be evaluated as,

$$k_t = \alpha \frac{\Delta t^{\text{imp}}}{\Delta t^{\text{exp}}} \frac{n_{\text{ppc}}^{\text{imp}}}{n_{\text{ppc}}^{\text{exp}}} \prod_{i=1}^2 \frac{\Delta x_i^{\text{imp}}}{\Delta x_i^{\text{exp}}}, \quad (\text{A.1})$$

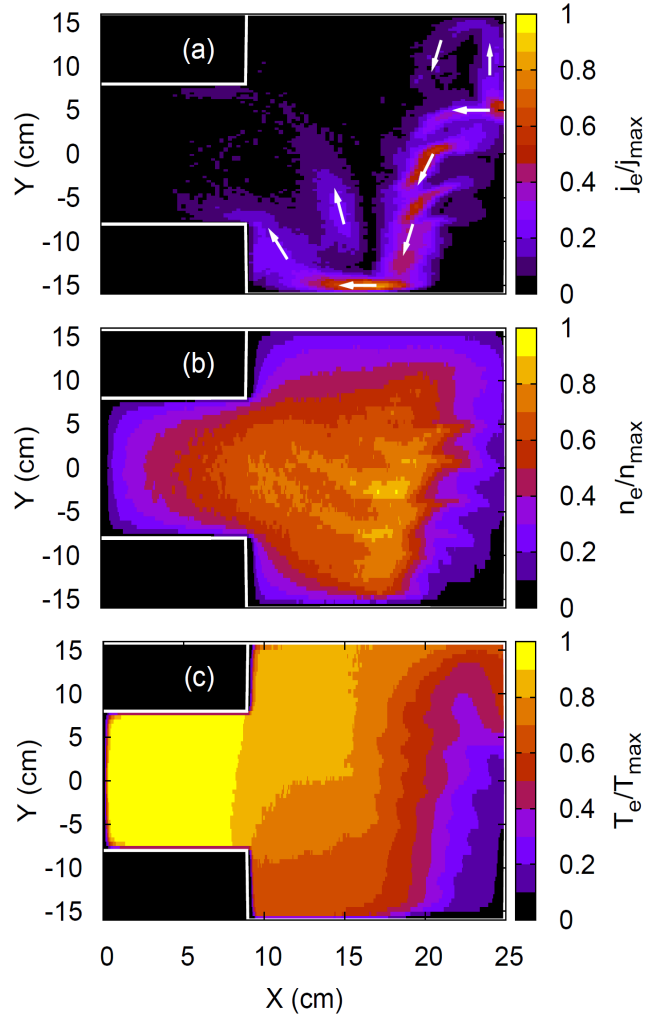


Figure A.2: (Color) 2D explicit PIC-MCC model. The negative ion source characteristics are hypothetical. In (a) electron current density profile, (b) electron density and (c) electron temperature. Normalization factors are  $j_{max} \simeq 140 \text{ A/m}^2$ ,  $n_{max} \simeq 3.9 \times 10^{15} \text{ m}^{-3}$  and  $T_{max} \simeq 10 \text{ eV}$ . Arrows show the preferred direction followed by the electron current. Absorbed power is set to  $P = 160 \text{ W/m}$  in the discharge area (LHS region of the source), the expansion chamber (RHS box) is magnetized with a field directed along the (Oz) axis (out-of-plane) which is assumed Gaussian longitudinally, and constant transversely; maximum strength is  $B_0 = 20 \text{ G}$ . The PG bias voltage is  $V_{PG} = 55 \text{ V}$ , the bias plate is set at a potential of 20V and the background gas density is  $n_{H_2} = 4 \times 10^{19} \text{ m}^{-3}$ . Lastly, the numerical resolution is  $384 \times 512$  grid nodes.

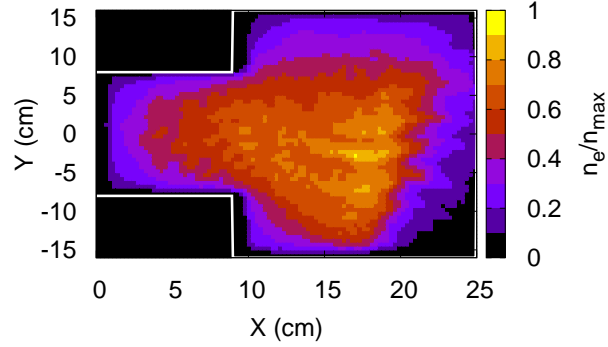


Figure A.3: (Color) 2D electron density profile calculated with the implicit model. Normalization factor is  $n_{\max} \simeq 3.7 \times 10^{15} \text{ m}^{-3}$ . Same simulation conditions as in Fig. A.2, i.e., an absorbed power  $P_{\text{abs}} = 160 \text{ W/m}$ , a bias voltage  $V_{\text{PG}} = 55 \text{ V}$  and, lastly, a magnetic field strength  $B_0 = 20 \text{ G}$ . Grid size is  $\Delta x_i \lesssim 7\lambda_{De}$  (corresponding to a resolution of  $96 \times 128$  grid nodes) and time step  $\bar{\omega}_p \Delta t \simeq 3.2$ . 2D implicit PIC-MCC model.

where  $\Delta t^{\text{imp}}$  ( $\Delta t^{\text{exp}}$ ) is the implicit (explicit) time step,  $\Delta x_i^{\text{imp}}$  ( $\Delta x_i^{\text{exp}}$ ) the grid size,  $n_{\text{ppc}}^{\text{imp}}$  ( $n_{\text{ppc}}^{\text{exp}}$ ) the number of particles per cell and  $\alpha$  a coefficient which accounts for the intrinsic running time difference between the two type of algorithms. Using a standard first order particle weighting scheme, a linear interpolation of the fields at the particle location and applying the implicit mover only to the electrons (ions trajectories are evaluated employing an explicit leap-frog scheme), we find  $\alpha = 0.81$ . Consequently, for the cases shown in Fig. A.1, the cost for using the finest resolution in the explicit model compared to its implicit counterpart is  $k_t \sim 110$  times larger.

The addition of a magnetic field reduces the applicability of the implicit model. Typically, we find that for low magnetic fields (or similarly, Hall parameters), the restriction on the grid size increase gradually. In the conditions of Fig A.2, that is, a magnetic field directed along the (Oz) axis (out of the simulation plane) and strength  $B = 20 \text{ G}$ . The maximum grid size can be as large as  $\Delta x_i \simeq 8\lambda_{De}$ ; for larger Hall parameters, arbitrary magnetic field strength may be simulated but with a stricter constraint on the grid size, i.e.,  $\Delta x_i \simeq 4\lambda_{De}$ . Note that this still makes the use of an implicit model relevant; in 3D for instance, a grid size twice as large as in an explicit calculation and a time step  $\bar{\omega}_p \Delta t \simeq 1$  would decrease running time by  $k_t \sim 25$ .

Figure A.3 shows the 2D electron density profile calculated by the implicit model for the exact same conditions as Fig. A.2, that is, an absorbed power  $P_{\text{abs}} = 160 \text{ W/m}$ ,

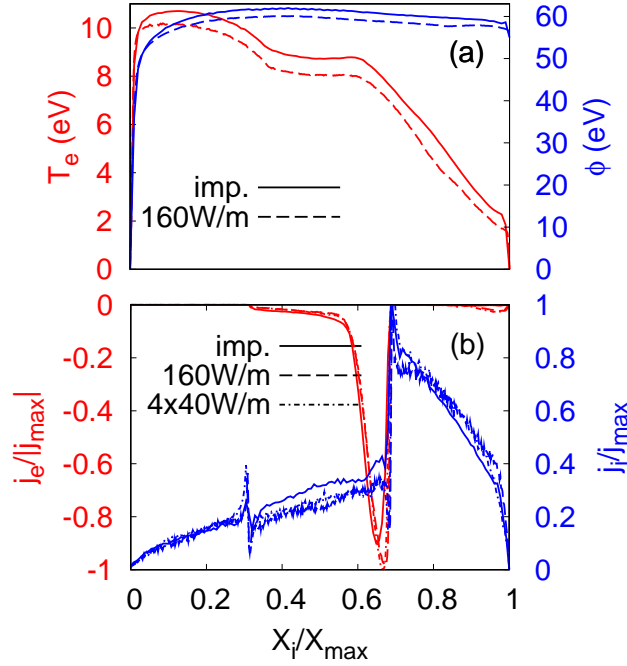


Figure A.4: (Color) In (a), the axial temperature (left axis, red color) and ambipolar potential (right axis, blue color) profiles are shown. The abscissa is normalized with respect to the ion source length,  $X_{\max} = 25$  cm. (b) Electron (left axis, red color) and ion (right axis, blue color) current density profiles collected on the PG grid;  $X_{\max} = 32$  cm. Normalization factor is  $|j_e^{\max}| \simeq 90$  A/m<sup>2</sup> for the electrons and  $j_i^{\max} \simeq 4.1$  A/m<sup>2</sup> for the ions. Total absorbed RF power in the discharge region is  $P = 160$  W/m. Plasma parameters calculated with the implicit model are displayed (solid lines), resolution is  $96 \times 128$  grid nodes. Next, solution from the explicit algorithm using  $384 \times 512$  (dashed-lines) and  $192 \times 256$  (dotted-dashed-lines) grid nodes. The latter corresponds to a lower absorbed power  $P = 40$  W/m which was rescaled to match the simulated power.

a bias voltage  $V_{\text{PG}} = 55$  V and a maximum magnetic field strength  $B = 20$  G. Normalized grid size is at most  $\Delta x_i \simeq 7\lambda_{De}$  ( $96 \times 128$  grid nodes) and time step  $\bar{\omega}_p \Delta t \simeq 3.2$  which shortens the running time by a factor  $k_t \simeq 160$ . The features of the drift-wave like instability (density fluctuations) are retained. Next, Fig. A.4 displays the axial temperature and ambipolar potential profiles together with electron and ion current density impacting the PG grid. In both figures, the difference between the plasma parameters calculated by the explicit and implicit models is below 10%. Lastly, one may deduce from Fig. A.4(b) that the plasma is not current-free at the

entrance of the sheath. This originates from the decoupled electron and ion dynamics in the magnetic field. The former are strongly magnetized with the latter are not. Nevertheless, the total current collected on the walls of the device is null (no external currents are injected).

## A.3 The direct implicit particle in cell method

### A.3.1 Leap-frog Poisson system

There are mainly two types of implicit leap-frog schemes used in the literature [32, 141–143]: (i) the  $D_1$  scheme which introduces the implicit acceleration term,  $a^{n+1}$  (“n” stands for the current time step where particle positions and coordinates are explicitly known) directly on the velocity equation and (ii) the second scheme, so-called “ $C_1$ ”, includes  $a^{n+1}$  within the equation associated with the update of the particle position. This apparent small difference between the two approaches does have non negligible consequences on the calculation of the particle trajectories. The  $D_1$  scheme has a stronger damping rate for numerically unresolved high frequency modes, i.e., when  $\omega\Delta t \gg 1$ , where  $\omega$  is a frequency resulting from the decomposition of the particle motion into a sum of harmonic oscillations and introducing the Fourier representation. When simulating the physics of a plasma discharge in steady state conditions, typically one wishes to damp the plasma wave which grows from noise in particle simulations. Solving the finite differenced implicit Poisson equation coupled to the  $D_1$  leap-frog scheme becomes a quite complex task when including a magnetic field. The fact that the implicit acceleration appears in the velocity equation implies that the susceptibility, which results naturally in Poisson’s equation from an implicit estimation of the charge separation  $\sum \rho_s^{n+1}/\varepsilon_0$ , has a tensorial form [32, 142, 144]. In contrast, the implicit determination of the source term in Poisson’s equation using the  $C_1$  leap-frog scheme provides an expression for the susceptibility which is always scalar. The algorithm which we describe in this work makes use exclusively of a C class type scheme [141, 142] (because it is the simplest of the two schemes to implement for magnetized plasma conditions); we recurrently check energy conservation ensuring that the damping rate of the leap-frog solver is sufficient. The finite differenced

equations solved numerically are the following,

$$\frac{\mathbf{v}_s^{n+1/2} - \mathbf{v}_s^{n-1/2}}{\Delta t} = \mathbf{a}_E^n + \mathbf{a}_M^n, \quad (\text{A.2})$$

$$\frac{\mathbf{x}_s^{n+1} - \mathbf{x}_s^n}{\Delta t} = c_0(\mathbf{a}_E^{n+1} - \mathbf{a}_E^n)\Delta t + c_1(\mathbf{a}_E^n - \mathbf{a}_E^{n-1})\Delta t + \mathbf{v}_s^{n+1/2}, \quad (\text{A.3})$$

where

$$\mathbf{a}_E^n = \frac{q_s}{m_s} \mathbf{E}^n(\mathbf{x}_s^n), \quad (\text{A.4})$$

is the acceleration term resulting from the electrostatic field  $\mathbf{E}$  calculated at each time steps self-consistently via Poisson's equation,

$$\mathbf{a}_M^n = \frac{q_s}{m_s} \left[ \frac{\mathbf{v}_s^{n+1/2} + \mathbf{v}_s^{n-1/2}}{2} \times \mathbf{B}(\mathbf{x}_s^n) \right], \quad (\text{A.5})$$

is the acceleration induced by the prescribed static magnetic field  $\mathbf{B}$ ,  $\mathbf{v}_s(\mathbf{x}_s)$  is the particle velocity (position) vector, "s" is the index of the specie and lastly  $c_0$  and  $c_1$  are coefficients associated with the degree of implicitness of the solver.  $c_0 = c_1 = 0$  corresponds to the explicit leap-frog solver which is symplectic. The highest damping rate is reached for  $c_0 = 0.302$  and  $c_1 = 0.04$  [141].  $\mathbf{E}^n$  and  $\mathbf{B}$  are evaluated at position  $\mathbf{x}_s^n$  while  $\mathbf{E}^{n+1}$  at  $\mathbf{x}_s^{n+1}$ . In an implicit PIC algorithm, one solves the leap-frog Poisson system in three steps: first update the velocity of all the particles using Eq. (A.2), which is explicit, then update the particle position [Eq. (A.3)] only for the explicit term, that is,

$$\frac{\tilde{\mathbf{x}}_s - \mathbf{x}_s^n}{\Delta t} = (c_1 - c_0) \mathbf{a}_E^n \Delta t - c_1 \mathbf{a}_E^{n-1} \Delta t + \mathbf{v}_s^{n+1/2}. \quad (\text{A.6})$$

The implicit evaluation of Poisson's equation requires an estimate for the future charge density  $\rho_s^{n+1}$ . The quantity  $\mathbf{x}_s^{n+1}$  being unknown, the density is expanded around  $\tilde{\mathbf{x}}_s$  assuming  $\delta\mathbf{x}_s = \mathbf{x}_s^{n+1} - \tilde{\mathbf{x}}_s$  is small. Note that in the model, we calculate the electron motion using the implicit mover, Eqs. (A.2)-(A.3), while ions (due to their much larger mass) are pushed via a classical explicit leap-frog evaluation (equivalent to

taking  $c_0 = c_1 = 0$ ). The implicit charge density thus becomes,

$$\begin{aligned}\rho_s^{n+1}(\mathbf{x}_g) &= \sum_i \frac{q_s}{\Delta A} S(\mathbf{x}_g - \mathbf{x}_i^{n+1}), \\ &= \sum_i \frac{q_s}{\Delta A} S(\mathbf{x}_g - \tilde{\mathbf{x}}_i - \delta \mathbf{x}_i), \\ &\simeq \tilde{\rho}_s(\mathbf{x}_g) - \frac{q_s}{\Delta A} \sum_i \delta \mathbf{x}_i \frac{\partial}{\partial \mathbf{x}_g} S(\mathbf{x}_g - \tilde{\mathbf{x}}_i),\end{aligned}\tag{A.7}$$

where  $\Delta A$  is the surface area of the grid cell ( $\Delta A = \Delta x \Delta y$  in 2D),  $\tilde{\rho}_s(\mathbf{x}_g) = (q_s/\Delta A) \sum_i S(\mathbf{x}_g - \tilde{\mathbf{x}}_i)$  is the charge density at the grid nodes evaluated from the particle positions  $\tilde{\mathbf{x}}_i$ .  $S(\mathbf{x} - \tilde{\mathbf{x}}_i)$  is the shape function, which describes the spatial extension of a given particle,  $\mathbf{x}$  being the observation point (an independant variable). In principle,  $\delta \mathbf{x}_i$  should be evaluated at  $\mathbf{x}_i^{n+1}$ , but in practice the least computationally intensive and most stable numerical method is commonly employed, so-called simplified differencing. In the latter case,  $\delta \mathbf{x}_i$  is evaluated at the grid nodes  $\mathbf{x}_g$  [144–147]. Equation (A.7) is then modified as follows,

$$\rho_s^{n+1}(\mathbf{x}_g) \simeq \tilde{\rho}_s(\mathbf{x}_g) - \varepsilon_0 \nabla \chi_s \mathbf{E}^{n+1},\tag{A.8}$$

where  $\chi_s = c_0 \Delta t^2 q_s^2 \tilde{n}_s / (m_s \varepsilon_0)$  is the implicit susceptibility associated with charged particle specie “s”. We treat solely electrons implicitly and the modified Poisson’s equation is then

$$\varepsilon_0 \nabla \cdot (1 + \chi_e) \mathbf{E}^{n+1} = \tilde{\rho}_e + \sum_{i=1}^s \rho_i^n,\tag{A.9}$$

where the right-hand-side (RHS) sum is only for the ions. Once  $\mathbf{E}^{n+1}$  is known on the grid nodes, one may calculate the correction to the particle trajectories (again in our case only the electrons),

$$\mathbf{x}_s^{n+1} \simeq \tilde{\mathbf{x}}_s + c_0 \Delta t^2 \frac{q_s}{m_s} \mathbf{E}^{n+1}(\tilde{\mathbf{x}}_s).\tag{A.10}$$

Formally, the last term of the RHS of Eq. (A.10) should be calculated at  $\mathbf{x}_s^{n+1}$ . This requires an iterative evaluation of Eqs (A.2)-(A.10) not followed in practice due to the increase in complexity (and associated simulation run time) added to the algorithm without a substantial gain in accuracy [145]. Typically the method outlined here is

proper as long as fields or density gradients are well resolved on the grid cell.

An implicit algorithm counteracts the intrinsic numerical heating feature of the explicit method, when the grid size and time step exceed some limits [32, 33], by introducing damping of high frequency mode (typically noise). For that reason, the time step in an implicit calculation is bounded: (i) it must be set higher than some lower limit (which depends on the grid size), to obtain a satisfactory damping rate and (ii) the transit length for the vast majority of particle in the distribution function must not exceed one grid cell per step, time step must be adapted accordingly. In short, when  $v_{th}\Delta t/\Delta x_i > 1$ , sampling of the fields (which finest resolution is defined by the mesh) is improper, introducing errors in the calculation of plasma parameters. In terms of transit time, one must consequently remain within the range  $0.5 \lesssim v_{th}\Delta t/\Delta x_i \lesssim 1$ .

### A.3.2 Boundary conditions

The implicit Poisson equation, Eq. (A.9), is solved iteratively in the interior points of the simulation domain. We implemented a multi-grid method [35] to calculate the potential  $\phi^{n+1}(\mathbf{x}_g)$  on the grid nodes. For perfectly conducting walls the potential value is provided and for dielectric materials, we calculate self-consistently the potential from the charges accumulated locally at the wall in a rather simple but sufficient manner,

$$\phi_w(\mathbf{x}_w) = \phi_0 + C^{-1} \sum_s q_s(\mathbf{x}_w, T), \quad (\text{A.11})$$

where  $\phi_w$  is the wall potential,  $\phi_0$  the reference potential inside the dielectric,  $\mathbf{x}_w$  the physical location of the wall,  $q_s(\mathbf{x}_w, T)$  the charge collected locally on the wall during a time interval  $T$  for each particle species,  $C = \varepsilon d$  the (numerical) capacitance,  $\varepsilon$  the dielectric permittivity and  $d$  its width. The capacitance should be chosen large enough so that a significant amount of charge accumulation (which would minimize fluctuations) is necessary in order to modify the wall potential value. The potential self-adjusts until steady-state conditions are reached.

The electric field at the boundary, for both conductors and dielectrics, is calculated by a linear extrapolation with respect to field values located at the two closest interior nodes. For instance, if the left-hand-side (LHS) wall is located at node index  $(i_x, i_y)$ ,

then

$$\mathbf{E}(i_x, i_y) = 2\mathbf{E}(i_x + 1, i_y) - \mathbf{E}(i_x + 2, i_y). \quad (\text{A.12})$$

This approach, which is not based on the conventionnaly employed Gauss law to deduce the field values at the boundary is robust even when the sheath is not resolved on the grid cell, that is when  $\Delta x_i \gg \lambda_{De}$ . The extrapolation provides an estimate for the field which is lower than found in an explicit simulation due to the larger grid size but nevertheless the particles in the sheath gain the right amount of kinetic energy and we recover the appropriate particle fluxes and potential drop. The whole sheath region is generally contained over one grid cell only. Without loss of generality, in the PIC simulations presented in this work we exclusively used metallic boundary conditions.



# References

- [1] D. Faircloth. Ion sources for high-power hadron accelerators. in Proceedings of the CAS-CERN Accelerator School: High Power Hadron Machines, Bilbao, Spain, edited by R. Bailey, 2013.
- [2] A. Shishlo, J. Galambos, A. Aleksandrov, V. Lebedev, and M. Plum. First observation of intrabeam stripping of negative hydrogen in a superconducting linear accelerator. *Phys. Rev. Lett.*, 108:114801, Mar 2012.
- [3] R.S. Hemsworth and T. Inoue. Positive and negative ion sources for magnetic fusion. *Plasma Science, IEEE Transactions on*, 33(6):1799 – 1813, dec. 2005.
- [4] G. Fubiani, R. S. Hemsworth, H. P. L. de Esch, and L. Svensson. Analysis of the two accelerator concepts foreseen for the neutral beam injector of the international thermonuclear experimental reactor. *Phys. Rev. ST Accel. Beams*, 12:050102, May 2009.
- [5] E. Speth, H.D. Falter, P. Franzen, U. Fantz, M. Bandyopadhyay, S. Christ, A. Encheva, M. Früschle, D. Holtum, B. Heinemann, W. Kraus, A. Lorenz, Ch. Martens, P. McNeely, S. Obermayer, R. Riedl, R. Süß, A. Tanga, R. Wilhelm, and D. Wunderlich. Overview of the rf source development programme at ipp garching. *Nuclear Fusion*, 46(6):S220, 2006.
- [6] K Ikeda, H Nakano, K Tsumori, M Kasaki, K Nagaoka, M Osakabe, Y Takeiri, and O Kaneko. Identification of the extraction structure of  $h^-$  ions by  $h_\alpha$  imaging spectroscopy. *New Journal of Physics*, 15(10):103026, 2013.
- [7] R. Hemsworth, H. Decamps, J. Graceffa, B. Schunke, M. Tanaka, M. Dremel, A. Tanga, H.P.L. De Esch, F. Geli, J. Milnes, T. Inoue, D. Marcuzzi, P. Sonato, and P. Zaccaria. Status of the iter heating neutral beam system. *Nuclear Fusion*, 49(4):045006, 2009.
- [8] G. McCracken and P. Stott. *Fusion: The Energy of the Universe*. Academic Press, 2012.

- [9] J. Jacquinot, F. Albajar, B. Beaumont, A. Becoulet, T. Bonicelli, D. Bora, D. Campbell, A. Chakraborty, C. Darbos, H. Decamps, G. Denisov, R. Goulding, J. Graceffa, T. Gassmann, R. Hemsworth, M. Henderson, G.T. Hoang, T. Inoue, N. Kobayashi, P.U. Lamalle, A. Mukherjee, M. Nightingale, D. Rasmussen, S.L. Rao, G. Saibene, K. Sakamoto, R. Sartori, B. Schunke, P. Sonato, D. Swain, K. Takahashi, M. Tanaka, A. Tanga, and K. Watanabe. Progress on the heating and current drive systems for iter. *Fusion Engineering and Design*, 84(26):125 – 130, 2009. Proceeding of the 25th Symposium on Fusion Technology (SOFT-25).
- [10] P. Sonato, P. Agostinetti, G. Anaclerio, V. Antoni, O. Barana, M. Bigi, M. Boldrin, M. Cavenago, S. Dal Bello, M. Dalla Palma, A. Daniele, M. D’Arienzo, A. De Lorenzi, A. Ferro, A. Fiorentin, E. Gaio, E. Gazza, L. Grando, F. Fantini, F. Fellin, A. Luchetta, G. Manduchi, F. Milani, D. Marcuzzi, L. Novello, R. Pasqualotto, M. Pavei, R. Pengo, S. Peruzzo, A. Pesce, N. Pilan, R. Piovano, N. Pomaro, M. Recchia, W. Rigato, A. Rizzolo, G. Serianni, M. Spolaore, P. Spolaore, S. Sandri, C. Taliercio, V. Toigo, M. Valisa, P. Veltri, P. Zaccaria, A. Zamengo, and L. Zanotto. The iter full size plasma source device design. *Fusion Engineering and Design*, 84(2-6):269 – 274, 2009. Proceeding of the 25th Symposium on Fusion Technology (SOFT-25).
- [11] D. Marcuzzi, M. Dalla Palma, M. Pavei, B. Heinemann, W. Kraus, and R. Riedl. Detailed design of the rf source for the 1 mv neutral beam test facility. *Fusion Engineering and Design*, 84(7-11):1253 – 1258, 2009.
- [12] U. Fantz, P. Franzen, W. Kraus, M. Berger, S. Christ-Koch, M Fröschle, R. Gutser, B. Heinemann, C. Martens, P. McNeely, R. Riedl, E. Speth, and D. Wunderlich. Negative ion rf sources for iter nbi: status of the development and recent achievements. *Plasma Phys. Control. Fusion*, 49:B563, 2007.
- [13] M. Fröschle, U. Fantz, P. Franzen, W. Kraus, R. Nocentini, L. Schiesko, and D. Wunderlich. Magnetic filter field for elise-concepts and design. *Fusion Engineering and Design*, 88(6-8):1015 – 1019, 2013. Proceedings of the 27th Symposium On Fusion Technology (SOFT-27); Liège, Belgium, September 24-28, 2012.
- [14] P Franzen, D Wunderlich, U Fantz, and the NNBI Team. On the electron extraction in a large rf-driven negative hydrogen ion source for the iter nbi system. *Plasma Physics and Controlled Fusion*, 56(2):025007, 2014.
- [15] P. McNeely, S. V. Dudin, S. Christ-Koch, U. Fantz, and the NNBI Team. A langmuir probe system for high power rf-driven negative ion sources on high potential. *Plasma Sources Sci. Technol.*, 18:014011, 2009.

- 
- [16] C. Wimmer and U. Fantz. Dependence of the source performance on plasma parameters at the batman test facility. *AIP Conference Proceedings*, 1655, 2015.
- [17] U. Fantz, P. Franzen, W. Kraus, H. D. Falter, M. Berger and S. Christ-Koch, M. Fröschle, R. Gutser, B. Heinemann, C. Martens and P. McNeely, R. Riedl, E. Speth, and D. Wunderlich. Low pressure and high power rf sources for negative hydrogen ions for fusion applications (iter neutral beam injection) (invited). *Review of Scientific Instruments*, 79(2):02A511, 2008.
- [18] G. Fubiani, G. J. M. Hagelaar, J. P. Boeuf, and S. Kolev. Modeling a high power fusion plasma reactor-type ion source: Applicability of particle methods. *Physics of Plasmas*, 19(4):043506, 2012.
- [19] G. Fubiani and J. P. Boeuf. Role of positive ions on the surface production of negative ions in a fusion plasma reactor type negative ion source insights from a three dimensional particle-in-cell monte carlo collisions model. *Physics of Plasmas*, 20(11):–, 2013.
- [20] J. P. Boeuf, J. Claustre, B. Chaudhury, and G. Fubiani. Physics of a magnetic filter for negative ion sources. ii. e x b drift through the filter in a real geometry. *Physics of Plasmas*, 19(11):113510, 2012.
- [21] G J M Hagelaar, G Fubiani, and J-P Boeuf. Model of an inductively coupled negative ion source: I. general model description. *Plasma Sources Science and Technology*, 20(1):015001, 2011.
- [22] W. B. Kunkel. Hall effect in a plasma. *American Journal of Physics*, 49(8):733–738, 1981.
- [23] G. Fubiani and J. P. Boeuf. Plasma asymmetry due to the magnetic filter in fusion-type negative ion sources: Comparisons between two and three-dimensional particle-in-cell simulations. *Physics of Plasmas*, 21(7), 2014.
- [24] K. Nanbu. Probability theory of electron-molecule, ion-molecule, molecule-molecule, and coulomb collisions for particle modeling of materials processing plasmas and cases. *Plasma Science, IEEE Transactions on*, 28(3):971 –990, 2000.
- [25] G.A. Bird. *Molecular Gas Dynamics and the Direct Simulation of Gas Flows*. Oxford engineering science series. Clarendon Press, 1998.
- [26] P McNeely, D Wunderlich, and the NNBI Team. Neutral depletion in an h source operated at high rf power and low input gas flow. *Plasma Sources Sci. Technol.*, 20(4):045005, 2011.

- [27] <http://www.openmp.org>.
- [28] K. Miyamoto, S. Okuda, S. Nishioka, and A. Hatayama. Effect of basic physical parameters to control plasma meniscus and beam halo formation in negative ion sources. *Journal of Applied Physics*, 114(10), 2013.
- [29] S Mochalsky, D Wunderlich, B Ruf, U Fantz, P Franzen, and T Minea. On the meniscus formation and the negative hydrogen ion extraction from iter neutral beam injection relevant ion source. *Plasma Physics and Controlled Fusion*, 56(10):105001, 2014.
- [30] F Taccogna, P Minelli, and S Longo. Three-dimensional structure of the extraction region of a hybrid negative ion source. *Plasma Sources Science and Technology*, 22(4):045019, 2013.
- [31] J P Boeuf, G Fubiani, and L Garrigues. Issues in the understanding of negative ion extraction for fusion. *Plasma Sources Science and Technology*, 25(4):045010, 2016.
- [32] C. K. Birdsall and A. B. Langdon. *Plasma Physics Via Computer Simulation*. IOP Publishing, 1998.
- [33] R. W. Hockney and J. W. Eastwood. *Computer Simulation Using Particles*. McGraw-Hill, 1981.
- [34] K.J Bowers. Accelerating a particle-in-cell simulation using a hybrid counting sort. *Journal of Computational Physics*, 173(2):393 – 411, 2001.
- [35] W. L. Briggs, V. E. Henson, and S. F. McCormick. *A Multigrid Tutorial*. SIAM, 2000.
- [36] J P Boeuf, G J M Hagelaar, P Sarrailh, G Fubiani, and N Kohen. Model of an inductively coupled negative ion source: Ii. application to an iter type source. *Plasma Sources Science and Technology*, 20(1):015002, 2011.
- [37] M. A. Lieberman and A. J. Lichtenberg. *Principles of Plasma Discharges and Materials Processing*. Wiley Interscience, 2005.
- [38] G Fubiani and J P Boeuf. Three-dimensional modeling of a negative ion source with a magnetic filter: impact of biasing the plasma electrode on the plasma asymmetry. *Plasma Sources Science and Technology*, 24(5):055001, 2015.
- [39] Kenichi Nanbu. Direct simulation scheme derived from the boltzmann equation. i. monocomponent gases. *Journal of the Physical Society of Japan*, 49(5):2042–2049, 1980.

- 
- [40] Yukikazu Itikawa. Momentum-transfer cross sections for electron collisions with atoms and molecules. *Atomic Data and Nuclear Data Tables*, 14(1):1 – 10, 1974.
- [41] R. K. Janev. *Atomic and Molecular Processes in Fusion Edge Plasmas*. Springer, 1995.
- [42] J F Williams. Electron scattering from hydrogen atoms. ii. elastic scattering at low energies from 0.5 to 8.7 ev. *Journal of Physics B: Atomic and Molecular Physics*, 8(10):1683, 1975.
- [43] J F Williams. Electron scattering from atomic hydrogen. iii. absolute differential cross sections for elastic scattering of electrons of energies from 20 to 680 ev. *Journal of Physics B: Atomic and Molecular Physics*, 8(13):2191, 1975.
- [44] Igor Bray, Dmitry A. Konovalov, and Ian E. McCarthy. Electron scattering by atomic hydrogen: Elastic and inelastic phenomena at 13.9–200 ev. *Phys. Rev. A*, 44:5586–5598, 1991.
- [45] R. K. Janev, D. Reiter, and U. Samm. Collision processes in low-temperature hydrogen plasmas. Technical Report 4105, FZ-Juelich, 2003.
- [46] S. J. Buckman and A. V. Phelps. Vibrational excitation of d[<sub>2</sub>] by low energy electrons. *The Journal of Chemical Physics*, 82(11):4999–5011, 1985.
- [47] Jung-Sik Yoon, Mi-Young Song, Jeong-Min Han, Sung Ha Hwang, Won-Seok Chang, BongJu Lee, and Yukikazu Itikawa. Cross sections for electron collisions with hydrogen molecules. *Journal of Physical and Chemical Reference Data*, 37(2):913–931, 2008.
- [48] J. P. England, M. T. Elford, and R. W. Crompton. A study of the vibrational excitation of h<sub>2</sub> by measurements of the drift velocity of electrons in h<sub>2</sub>ne mixtures. *Australian Journal of Physics*, 41:573–586, 1988.
- [49] D. K. Gibson. The cross sections for rotational excitation of h<sub>2</sub> and d<sub>2</sub> by low energy electrons. *Australian Journal of Physics*, 23:683–696, 1970.
- [50] M. G. Heaps and A. E. S. Green. Energy spreading and angular distribution of a beam of electrons in molecular hydrogen. *Journal of Applied Physics*, 46(11):4718–4725, 1975.
- [51] H. Ehrhardt, L. Langhans, F. Linder, and H. S. Taylor. Resonance scattering of slow electrons from h<sub>2</sub> and co angular distributions. *Phys. Rev.*, 173:222–230, 1968.

- [52] R. H. Garvey, H. S. Porter, and A. E. S. Green. Relativistic yield spectra for  $\text{h}[\text{sub } 2]$ . *Journal of Applied Physics*, 48(10):4353–4359, 1977.
- [53] R. K. Janev. *Elementary Processes in Hydrogen-Helium Plasmas*. Springer, 1987.
- [54] St. Kolev, G. J. M. Hagelaar, and J. P. Boeuf. Particle-in-cell with monte carlo collision modeling of the electron and negative hydrogen ion transport across a localized transverse magnetic field. *Physics of Plasmas*, 16(4):042318, 2009.
- [55] F Gaboriau and J P Boeuf. Chemical kinetics of low pressure high density hydrogen plasmas: application to negative ion sources for iter. *Plasma Sources Science and Technology*, 23(6):065032, 2014.
- [56] M. Bandyopadhyay and R. Wilhelm. Simulation of negative hydrogen ion production and transport. *Review of Scientific Instruments*, 75(5):1720–1722, 2004.
- [57] Predrag S. Krstić. Inelastic processes from vibrationally excited states in slow  $\text{h}^+ + \text{h}_2$  and  $\text{h} + \text{h}_2^+$  collisions: Excitations and charge transfer. *Phys. Rev. A*, 66:042717, 2002.
- [58] Predrag S. Krstić. Vibrationally resolved collisions in cold hydrogen plasma. *Nuclear Instruments and Methods in Physics Research Section B: Beam Interactions with Materials and Atoms*, 241(14):58 – 62, 2005.
- [59] A. V. Phelps. Cross sections and swarm coefficients for  $\text{h}[\text{sup } + ]$ ,  $\text{h}[\text{sub } 2][\text{sup } + ]$ ,  $\text{h}[\text{sub } 3][\text{sup } + ]$ ,  $\text{h}$ ,  $\text{h}[\text{sub } 2]$ , and  $\text{h}[\text{sup } - ]$  in  $\text{h}[\text{sub } 2]$  for energies from 0.1 eV to 10 keV. *Journal of Physical and Chemical Reference Data*, 19(3):653–675, 1990.
- [60] A. V. Phelps. Energetic ion, atom, and molecule reactions and excitation in low-current  $\text{h}_2$  discharges: Model. *Phys. Rev. E*, 79:066401, 2009.
- [61] P S Krstić and D R Schultz. Elastic processes involving vibrationally excited molecules in cold hydrogen plasmas. *Journal of Physics B: Atomic, Molecular and Optical Physics*, 36(2):385, 2003.
- [62] P. S. Krstic and D. R. Schultz. Elastic and related transport cross sections for collisions among isotopomers of  $\text{h}^+ + \text{h}$ ,  $\text{h}^+ + \text{h}_2$ ,  $\text{h}^+ + \text{he}$ ,  $\text{h} + \text{h}$  and  $\text{h} + \text{h}_2$ . *Atomic and Plasma-Material Interaction Data for Fusion*, 8:1–699, 1998.
- [63] C. F. Barnett. Collisions of  $\text{h}$ ,  $\text{h}_2$ ,  $\text{he}$ , and  $\text{li}$  atoms and ions with atoms and molecules. Technical Report ORNL-6086, Oak ridge national laboratory, 1990.

- 
- [64] T. Tabata and T. Shirai. Analytic cross sections for collisions of  $h^+$ ,  $h_2^+$ ,  $h_3^+$ ,  $h$ ,  $h_2$ , and  $h$  with hydrogen molecules. *Atomic Data and Nuclear Data Tables*, 76(1):1 – 25, 2000.
- [65] J. D. Callen. Fundamentals of plasma physics. Lecture Notes, University of Wisconsin, Madison, <http://homepages.cae.wisc.edu/~callen/book.html>, 2003.
- [66] V. E. Golant, A. P. Zhilinsky, and I. E. Sakharov. *Fundamentals of plasma physics*. John Wiley & Sons, 1980.
- [67] Eirene database, <http://www.eirene.de/html/surfacedata.html>.
- [68] S. Krischok, H. Müller, and V. Kempter. Surface induced dissociation in slow collisions of  $h_2^+$  and  $o_2^+$ : information from the ion impact electron spectra. *Nuclear Instruments and Methods in Physics Research Section B: Beam Interactions with Materials and Atoms*, 157(14):198 – 207, 1999.
- [69] G. Cartry, L. Schiesko, C. Hopf, A. Ahmad, M. Carrre, J. M. Layet, P. Kumar, and R. Engeln. Production of negative ions on graphite surface in  $h_2/d_2$  plasmas: Experiments and srim calculations. *Physics of Plasmas*, 19(6), 2012.
- [70] M Seidl, H L Cui, J D Isenberg, H J Kwon, B S Lee, and S T Melnychuk. Negative surface ionization of hydrogen atoms and molecules. *Journal of Applied Physics*, 79(6):2896, 1996.
- [71] D Wunderlich, R Gutser, and U Fantz. Pic code for the plasma sheath in large caesiated rf sources for negative hydrogen ions. *Plasma Sources Science and Technology*, 18(4):045031, 2009.
- [72] R McAdams, A J T Holmes, D B King, and E Surrey. Transport of negative ions across a double sheath with a virtual cathode. *Plasma Sources Sci. Technol.*, 20(3):035023, 2011.
- [73] W. Eckstein and J.P. Biersack. Reflection of low-energy hydrogen from solids. *Applied Physics A*, 38(2):123–129, 1985.
- [74] A. Ando, K. Tsumori, Y. Takeiri, O. Kaneko, Y. Oka, T. Okuyama, H. Kojima, Y. Yamashita, R. Akiyama, T. Kawamoto, K. Mineo, T. Kurata, and T. Kuroda. Cesium seeded experiments on the 1/3 scaled ion source for large helical device. *AIP Conference Proceedings*, 287(1):339–352, 1992.
- [75] D. Ciric. private communication.

- [76] S. E. Parker and C. K. Birdsall. Numerical error in electron orbits with large  $\omega_{ce}\delta t$ . *Journal of Computational Physics*, 97:91, 1991.
- [77] G J M Hagelaar and N Oudini. Plasma transport across magnetic field lines in low-temperature plasma sources. *Plasma Physics and Controlled Fusion*, 53(12):124032, 2011.
- [78] J. P. Boeuf, B. Chaudhury, and L. Garrigues. Physics of a magnetic filter for negative ion sources. i. collisional transport across the filter in an ideal, 1d filter. *Physics of Plasmas*, 19(11):–, 2012.
- [79] G. Ecker and H. Kanne. Cylindrical plasma column in a transverse magnetic field. *Physics of Fluids (1958-1988)*, 7(11):1834–1842, 1964.
- [80] F. Gaboriau, R. Baude, and G. J. M. Hagelaar. Experimental evidence of the increased transport due to the wall bounded magnetic drift in low temperature plasma. *Appl. Phys. Lett.*, 104(21):214107, 2014.
- [81] L Schiesko, P McNeely, P Franzen, U Fantz, and the NNBI Team. Magnetic field dependence of the plasma properties in a negative hydrogen ion source for fusion. *Plasma Physics and Controlled Fusion*, 54(10):105002, 2012.
- [82] P. Franzen, H.D. Falter, U. Fantz, W. Kraus, M. Berger, S. Christ-Koch, M. Fröschle, R. Gutser, B. Heinemann, S. Hilbert, S. Leyer, C. Martens, P. McNeely, R. Riedl, E. Speth, and D. Wunderlich. Progress of the development of the ipp rf negative ion source for the iter neutral beam system. *Nuclear Fusion*, 47(4):264, 2007.
- [83] M. Bacal. Effect of fast positive ions incident on caesiated plasma grid of negative ion source. *Review of Scientific Instruments*, 83(2):02B101, 2012.
- [84] D Wunderlich, L Schiesko, P McNeely, U Fantz, P Franzen, and the NNBI-Team. On the proton flux toward the plasma grid in a rf-driven negative hydrogen ion source for iter nbi. *Plasma Physics and Controlled Fusion*, 54(12):125002, 2012.
- [85] S Christ-Koch, U Fantz, M Berger, and NNBI Team. Laser photodetachment on a high power, low pressure rf-driven negative hydrogen ion source. *Plasma Sources Science and Technology*, 18(2):025003, 2009.
- [86] L. Schiesko. private communication.
- [87] K. N. Leung and M. Bacal.  $h^-$  ion density measurement in a tandem multicusp discharge. *Review of Scientific Instruments*, 55(3):338–341, 1984.

- 
- [88] S. Mochalsky, A. F. Lifschitz, and T. Minea. Extracted current saturation in negative ion sources. *Journal of Applied Physics*, 111(11), 2012.
- [89] F. Taccogna, P. Minelli, S. Longo, M. Capitelli, and R. Schneider. Modeling of a negative ion source. iii. two-dimensional structure of the extraction region. *Physics of Plasmas*, 17(6):063502, 2010.
- [90] Yu. I. Belchenko, Y. Oka, O. Kaneko, Y. Takeiri, K. Tsumori, M. Osakabe, K. Ikeda, E. Asano, and T. Kawamoto. Negative ion source improvement by introduction of a shutter mask. *Review of Scientific Instruments*, 75(5):1726–1728, 2004.
- [91] M. Kashiwagi, N. Umeda, H. Tobar, A. Kojima, M. Yoshida, M. Taniguchi, M. Dairaku, T. Maejima, H. Yamanaka, K. Watanabe, T. Inoue, and M. Hanada. Development of negative ion extractor in the high-power and long-pulse negative ion source for fusion application. *Review of Scientific Instruments*, 85(2), 2014.
- [92] G.D. Alton. 3. sources of low-charge-state positive-ion beams\*. In F.B. Dunning and Randall G. Hulet, editors, *Atomic, Molecular, and Optical Physics: Charged Particles*, volume 29, Part A of *Methods in Experimental Physics*, pages 69 – 168. Academic Press, 1995.
- [93] M Berger, U Fantz, S Christ-Koch, and NNBI Team. Cavity ring-down spectroscopy on a high power rf driven source for negative hydrogen ions. *Plasma Sources Science and Technology*, 18(2):025004, 2009.
- [94] T. Inoue, E. Di Pietro, M. Hanada, R. S. Hemsworth, A. Krylov, V. Kulygin, P. Massmann, P. L. Mondino, Y. Okumura, A. Panasenkov, E. Speth, and K. Watanabe. Design of neutral beam system for iter-feat. *Fusion Eng. Design*, 56-57:517, 2001.
- [95] ITER Physics Basis Editors, ITER Physics Expert Group Chairs and Co-Chairs, ITER Joint Central Team and Physics Integration Unit, and ITER EDA. Iter physics basis. *Nucl. Fusion*, 39:2137, 1999.
- [96] K. Watanabe, Y. Fujiwara, M. Hanada, M. Kashiwagi, T. Kitagawa, K. Miyamoto, T. Morishita, Y. Okumura, T. Takayanagi, and M. Taniguchi. Hydrogen negative ion beam acceleration in a multiaperture five-stage electrostatic accelerator. *Rev. Sci. Instrum.*, 71:1231, 2000.
- [97] V. Vahedi and M. Surendra. A monte carlo collision model for the particle-in-cell method: applications to argon and oxygen discharges. *Comp. Phys. Comm.*, 87:179, 1995.

- [98] W. G. Graham. Properties of alkali metals adsorbed onto metal surfaces. In Th. Sluyters, editor, *Proceedings of the Second International Symposium on the Production and Neutralization of Negative Hydrogen Ions and Beams*, page 126. Brookhaven National Laboratory, Upton, NY, 1980.
- [99] H. P. L. de Esch. Private communication.
- [100] J. Pamela. A model for negative ion extraction and comparison of negative ion optics calculations to experimental results. *Rev. Sci. Instrum.*, 62:1163, 1991.
- [101] J. D. Jackson. *Classical Electrodynamics*. John Wiley & Sons, 1998.
- [102] R. Trainham, C. Jacquot, D. Riz, A. Simonin, K. Miyamoto, Y. Fujiwara, and Y. Okumura. Negative ion sources for neutral beam injection into fusion machines. *Rev. Sci. Instrum.*, 69:926, 1998.
- [103] T. Koshikawa and R. Shimizu. Secondary electron and backscattering measurements for polycrystalline copper with a spherical retarding-field analyser. *J. Phys. D*, 6:1369, 1973.
- [104] T. Matsukawa, R. Shimizu, and H. Hashimoto. Measurements of the energy distribution of backscattered kilovolt electrons with a spherical retarding-field analyser. *J. Phys. D*, 7:695, 1974.
- [105] E. H. Darlington. Backscattering of 10-100 keV electrons from thick targets. *J. Phys. D*, 8:85, 1975.
- [106] E. J. Sternglass. Backscattering of kilovolt electrons from solids. *Phys. Rev.*, 95(2):345, 1953.
- [107] M. A. Furman and M. T. F. Pivi. Probabilistic model for the simulation of secondary electron emission. *Phys. Rev. STAB*, 5(12):124404, 2002.
- [108] P-F. Staub. Bulk target backscattering coefficient and energy distribution of 0.5-100 keV electrons: an empirical and synthetic study. *J. Phys. D*, 27:1533, 1994.
- [109] M. B. E. Bruining. *Physics and applications of secondary electron emission*. Pergamon press ltd, 1954.
- [110] Y. F. Chen. Angular distribution of electrons elastically backscattered from non-crystalline solid surfaces. *J. Phys. D*, 28:2163, 1995.

- 
- [111] E. W. Thomas. Particle interactions with surfaces. Technical Report ORNL-6088, Oak ridge national laboratory, 1985.
- [112] A. M. D. Assa'd and M. M. El Gomati. Backscattering coefficients for low-energy electrons. *Scanning Microscopy*, 12:1, 1998.
- [113] P. J. Ebert, A. F. Lauzon, and E. M. Lent. Transmission and backscattering of 4.0- to 12.0-mev electrons. *Phys. Rev.*, 183:422, 1969.
- [114] K. A. Wright and J. G. Trump. Back-scattering of megavolt electrons from thick targets. *J. Appl. Phys.*, 33:687, 1962.
- [115] L. Wang, Y. Y. Lee, G. Mahler, W. Meng, D. Raparia, J. Wei, and S. Henderson. Stripped electron collection at the spallation neutron source. *Phys. Rev. STAB*, 8:094201, 2005.
- [116] V. Baglin, I. Collins, B. Henrist, N. Hilleret, and G. Vorlaufer. A summary of main experimental results concerning the secondary electron emission of copper. Technical Report (LHC Project Report) 472, CERN, 2002.
- [117] B. Henrist, N. Hilleret, M. Jimenez, C. Scheuerlein, M. Taborelli, and G. Vorlaufer. Secondary emission data for the simulation of electron cloud. Technical Report (Yellow Report) CERN-2002-001, CERN, 2002.
- [118] Ya. M. Fogel, A. G. Koval, Yu. Z. Levchenko, and A. F. Khodyachikh. Composition of slow ions produced during the ionization of gases by negative ions. *Soviet Phys. JETP*, 12:384, 1961.
- [119] B. Svensson and G. Holmén. Electron emission from aluminium and copper under molecular-hydrogen-ion bombardment. *Phys. Rev. B*, 25:3056, 1982.
- [120] R. A. Baragiola, E. V. Alonso, and A. Oliva Florio. Electron emission from clean metal surfaces induced by low-energy light ions. *Phys. Rev. B*, 19:121, 1979.
- [121] W. Eckstein and F. E. P. Matschke. Charge-state fractions of hydrogen backscattered from gold. *Phys. Rev. B*, 14:3231, 1976.
- [122] A. Krylov and R. S. Hemsworth. Gas flow and related beam losses in the iter neutral beam injector. *Fusion Eng. Design*, 81:2239, 2006.
- [123] S. Dushman and J. M. Lafferty. *Scientific foundations of vacuum technique*. John Wiley & Sons Inc, 1962.

- [124] K. N. Leung, O. A. Anderson, C. F. Chan, W. S. Cooper, G. J. de Vries, C. A. Hauck, W. B. Kunkel, K. W. Kwan, A. F. Lietzke, P. Purgalis, and R. P. Wells. Development of an advanced "volume" h- sources for neutral beam application. *Rev. Sci. Instrum.*, 61:2378, 1990.
- [125] J. W. Kwan, G. D. Ackermann, O. A. Anderson, C. F. Chan, W. S. Cooper, G. J. deVries, W. B. Kunkel, K. N. Leung, P. Purgalis, W. F. Steele, and R. P. Wells. Testing of an advanced "volume" h- source and pre-accelerator. *Rev. Sci. Instrum.*, 62:1521, 1991.
- [126] A. Ando, Y. Yakeiri, K. Tsummori, O. Kaneko, Y. Oka, R. Akiyama, T. Kawamoto, K. Minone, T. Kurata, and T. Kuroda. Experiments on the multiampere negative ion source in national institute for fusion science. *Rev. Sci. Instrum.*, 63:2683, 1992.
- [127] Y. Okumura, M. Hanada, T. Inoue, H. Kojima, Y. Matsuda, Y. Ohara, M. Seki, and K. Watanabe. Cesium mixing in the multi-ampere volume h- ion source. In A. Hershcovitch, editor, *Proceedings of the Fifth International Symposium on the Production and Neutralization of Negative Hydrogen Ions and Beams*, volume 210, pages 169–183. AIP Conf. Proc, 1990.
- [128] M. Hanada, T. Inoue, M. Mizuno, Y. Ohara, Y. Okumura, Y. Suzuki, H. Tanaka, M. Tanaka, and K. Watanabe. Negative ion production in a large semicylindrical ion source. *Rev. Sci. Instrum.*, 63:2699, 1992.
- [129] G. Fubiani, J. Qiang, E. Esarey, W.P. Leemans, and G. Dugan. Space charge modeling of dense electron beams with large energy spreads. *Phys. Rev. STAB*, 9:064402, 2006.
- [130] H.P.L. de Esch, R.S. Hemsworth, and P. Massmann. Updated physics design iter-singap accelerator. *Fusion Eng. Design*, 73:329, 2005.
- [131] G. Fubiani, H. P. L. de Esch, A. Simonin, and R. S. Hemsworth. Modeling of secondary emission processes in the negative ion based electrostatic accelerator of the international thermonuclear experimental reactor. *Phys. Rev. ST Accel. Beams*, 11, Jan 2008.
- [132] M. Taniguchi, T. Inoue, N. Umeda, M. Kashiwagi, K. Watanabe, H. Tobari, M. Dairaku, and K. Sakamoto. Acceleration of ampere class h<sup>-</sup> ion beam by mev accelerator. *Rev. Sci. Instrum.*, 79:02C110, 2008.
- [133] R. D. DuBois and A. Kövèr. Single and double ionization of helium by hydrogen-atom impact. *Phys. Rev. A*, 40:3605, 1989.

- 
- [134] L. Svensson, D. Boilson, H.P.L. de Esch, R.S. Hemsworth, and A. Krylov. Experimental results from the cadarache 1mv test bed with singap accelerators. *Nucl. Fusion*, 46:S369, 2006.
- [135] H.P.L. de Esch, L. Svensson, T. Inoue, M. Taniguchi, N. Umeda, M. Kashiwagi, and G. Fubiani. Results of the singap neutral beam accelerator experiment at jaea. *Fusion Engineering and Design*, 84(2-6):669 – 675, 2009.
- [136] T. Inoue, M. Kashiwagi, M. Taniguchi, M. Dairaku, M. Hanada, K. Watanabe, and K. Sakamoto. 1mev, ampere class accelerator r&d for iter. *Nucl. Fusion*, 46:S379, 2008.
- [137] L Schiesko, P Franzen, and U Fantz. Investigation of the magnetic field influence on the plasma parameter homogeneity in a large  $h^-/d^-$  rf ion source relevant for iter. *Plasma Sources Science and Technology*, 21(6):065007, 2012.
- [138] T. Inoue, M. Taniguchi, M. Kashiwagi, N. Umeda, H. Tobar, M. Dairaku, J. Takemoto, K. Tsuchida, K. Watanabe, H. Yamanaka, A. Kojima, M. Hanada, and K. Sakamoto. Acceleration of 1 mev  $h^-$  ion beams at iter nb-relevant high current density. Technical report, International Atomic Energy Agency (IAEA), 2012. IAEA-CN-197.
- [139] A. Simonin, Jocelyn Achard, K. Achkasov, S. Bechu, C. Baudouin, O. Baulaigue, C. Blondel, J.P. Boeuf, D. Bresteau, G. Cartry, W. Chaibi, C. Drag, H.P.L. de Esch, D. Fiorucci, G. Fubiani, I. Furno, R. Futtersack, P. Garibaldi, A. Gicquel, C. Grand, Ph. Guittienne, G. Hagelaar, A. Howling, R. Jacquier, M.J. Kirkpatrick, D. Lemoine, B. Lepetit, T. Minea, E. Odic, A. Revel, B.A. Soliman, and P. Teste. R&d around a photoneutralizer-based nbi system (siphore) in view of a demo tokamak steady state fusion reactor. *Nuclear Fusion*, 55(12):123020, 2015.
- [140] A. Simonin. Private communication.
- [141] B. I. Cohen, A. B. Langdon, and A. Friedman. Implicit time integration for plasma simulation. *Journal of Computational Physics*, 46:15, 1982.
- [142] A. Bruce Langdon, Bruce I. Cohen, and Alex Friedman. Direct implicit large time-step particle simulation of plasmas. *Journal of Computational Physics*, 51(1):107 – 138, 1983.
- [143] A. B. Langdon. Analysis of the time integration in plasma simulation. *Journal of Computational Physics*, 30:202, 1979.

- 
- [144] A. B. Langdon. Implicit plasma simulation. *Space Science Reviews*, 42:67, 1985.
- [145] D. W. Hewett and A. B. Langdon. Electromagnetic direct implicit plasma simulation. *Journal of Computational Physics*, 72:121, 1987.
- [146] Bruce I. Cohen, A. Bruce Langdon, Dennis W. Hewett, and Richard J. Proccassini. Performance and optimization of direct implicit particle simulation. *Journal of Computational Physics*, 81(1):151 – 168, 1989.
- [147] Matthew R. Gibbons and Dennis W. Hewett. The darwin direct implicit particle-in-cell (dadipic) method for simulation of low frequency plasma phenomena. *Journal of Computational Physics*, 120(2):231 – 247, 1995.